To the Graduate Council:

I am submitting herewith a dissertation written by Galen C. Richeson entitled "PROCESSING–STRUCTURE–PROPERTY RELATIONSHIPS IN ELASTIC COPOLYESTER-ETHER FILAMENTS." I have examined the final copy of this dissertation for form and content and recommend that it be accepted in partial fulfillment of the requirements for the degree of Doctor of Philosophy, with a major in Polymer Engineering.

J. E. Spruiell

Joseph E. Spruiell, Major Professor

We have read this dissertation
and recommend its acceptance:

Edward S. Clark

Robert S. Benson

John L. Crouse

Jan-chyang Lin

Accepted for the Council:

Lew Minkel

Vice Provost
and Dean of The Graduate School

PROCESSING–STRUCTURE–PROPERTY RELATIONSHIPS IN ELASTIC COPOLYESTER-ETHER FILAMENTS

A Dissertation

Presented for the

Doctor of Philosophy

Degree

The University of Tennessee, Knoxville

Galen C. Richeson

December 1988

ACKNOWLEDGEMENTS

The author would like to thank his advisor Professor Joseph E. Spruiell for his guidance during the course of this research. He would also like to thank Dr. E.S. Clark, Dr. R.S. Benson, Dr. J.S. Lin, and Dr. J.L. Crouse for serving on his committee and for their helpful suggestions. Special thanks is extended to Dr. D.C. Bogue for his support and encourgement. The author also appreciates the advice and assistance he received from many of his fellow graduate students.

The author wishes to thank Doug and Jack in the Machine Shop and Ron and Steve in the Electronics shop for their technical support and input.

The author is especially grateful to the Center for Materials Processing, members of the Polymer Consortium, and to the American Cyanamid Company for their financial support. He would also like to acknowledge Celanese Plastics and Specialties Company (now Hoechst–Celanese) and the E.I. duPont de Nemours & Company for providing the copolyester-ether and poly(tetramethylene terephthalate) resins used in this research.

ABSTRACT

Elastic filaments have been produced by melt-spinning poly(tetramethylene terethalate)/poly(tetramethylene oxide) (PTMT/PTMO) copolymers of various hard segment contents (HSC). The microstructure and mechanical properties were found to be strongly dependent on composition, spinning speed, and annealing treatment.

The crystallization rate and crystallization temperature both decrease as HSC decreases. Because of the sluggish crystallization kinetics in some compositions, a water quench bath was used in the spinning process.

All the samples exhibited two-point small angle x-ray scattering patterns which indicate a lamellar structure with some degree of preferred orientation. As the spin draw ratio increases, the lamellae become increasingly aligned with their long axis perpendicular to the fiber axis. Annealing promotes phase separation in these samples through hard segment crystallization. Larger crystallites grow primarily in their equatorial crystallographic directions, although some crystallite thickening was noted in compositions having a high HSC. There is some evidence that smaller crystallites may melt during the annealing treatment. The relationship of the long period to the hard segment content and the annealing temperature are discussed in terms of the interdomain spacing.

Mechanical tests were performed on the filaments and structure-property relationships were investigated. One interesting result is that the modulus of

the copolymer filaments decreases upon annealing, while that of the PTMT homopolymer increases. These results and the effect of composition on the modulus were intepreted in terms of the relative portion of tie molecules and the modulus of the amorphous phase. Ultimate properties such as tenacity and elongation to break were found to depend more on the chain orientation than on the degree of phase separation.

Selected filaments were further processed by cold drawing, hot drawing, and by drawing and annealing. The effects of these operations on the stress-strain behavior and elastic properties are discussed and compared to the properties of the undrawn filaments. The relationship of the mechanical properties to the filament microstructure is discussed. Drawing reduces plastic deformation and increases elastic recovery. Different types of behavior are observed depending on whether the filaments are fixed or free annealed. There is a trade-off between high elastic recovery and high extensibility.

TABLE OF CONTENTS

CHAPTER		PAGE
1.	INTRODUCTION	1
2.	LITERATURE SURVEY	4
2.1	Overview of Thermoplastic Elastomers	4
2.2	Segmented Copolyester-ethers	11
2.2.1	Chemical and Molecular Structure	11
2.2.2	General Morphological Features	12
2.2.3	Mechanical and Physical Properties	29
2.2.4	Optimum Morphology for Elastic Recovery	39
2.3	Homopolymers of Interest	39
2.3.1	Poly(tetramethylene terephthalate)	39
2.3.2	Poly(tetramethylene oxide)	48
2.4	Deformation Studies	50
2.4.1	Structural Models for Block Copolymers	50
2.4.2	Structure Changes During Deformation of Copolyether-esters	52
2.4.3	Structural Changes During Deformation of Other TPEs	56
2.5	Copolymer Crystallization	65
2.6	Fiber Processing	72
2.6.1	Melt Spinning	72

2.6.2 Drawing 86
2.6.3 Annealing 90

3. CHARACTERIZATION TECHNIQUES 97

3.1 Wide-Angle X-ray Diffraction (WAXD) 97
3.1.1 Orientation Functions 98
3.1.2 Line Broadening 101
3.1.3 Crystallite Volume 103
3.2 Small Angle X-ray Scattering 105
3.2.1 Small Angle X-ray Scattering (SAXS) 105
3.2.2 Long Period 106
3.2.3 Determination of the Degree of Phase Separation 106
3.3 Thermal Analysis 109
3.4 Birefringence 109
3.5 Density 111
3.6 Dynamic Mechanical Data 114
3.7 Shrinkage in Boiling Water 115
3.8 Mechanical Properties 116
3.8.1 Tensile Properties 116
3.8.2 Elastic Properties 116

4. MATERIALS AND CRYSTALLIZATION KINETICS . . . 119

4.1 Materials 119
4.2 Quiescent Crystallization Behavior 121

4.2.1 Isothermal Crystallization 122
4.2.2 Non-isothermal Crystallization 131
4.2.3 Crystallization from the Glassy State 131

5. FIBER FORMATION AND HEAT TREATMENT 135
5.1 Melt Spinning Techniques 135
5.2 Crystallization Behavior During Spinning 137
5.3 Annealing Treatment 140

6. STRUCTURE DEVELOPMENT IN MELT SPUN FILAMENTS 143
6.1 Structural Features 143
6.1.1 Orientation 148
6.1.2 Degree of Phase Separation 157
6.1.3 Morphology 162
6.2 Discussion of Structure 183
6.3 Conclusions 191

7. MODULUS-STRUCTURE RELATIONSHIPS 195
7.1 Modulus Results 195
7.2 Analysis 198
7.2.1 Continous Crystalline Phase 203
7.2.2 Tie Molecule Model 207
7.2.3 Continous Amorphous Phase 214

7.2.4 Solution Model 219
7.2.5 Solution Model with Tie Molecules 225
7.2.6 Effects of Orientation 235
7.3 Conclusions 236

8. DEFORMATION BEHAVIOR AND MECHANICAL PROPERTIES OF THE MELT-SPUN FILAMENTS 238

8.1 Structural Changes During Deformation 238
8.2 Stress at Large Deformations 248
8.3 Elastic Properties 250
8.4 Ultimate Properties 259
8.4.1 Elongation to Break 259
8.4.2 Tenacity 262
8.5 Conclusions 265

9. DRAWN FILAMENTS 268

9.1 Introduction 268
9.2 Drawing and Annealing Treatment 270
9.3 Structure 275
9.3.1 Orientation 277
9.3.2 Degree of Phase Separation 281
9.3.3 Morphology 285
9.4 Stress-Strain Behavior and Tensile Properties 293
9.4.1 Discussion of Structure 301

9.4.2 Relationship of Tensile Properties to Structure 304
9.5 Deformation Behavior 307
9.6 Cyclic Testing 326
9.6.1 Elastic Recovery of H7246 Filaments 326
9.6.2 Elastic Recovery of H4056 Filaments 341
9.6.3 Effect of Crystallite Size 345
9.6.4 Effect of Composition 348
9.7 Discussion and Conclusions 348

10. CONCLUSIONS 358
10.1 Structure Development in As-spun Filaments 358
10.2 Modulus–Structure Relationships 360
10.3 Deformation Behavior and Mechanical Properties of As-Spun Filaments 362
10.4 Structure and Properties of Drawn Filaments 364

LIST OF REFERENCES 367

APPENDIX 380

VITA 397

LIST OF TABLES

TABLE		PAGE
2.1	Typical mechanical properties of Hytrel® type copolyesters. . .	32
2.2	Characteristics of some copolyester elastomers.	33
4.1	Composition and approximate phase transition temperatures of the copolyester-ethers used in this study.	120
4.2	Crystallization half-times, Avrami exponents and crystallization rate constants.	123
6.1	Percent shrinkage of as-spun filaments after immersion in boiling water.	153
6.2	Percent shrinkage of annealed filaments after immersion in boiling water.	156
6.3	Density of as-spun filaments as a function of composition and spinning speed.	158
7.1	Experimental data used in the Takayanagi analysis.	202
7.2	Values of γ_a^2 predicted by the "crystalline matrix" model using the observed values of the modulus and the data for β_a.	206
7.3	Fraction of taut tie molecules predicted by the "tie molecule" model using the experimental data shown.	212
7.4	Macroscopic modulus E_{comp} predicted by the "amorphous matrix" model using experimental data for β_c and γ_c.	218

7.5 Modulus of the amorphous phase predicted by the "solution" model using the experimental data shown. 223

8.1 Ratios of mean square electron density fluctuations. 242

8.2 Long periods observed for the H4056 filament in the strained state. 244

8.3 Long periods observed for the H4056 filament after retraction. . 244

9.1 Draw ratios and diamenters of drawn filaments. 274

9.2 Final strain ratio and shrinkage of cold drawn filaments during free annealing. 276

9.3 Crystalline chain orientation functions for the drawn filaments. 278

9.4 Percent shrinkage of as-spun and drawn filaments after two minutes in boiling water. 280

9.5 Type of crystalline phases present in filaments spun at 50 m/min and drawn. 290

9.6 Long period (in Å) of filaments spun at 50 m/min and drawn. . 292

9.7 Ultimate elongations ($\frac{L-L_0}{L_0}$) of as-spun and drawn filaments. . . 297

9.8 Tenacities (in MPa) of the drawn filaments. 298

9.9 Moduli (in MPa) of the drawn filamants. 299

9.10 Long periods observed for the drawn H4056 filament in the strained state. 312

9.11 Long periods observed for the drawn H4056 filament after retraction. 312

9.12 Long periods observed for the drawn and fixed annealed H4056 filament in the strained state. 316
9.13 Long periods observed for the drawn and fixed annealed H4056 filament after retraction. 316
9.14 Long periods observed for the drawn and free annealed H4056 filament in the strained state. 320
9.15 Long periods observed for the drawn and free annealed H4056 filament after retraction. 320
9.16 Long periods observed for the drawn and free annealed H7246 filament in the strained state. 324
9.17 Long periods observed for the drawn and free annealed H7246 filament after retraction. 324
9.18 Effect of composition on maximum elongation and elastic properties. 353

LIST OF FIGURES

FIGURE		PAGE
2.1	Different types of domain morphologies encountered in styrene butadiene block copolymers.	6
2.2	Representation of domain structures in a segmented polyurethane.	8
2.3	Model depicting the morphology (a) at equilibrium at room temperature and (b) shortly after annealing.	9
2.4	Schematic illustration of the Hytrel® morphology.	14
2.5	Schematic of the morphology of polyester based thermoplastic elastomers.	16
2.6	Typical stress-strain curve of a copolyester-ether.	30
2.7	Ideal morphology for copolyester-ether elastic filaments.	40
2.8	The crystalline forms of PTMT.	42
2.9	Tashiro model of the α to β transformation in PTMT.	43
2.10	Stress-strain curves of PTMT monofilaments annealed at various temperatures for one hour.	47
2.11	Different types of interdomain chains in block copolymers.	51
2.12	Hard and Soft segment orientation functions for samples spin cast at 110°C.	55
2.13	Cyclic stress-strain behavior of a copolyester-ether film.	57
2.14	Model of the morphology of oriented polyurethane elastomer.	60
2.15	Model for the deformation of lamellar SBS copolymers.	64

2.16 Change in relative crystallinity θ calculated as a function of time for random copolymers with n_b= 0.01, 0.02, and 0.05. 68

2.17 Weight fraction of crystallinity as a function of time and crystallization temperature for several different compositions. . . . 71

2.18 Orientation development in the spinline. 74

2.19 Morphological models of structure development during melt spinning of polyethylene. 80

2.20 Schematic of elongational changes that take place during fiber processing. 91

3.1 Relationship between new and old unit cell axes. 99

3.2 Projection of the model crystallite onto the basal plane. 104

3.3 Predicted and experimentally observed values of density as a function of composition. 113

3.4 Schematic diagram showing how strain recovery and work recovery are calculated from cyclic stress-strain curves. 118

4.1 Relative degree of conversion as a function of time for H4056. . 124

4.2 Relative degree of conversion as a function of time for H7246. . 125

4.3 Relative degree of conversion as a function of time for PTMT. . 126

4.4 Half-times of crystallization for the copolyesters as a function of the crystallization temperature. 129

4.5 Half-times of crystallization as a function of the degree of undercooling for the copolyesters. 130

4.6 Crystallization temperature of the copolyester-ethers as a function of composition and cooling rate. 132

4.7 DSC curves showing crystallization from the glassy state. The crystallization peaks for H4056, H6346, H7246, and H7246 are at -12°, 14°, 18°, and 40°C, respectively. 133

5.1 Schematic diagram of the spinline, water bath, and winder. . . 136

5.2 Birefringence of the water quenched filaments as a function of time. 138

5.3 Schematic diagram of (a) an aluminum frame used to hold the filaments at fixed length and (b) the annealing chamber. 142

6.1 WAXD patterns of highly oriented filaments of (a) H4056 and (b) PTMT. 144

6.2 Result of dynamic mechanical testing on H4056 and H7246 filaments that have been drawn and free annealed. 145

6.3 Small angle x-ray scattering patterns of the as-spun filaments. . 147

6.4 Small angle x-ray scattering patterns of annealed filaments. . . 149

6.5 Crystalline orientation functions $f_{c,z}$ of the as-spun filaments as a function of spin draw ratio. 151

6.6 Birefringence of the as-spun filaments as a function of spin draw ratio. 152

6.7 Effect of annealing on the crystalline orientation functions $f_{c,z}$ of the filaments spun at 300m/min. 155

6.8 Relative degree of phase separation ε for each composition as a function of spin draw ratio. 159
6.9 Density of the filaments spun at 300m/min as a function of annealing temperature. 160
6.10 Effect of annealing temperature on the relative degree of phase separation of filaments spun at 300m/min. 161
6.11 Relative degree of phase separation as a function of the degree of undercooling experienced by the filaments during annealing. 163
6.12 DSC traces of filaments spun at 50m/min. 165
6.13 DSC traces of filaments spun at 50m/min and annealed at 141°C. 166
6.14 Apparent width of the crystallites in the direction normal to the (100) crystallographic planes as a function of annealing temperature. 168
6.15 Apparent width of the crystallites in the direction normal to the (010) crystallographic planes as a function of annealing temperature. 169
6.16 Apparent width of the crystallites in the direction normal to the (100) crystallographic planes as a function of composition. . . . 170
6.17 Apparent width of the crystallites in the direction normal to the (010) crystallographic planes as a function of composition. . . . 171
6.18 Apparent thickness of the crystallites as a function of temperature. 173
6.19 Apparent thickness of the crystallites as a function of the degree of undercooling ΔT_u. 174

6.20 Apparent size of the crystallites as a function of the degree of undercooling ΔT_u. 176
6.21 Apparent size of the crystallites as a function of composition at each annealing temperature. 177
6.22 Long period of the as-spun filaments as a function of the spin draw ratio. 178
6.23 Long period of the filaments spun at 300m/min as a function of annealing temperature. 179
6.24 Long period of the filaments spun at 300m/min as a function of composition at each annealing temperature. 181
6.25 Long period of the filaments spun at 300m/min as a function of the degree of undercooling ΔT_u. 182
6.26 Thickness of the amorphous layer as a function of composition and annealing temperature. 188
6.27 Model of the domain structure explaining the effect of composition on the long period. 189
6.28 Thickness of the amorphous layer in filaments spun at 300m/min as a function of the degree of undercooling ΔT_u. 190
6.29 Model of the domain structure explaining the change in long period with annealing temperature. 192
7.1 Modulus of the as-spun filaments as a function of SDR and composition. 196

7.2 Effect of annealing temperature on the modulus of filaments spun at 300m/min. 197
7.3 Model of the structure based on a continuous crystalline phase. 204
7.4 Model of the structure assuming the crystallites are dispersed within the amorphous matrix but connected by tie molecules. . 208
7.5 Variation of the composite modulus with the relative fraction of tie molecules γ_t^2. 210
7.6 Variation of γ_t^2 with observed values of modulus. 213
7.7 Calculated values of γ_t^2 needed to explain the decrease in modulus upon annealing. 215
7.8 Morphological model based on a continuous amorphous phase. 216
7.9 Variation of the composite modulus with the modulus of the amorphous phase and the crystallite thickness. 221
7.10 Modulus of the amorphous phase as a function of the macroscopic modulus. 224
7.11 Plot of the amorphous modulus as a function of the observed DPS. 226
7.12 Values of E_a as a function of the fraction of tie molecules for several values of E_{comp}. 229
7.13 Possible combinations of E_a and γ_t^2 that would result in the observed macroscopic modulus in H4056 at each annealing temperature. 230

7.14 Possible combinations of E_a and γ_t^2 that would result in the observed macroscopic modulus in H5556 at each annealing temperature. 231

7.15 Possible combinations of E_a and γ_t^2 that would result in the observed macroscopic modulus in H6346 at each annealing temperature. 232

7.16 Possible combinations of E_a and γ_t^2 that would result in the observed macroscopic modulus in H7246 at each annealing temperature. 233

8.1 SAXS patterns of stretched and stretched and relaxed H4056 filaments. 239

8.2 One-dimensional data slices in the meridional direction corresponding to the SAXS patterns shown in Figure 8.1. 243

8.3 Stress-strain curve for a H4056 filament spun at 50m/min and free annealed. 246

8.4 Stress at 150% strain as a function of crystallite separation. . . 249

8.5 Cyclic stress-strain behavior of an H4056 filament. 251

8.6 Strain recovery and work recovery calculated from the cyclic data shown in Figure 8.5. 252

8.7 Strain recovery of H4056 filaments of different SDRs before and after fixed annealing at 100°C. 254

8.8 Work recovery of H4056 filaments of different SDRs before and after fixed annealing at 100°C. 255

8.9 Strain recovery of H7246 filaments of different SDRs before and after fixed annealing at 180°C. 257

8.10 Work recovery of H7246 filaments of different SDRs before and after fixed annealing at 180°C. 258

8.11 Relationship of ultimate elongation to composition and crystalline orientation. 260

8.12 Relationship of ultimate strain to composition and annealing temperature. 261

8.13 Tenacity as a function of crystalline orientation. 263

8.14 Tenacity as a function of annealing temperature for each composition. 264

9.1 Stress-strain behavior of a H4056 filament during cycling to 250% elongation. 269

9.2 Schematic of continuous drawing apparatus. 272

9.3 Degree of phase separation as a function of composition and processing conditions. 282

9.4 Rheovibron data showing the difference in T_g between free and fixed annealed drawn filaments of H4056. 283

9.5 Rheovibron data showing the difference in T_g between free and fixed annealed drawn filaments of H7246. 284

9.6 SAXS patterns of H4056 processed in different ways. 286

9.7 SAXS patterns of H7246 processed in different ways. 287

9.8 Crystallite size index as a function of composition and processing conditions. 289
9.9 Comparison of stress-strain curves of H4056 filaments receiving different drawing and annealing treatments. 294
9.10 Comparison of stress-strain curves of H7246 filaments receiving different drawing and annealing treatments. 295
9.11 Modulus of filaments processed in different ways as a function of their DPS. 300
9.12 Structural model of drawn and fixed annealed filaments. 303
9.13 Structural model of drawn and free annealed filaments. 305
9.14 SAXS patterns of a drawn H4056 filament. 309
9.15 One dimensional data slices corresponding to the SAXS patterns shown in Figure 9.14. 311
9.16 SAXS patterns of a drawn and fixed annealed H4056 filament. 313
9.17 One dimensional data slices corresponding to the SAXS patterns shown in Figure 9.16. 315
9.18 SAXS patterns of a drawn and free annealed H4056 filament. . 317
9.19 One dimensional data slices corresponding to the SAXS patterns shown in Figure 9.18. 319
9.20 SAXS patterns of a drawn and free annealed H7246 filament. . 322
9.21 One dimensional data slices corresponding to the SAXS patterns shown in Figure 9.20. 323

9.22 Effect of spin draw ratio on the strain recovery of "as-spun" and "hot drawn" filaments of H7246. 328
9.23 Effect of spin draw ratio on the work recovery of "as-spun" and "hot drawn" filaments of H7246. 329
9.24 Effect of draw temperature on the strain recovery of H7246 filaments before and after annealing. 331
9.25 Effect of draw temperature on the work recovery of H7246 filaments before and after annealing. 332
9.26 A comparison of the strain recovery of fixed and free annealed filaments of H7246 before and after drawing. 334
9.27 A comparison of the work recovery of fixed and free annealed filaments of H7246 before and after drawing. 335
9.28 Strain recovery of selected H7246 filaments. 338
9.29 Work recovery of selected H7246 filaments. 339
9.30 Strain recovery of selected H4056 filaments. 342
9.31 Work recovery of selected H4056 filaments. 343
9.32 Effect of crystallite size on the strain recovery of H7246 filaments stretched to different levels of extension. 346
9.33 Effect of crystallite size on the strain recovery of H4056 filaments stretched to different levels of extension. 347
9.34 Effect of composition on the strain recovery of drawn and free annealed filaments. 349

9.35 Effect of composition on the work recovery of drawn and free annealed filaments. 350
9.36 Effect of composition on the strain recovery of drawn and fixed annealed filaments. 351
9.37 Effect of composition on the work recovery of drawn and fixed annealed filaments. 352

CHAPTER 1

INTRODUCTION

Thermoplastic elastomers (TPEs) are a new class of polymers which have been developed within the last twenty years. They exhibit characteristics of cross-linked elastomers but can be processed by conventional thermoplastic techniques.

Since TPEs combine the performance of rubber with the processing economy of thermoplastics, they have found wide acceptance in an area formerly dominated by cross-linked elastomers. As advances in polymer technology are made and new polymers with superior properties are developed, more opportunities are being found for their use in new applications and as replacements in existing applications. The copolyester-ethers are a part of this advancing technology. They have found widespread use as hose and tubing products, wire and cable insulation, and drive belts, as well as a number of molded products. Recently, there has been an interest in producing elastic filaments from the copolyester-ethers for use as medical sutures. They provide a unique combination of high modulus and tensile strength combined with the ability to recover from deformation.

The physical and mechanical properties of copolyester-ethers are determined to a large extent by their microstructure. The degree of phase sepa-

ration, total crystallinity, orientation of the chain segments, and the size and shape of the domains can vary widely depending on the composition and processing conditions used. In order to control the properties of the product, one must understand the relationships between materials, processing conditions, and microstructure.

Although there are a number of papers which deal with the structure and properties of isotropic samples made by compression molding or casting techniques [16,32,34,37,59,114,112,111,154,156,195], little attention has been given to the behavior of copolyester-ethers during processing operations which produce anisotropic or inhomogenious samples such as extrusion, injection molding, or melt spinning [1,27,195,222].

A number of questions remain unanswered or are not completely understood. For instance, how does the microstructure produced in samples that crystallize during elongational flow vary with deformation rate and composition? How is the crystallization behavior affected by composition? How are the modulus, strength, and elasticity affected by changes in the microstructure brought about by different processing conditions? The research program of which this dissertation is a part is directed toward answering such questions.

In this dissertation a method was developed for melt spinning elastic filaments from the copolyester-ethers. The microstructures of the filaments were studied as a function of composition, spinning and drawing conditions, and annealing treatment. The tensile and elastic properties of the filaments were determined and correlated with pertinent structural features. The primary

goal of this research was to develop a better understanding of the processing-structure-property relationships of melt spun copolyester-ether filaments. The insight gained by these studies will provide fundamental information that may prove useful in understanding the behavior of these copolymers in other processes which produce anisotropic products, such as extrusion and coating operations or blow molding.

CHAPTER 2

LITERATURE SURVEY

2.1 Overview of Thermoplastic Elastomers

The unusual properties of the thermoplastic elastomers (TPEs) can be explained by the morphology of the polymers. They are usually ABA triblock, (AB) segmented, star block, or graft copolymers consisting of "hard" and "soft" segments [33,75,114,198]. The soft segments are amorphous chains of an elastomeric nature. The hard segments act to physically crosslink the soft segments by undergoing some thermally reversible physical association. The physical association of the hard segment can be due to crystallization, glassy phase separation, hydrogen bonding, or in some cases, ionic bonding [37,101,195]. Thus, at low temperatures these polymers act as elastomers because of the physical crosslinks which prevent long range flow. At higher temperatures, however, the physical bonds are broken and the polymers behave as conventional thermoplastics [37,101,114,156,195].

There are several main categories of thermoplastic elastomers [37,50,75] [110,196]. The styrene block copolymers are the largest group in terms of production volume, and the least expensive. Polystyrene (S) is combined with polyisoprene (I), polybutadiene (B), or ethylene-butadiene copolymer (EB) to

form triblock or alternating block copolymers; e.g., SBS, SIS, SEBS, $(SB)_n$, and $(SI)_n$ [37,50].

The SBS type copolymers are completely amorphous. The physical cross-links result not from crystallization or hydrogen bonding but by the formation of a separate glass phase within a continuous elastomeric matrix. The mutual incompatibility of polystyrene and polybutadiene segments causes the phase separation. In the ABA triblock polymers, the polystyrene blocks are on either end of the polybutadiene segment. When the glassy polystrene domains are formed, the ends of the polybutadiene chains become physically entrapped. the immobilization of the polybutadiene segment ends, in effect, crosslinks the elastomer [37].

Several types of domain shapes have been reported: spheres, ellipsoids, long cylindrical rods and lamellae [3,84,158]. Aggarwal [3] has shown possible structures for ABA triblock or AB diblock copolymers. These have been reproduced in Figure 2.1. The specific geometry is often determined by the volume ratio of the two phases. Shen [158] reports that the progressive changes in morphology can be observed by adding one of the homopolymers to the copolymer. In cast films, the geometry is sometimes affected by the type of solvent and its rate of evaporation [84].

More detail on the structure and properties of styrene-butadiene type TPEs can be found in reviews by Matsuo [120] and West and Cooper [198].

The polyurethanes are the second most common group of thermoplastic elastomers. They generally consist of polyether or polyester soft segments

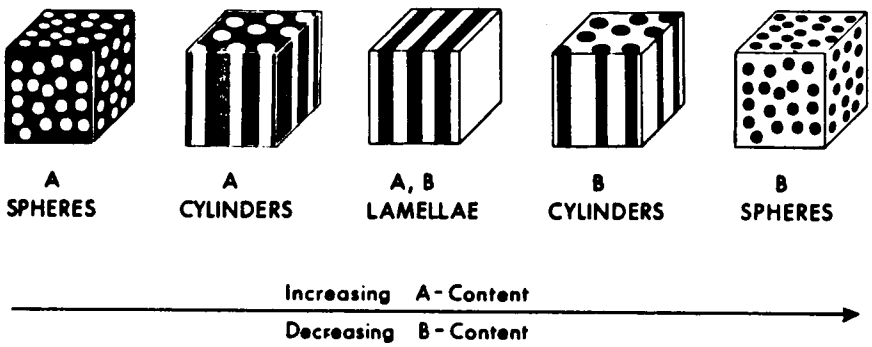
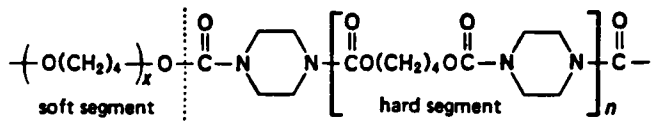


Figure 2.1: Different types of domain morphologies encountered in styrene butadiene block copolymers.

Source: S.L. Aggarwal, *Block Copolymers,* (New York: Plenum Press, 1970) pg. 102.

(molecular weight of about 1000) and a polyurethane hard segment. The hard segments are generally composed of aromatic diisocyanate chains extended with low molecular weight diols [50,147,149]. The structural formula for a typical polyurethane is shown below:



The physical bonding in this group results from phase separation, and sometimes crystallization and/or hydrogen bonding [37,198,21]. The hard domains act as filler and as physical cross-links. The domain structure is much smaller than in the SBS type block copolymers due to the shorter segment lengths and therefore is not as clearly visible. Complete phase separation probably does not occur. This is supported by evidence that hydrogen bonding occurs between the hard and soft blocks in some polyurethanes [21]. Phase separation is believed to occur to a higher degree in the polyether based copolymers than in the polyester based copolymers, possibly due to interactions between the ester and urethane groups [42].

A couple of models have been proposed for the domain structure in the segmented polyurethanes. These are shown in Figure 2.2 [154] and Figure 2.3 [204]. The first model represents both phases as being continuous. Phase separation is presumed to be incomplete with some polyurethane hard segments

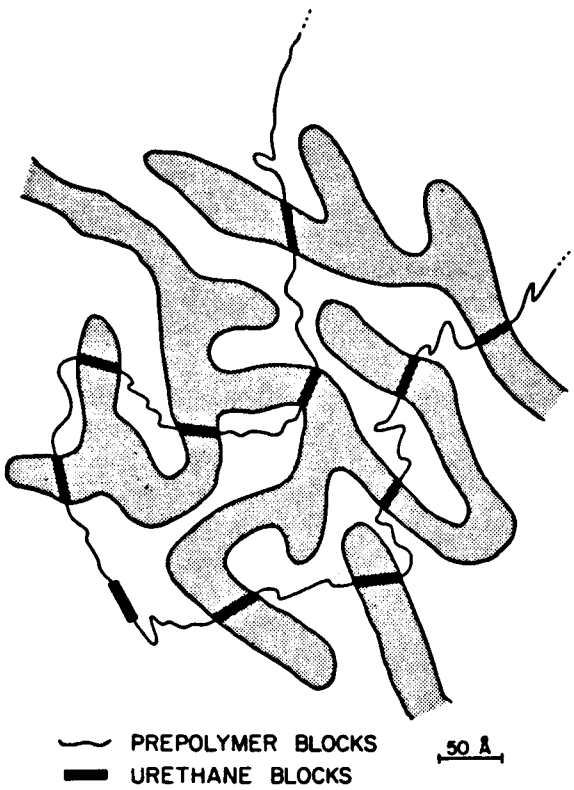


Figure 2.2: Representation of domain structures in a segmented polyurethane.

Source: R.W. Seymour, G.M. Estes, and S.L. Cooper, *Macromolecules,* **3**, 579 (1970).

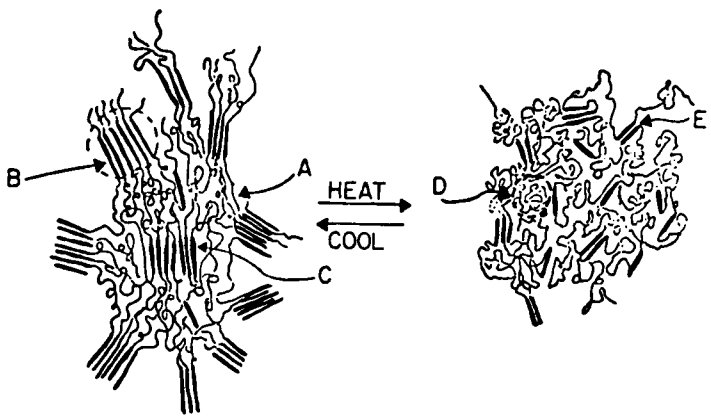


Figure 2.3: Model depicting the morphology (a) at equilibrium at room temperature and (b) shortly after annealing.

Source: G.L. Wilkes and J.A. Emerson, *J. Appl. Phys.*, **47(10)**, 4261-4264 (1976).

dispersed in the elastomeric phase [154]. The second model shows a fringed micelle type morphology. Raising the temperature is believed to induce phase mixing. Upon cooling, the phases eventually separate giving the original morphology [204].

For more information on the microstructure and properties of polyurethane TPEs the reader is referred to reviews by Matsuo [120], West and Cooper [198], and Allport and Janes [6].

Polyolefin blends are the third largest thermoplastic elastomers in volume. These were first made by blending polypropylene (PP) and ethylene propylene diene monomer (EPDM). The EPDM could then be lightly cross-linked to obtain optimum properties. Later, it was discovered they could be made by blending PP, high density polyethylene (HDPE), or PP copolymer with EPDM or ethylene-propylene rubber (EPR) with no cross-linking. The PP or HDPE can also be blended with finely particulate and fully cured rubbers to form thermoplastic elastomers [45,50,75,196].

The copolyesters are the next largest class of TPEs in volume. They consist of repeatedly alternating polyester and polyether blocks. The hard segment is a crystallizable polyester, usually poly(tetramethylene terephthalate) (PTMT) with a number average molecular weight in the range of 600 to 3000. PTMT is known by several other names including poly(butylene terephthalate) (PBT) and 4GT. The soft segment is usually based on poly(tetramethylene ether) glycol terephthalate (PTMEG) with a molecular weight of about 1000 or 2000. PTMEG is sometimes referred to as poly(tetramethylene oxide)

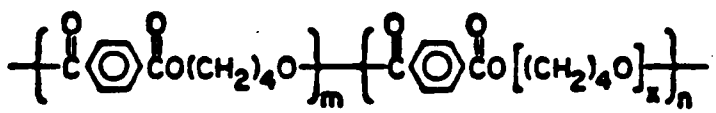
(PTMO), or poly(oxytetramethylene) (POTM). The structure and properties of these copolymers will be discussed in some detail in Section 2.2.

There are other thermoplastic elastomers such as 1,2–polybutadiene, polyethylene grafted with butyl rubber, trans 1,4–polyisoprene, polypivalolactone grafted onto various elastomeric backbones, and polycarbonate siloxane random copolymers, but their production volume is very small at the present time [33,50,196]. An overall view of the different classes of thermoplastic elastomers has been presented in a paper by Wells [196] and in an extensive review articles by Dreyfus, Fetters, and Hansen [50], The general structure–property relationships of block copolymers have been reviewed by Dawkins [49].

2.2 Segmented Copolyester-ethers

2.2.1 Chemical and Molecular Structure

DuPont commercialized the first copolyester thermoplastic elastomers in 1972. These copolymers consist of sequences of poly(tetramethylene ether glycol)-terephthalate (PTMEG-T) joined with polytetramethylene terephthalate (PTMT) sequences as shown below [159]:



PTMT (Hard Segment) MW = 220

PTMEG-T (Soft Segment) MW~1120

The molecular weight of the polyether block is about 1000 while the polyester is of sufficient length to crystallize (D.P. 6 to 24). Total molecular weight of the copolymer is usually from 20,000 to 40,000 [34,37,50,112,156,195]. A series of copolyester-ethers are commercially available in a wide range of compositions under the tradename "Hytrel®".

Other segmented polyether-polyester thermoplastic elastomers have been made [34,59,195,205] on a limited basis for research purposes. The ester segments generally have been based on polymethylene terephthalates, (2GT, 3GT, 5GT, 6GT, 10GT) and other esters such as 1,2 propylene terephthalate and tetramethylene isophthalate. The polyethers are usually poly(tetramethylene oxide) of block molecular weight 1000 (PTMO-1000) or 2000 (PTMO-2000). In one case, a series of 6GT/PTMO-2000 copolymers were made in which the weight percent of polyether was varied from 10-80%. Additional copolymers were made with varying block lengths of PTMO [59,195].

In another case, modified copolyesters were made which consisted of 25 wt.-% PTMO (molecular weight of 1000) and PTMT hard blocks modified by tetramethylene-1,4- cyclohexanedicarboxylate (4GC) [112]. Using these copolymers the effects of the type of polyester, segment length, and composition could be studied.

2.2.2 General Morphological Features

There has been considerable discussion as to the exact nature of the morphology in polyether-ester type copolymers. Different viewpoints have been

presented by Cella [37], Seymour et al. [156] and Wegner et al. [195].

Cella has investigated the morphology of a series of segmented copolyester-ethers of various compositions using electron microscopy, thermal analysis, and X-ray diffraction techniques. Shortly after the commercial introduction of the copolyester-ethers by DuPont, Cella suggested a model for their structure. The PTMT segments were found to crystallize as long thin lamellae about 100Å thick in the chain direction and up to several thousand angstroms in length. The lamellae were believed to be interconnected by short PTMT chain segments (tie molecules) in addition to being connected by the relatively long, soft segments composing the elastomeric domains, thus forming a three-dimensional network as shown in Figure 2.4. Thus, the crystalline domains act as the intermolecular tie points or physical crosslinks. This model was used to explain some of the unusual mechanical properties of the polymers such as stress-softening. These will be discussed in more detail in Section 2.2.3.

A few years later, Seymour et al. [156] presented a model for the morphology more similar to that of common semicrystalline thermoplastics than to domain forming copolymers. Low angle light scattering patterns indicated a spherulitic type morphology. Polarized light microscopy confirmed the presence of well-developed spherulitic structures across the entire composition range (20–65 wt.% PTMO) in both melt pressed and injection molded bars, as well as in solution cast films. The spherulitic skeleton was believed to consist of crystalline PTMT segments while the interradial regions were thought to be a mixed phase of uncrystallized PTMT segments and amorphous PTMO. This

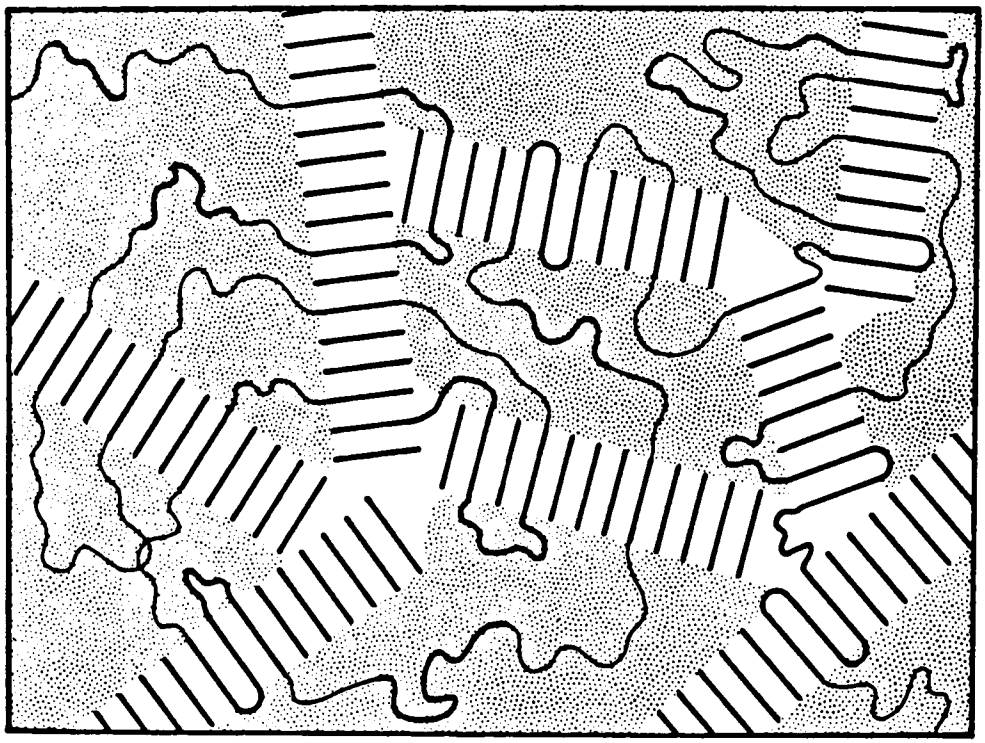


Figure 2.4: Schematic illustration of the Hytrel® morphology. —— PTMT segment, ——PTMO segment, A - crystalline domain, B - junction of crystalline lamellae, C - non- crystalline PTMT segment.

Source: R.J. Cella, *J. Polym. Sci.*, **42**, 727-740 (1973) and *Encycl. Polym. Sci. Technol., Suppl. Vol.2*, 485-510 (1977).

view was supported by dynamic mechanical properties and thermal analysis. A single peak was observed in a plot of the loss tangent as a function of temperature, indicating that the PTMO and amorphous PTMT do not exist in separate phases. Thermal analysis showed a single glass transition temperature. The dynamic mechanical properties further indicated that a change in the overall composition caused a parallel change in the composition of the amorphous phase.

Seymour et al. [156] say that these results are inconsistent with a two phase model based on pure phases of hard and soft segments, but that they would be the anticipated result for a semicrystalline copolymer in which the composition of the amorphous phase could be varied. A schematic model of the proposed structure was presented (Figure 2.5).

Chemical etching techniques were used to obtain direct evidence of chain folding in these copolymers. The lamellar fold period of the copolymer was found to be equal to that of the polyester homopolymer: 7 to 8 monomer units. The fold period was found to be independent of PTMO content or segment length.

Wegner et al. [195] was not fully satisfied with either of the previous two models saying that neither model can predict the changes in morphology that occur when the samples are annealed or highly oriented and that neither model can relate the degree of crystallinity and the physical crosslink density to the molecular structure of a given copolyester with a given segment length distribution. They go on to present their own model which they say better

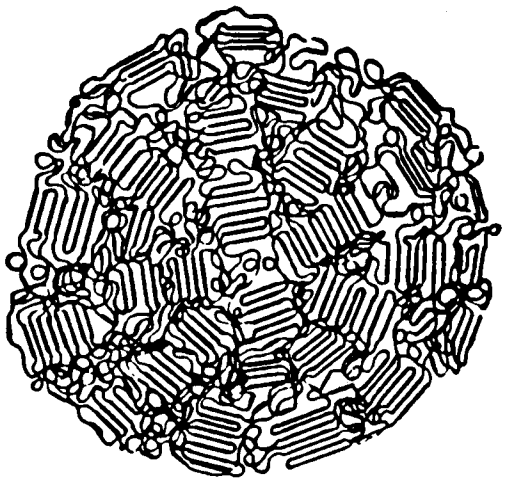


Figure 2.5: Schematic of the morphology of polyester based thermoplastic elastomers.

Source: R.W. Seymour, J.R. Overton, and L.S. Corley, *Macromolecules,* **8(3)**, 331-335 (1975).

characterizes the morphology and annealing behavior.

A series of six segmented copolyesters which differed in average soft segment length and hard segment content were studied using thermal analysis, density, dynamic mechanical measurements, and x-ray diffraction techniques. The soft segments were based on PTMO of molecular weight 1000 or 2000. The hard segment content varied from 36 to 72 wt.-%.

In general, the elastomers were found to consist of crystalline domains of hard segments, and an amorphous mixed phase of hard and soft segments, in agreement with Seymour's model. The copolymer with the highest HSC and longest soft segment blocks exhibited three phases: namely crystalline domains of both hard and soft segments embedded in an amorphous mixed phase of uncrystallized hard and soft segments.

Wegner et al. concluded from the melting and crystallization behavior that in most samples only a small fraction of the hard segments crystallize. The remainder mixed with the soft segments to form a homogeneous amorphous matrix. Furthermore, the crystalline domain were thought to be selectively composed of hard segments of a given length. They suggested this length was the length of the hard segments having the greatest frenquency.

According to Wegner, the SAXS data indicate that average distances between crystalline domains are so large that several (4-6) sequences of hard and soft segments are necessary to tie adjacent crystallite surfaces.

Wegner, however, could not explain the enormous increase in long spacing observed upon annealing with his model. He did not think that Seymour's

model, which involved a great deal of chain folding, was appropriate and suggested that some type of fringed micelle morphology would better explain the observed behavior.

Briber and Thomas [32] have studied the morphology and crystallization behavior in thin films of PTMT/PTMO crystallized from the melt. The copolymers were based on PTMO of molecular weight 1000 and varied in HSC from 36 to 81 wt.-% PTMT. Transmission electron micrographs show well defined lamellae in compositions containing 49 wt.-% PTMT and higher. The lamellae show electron diffraction patterns characteristic of single crystals, while the matrix material shows only diffuse amorphous scattering. These results support a two-phase model consisting of relatively pure PTMT crystallites dispersed in an amorphous matrix of PTMO sequences and uncrystallized PTMT segments.

The dimensions of the crystallites were found to depend on the crystallization temperature with larger crystallites forming at higher temperatures. The authors explain that since the stable crystallite size increases with temperature only the longer sequences are able to crystallize at the higher temperatures. As the crystallization temperature is lowered, the shorter sequences are able to crystallize. Relatively small crystallites formed in the matrix material after storage at room temperature for three months. Their results indicate that fractionation of the hard segments can take place during crystallization due to a coupling of the sequence length with the stable crystallite size at a given crystallization temperature.

The general structure and properties of the segmented copolyester have been summarized in an article by Cella [37].

Effect of Composition and Segment Length on the Morphology

The commercial polyester-ether copolymers are best described as multi- block copolymers with polyether blocks of fixed sizes and polyester blocks of variable length: the length of the poly(tetramethylene oxide) terephthalate (PTMO-T or PTMEG-T) segment is fixed by the molecular weight of the reactant PTMO. The polyester block may be of various lengths depending on the molar ratio present during polymerization [59]. The HSC and average block length of the polyester sequences increases as the mole fraction of PTMT monomer is increased.

The glass transition temperature has been shown by several investigators [37,112] to increase with increasing hard segment content. Two reasons have been suggested for this. First, phase separation is probably not complete. As hard segment content increases, more and more hard segments become dispersed within the elastomeric phase. Secondly, increasing hard segment content may result in a higher level of physical cross-linking which effectively limits the mobility of the soft segments [37].

Lilaonitkul et al. [111] and others [156] found that as the hard segment content in the copolymer increased, the amorphous phase changed from a predominantly soft segment rich phase to a non-crystalline PTMT phase. Lilaonitkul et al. [111] indicated that the two components of the amorphous

phase become more compatible as the PTMT content (and thus the sequence length) decreased.

Lilaonitkul, West, and Cooper [114] reported that "while segment incompatibility does not lead to the amorphous component microphase separation usually observed in block polymer systems, it may serve to enhance hard segment crystallization such that an unexpected high degree of crystallinity for the PTMT sequences results." Raising the hard segment content was found to increase the crystallinity significantly.

Depending on the hard segment content (PTMT in this case) and the sample preparation technique, various types of morphology could be produced. Compression molded samples of low PTMT content (34 wt.-%) had a non-spherulitic but interconnected structure. At higher PTMT levels, spherulitic structures were observed. Samples spin cast from 1,1,2- trichloroethane produced negatively birefringent spherulites (Type II), spherulites in which the optical axis lay at 45°to the radius (Tpye I), or no spherulites depending on the PTMT content. Samples slowly cast (very low evaporation rate) from the same solvent gave Type II spherulites at low PTMT levels and no spherulites at high ($> 63\%$) PTMT concentrations. Samples containing 33 wt.-% PTMT segments formed positively birefringent spherulites when they were slowly cast from a mixture of m-cresol and 1,1,2–trichloroethane. Type II spherulites were formed in samples containing more that 33 wt.-% PTMT segments [114,112].

Average spherulilte size was also found to be a function of PTMT content and casting techniques. Spherulite size increased linearly with increasing

PTMT weight fractiion for compression molded samples, while a maximum at 50 wt.% was observed for solution cast samples [114].

As stated earlier, Wegner [195] reported that the long period observed for a series of copolyesters increased with increasing hard segment block length.

In experiments with poly(hexamethylene terephthalate)/poly(tetramethylene oxide) (PHMT/PTMO) block copolymers, Ghaffar and Goodman [59] found the crystallization behavior depended on the content and molecular weights of the polyether blocks. At molecular weights less than 2000, the polyether phase was wholly amorphous. With copolymers containing more than 60% by weight of polyether with block molecular weight 2000, two crystalline phases were observed. A crystalline polyether phase was observed in all samples having a PTMO block molecular weight higher than 2000. These results are consistent with Wegner et al. [195] who also reported a crystalline polyether phase in copolymers having blocks of PTMO–2000.

They obtained some interesting results with a series of copolymers consisting of 50% by weight of poly(tetramethylene oxide) of molecular weight 2000 (PTMO-2000) and 50% by weight of various polyesters. In those cases where the related homopolyester crystallized at room temperature, the polyester segments crystallized in the copolymer. If the polyester did not crystallize, then a crystalline polyether phase was formed. The authors concluded that the main features of the structure were determined by the faster crystallizing species, with the other component following the structural pattern that was laid down by the first.

The authors suggested that at small block lengths (PTMO M_n=1000 and 2000) the polyether segments did not have the mobility to crystallize since their chains ends were tied down by the faster crystallizing polyester segments. At higher PTMO molecular weights, however, the ether segments were long enough to crystallize even though their ends were still fixed.

In the copolymer samples containing 50% PTMO-2000, the polyether phase crystallized when extended by 100 to 200% of its original length. After relaxation from 600%, some residual polyether crystallinity remained.

Effect of Processing on the Morphology

The copolyether-esters are relatively stable over a wide range of processing temperatures. Hytrel® 55D (durometer hardness grade) which melts around 200°C [33] can be processed at temperatures as low as 220°C and as high as 300°C. For comparison, thermoplastic polyurethanes begin to degrade at 220°C. Because of the availability of a large range of compositions and the temperature dependence of the viscosity, the copolyesters can be processed by a variety of techniques typically associated with thermoplastics, including melt-casting, solution casting, extrusion, compression molding, injection molding, rotational molding, and blow molding [94,101,203,211].

The rheological properties of the copolyether-ester type polymers are similar to those of the polyester-based thermoplastic urethanes. At the high shear rates (> 100 sec^{-1}) encountered in injection molding and certain extrusion operations, the viscosity decreases with increasing shear rates for both

types of polymers. However, at low shear rates, the viscosity of the copolymers becomes relatively independent of the shear rate. The viscosity of the copolyesters are relatively low (10^4-10^5 poise) at low shear rates while the viscosity of the polyurethanes is over one million poise. This low viscosity allows the copolyesters to be roto-molded and used in melt casting and wire coating operations [94,101,203,211].

The copolyesters can be easily processed by conventional thermoplastic techniques. Starting with the pellet form, the polymer may be injection molded or extruded to form fibers, tubes, films or profiles. The rheological properties allow the polymer to be melt cast or blow molded. Both of these methods involve extruding the polymer directly into a mold at low mold pressures (< 300 psi). In extrusion operations, the high modulus at elevated temperatures and the rapid crystallization rates of the copolyesters make fabrication of tubing and profiles easier [33].

The morphology and properties of thermoplastic elastomers are greatly influenced by processing conditions. The method of sample preparation, orientation effects and the thermal history must be carefully studied in order to better understand the morphology and properties of the final product.

If the sample is solution cast, careful attention must be given to the choice of solvent, its rate of evaporation, and the casting temperature. Lilaonitkul et al. [114] were able to produce three different spherulite morphologies in PTMT/PTMO copolymers depending on the copolymer composition and the processing history. Samples that were allowed to dry slowly often gave different

spherulite structures than films that were dried quickly [112]. Sometimes, when a highly volatile solvent such as chloroform was used, no spherulites were observed.

Buck et al. [34] found the largest lamellae in PTMT/PTMO samples made by solution or melt casting and compression molding when relatively long times were allowed for crystallization. Lamellae in these samples were approximately 50-100Å in thickness and 1000-2000Å in lateral dimensions. If the samples were quenched, much smaller dimensions were observed: 15 to 25Å by 100 to 300Å. Quenching produced clear films while other methods produced opaque films.

Lilaonitkul et al. [114] found spherulite size to be a function of hard segment content and fabrication method. The spherulite size in compression molded samples was found to increase rapidly and linearly with increasing PTMT content, while in spin cast films a maximum size was observed at about 50% PTMT. The maximum spherulite sizes observed were about $3\mu m$ and $4.5\mu m$ for spin cast and melt cast films, respectively.

Sheaves of lamellae, the precursors of spherulites, were observed by Buck et al. [34] in melt cast samples. They explain that the melt cast samples cool the slowest and therefore offer the best opportunity for the lamellae to organize into more highly ordered structures. Spherulites with diameters of up to $10\mu m$ were reported present in the melt cast samples.

Injection molded materials were found to have a more complex morphology. Using transmission electron microscopy (TEM), they found well- defined

lamellae, about 60Å thick and 1000Å long, oriented essentially parallel to each other. This was thought to be the result of surface nucleation effects and their response to local melt flow patterns. Lamellae in the interior tended to be smaller and showed less orientation [34].

Zhu and Wegner [223] have studied the morphology of copolyester-ether films processed in several ways. Spherulitic structures were produced in films crystallized from the melt. If the copolymers were quenched rapidly from the melt, a " network of interlocked individual lamellae" were formed. Shearing during crystallization produced a shish-kebab like structure.

Abhiramen et al. [1] spun fibers from segmented copolyesters having PTMT as the hard segment and a modified poly(ethylene oxide) as the soft segment. Spinning at 500-1000 m/min into a water bath produced filaments with a high degree of orientation in the crystalline phase and a "significant degree of amorphous orientation". The amorphous orientation caused the filaments to shrink in boiling water. The amorphous orientation increased slightly as the take-up velocity was increased. Differences in the amorphous orientation were not readily apparent until the filaments were stretched 20% or more. The differences in orientation became more obvious at high elongations.

Effect of Annealing on the Morphology

Lilaonitkul and Cooper [112] report that during annealing, melting and recrystallization of unstable small crystallites and secondary crystallization occurs. This results in the formation of thicker crystals and a slightly higher level of

crystallinity. Buck et al. [34], using SAXS techniques, found the long period spacing increased in oriented samples with increasing annealing temperatures. The increase was attributed to a thickening of the lamellae. Long period spacing closely corresponded to integral multiples of the chain axis crystallographic repeat distance (11.6Å), which prompted the authors to suggest that the lamellae thickened by successive addition of integral numbers of PTMT units.

Lilaonitkul et al. [112] found that annealing at 150°C did not alter the overall morphology of any of the three types of spherulites found in the PTMT/PTMO samples. It seems the original spherulitic structures were relatively stable. Although spherulite size and type did not change, the SALS pattern became more clearly defined and the scattered intensity increased. This was believed to be the result of increased crystal perfection and order.

Zhu and Wegner [222] found the long period increased as the degree of undercooling (ΔT_u) decreased. The melting point remained virtually the same, which indicates that the thickness of the lamellae does not change significantly during annealing. They conclude that the large change in long period results not from a thickening of the lamellae, but from an increase in the space between adjacent lamellae. No mechanism for this occurrence is postulated.

Free annealing lead to a relaxation of the amorphous chains in the melt spun filaments investigated by Abhiramen et al. [1]. The differences in amorphous orientation produced by different take-up velocities were smaller as a result of this relaxation.

Abhiramen et al. also note that the long period in unannealed filaments

was reduced upon stretching, while it increased in annealed filaments. These results indicate that a significant rearrangement of the structure occurs in the unannealed filaments during stretching. Annealing was said to create a more stable structure that did not tear apart as easily during stretching.

Wegner et al. [195] found that the prior draw ratio of samples annealed with fixed length had little effect on the value of the long period. Only slightly higher values were obtained for drawn samples than for unoriented samples.

Bandara and Droscher [16] studied thin films of PTMT/PTMO produced by compresssion molding and quenching in ice water. The resulting films were studied by SAXS and DSC techniques. The quenched films were found to possess a significant level of crystallinity after this treatment.

The degree of phase separation (DPS) was found to increase as the degree of undercooling was decreased. The SAXS analysis indicates there is a crystalline core averaging about 35 to 45Å thick depending on the composition. The amorphous layer was found to vary greatly in thickness. The two phases are believed to be separated by a diffuse boundary layer about 9Å thick. They believe that a large fraction of the segments are unable to crystallize at high ΔT_u, especially longer sequences which may lack the mobility to diffuse to the growth center. Annealing produces a large decrease in the internal surface area, while there is a large increase in the chord length of the crystalline domains. For these reasons, the increase in crystallinity is attributed to an increase in domain size rather than in the number of domains. The melting temperature did not increase appreciably upon annealing as would be expected if the lamellae had

grown thicker, so the crystallites must grow in the lateral directions. They conclude that crystallization is limited to increases in the size and perfection of existing lamellae.

They believe that the multiple melting peaks observed in DSC scans result from lamellae of different thicknesses or single lamellae with regions of different thicknesses. These results are consistent with Zhu and Wegner who report a variation of the lamellar thickness with crystallization temperature.

The multiple melting peaks have been examined in more detail by Stevenson and Cooper [183]. Four types of melting endotherms were identified. Type I is a relative small endotherm that appears several degrees above the annealing temperature. Its size and exact location depends on the crystallization temperature T_c and the length of time at T_c. This endotherm is attributed to a clustering of PTMT segments. Type II endotherms are larger and appear at a somewhat higher temperature than Type I. The size and position of this melting peak is strongly dependent on T_c. These endotherms are believed to be the result of the melting of crystallites formed during isothermal crystallization at T_c. Type III endotherms, which appear between 215 and 230°C, show little dependence on T_c unless it is close to the melting temperature. These endotherms are associated with the melting of crystallites formed during cooling to T_c. The relative size of Types II and III depends upon the cooling rate and the time allowed for crystallization at T_c. Type IV endotherms appear between 230 and 234°C and are small in comparision to Types II and III. The size of this endotherm depends on a number of parameters including

the heating rate during the DSC scan. This suggests that this endotherm is associated with crystallites that form during the scan. Less thermally stable crystals may melt and recrystallize into more stable, higher melting crystals.

They [183] warn that due to recrystallization during heating, the DSC scan at low heating rates may not be representative of the original crystallite population in the material and that caution must be used when making morphological interpretations or determinations of crystallinity based on such scans.

2.2.3 Mechanical and Physical Properties

Stress-Strain Behavior

A typical stress-strain curve for Hytrel® is shown in Figure 2.6. Cella [37] and Witsiepe [205] divide the curve into three regions. At low elongations ($< 25\%$), the force increases rapidly with strain. Up to about 10% elongation the deformation is reversible, with little hysteresis or permanent set. In the second region (50-200% strain), the copolmer undergoes draw. Necking may or may not occur depending on the temperature and strain rate. The deformation is irreversible with a large amount of permanent set resulting. Above 200%, the force increases with extension about as expected for a cured elastomer.

The stress-strain behavior was explained as follows. At low levels of elongation, the extension is due to the pseudo-elastic deformation of crystalline domains and the short tie molecules that connect them. The draw behavior at higher levels of strain is the result of extensive crystallite deformation, disrup-

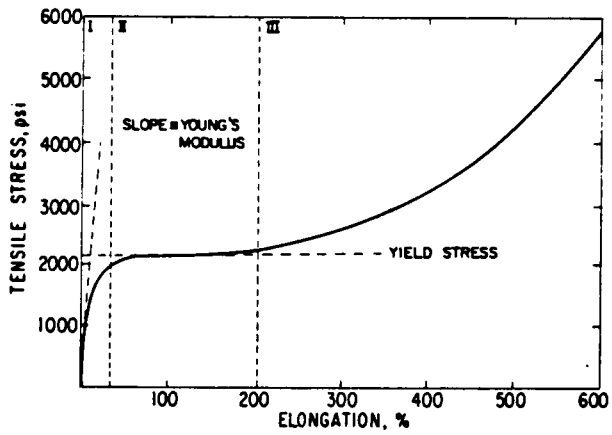


Figure 2.6: Typical stress-strain curve of a copolyester-ether.

Source: R.J. Cella, *J. Polym. Sci.*, **42**, 727-740 (1973) and *Encycl. Polym. Sci. Technol., Suppl. Vol.2,* 485-510 (1977).

tion of the crystalline matrix network, and development of orientation. As the crystallites become more fully oriented, the stress is increasingly borne by the continuous elastomeric matrix [37].

Effects of Composition and Segment Length on the Physical and Mechanical Properties

Mechanical and physical properties depend upon the type and amount of hard segment present in the copolymer as well as the block lengths of both hard and soft segments [34,94,112,196,203,206]. A wide variety of materials can be obtained ranging from hard plastics and semicrystalline elastomers at high polyester content or soft elastic gums at very high polyether content.

Witsiepe [205] has studied the effect of hard segment type on the crystallization behavior and physical properties of the copolyether-esters. Polymers having PTMT hard segments crystallized much more rapidly than polymers made with other ester hard segments such as PET. Injection molded parts from PTMT copolymers hardened much more quickly and obtained a higher degree of hardness than parts made from PET copolymers.

Typical mechanical and physical properties are given in Table 2.1 for four different compositions of copolyester-ethers based on a PTMT hard segment. PTMT content increases from left to right. Table 2.2 shows Young's modulus and certain physical properties as a function of PTMT content and segment length.

Mechanical properties such as modulus, strength, creep resistance, and

Table 2.1: Typical mechanical properties of Hytrel® type copolyesters.

Property	ASTM method	Elastomer grade[a] 40D	55D	63D	72D
Specific gravity	D 720	1.17	1.20	1.22	1.25
Tensile strength, psi	D 638	3700	5500	5700	5700
Ultimate elongation, percent	D 638	450	450	350	350
Yield point (Y) or 25 percent modulus (M)	D 638	1100 (M)	2000 (M)	2500 (Y)	3800 (Y)
Stress at 15 percent compression, psi	D 575 A	1100	2500	3100	4400
Flexural modulus, psi	D 790	7000	30,000	50,000	75,000
Resilience, Bashore, percent	D 2632	62	53	43	26
Compression-set resistance[b]					
At 25 percent deflection	D 359 B	60	56	NA[c]	NA
At constant load of 1350 psi	D 359 A	27	4	2	2
Tear strength, pounds per inch	D 624				
Die B		631	935	1055	NA
Die C		700	900	860	NA
Resistance to flex-cut growth, cycles to failure × 10^5					
Ross (pierced)	D 1052	>21	>10	2.8	NA
De Mattia (pierced)	D 813	>2	>0.7	NA	NA
Notched Izod impact strength, foot-pounds per inch	D 256 A				
At 75°F		84	>204	>204	3.9
At −40°F		>20[e]	>204	0.5	0.8
Taber abrasion[e], milligrams per 1000 cycles	D 1044	3	5	8	13
Softening point, Vicat, °F	D 1525	234	356	363	397
Heat-deflection temperature, °F	D 648				
At 66 psi		130	215	230	330
At 264 psi		NA	120	170	185
Brittleness temperature, °F	D 746	<−94	<−94	<−94	<−94
Coefficient of linear expansion, inches per inch per °C × 10^5	D 696	20	18	17	21
Water absorption, 24 hours, percent	D 570	0.8	0.5	0.3	0.3

[a] Grade numbers correspond to durometer hardness values.
[b] Tested 22 hours at 158°F.
[c] Not applicable.
[d] No break.
[e] Using CS-17 wheel with 1000-gram load.

Source: G. Zaiser, *Plastics Engineering*, **34(5)**, 61–64 (1978).

Table 2.2: Characteristics of some copolyester elastomers.

	H33	H50	H57	H63	H76	H84
4GT content, wt%	33	50	57	63	76	84
Av 4GT block length, L	2.64	4.95	6.43	8.14	14.8	24.26
DSC[a]						
T_g, °C	−68	−59	−55	−51	−33	−9
T_m, °C	163	189	196	200	209	214
ΔH_f, J/g	16	33	41	48	58	61
% crystallinity	11.5	22.9	28.6	33.3	40.7	42.8
Young's Modulus, E_y, MPa	36.8	102	—	132	328	375
Rheovibron[a]						
E'' peak, °C[b]	−63	−58	−53	−48	−30	−4
tan δ peak, °C[b]	−51	−42	−34	−27	10	30

[a] Compression-molded samples.
[b] β Relaxation.

Source: A. Lilaonitkul and S.L. Cooper, *Rubb. Chem. Technol.*, **50(1)**, 1-23 (1977).

tensile set are closely related to the type of polyester hard segment, copolymer composition and the level of crystallinity. Low temperature flexibility, tensile strength and tear strength also vary with hard segment content but are more strongly influenced by the soft segment chemical structure and composition [205].

Young's modulus, yield stress, tensile strength, and tear resistence all increase with increasing PTMT content [37,205]. The elongation to break decreases with increasing PTMT content.

The modulus was found not only to vary with hard segment content but also with the type of hard segment. In a series of copolymers having PTMO as the soft segment and various terephthalates (2GT, 3GT, 4GT(PTMT), 5GT, 6GT) as the hard segment, the modulus was found to increase with increasing melting temperature of the corresponding polyester homopolymer [205].

Tear strength, however, could not be clearly related to the hard segment melting point. Instead, it seemed to depend more on the amorphous phase composition. For example, at a given hard segment content, replacement of the polytetramethylene ether soft segments with polypropylene ether soft segments lowered the tear resistance (and tensile strength) [205].

The tensile set (% strain remaining after release from a given elongation) and hysteresis both increase with increasing PTMT content while creep decreases with increasing PTMT content [34].

The creep rate generally increases with increasing initial (elastic) strain but is fairly independent of temperature over the range studied (24-90°C) [34].

Physical properties such as T_m, T_g, hardness, clarity, density and solubility also vary with segment lengths and copolymer composition. The hardness of the copolymer increases with increasing hard segment content. As mentioned before, soft elastic gums are obtained at low PTMT content and hard plastics are obtained at high PTMT content (see Table 2.1 for the hardness range of the commercial Hytrel® polymers).

Both glass transition and melting temperatures increase with increasing hard segment content [37,112] (see Table 2.2). The change in T_g with composition was said to be an indication that the amorphous phase is a compatible mixture of soft and hard segments [112]. Witsiepe [205] indicated the changes in T_g were probably due to more hard segments being forced into the amorphous regions. He also pointed out that as the hard segment content increases the level of pseudo-crosslinking increases, resulting in a decrease in the length of unrestricted soft segment chains.

The melting points of the copolyester-ethers have been shown to increase with increasing PTMT content, with T_m approaching the melting point of the homopolymer. Cella [37] believes this reflects the increasing length of the crystallizable segments as PTMT content is increased.

Boussias et al. [26] found that not only did the T_m of the crystalline phase decrease with increasing polyether content, it decreased with decreasing polyether block length at a given composition. However, if total polyether content is decreased as a result of decreasing block length, then T_m is increased [195]. These results are more easily interpreted in terms of the hard segment

block length. For a given HSC, the polyester block length is shortened as the molecular weight of the polyether prepolymer is decreased. The decrease in melting temperature reflects the shorter average hard segment length in the crystal.

The density of the copolymers decrease with decreasing PTMT content and segment length. Boussias et al. [26] report a density of 1.236 g/cm^3 for a sample consisting of 72 wt.-% PTMT with a hard segment number average degree of polymerization (D.P.) of 12.5. This decreased to 1.124 g/cm^3 at 36 wt.-% and D.P. of 3.6.

Ghaffar et al. [59] found certain polyester-ether melts to be opaque. Copolymers from poly(hexamethylene terephthalate) (6GT) and PTMO of molecular weight 2000 were clear at greater than 50 wt.-% polyether. With a PTMO molecular weight of 3000 or greater, the melts were opaque at 50 wt.-% polyether. Simple blends of PTMO-2000 or PTMO terephthalate and 6GT (M_n=15,000) were clear at all compositions.

Witsiepe [205] reports the polyester-ether compolymers are insoluble below their melting points in most solvents. They are, however, soluble in proton donor solvents such as phenols, cresols, and a few partially chlorinated hydrocarbons (chloroform, 1,1,2-trichloroethane, 1,1,2,2-tetrachloroethane). The copolymers are completely soluble in m-cresol without producing a significant gel fraction. This makes it an excellent solvent for gel chromatographic fractionation and measurements of dilute solution viscosity and osmotic pressure.

Whittock [203] reports that the unusual resistance of these copolymers

to oils and most solvents improves with increasing crystalline content. For industrial applications, the copolymers are resistent to iso-octane/toluene mixtures, high-aromatic fuels and nitromethane, phosphate and chlorinated hydraulic fluids, "common solvents", salt solutions, dilute bases, and mineral acids. They are attacked, however, by hot concentrated mineral acids and bases.

Effect of Processing on Mechanical and Physical Properties

Lilaonitkul et al. [114] were able to produce three different spherulite morphologies in PTMT/PTMO copolymers depending on the copolymer composition and the processing history. The different types of spherulites had different tensile properties. All structures had about the same Young's modulus, but beyond the yield point (about 25% extension), substantially different stresses were observed for a given extension in each of the different types of structure [113].

Abhiraman [1] found that the modulus of the melt spun filaments did not vary much with spinning speed, but decreased upon annealing. The tenacity increased with spinning speed in unannealed filaments, but was about the same in all the "relaxed" filaments. The elongation to break in unannealed filaments was reduced as spinning speed increased. The effect was less pronounced in annealed samples. The strain recovery seemed to be independent of spinning speed.

Lilaonitkul et al. [113] report that drawn and heat set samples exhibit

a substantial increase (on the order of 15X) in their mechanical strength compared to undrawn samples.

Nielson [131] found creep in Hytrel®s to be very sensitive to the heat treatment received during fabrication. Samples which were quenched had a much greater creep rate than those allowed to cool slowly. Quenching was thought to reduce the crystallinity of the hard blocks and possibly the perfection of the crystallites, thereby reducing the stability of the samples.

Effects of Annealing on Mechanical and Physical Properties

Properties such as modulus, tensile strength, tensile set, creep rate, hardness, and density which are related to hard segment content and degree of crystallinity would be expected to change with annealing treatments.

Zhu and Wegner [223] found that the modulus of samples quenched from the melt increased upon annealing. Also, the modulus tended to increase with increasing HSC. These two observations lead the authors to suggest that the modulus is a linear function of the volume fraction of crystallinity. Abhiraman [1], however, found the modulus to decrease upon annealing.

Witsiepe[205] found the mechanical properties of the slower crystallizing copolymers (PET based) to depend greatly on the thermal conditions during and after molding. The faster crystallizing copolymers (PTMT based) were affected to a much lesser extent. Witsiepe reports that, in general, annealing for several hours at 60°–90°C below the copolymer melting temperature leads to improved "compression set" and resistance to creep. Such annealing

also leads to higher tensile strengths at elongations greater than 100%, but decreased tangent modulus and hardness. The most notable change in PTMT type copolymers was in compression set. A plot of compression set as a function of annealing temperature showed 70°–80°C below T_m to be the optimum temperature for improvement of this property.

More detailed information on the physical and mechanical properties of the segmented copolyesters can be found in a review by S.C. Wells [197].

2.2.4 Optimum Morphology for Elastic Recovery

Abhiraman, Kim, and Wagener [1] have studied the formation of elastic fibers by melt spinning of polyester-ethers. The hard segment is based on PTMT, while the soft segment is based on poly(ethylene oxide) (PEO) that has been chemically modified to prevent its crystallization. An "ideal morphology" for these filaments was presented that would maximize the recovery from deformation. The main features of their model are presented in Figure 2.7.

2.3 Homopolymers of Interest

2.3.1 Poly(tetramethylene terephthalate)

Crystal Structure

Perhaps the most interesting feature about the crystal structure of poly(tetramethylene terephthalate) (PTMT) or poly(butylene terephthalate) (PBT) is its polymorphism. Two crystalline forms, α and β, exist depending on the state

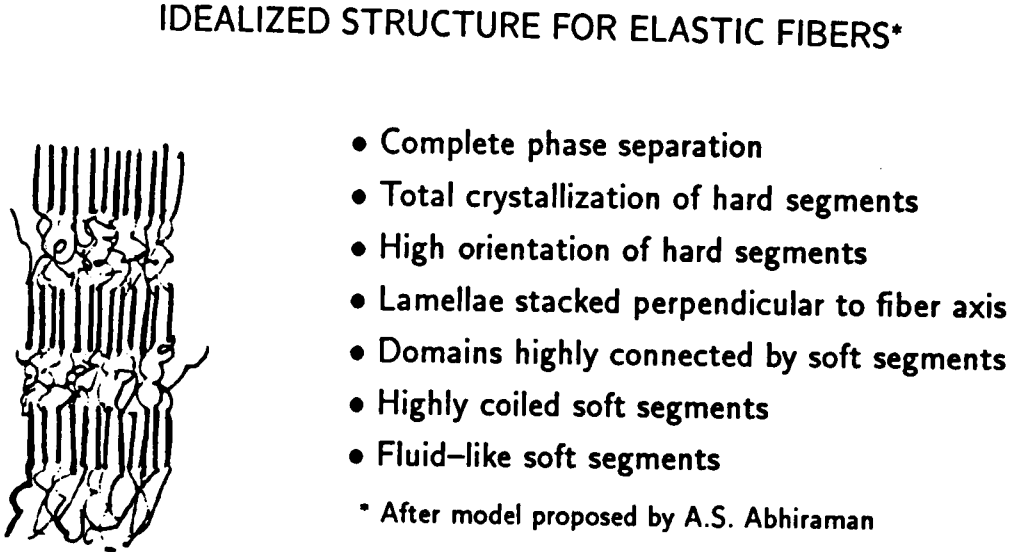


Figure 2.7: Ideal morphology for copolyester-ether elastic filaments.

Source: A.S. Abhiraman, Y.M. Kim, and K.P. Wagener, *J. Polym. Sci.: Polym. Phys.*, **25**, 205-228 (1987).

of strain (see Figure 2.8) [189]. The transition from the α to β phase upon extension of the sample has been followed by WAXD, SAXS, DSC, and infrared scanning techniques [31,73,170,171,179,180,21,209]. Perhaps the most sensitive method of following the transition is by quantitative analysis of the infrared spectra. Tashiro et al. [189], using this method, found that the amount of β phase increased in proportion to the strain. Increases were noted at strains as low as 1%. The bulk of the transition, however, occurred in the range of 4 to 12%, which corresponds to a plateau in the stress-strain curve.

Tashiro [189] has presented a series model for the transformation process (Figure 2.9). Crystalline regions (blocks) and amorphous regions (coils) were placed in series to explain the increase in plateau length in the stress-strain curve with an increase in crystallinity. This model also handles the increase in long period with increasing strains as detected by SAXS.

There is some controversy as to the exact unit cell dimensions of the two crystalline forms, but all agree on a triclinic cell [73,90,124,179,189,209]. The values presented by Hall and Pass [73] for the α-form will be used in this research. Their values are:

a = 4.86Å	α = 99.7°
b = 5.96Å	β = 116.0°
c = 11.65Å	γ = 110.8 °

Unit cell volume = 261.6Å^3

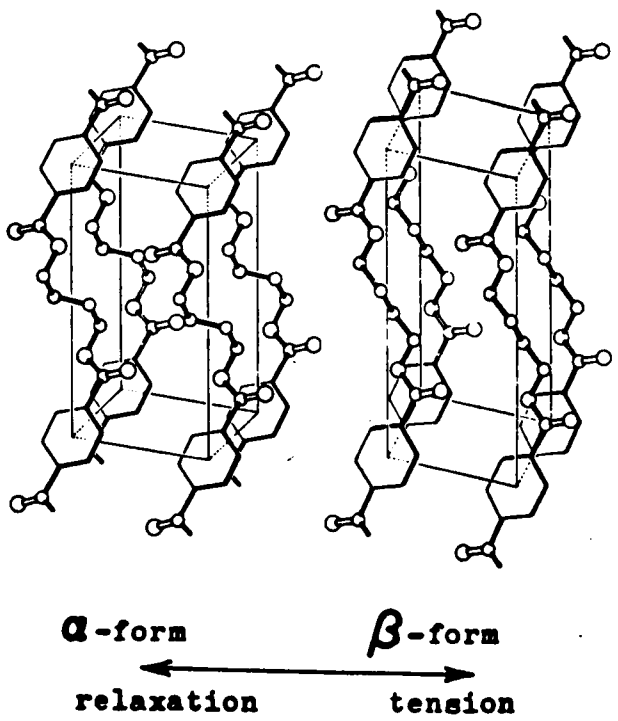


Figure 2.8: The crystalline forms of PTMT.

Source: K. Tashiro, Y. Nakai, M. Kobayashi, and H. Tadokoro, *Macromolecules,* **13**, 137-145 (1980).

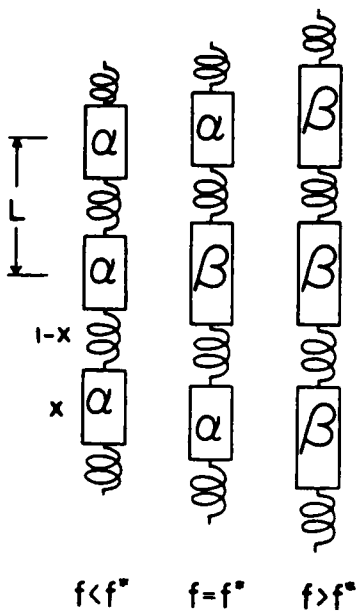


Figure 2.9: Tashiro model of the α to β transformation in PTMT.

Source: K. Tashiro, Y. Nakai, M. Kobayashi, and H. Tadokoro, *Macromolecules,* **13**, 137-145 (1980).

Yokouchi et al. [209] present the following values for the β form:

a = 4.95Å	α = 101.7°
b = 5.67Å	β = 121.8°
c = 12.95Å	γ = 99.9°

The main difference between the two forms is the large increase in the β-form crystallographic repeat distance along the chain direction (c-axis).

Morphology

Several investigators have studied the superstructure of PTMT with some presenting mechanical or physical properties [35,39,82,81,142,182]. Stein et al. [142,182] have found a spherulitic superstructure in films crystallized from the melt or solution cast. Spherulites melt cast at low temperatures gave H_v scattering patterns with intensity maxima at azimuthal angles of 0°and 90°. These were termed "unusual" spherulites. Spherulites formed at higher temperatures gave intensity maxima at 45°as would be expected for "regular" spherulites. These different types of spherulites were observed by Lilaonitkul et al. [112] in the PTMT/PTMO copolymers.

Stein et al. [182] proposed that the regular spherulites were more thermodynamically stable than the "unusual" type but formed at slower rates which required less undercooling. Both the degree of crystallinity and spherulite size increased with increasing crystallization temperatures.

Solution cast films were found to have regular spherulites. Stein et al. [182] point out that the much slower rate of crystallization would be expected to produce the more stable regular spherulites, according to their hypothesis.

No type of superstructure, however, was detected by Stein et al. [182] in samples crystallized from the glassy, amorphous state. The authors felt that a high nucleation density produced a superstructure too small to be detected by light scattering techniques. Crystallinities of 22% and 30% were reported at annealing temperatures of 120°and 180°C, respectively.

The multiple melting behavior of PTMT has been studied by Hobbs and Pratt [83]. The two melting endotherms show a dependence on cooling and heating rate. The endotherm at the lower temperature is attributed to crystallites which form during cooling. The crystallites formed at high cooling rates are unstable and recrystallize during heating in the DSC, producing the peak observed at 220°C. As the heating rate is increased, the low temperature peak increases in size at the expense of the endotherm at 220°C. The authors explain that as the heating rate is increased, less time is available for reorganization into more stable, higher melting crystallites. Extrapolation indicates that heating rates of 200°C/min or higher are needed to eliminate the high temperature endotherm associated with the melting of crystallites formed by recrystallization during the scan. Thus, the high temperature endotherm is not characteristic of the material in its room temperature state.

Mechanical and Physical Properties

PTMT is different from most other polymers in having a plateau in its stress-strain curve at low elongations (10%). This phenomena is quite evident in the stress-strain curves shown by Tashiro et al. [189] for a series of uniaxially oriented samples annealed at various temperatures (Figure 2.10).

Although the degree of crystallinity increased almost linearly with annealing temperature (from about 10% at 80°C to 36% at 200°C), the stress in the plateau region was shown to be almost constant. The strain at the end of the plateau, however, increased with increasing crystallinity.

The work of Callear and Shortall [35] shows that PTMT exhibits yielding and necking at elongations greater than about 15-20%. The samples exhibited ductile fractures with maximum elongations from 60% to 100% depending on the morphology and degree of crystallinity.

Gilbert and Hybart [66] report a T_g of 23°C while Stein et al. [182] report 28°C. Tashiro et al. [189] found the crystalline melting temperature to change with strain for samples annealed at 130°C and subsequently drawn. At low strains (0-4%), only the α phase melting endotherm at 221°C was observed in DSC traces. Melting peaks for both α and β phases were observed at strains ranging from 5% to 10%. At higher strains only the β phase melting endotherm at 227°C was observed.

Stein and Misra [182] reported an amorphous density of 1.282 g/cm^3 and a crystalline density of 1.396 g/cm^3. The highest experimental density

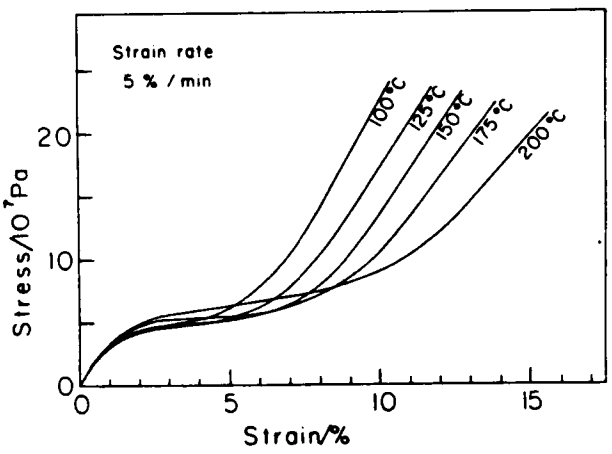


Figure 2.10: Stress-strain curves of PTMT monofilaments annealed at various temperatures for one hour.

Source: K. Tashiro, Y. Nakai, M. Kobayashi, and H. Tadokoro, *Macromolecules,* **13**, 137-145 (1980).

they observed for PTMO in their studies was 1.325 g/cm^3, which corresponds to 40% crystallinity.

2.3.2 Poly(tetramethylene oxide)

Poly(tetramethylene oxide) (PTMO) is a soft elastic gum that flows readily under stress [205]. Under certain conditions the polymer will partially crystallize [59,195,199]. A glass transition temperature of -84°C and a crystalline melting temperature of 38.3°were reported for this polymer [199]. A density of 0.980 g/cm^3 was reported for amorphous PTMO [195] and a value of 1.18 was calculated for the crystalline phase based on the unit cell parameters.

The crystal structure has been studied and reported by Imada et al. [86] and Cesari, Perego, and Mazzei [38]. The unit cell is monoclinic. Imada et al. present the following values for the unit cell parameters:

a = 5.48Å	α = 90.0°
b = 8.73Å	β = 134.2°
c = 12.07Å	γ = 90.0°

The values presented by Cesari et al. varied only slightly from those of Imada et al.

The strongest WAXD reflections are the (020) occurring at 2θ=19.8°and the (110) at 2θ=24.4°.

Kretz et al. [106] have studied the molecular orientation in a series of

uniaxially drawn PTMO samples using X-ray and NMR techniques. The orientation of the crystalline phase was directly linked to the draw ratio. Orientation of the amorphous chains appears to be limited to the layer of constrained chains at the surface of the lamellae. No appreciable orientation was detected in the less constrained amorphous material. The authors report, however, that the mobility of these chains decrease upon drawing.

Wetton and Allen [199] calculated a crystallinity of 33% by weight for an isotropic sample using X-ray techniques. This sample had a density of 1.036 g/cm^3 at 20°C [199], which corresponds to 32 wt.-% crystallinity based on the values presented for the density of the amorphous and crystalline phases. In the drawn samples studied by Kretz et al. [106], DSC techniques revealed crystallinities which ranged from 40–65% by weight depending on the molecular weight and draw ratio.

In polyester/ether copolymers in which the PTMO had a block molecular weight of at least 2000, the PTMO was shown to partially crystallize if it were the faster crystallizing homopolymer. If the polyester had the higher rate of crystallization, the PTMO remained amorphous [59]. Extension of molded samples up to 300% was found to cause a partially reversible crystallization of the polyether segments in these compositions [59]. The effect of composition and block length on the crystallization behavior of the PTMO phase was discussed in more detail in Section 2.2.2.

2.4 Deformation Studies

2.4.1 Structural Models for Block Copolymers

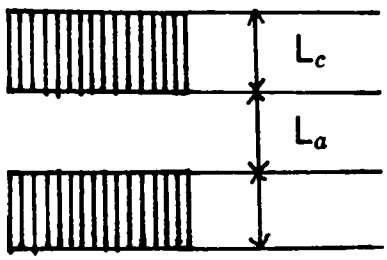
Simple models for the microstructure of semi-crystalline block copolymers have been presented and used by Gaylord and Lohse [61,60] to explain the mechanical properties of these systems at low elongations. Spherical, cylindrical, and lamellar morphologies were considered. Four basic types of interdomain chains, i.e., chains between the crystalline domains, were defined: interdomain bridges, loops, cilia, and floating chains. These are represented schematically in Figure 2.11 for a lamellar type morphology.

The relative extension of the interdomain material under a macroscopic deformation can be derived assuming the overall deformation is affine and that the hard segment domains themselves do not deform:

$$L_a' = (L_c + L_a)\lambda - 1$$

$$L_a'/L_a = \lambda + (\lambda - 1)L_c/L_a \tag{2.1}$$

where λ is the macroscopic extension, L_c is the domain thickness, and L_a and L_a' refer to the interdomain spacings before and after stretching, respectively. The dimensions L_c and L_a are defined as shown in the following schematic:



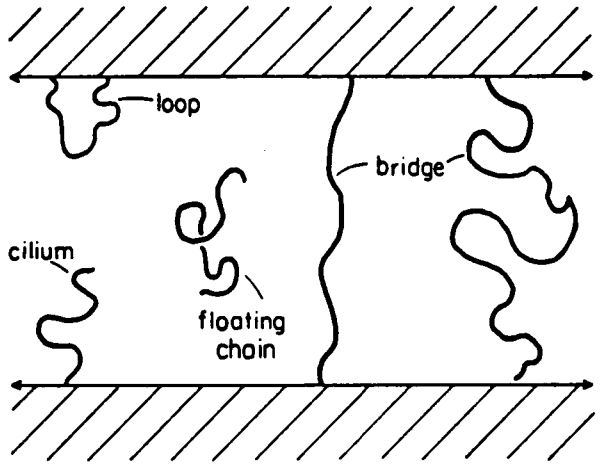


Figure 2.11: Different types of interdomain chains in block copolymers.

Source: R.J. Gaylord, *Polym. Eng. Sci.*, **19(14)**, 955-965 (1979).

For each type of morphology, the modulus of the bridge chain increases as the ratio L_c/L_a increases. The modulus is highest for a lamellar domain type morphology in which the sample is stretched normal to the lamellar plane.

The contribution of a loop, cilium, and floating chain to Young's modulus all decrease rapidly as the ratio χ of the interdomain spacing L_a to the mean square end to end distance $< r^2 >$ of the unperturbed, unconfined chain increases. This is explained in terms of a domain impenetrability effect. The contribution of the bridge chain, however, passes through a minimum near $\chi = 1$. At values of χ less than one, the modulus decreases as χ increases as a result of the domain impenetrability effect but at values of χ greater than one, the modulus increases with χ due to the inherent elastic nature of the bridge.

Their model also predicts a decrease in the modulus of the loops, cilia, and floating chains as the temperature is raised. The same behavior is predicted for the bridge chains at sufficiently low temperatures.

Thus, they conclude, the deformation behavior of a block copolymer depends on the morphology of the particular copolymer, the type of interdomain chain, and the type of deformation. The contour length of the interdomain chain, the separation of the domains, and the thickness of the domains are all important variables influencing the behavior.

2.4.2 Structure Changes During Deformation of Copolyether-esters

The effects of large deformations on the morphology of polyether-esters have been studied by a number of investigators [34,37,59,112,126,156,195,20].

Buck et al.[34] used wide angle X-ray diffraction (WAXD) and small angle X-ray scattering (SAXS) to study extruded filaments of PTMT/PTMO copolymers. Crystallite orientation was found to increase with extension up to about 300% elongation; beyond this value little further orientation occurred. WAXD patterns of drawn filaments showed the PTMT repeating units were aligned parallel to the draw direction while electron microscopy showed the lamellae were aligned in the transverse direction. Hence, the PTMT chains traverse the lamellae parallel to the thickness direction [34,37].

Mody and Wilkes [126] found the birefringence to increase almost linearly with extension up to about 220%. In addition, the birefringence at a fixed extension increased with increasing hard segment content [126].

Small angle light scattering experiments performed by Seymour et al. [156] and Lilaonitkul et al. [112] on stretched samples indicate the spherulites deformed into ellipsoids with their major axes parallel to the stretching direction. From low extensions, the spherulites returned to their original shape upon removal of the stress. At extensions greater than 25%, the deformation become increasingly irreversible. Mody [126] explains that the soft segments nearly disorient completely when strain is removed, whereas the hard segment remains partially oriented. A plot of film extension versus spherulite extension (not shown) suggested to Lilaonitkul et al. that interspherulitic slippage and microvoid development were occurring. The number of microvoids were found to increase with increasing hard segment content [112].

Both hard segment and soft segment orientation was studied by Lilaonit-

kul and Cooper [112] using differential infrared dichroism. Step-strain (rapid 150% strain) experiments suggested that the soft segments orient rapidly as the strain is applied, but then they try to relax into a more entropy-favorable random conformation. Relaxation of the soft segments caused some reorientation of the hard segments. The amount of relaxation decreased with increasing hard segment content.

Orientation functions were calculated for both hard and soft segments and were plotted as a function of strain (Figure 2.12). The hard segment phase exhibited negative orientation factors (chain axes tending to orient perpendicular to the stretch direction) at low elongations. At higher elongations positive orientation factors were produced, increasing with increasing extension (no data given for extensions greater than 200%). Soft segment orientation factors were positive (chains tending to orient parallel to the stretch direction) at all strain levels. The results were interpreted as follows: At low elongations, spherulite deformation caused the lamellae to orient as a unit in the stretching direction resulting in a chain orientation perpendicular to the stretching direction. At higher elongations, the lamellae broke down and the chains oriented in the stretching direction. The amorphous soft segments, including uncrystallized polyester tended to orient parallel to the stretch direction regardless of the crystallite behavior.

The stress-strain behavior of copolyester-ether films during cyclic testing were studied by Lilaonitkul, West, and Cooper [114]. The sample recovers well from low elongations, but there is a large amout of permanent set at the

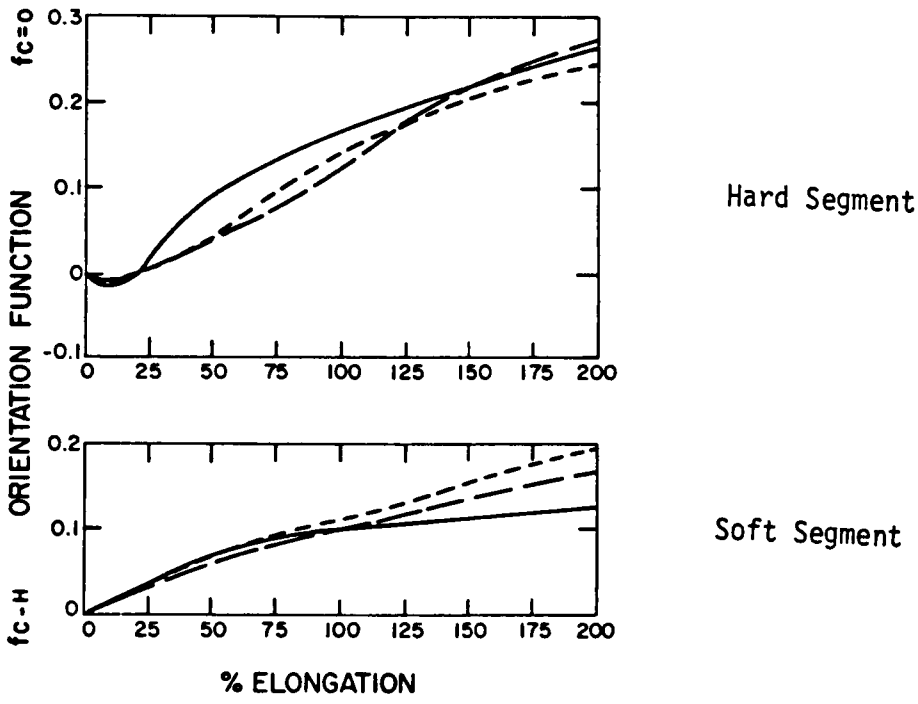


Figure 2.12: Hard and Soft segment orientation functions for samples spin cast at 110°C.

Source: A. Lilaonitkul and S.L. Cooper, *Rubb. Chem. Technol.*, **50(1)**, 1-23 (1977).

higher elongations. Two other important features were noted. First, extensions at strains lower than those previously applied result in lower stress levels. Secondly, at extensions higher than those previously applied, the stress level is approximately independent of the previous strain history. A single strain cycle to 250% is compared in Figure 2.13 to successively increasing strain cycles up to 250%.

Bogart, Gibson, and Cooper [20] studied the effect of heat setting on several thermoplastic elastomers varying in the crystallizability of the hard segment. The SAXS pattern of the copolymer having the non-crystalline hard segment showed no preferred orientation after the heat set treatment (stretched 200% and annealed). The SAXS pattern of the copolyester-ether on the other hand shows significant levels of preferred orientation. They conclude that the anisotropy in the semi-crystalline polymer is due to intradomain ordering. This limits the recovery of the domain shape after deformation.

2.4.3 Structural Changes During Deformation of Other TPEs

Polyurethanes

Desper, Schneider, Jasinski, and Lin [48] have studied the microstructure after deformation in three different types of polyurethanes. All are based on a soft segment of PTMO of molecular weight 1000 and a hard segment of either toluene diisocyanate (TDI) or bis(*p*-phenyl isocyamide) (MDI), but differ in the type of curing agent used and the type of hard segment domain formed. The amine and diol cured polyurethanes form a regular repeating domain structure

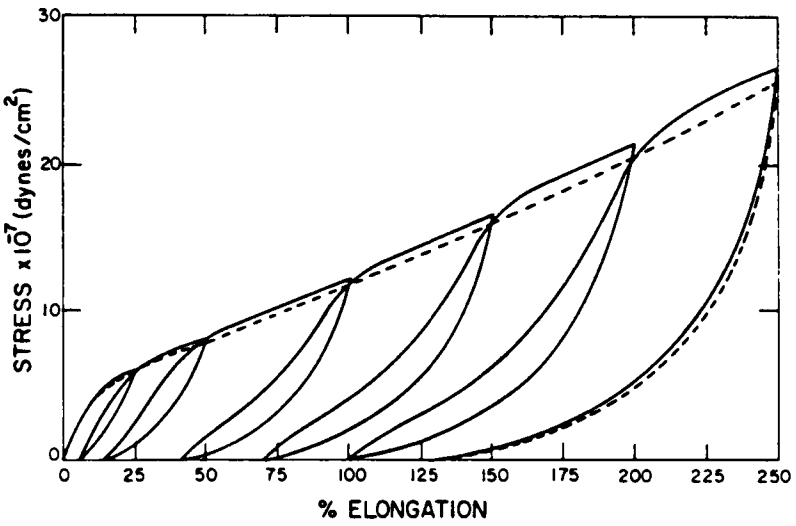


Figure 2.13: Cyclic stress-strain behavior of a copolyester-ether film. A single strain cycle to 250% is compared to the successively increasing strain cycles.

Source: A. Lilaonitkul, J. West, and S.L. Cooper, *J. Macromol. Sci.-Phys.*, **B12(4)**, 563–597 (1976).

as shown by discrete SAXS scattering. Three different modes of deformation were observed: a shear mode, a tensile mode, and a rotation or translation of independent particles.

The amine cured polyurethane was thought to have disk shaped domain structures. During stretching, the disks tilt away from the stretch direction causing the soft segment phase to deform in shear. In the diol cured polyurethane, the hard segment domains behaved like cylinders in which the thickness and diameter were of comparable dimensions. This material deformed in a tensile mode. The repeat direction of the microstructure is along the cylinder axis. When the material is deformed the cylinders line up with their axes toward the stretch direction. The soft segments are deformed in tension. The triol cured polyurethanes are characterized by chemical crosslinking within the hard segment domains, but no regularly repeating array of domains are formed. Since the shape of the hard segment domain could not be established, the deformation mechanism could not be uniquely determined. If the domains are assumed to be elongated in shape, the results would indicate a rotation of the long axis toward the stretch direction. If the domains are assumed to be more spherical in shape, the results would indicate a simple translation of the domains in the stretch direction.

The amine and triol cured polyurethanes deformed in a reversible manner, while the diol cured polyurethanes were permanently deformed by stretching. The high elastic recovery of the amine and triol cured polyurethanes was attributed to the resistence of the hard segment domains to plastic deformation.

In the triol cured polyurethane, the chains within the hard segment domain are chemically cross-linked, while in the amine cured polyurethane, strong hydrogen bonding prevents chain slippage within the hard segment domain. The diol cured polyurethane shows much weaker hydrogen bonding than the amine cured polyurethane. As a result, its hard segment domains are much more easily disrupted.

Bonart [23] has used x-ray diffraction techniques to study the hard segment orientation as a function of strain in segmented polyurethanes which exhibited hydrogen bonding. Below elongations of about 200%, the chain axes in the hard segments were found to orient perpendicular to the stretch direction. A model of hard segment domains in a soft segment matrix was proposed to explain this behavior. The force is initially transmitted by the soft segments. As these segments become taut, they exert a torque on the hard segment domains causing their long axes to line up parallel to the stretch direction. Since the chains run across the width of the hard segment domains, they are aligned perpendicular to the stretch direction. At higher elongations ($> 200\%$), the hard segment domains begin to break up and become increasingly oriented in the stretch direction. Bonart suggests that stress softening and the hysteresis phenomena are the result of the hard segment deformation. Models of the structure at low and high elongations were presented and are reproduced in Figure 2.14.

In another paper, Bonart et al. [24] report the results of experiments performed on polyurethanes with crystalline and paracrystalline domains. During

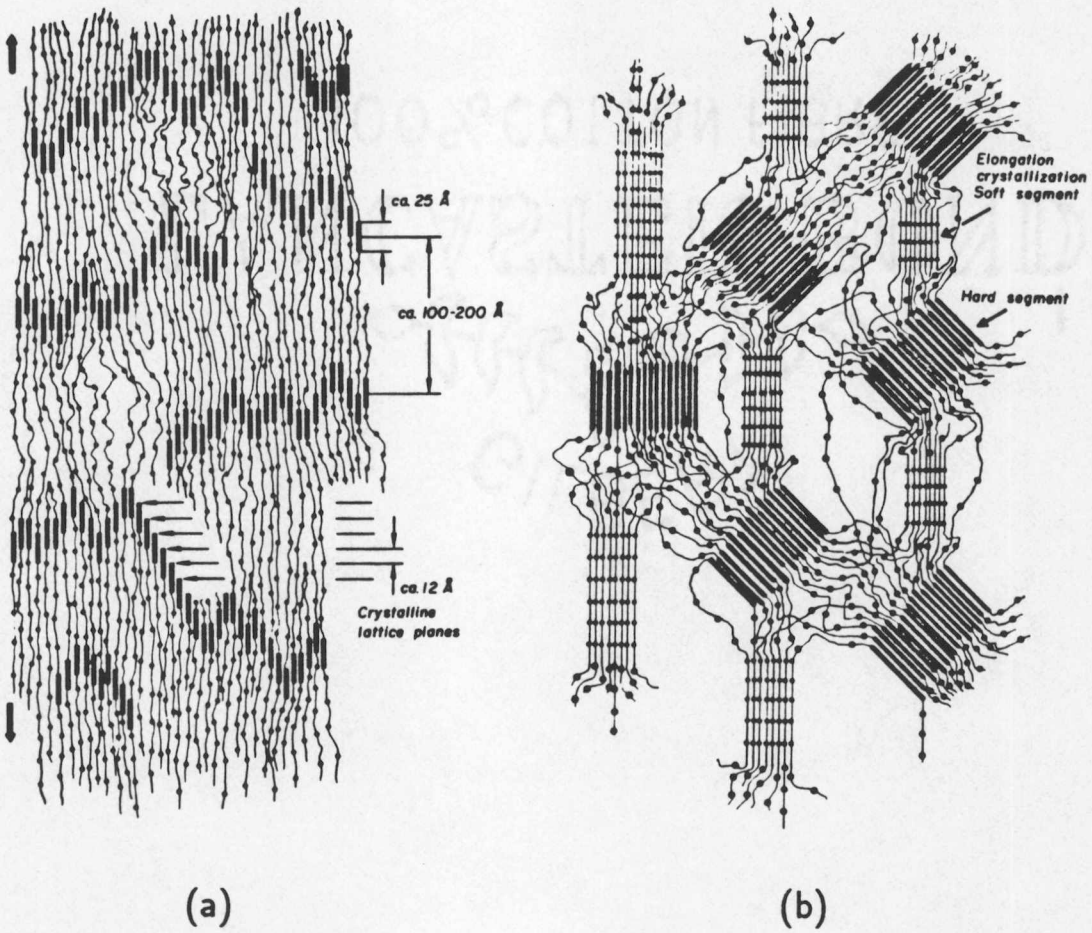


Figure 2.14: Model of the morphology of oriented polyurethane elastomer. (a) Material stretched about 200%, (b) material stretched about 500% and fixed in water at about 80°C.

Source: R. Bonart, *J. Macromol. Sci., Phys.*, **B2(1)**, 115-138 (1968).

orientation, the paracrystalline segments behaved as described above, but the crystalline segments behaved very differently, acting more like an inert filler. The chain axes of the hard segment domains were found to preferentially orient perpendicular to the stretch direction, even at high elongations.

If the hard segment is of sufficient length to permit microcrystallinity, a spherulitic morphology may result. Samuels and Wilkes [147] have studied a series of segmented polyurethanes base on PTMO soft segments and a piperazine-butanediol hard segment. After deformation, WAXD patterns indicated the hard segments had become oriented in the stretch direction. The orientation remained after releasing the stress. Even annealing without restraint did not reduce the hard segment orientation. In fact, the x-ray patterns indicated that the orientation may have increased some.

The deformation of the superstructure was followed using light scattering techniques. The patterns indicated the spherulites had become elongated in the stretch direction. The ratio of the major axis to the minor axis in the anisotropic spherulites was determined by the sample extension ratio.

SBS Type Copolymers

Several investigators have studied the effects of orientation on the morphology of SBS or SIS block polymers [18,54,56,173,174]. Fujimura et al. [56] reported that when certain SBS samples were stretched beyond the yield point, they became rubbery and exhibited a high elasticity and large recoverable deformation. The deformation was described as the breakup of a rigid macrostructure.

Beecher et al. [18] found that SIS samples with a long range polystyrene (PS) network (interconnected spherical PS domains) showed a yield point and draw region in their stress-strain curves. In a typical stress-strain curve for SIS samples of this type, the stress increased up to the yield point (about 5% elongation), then decreased until about 20% strain. The stress remained constant from 20% up to about 180% elongation. A neck propagated across the specimen in this range. At higher elongations, the stress rose rapidly and the sample broke shortly thereafter.

During tensile testing, the samples cast from tetrahydrofuran/methyl ethyl ketone (THF/MEK) exhibited the yielding characteristic of a long range PS network. If the samples were stretched a second time, no yield point was observed and the samples behaved in a more elastic manner. The difference between the curves suggested that some rigid structure was broken down during drawing. The stress–strain curves of the compression molded samples were similar to those cast from the THF/MEK solutions, except for the absence of a distinct yield point. Stress-strain curves for the samples cast from benzene/heptane solutions appeared more "rubber like". There was no yield point or drawing region in contrast to the previously described samples. Samples cast from CCl_4 behaved in what the authors called a "leathery" fashion. During cyclic testing, no additional "set" was observed after the second extension, but recovery was slow [18].

Using electron microscopy, Beecher et al. observed the deformation of SIS samples which possessed a long range PS network. At low elongations, they

found the spherical PS domains lined up in rows perpendicular to the direction of stress, with the tie molecules aligned parallel to the stretch direction. At slightly higher elongations (still less than 200%), the balls oriented in "V-shaped" patterns and then eventually broke down into individual particles. As the network was broken down, the PS domains became ellipsoidal in shape.

Those samples which did not possess a long range network deformed in a similar but less well defined manner. Since there were fewer interparticle connections, the structure was much more diffuse. The same row orientation and chevron patterns were observed, but the patterns were less distinct. There seemed to be no difference, however, in the deformation of the PS spheres into ellipsoidal shapes.

Above elongations of 200%, the different types of samples behaved in similar ways. No additional deformation of the PS domains was observed in the range of 200–800% elongation. At higher elongations, the domains deformed with extension until the sample broke [18].

Fujimura et al. [56] observed much the same deformation mechanism for SBS samples with lamellar-like domains as Beecher did for SIS films with spherical PS domains; they also presented a model of the process. Their model is reproduced in Figure 2.15. In this figure, the change of structure from (a) to (b) represented the expansion of the lamellar spacing in the initial stages of deformation. The change in structure from (b) to (c) and (d) was thought to occur during yielding and necking. The irregular deformation of the lamellar domains involved kinking, shearing, orientation, and destruction of the

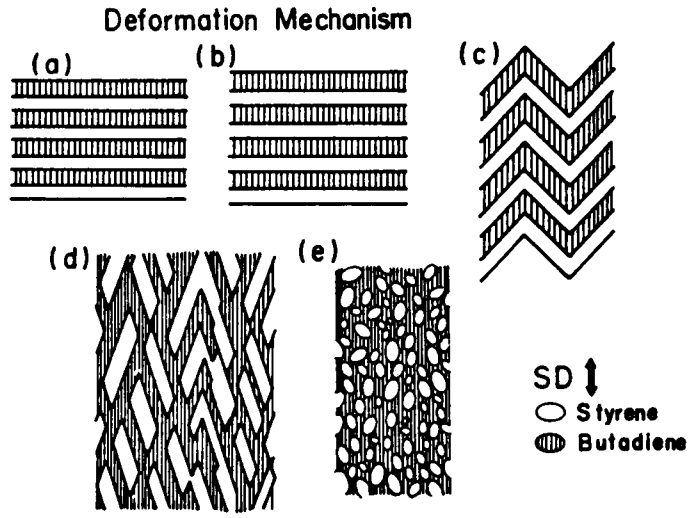


Figure 2.15: Model for the deformation of lamellar SBS copolymers.

Source: M. Fujimura, T. Hashimoto, and H. Kawai, *Rubb. Chem. Tech.*, **51**, 215-224 (1978).

lamellae. Eventually, the PS domains fragmented and became dispersed in the rubber matrix.

The deformation and recovery in the copolyether-esters, polyurethanes, and the SBS type copolymers involve entropic mechanisms and can be interpreted in terms of rubber elasticity theory. There is, however, another class of polymers in which the elastic behavior arises from energetic rather than entropic effects. The deformation mechanisms in these "hard elastic" polymers may involve elastic bending of lamellae [188,176,132], microvoid formation between lamellae [40,145,188], or reversible shear of lamellae between fixed tie points [40]. More information on hard elastic polymers can be found in a recent review by Clark [41].

Mechanisms involving bending or reversible shearing of lamellae may play a role in the elastic deformation of the copolyether-esters at low elongations.

2.5 Copolymer Crystallization

Any theory of crystallization of copolymer systems must take into account not only the composition, but the arrangement of the monomeric units in the molecule (i.e. random, block, or alternating). In addition, one or both of the components may be crystallizable. In most cases, though, only one of the components will crystallize. The noncrystallizable copolymer units act to interrupt or terminate crystal growth. If the noncrystallizable unit is included

within the crystal it can be treated as a point defect depending upon its size. Often the size or number of inclusions will depend upon the rate of crystallization. Other problems include the effects of noncrystallizable units being pushed to the crystal surface, the segregation of molecules according to their composition or sequence length, and the possibility of chain folding [51,207].

Gornick and Mandelkern [70] have treated the effect of randomly introduced copolymer units on the nucleation rate and crystallization kinetics of a copolymer system. They limit their discussion to the case in which noncrystallizable units are excluded from the crystalline phase. They postulate that the accumulation of noncrystallizable units in the untransformed material will depress its melting point and reduce the effective degree of undercooling even during isothermal crystallization. They break the crystallization process down into two separate but concurrent steps: 1) nucleation of a stable phase and 2) growth of stable nuclei. They theoretically treat the effect of a noncrystallizing component on a three-dimensional homogeneous nucleation process. Their theory predicts that the nucleation rate will be significantly lowered by the addition of noncrystallizable units to the homopolymer and that the effect will be greatest at low undercoolings and will increase rapidly with increasing amounts of the noncrystallizing component. Hence, as the concentration of noncrystallizable units increases during the crystallization process, the degree of undercooling is reduced and the nucleation rate may fall off sharply, especially at low initial undercoolings.

They treat crystal growth by modifying the Avrami equation [10,11,12]

to allow for nucleation and growth rates which vary with the degree of transformation. The solution to their equation can only be obtained by a direct iterative process using numerical parameters. Using polyethylene with small weight fractions of $-CH(CH_3)-$ copolymer units as an example, they plot the degree of transformation as a function of time and undercooling. Curves calculated from the Avrami equation were plotted for comparison. These curves are shown in Figure 2.16. The isotherms calculated from their equation were not mutually superimposable as would be expected from the simple Avrami equation. Instead they tend to fan out at low amounts of supercooling and high degrees of transformation. The effects become more pronounced at higher copolymer concentrations. However, all the isotherms tend to be superimposable at the lower levels of crystallinity. The fanning out is interpreted as a retardation of the crystallization process due to the changing nature of the nucleation and growth processes with increasing crystallinity. The authors conclude that any attempt to fit these types of isotherms to the standard Avrami equation will lead to erroneous interpretation of the mechanism since the exponent "n" (in the Avrami equation) varies with the degree of transformation [70].

Perret and Skoulious [135] studied the crystallization and resulting morphology of triblock copolymers of poly(ϵ caprolactone) (PCL) and poly(ethylene oxide) (PEO) of various compositions. The PEO was capped on both ends by the PCL. All the copolymers were found to have a lamellar structure. The thickness of the lamellae in the PCL rich copolymer was found to be independent of the crystallization temperature and did not change upon subsequent

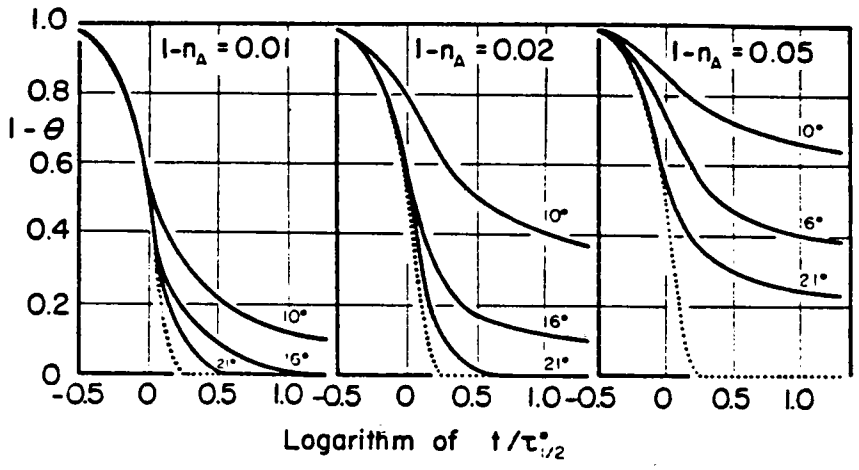


Figure 2.16: Change in relative crystallinity θ calculated as a function of time for random copolymers with n_b= 0.01, 0.02, and 0.05. The degree of undercooling $T_m - T$ is shown next to the curves. Dotted lines were calculated assuming a constant nucleation rate with n=4 (Avrami equation).

Source: F. Gornick, and L. Mandelkern, *J. Appl. Phys.*, **33**, 907 (1962).

annealing. This behavior is similar to that of the PCL homopolymer. The lamellar thickness of the PEO rich copolymers, however, was found to change with both crystallization and annealing temperatures, in accordance with the PEO homopolymer. Hence, the major component of the copolymer determines the behavior of the entire sequence. In the copolymer composed of equal amounts of each component, two crystalline phases are observed with the morphology determined by the crystallization temperature. The crystallization kinetics do not show the slow-down in growth rate observed for random copolymers [135,207].

Zhu, Wegner, and Bandara [223] have studied the crystallization kinetics and morphology of copolyester-ether films using light microscopy and DSC techniques. These researchers report two distinct crystallization regimes. At low undercoolings ($\Delta T_u < 30°C$), isothermal crystallization produced spherulitic type structures (Regime I). At high undercoolings ($\Delta T_u > 30°C$), or if the sample is quenched or crystallized from the glassy state, loose aggregates of individual lamellae were formed (Regime II).

Heterogeneous nucleation is observed in Regime I. The nucleation density increases sharply as ΔT_u or HSC is increased. This behavior is consistent with the model presented by Gornick and Mandelkern [70]. The nucleation density reaches a constant value within several minutes of reaching the crystallization temperature and remains constant throughout the crystallization process. A large volume fraction of material remains amorphous even after long crystallization times. The spherulites, in general, do not impinge upon

one another. The crystallinity remains relatively low.

Zhu and Wegner [222] found that upon annealing at a lower temperature, additional crystallization took place at the edge of the spherulites. No new spherulitic structures structures developed, so the increase in crystallinity at the lower temperature was believed to take place only within existing domains.

Zhu et al. report that the nucleation density in Regime II is much higher than in Regime I and could not be followed by light microscopy. The isothermal crystallization process was followed indirectly by DSC. The weight fraction of crystallinity as a function of time and crystallization temperature is shown for several different compositions in Figure 2.17. Much higher crystallinity is developed at these high undercoolings. The crystallization kinetics during isothermal crystallization follow an Avrami type behavior:

$$\frac{(w_c - w_h)t_c}{(w_c - w_h)t_\infty} = 1 - exp[-Kt_c^n] \tag{2.2}$$

where $(w_c - w_h)t_c$ refers to the crystallinity at time t_c, and $(w_c - w_h)t_\infty$ is the crystallinity at infinite crystallization times. The value of "K" decreased as the degree of undercooling increased. Non-integer values of "n" were obtained. This did not surprise Zhu et al. since the superstructure formed in this regime did not assume any type of regular geometrical shape such as spherical or dendritic. The value of "n" did not vary with temperature for a given copolymer, but varied strongly with composition. It was highest for the 54 wt.-% composition and lowest for the 45 wt.-% composition.

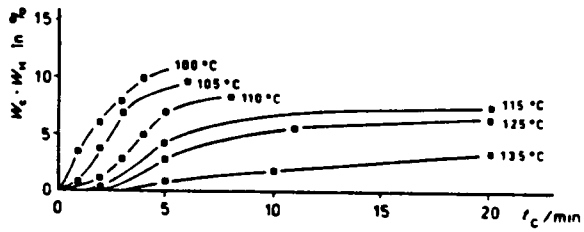


Fig. 4a

45 wt.-%

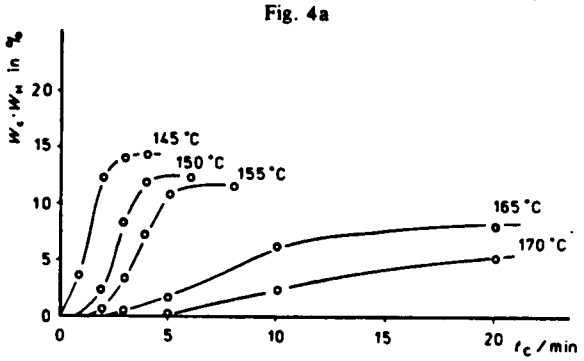
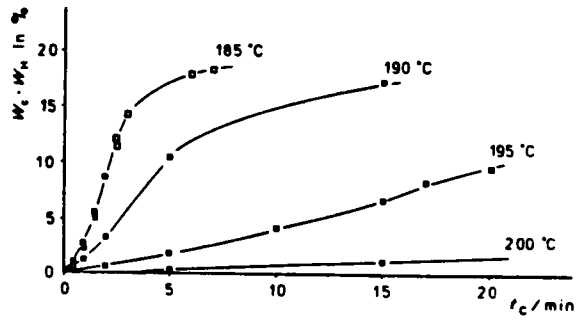


Fig. 4b

54 wt.-%



72 wt.-%

Figure 2.17: Weight fraction of crystallinity as a function of time and crystallization temperature for several different compositions. Top: 45 wt.-% HSC, Middle: 54 wt.-% HSC, Bottom: 72 wt.-% HSC.

Source: L. Zhu, G. Wegner, and U. Bandara, *Macromol.Chem.*, **182**, 3639-3651 (1981).

Zhu and Wegner [222] report that clear films were produced by quenching from the melt. Upon annealing, these samples remained clear, indicating that the nucleation density was very high and that crystallites much smaller than the wavelength of light were produced.

Briber and Thomas [32] have also studied the crystallization behavior of the copolyester-ethers. They found that after cooling the samples to room temperature, some of the short hard segment sequences remaining in the matrix crystallize. This new growth could form at the edge of existing crystallites or as smaller crystallites scattered throughout the amorphous matrix. The new crystallites took weeks to form at room temperature. These results imply that fractionation according to sequence length can occur. The authors explain that the fractionation occurs not as a result of incompatibility, but due to a coupling of the sequence length with the stable crystallite size at a given crystallization temperature.

2.6 Fiber Processing

2.6.1 Melt Spinning

Melt spinning involves the extrusion of a polymer melt through spinneret holes, draw down, solidification, and, usually, take-up of the filament onto a bobbin. As the molten filament leaves the die, it undergoes extensional flow when the take-up rate is higher than the velocity in the spinneret. As the material travels down the spinline, it cools due to heat transfer to the environment, and

eventually solidifies under stress. The orientation in the melt just above the "freeze line" is the origin of orientation in the solid filament. In crystallizable polymers, it may give rise to oriented crystal growth. Abhiraman et al. [1] has developed a theory relating the orientation in the melt of copolyester-ethers to the amorphous and crystalline orientation developed in the solid filament. A diagram of the orientation development is shown in Figure 2.18.

Rheology and Heat Transfer

The rheology and heat transfer aspects of melt spinning have been studied experimentally by Ziabicki [215,219,220,212], Kase and Matsuo [95], Ishibashi, Aoki, Ishii [87], Acierno et al. [2], and Nakamura et al. [130]. Kase and Matsuo [95] and Ziabicki [215,212,220] have derived the equations for the material balance, momentum balance, and heat balance. Under steady state conditions, the material balance leads to the following form of the continuity equation, which states that:

$$\rho V A = W \tag{2.3}$$

where ρ is the density, V is the fiber velocity, A is the cross-sectional area, and W is the mass flow rate. Under steady-state conditions, the momentum balance can be integrated and expressed as a force balance:

$$F_{ext} + F_{grav} = F_{rheo} + F_{inert} + F_{drag} + F_{surf} \tag{2.4}$$

where F_{ext}, F_{grav}, F_{rheo}, F_{inert}, F_{drag}, and F_{surf} denote, respectively, the take-up tension, force of gravity, rheological drag, inertial effects, air drag, and surface

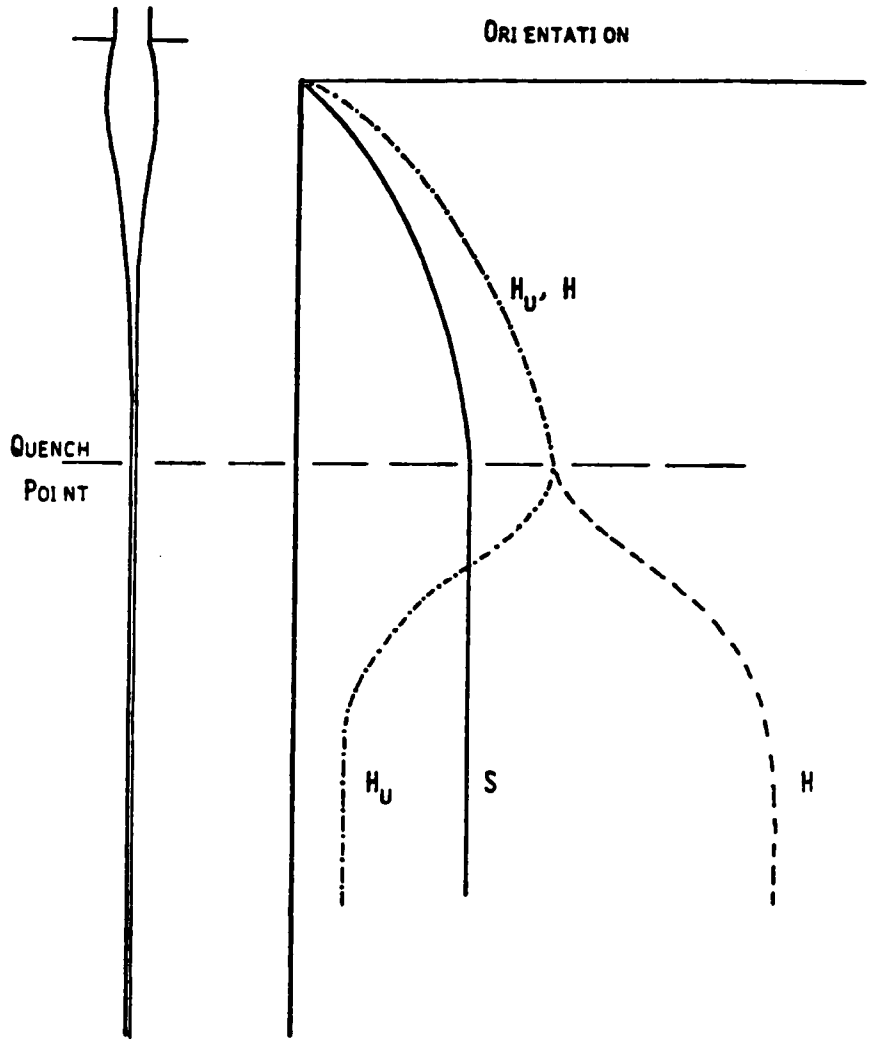


Figure 2.18: Orientation development in the spinline. "H" refers to the overall hard segment, "H_u" to the uncrystallized hard segment, and "S" to the soft segment.

Source: A.S. Abhiraman, Y.M. Kim, and K.P. Wagener, *J. Polym. Sci.: Polym. Phys.*, **25**, 205-228 (1987).

tension effects. These are expressed as follows:

$$F_{grav} = g \int_x^L \rho A dx \tag{2.5}$$

$$F_{rheo} = F_x \tag{2.6}$$

$$F_{inert} = W(V_L - V) \tag{2.7}$$

$$F_{drag} = \pi \int_x^L \sigma_d \, d \, dx \tag{2.8}$$

$$F_{surf} = \pi \sigma_s (d_L - d) \tag{2.9}$$

where x is the distance from the spinneret, L is the length of the spinline, F_x is the force at point x, σ_d is the drag force per unit area, σ_s is the surface tension, and d_x is the fiber diameter at point x.

When all terms other than F_{rheo} are either known or neglected, the rheological force can be calculated. If the fiber radius R or fiber velocity is known as a function of distance from the spinneret, then the stress at any point in the spinline can be calculated [212]:

$$\tau_{xx}(x) = F_{rheo}/\pi R^2(x) = \frac{f_{rheo} \, \rho \, V(x)}{W} \tag{2.10}$$

Conversely, if a suitable constitutive equation relating spinline stress to elongation viscosity and deformation rate $dV(x)/dx$ is substituted in the above equation, a differential equation in terms of V(x) will be obtained. These may be solved using the boundary conditions of constant extrusion and take-up velocities to give the velocity distribution in the spinline. The diameter can then be calculated from the continuity equation. Hence, the force balance and continuity equation provide the framework for studying the dynamic and kinematic details as related to specific spinning conditions.

Heat transfer is an important factor in determining the rate of solidification and crystallization along the spinline. Kase and Matsuo [95] have developed equations for a heat balance on a differential element of the molten fiber. Several assumptions were made in introducing the differential equations:

- The cross-section of the fiber is circular.
- Temperature is constant in the radial direction.
- Heat conduction along the fiber is negligible.

The equation of heat balance on a unit length of filament being cooled $\Delta\tau$ seconds as it moves downward is:

$$-2\pi rh(T-T_a)\Delta t - 2\pi r\sigma E(T^4-T_a^4)\Delta t = \pi r^2 \rho C_p \Delta t \qquad (2.11)$$

where

r = radius of the filament

h = heat transfer coefficient

T = fiber temperature

T_a = ambient air temperature

t = time

σ = Stefan-Boltzman constant

E = emissivity

ρ = density of the molten polymer

C_p = isobaric specific heat of the molten polymer.

Dees [46] has modified this equation to include the heat of crystallization:

$$\frac{\delta T}{\delta t} + V\frac{\delta T}{\delta x} = -\frac{2\sqrt{\pi}\, h\,(T - T_a)}{\rho\, C_p\, \sqrt{A}} + \frac{\Delta H}{C_p}\frac{dX}{dt} \tag{2.12}$$

where ΔH is the heat generated by crystallization, dX/dt is the rate of change of the crystalline fraction, and A is equal to r^2. Under steady state conditions, $\delta T/\delta t = 0$. The equation can then be rearranged to express the degree of crystallinity in terms of the fiber temperature and the cooling rate $\delta T/\delta t$:

$$\frac{\delta X}{\delta t} = \frac{2\sqrt{\pi}\, h\,(T - T_a)}{\rho\sqrt{A}\,\Delta H} + \frac{C_p}{\Delta H}\frac{\delta T}{\delta t} \tag{2.13}$$

This is essentially the same result obtained by Nakamura et al. [130]. However, they combine some of the variables into a "cooling parameter:"

$$R = \frac{2\sqrt{\pi}\, h}{\sqrt{A}\,\rho} \tag{2.14}$$

The cooling parameter depends on the diameter of the fiber and the heat transfer coefficient, which, in turn, depends on the air speed relative to the fiber. Ishibashi [87] has defined a cooling rate constant "m" expressed as:

$$m = const\; d^{-5/2} V^{1/3} \tag{2.15}$$

This shows the cooling rate depends much more on the diameter of the fiber,d, than on its velocity, V.

Structure Development During Melt Spinning

Conventional Spinning The structure (i.e., degree of orientation, level of crystallinity, and morphology) developed during melt spinning of a fiber can

be greatly influenced by spinning conditions. This was known as early as 1932 when Carothers and Hill [36] noted the effect of up-take velocity on the crystalline orientation and mechanical properties of their spun fibers. However, during the next few decades melt spinning developed into an art (based largely on empirical observations) rather than a science. Very little fundamental research of melt spinning was carried out until the work of Ziabicki and Kedzierska [214,216,219,220,215,217,218] and others [7,96,95,190,200] in the late fifties and sixties. Ziabicki and Kedzierska theorized and performed numerous experiments on the dynamics and kinematics of deformation in the spinline. They found orientation increased with spinning tension, the difference between take-up and extrusion velocity, and the inverse of filament diameter. Based on their experiments and the postulation of Sippel [172] they concluded that both the deformation rate (as measured by the velocity gradient dV/dx) and relaxation effects were factors which controlled orientation development.

Katayama, Amano, and Nakamura [97] made quantitative measurements of crystallinity on running spinlines of polyolefins using WAXD patterns. They found the rate of crystallization in the spinline to be many times higher than that of the unoriented polymer at the same crystallization temperature. Furthermore, the crystallization rate increased with increasing take-up speeds. Hence, these authors are probably the first to demonstrate the effect of molecular orientation and cooling on the crystallization kinetics. A morphological model of polyethylene was presented in which lamellae were stacked perpendicular to the fiber axis. The angle of tilt of the c-axis with respect to the fiber

axis was noted to change both with positions in the spinline and with spinning conditions.

Dees and Spruiell [47] have studied the kinematics of deformation and the development of crystallinity and orientation during melt spinning of polyethylene fibers. The crystallization kinetics and ultimate crystallinity were found to be controlled by a balance between the opposing effects of increasing orientation and increasing cooling rate. A morphological model was presented which explained the variation of the a, b, and c-axis orientation functions with position in the spinline and take-up velocity. Their model is shown in Figure 2.19.

Fung and Carr [57,58] investigated the effects of shear flow (caused by a skin-core structure at the crystallization boundary) on the morphology of as-spun polyethylene and polypropylene fibers. The fibers were found to possess a radial variation in birefringence with the highest values found at the surface of the filament.

Nadella et al. [128] investigated the effect of molecular weight and spinning conditions on the development of structure during melt spinning of polypropylene. On-line crystallization kinetics were studied as a function of take-up velocity for one polymer. An important conclusion was that molecular weight and spinning variables such as mass flow rate, extrusion temperature, and take-up velocity all influence the morphology mainly through their effect on spinline stress. Water quenching, as compared to air quenching, was found to change the crystal structure from monoclinic to smectic (paracrystalline),

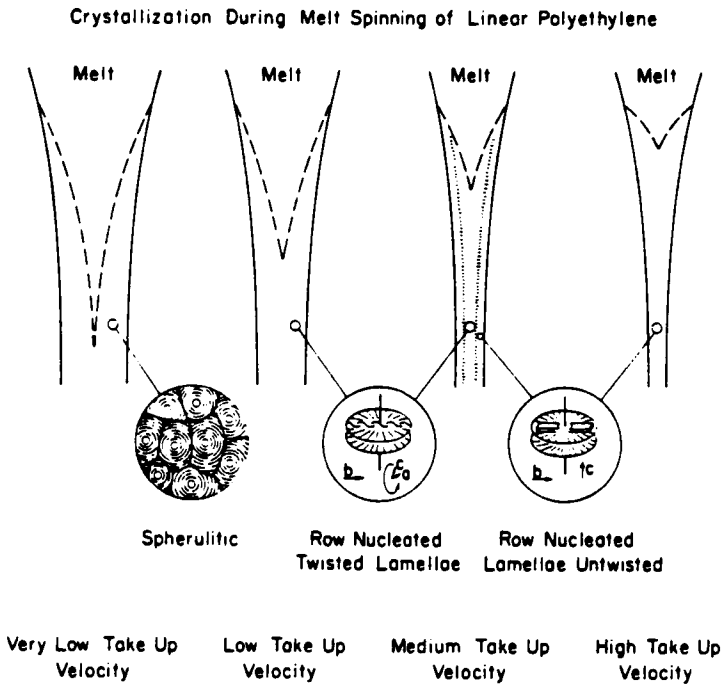


Figure 2.19: Morphological models of structure development during melt spinning of polyethylene.

Source: J.R. Dees and J.E. Spruiell, *J. Appl. Polym. Sci.*, **18**, 1053 (1974).

and hence reduce the crystallinity and chain axis orientation.

Gianchandani, Spruiell, and Clark [65] have measured molecular orientation, crystallinity, and relative amounts of α and γ crystalline phases in nylon-6 as a function of spin draw ratio. Total crystallinity, relative amount of γ-phase, and orientation all increased with increasing spin draw ratios.

Reviews of structure development during melt spinning of polyolefins and polyamides have been presented by Spruiell and White [178] and White and Spruiell [202], respectively.

High-Speed Spinning During the seventies, high-speed spinning of fibers became an important commercial process. An advantage of high-speed spinning over conventional spinning is that a partially oriented yarn can be produced which reduces the cost of the draw-twisting process. Other advantages include savings from a higher spinneret throughput, improved texturing properties, and improved dyeing absorption and evenness [153].

The commercial success of high-speed spinning has spawned a great deal of research on the structure development at high speeds. Most of the work has been devoted to polyester [153,74,29,30,64,169,167,164,165,168,208,133,134], with some research being done on nylon [166,161,80] and polypropylene [162,163].

Some of the main features observed during high-speed spinning of PET are as follows. Crystallinity begins to develop at speeds of about 3500-4500 m/min (SDR $\simeq$ 3000) and increases with take-up velocity up to about 6500 m/min (SDR $\simeq$ 4500). Crystallinities of as much as 40-50% have been calcu-

lated for the as-spun fibers [74,64,165,169,167,164,208,133,134,79]. Both the density and birefringence show a sharp increase in the range of 3000 to 6500 m/min followed by a slight decrease at higher speeds. Crystalline orientation factors (f_c) greater than 0.90 have been reported for fibers spun at 6000-7000 m/min [169,133,134,79]. Calculations of the amorphous orientation factor (f_a) from f_c and birefringence or sonic modulus indicate little or no preferred orientation below 2500 m/min. The amorphous orientation increases sharply from a low value at 3000 m/min to a maximum of about 0.65 at 6500 m/min [169,133,134]. A radial distribution of orientation, which increases with increasing take-up velocity, was attributed to temperature and stress gradients which existed across the filament diameter during spinning [165,208].

Supercooling and spinline stress at the "freeze point" have been identified as the major factors in determining the state of orientation and crystallinity. A critical stress for crystallization occurs at about 0.80 g/denier in PET [64]. Shimizu [167] observed a decrease in the spinning speed at which crystallinity developed, with an increase in molecular weight. This can be explained by an increase in spinline stress with increasing molecular weight. The increase in radial variation of orientation was shown to increase with spinning speed due to an increased temperature gradient across the filament [165]. Yasuda et al. [208] performed calculations which indicate the orientation distribution can be decreased by increasing the cooling air temperature during the spinning process. Shimizu et al. [164] report that the main effect of mass flow rate can be explained as a cooling effect due to a decrease in the fiber

diameter rather than an effect on the spin draw ratio.

On-line studies show that the development of orientation and crystallinity occur within a very narrow region of the spinline (a few centimeters). This is associated with a "necking" phenomenon in PET. The temperature in the crystallization zone T_c increases with increasing take-up velocity (increasing spinline stress) [64,133,134]. The crystallization temperature affects the degree of crystallinity, crystallite size, and the thermal-mechanical properties.

The mechanical properties of fibers produced by high-speed spinning vary significantly from those of conventionally drawn filaments [169,133,134]. The super high-speed spun filaments (>4000 m/min) have a relatively low Young's modulus despite a high degree of crystallinity. In fact, the mechanical properties were found to depend predominately on the amorphous orientation of the filaments rather than on the degree of crystallinity. The relatively low amorphous orientation of the as-spun fibers as compared to drawn filaments would then explain the lower Young's modulus and higher elongation to break [134]. An increase in the radial variation of orientation caused the mechanical properties to deteriorate, i.e., lower elongation to break and lower true stress at break [134].

Shimizu et al. [168] have studied the polymorphic structure of the polyester/ether poly(ethylene–1,2-diphenoxyethane–$p,p\prime$-dicarboxylate) produced by high speed spinning. Filaments spun at low speeds (2000 m/min) are amorphous. When they are annealed the α form is produced. At intermediate speeds (4000 m/min), x-ray patterns of the as-spun filaments show the exis-

tence of a small amount of imperfect β form. Upon annealing, a mixture of α and β is produced. At high speeds (6000 m/min), only a strong β phase is produced. The β form produced is stable and does not transform to α upon annealing. These results show that both α and β forms are thermally stable, with β being produced by crystallization under conditions of high stress [168].

The effect of take-up velocity on the polymorphic sturcture of nylon 6 has been studied by Shimizu [166,161] and Heuval and Huisman [80]. WAXD patterns indicate the existence of α, γ, and pseudohexagonal (h) crystalline forms. At speeds below 2000-3000 m/min, little or no crystallization occurs during spinning. The structure present in conditioned fibers can be attributed mostly to the slow, moisture- induced crystallization of the α form. The amount of γ phase in conditioned yarns increases with winding speed. At speeds greater than 3000-4000 m/min, γ phase is generated during spinning. At the highest speeds, crystallization approaches completion during spinning. The structure produced at these speeds is believed to consist of "a mixuture of large, well-oriented γ crystals and small α crystals of lower orientation." The γ phase is thought to be produced by an orientation-induced process. This view is supported by the substantially higher crystalline orientation factors obtained for the γ crystals than for α crystals [80]. Neither the α or γ phase is completely stable. A γ to α transition can be produced by drawing at high ratios, while α to γ transition occurs during annealing at high temperatures [166,80].

Shimizu [163] has reported the results of high-speed spinning of poly-

propylene in the range of 500 to 7000 m/min. The birefringence and degree of crystallinity increased rapidly with take-up velocity up to 2000 m/min. At higher speeds, there was only a gradual increase in these properties. Young's modulus and thermal shrinkage, however, increased greatly at the higher speeds. WAXD patterns showed high degrees of orientation and crystallinity at speeds greater than 1000 nm/min. Two-point SAXS patterns indicated the presence of a stratified lamellar structure at each spinning speed. The broad distribution of long periods observed in the patterns were believed to be a result of the non-isothermal crystallization process, i.e., a distribution of crystallization temperatures. The distribution of long periods narrowed upon annealing. The long period calculated at the peak intensity was relatively unaffected by the take-up velocity. This was explained as being due to a relatively constant average crystallization temperature.

Both an orientation-crystallization mechanism and a stretching mechanism which occurs during solidification were used to explain the physical properties. Under conditions of low stress (<2000 m/min), relatively unoriented crystals are formed. The amorphous material between crystals would be in a relaxed (unoriented) state. As the stretching stress increases, the crystallites become highly ordered. Then, at some critical stretching stress (corresponding to the leveling off of the birefringence), the noncrystalline chains are stretched and frozen between crystals; hence, the abrupt increase in modulus. Thermal shrinkage occurs during annealing when the highly oriented amorphous chains relax [162].

2.6.2 Drawing

Filaments spun at low to moderate speeds generally exhibit a low degree of orientation and chain extension. Even in filaments having a high degree of crystalline orientation, there may be considerable chain folding in the lamellae. Thus, undrawn filaments exhibit low moduli and tensile strength, high elongations to break, and large amounts of plastic (irreversible) deformation. In order to achieve high levels of orientation and chain extension, the filaments must be drawn. This involves the irreversible extension of the filament in the solid state at elongations that may reach a sizable portion the filament's breaking elongation. The drawing process may be carried out at room temperature (cold drawing) or at elevated temperature by heating the filament in a hot air chamber or by contact with a hot plate, drum, or pin (hot drawing).The optimum temperature depends on the polymer, but is usually just above the glass transition temperature to increase the mobility of the amorphous chains and lower the drawing stress. The temperature should not be to far above T_g though, or the chains may relax as fast as they are being oriented and there will be no net gain in orientation [177]. The optimum drawing conditions (draw ratio, draw rate, temperature and drawing medium) depend on the material, the level of orientation and morphology developed during melt spinning, and the desired mechanical and physical properties.

The following survey on drawing and annealing is not intended to be an exhaustive review of the literature but rather an emphasis of some of the important concepts involved in this stage of fiber processing. Much of the

following discussion is based on material presented in reviews by Ziabicki [212] and Samuels [146].

Effect on Orientation

Drawing involves major structural reorganization in the filament: i.e., changes in the orientation of the amorphous and crystalline regions, changes in the degree of crystallinity, and deformation of the crystalline superstructures.

In semi-crystalline polymers, the crystalline and amorphous regions generally respond differently to an externally applied deformation and develop different levels of orientation during drawing. Orientation of the amorphous chains generally increases as draw ratio increases, but not necessarily in direct proportion. Orientation of the crystalline phase is complicated by the existence of molecular superstructures such as spherulites. Low deformations can result in negative orientation such as shown by Lilaonitkul and Cooper [112] (see discussion Section 2.4.2). However, high crystalline orientation usually prevails at high stretch ratios.

Effect on Crystallinity and Morphology

The degree of crystallinity can increase, decrease, or remain the same during drawing.

Crystallization during the drawing process may occur as a result of two different processes: 1) kinematic factors and 2) orientation or stress induced crystallization. Kinematic factors involve increased molecular mobility due

to heat exchange with the environment (hot drawing) or to self-heating from the dissipation of deformation energy. Crystallization may also result from molecular orientation. Orientation can greatly speed up the crystallization rate [177] and lower the crystallization temperature. Rubbers are particularly prone to orientation induced crystallization [191,192]. Polymers which have shown an increase in crystallinity upon drawing include polyethylene [93,69,68,201], polypropylene [127,193], polyesters [144,8,225,122,63], nylon [13,8,91,139,85], polyvinyl chloride [89] and polyvinyl alcohol [99].

Crystal lattice transformations may also occur during drawing. This phenomenon has been observed in poly(tetramethylene terephthalate) [115,90] [31,194,189], nylon-6 [139,85,138,214,72], and polypropylene [43,157,88] to name a few.

Deformation of crystalline polymers may result in partial destruction or reorganization of crystalline material into a more defective structure, reducing the degree of crystallinity. There is often a reduction in crystallite size and perfection as a result of drawing [109,71]. Studies of polyethylene [68,69] show that it is the lateral dimension of the crystallite that is reduced the most. The total crystallite size can be reduced to less than one-tenth of its original size by drawing [69]. The amount of destruction usually increases as the drawing temperature is reduced. The lower the molecular mobility and the more perfect the original structure, the greater the destruction.

In the case of amorphous, non-crystallizable polymers there can be no change in phase. In semi-crystalline polymers, there may be no change in

crystallinity when there is a high level of molecular mobility in the amorphous phase. The crystallites can rotate or reorient without suffering damage as in the case of highly plasticized cellulose fibers [105]. Amorphous but crystallizable fibers such as poly(ethylene terephthalate) (PET) can remain amorphous during drawing if deformation takes place at low enough temperatures and at slow enough deformation rates to prevent self-heating [221].

The long period is usually reduced by drawing. In studies of polyethylene [136] and polypropylene [14], the long period was found to vary discontinuously with draw ratio. During cold drawing, the long period increased in proportion to the macroscopic deformation at low elongations, but at some critical draw ratio the long period dropped abruptly and remained almost constant to much higher elongations. At higher drawing temperatures, the long period increased with draw ratio. The main factor controlling the long period, however, seems to be the highest temperature experienced by the sample rather than the deformation itself.

Effect on Mechanical Properties

The change in orientation of the amorphous chains and crystallites and the changes in crystallinity and morphology brought about by drawing greatly influence the mechanical properties of the filaments. Drawing can also lead to the formation of voids in the filaments to the detriment of the ultimate properties. Modulus, yield strength, and tensile strength tend to increase with draw ratio, while the elongation to break and the total work of deformation

tend to decrease with increasing draw ratio. The elastically recoverable part of the deformation work, however, may show a maximum at some intermediate draw ratio [22].

2.6.3 Annealing

Drawn fibers may have low crystallinity and imperfect structures and may be dimensionally unstable. Drawn fibers are usually annealed at high temperature to perfect the structure and increase dimensional stability, i.e., reduce residual shrinkage or lower the ultimate elongation. Annealing brings about changes in structure that are usually associated with improvements in mechanical properties. The important consequences of annealing on the structure and properties of drawn filaments will be briefly discussed in this section.

Effect on Orientation and Shrinkage

Free annealing is associated with viscoelastic recovery manifested in macroscopic shrinkage, while annealing at fixed length is associated with stress relaxation. A schematic of the elongational changes that take place during drawing and annealing has been presented by Ziabicki and reproduced here in Figure 2.20.

The shrinkage in drawn filaments during free annealing is generally associated with orientation in the amorphous phase and increases as the level of orientation increases and as the annealing temperature is raised [212,146]. The

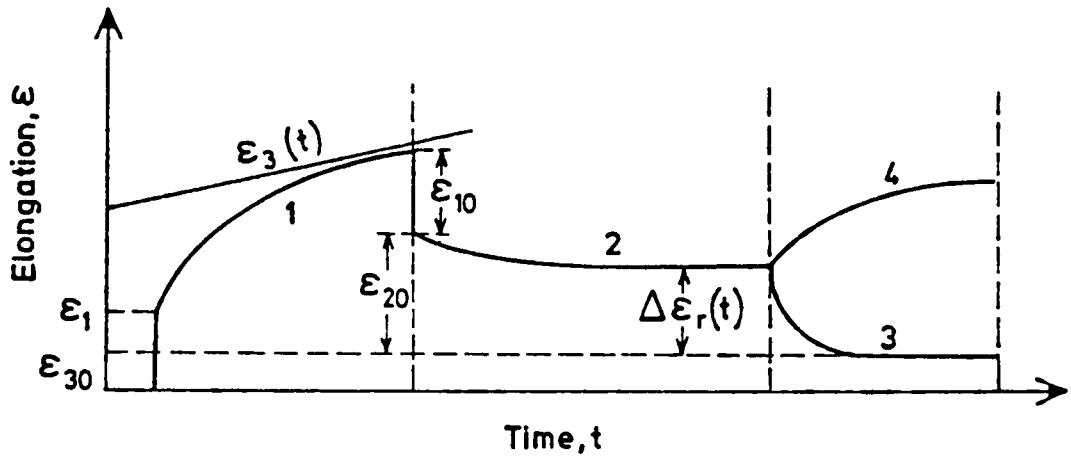


Figure 2.20: Schematic of elongational changes that take place during fiber processing. 1: Drawing; 2: recovery at low temperatures; 3: free annealing; 4: annealing under tension. $\varepsilon_{10}, \varepsilon_{20}$, and ε_{30} denote the instantaneous elastic, viscoelastic, and viscous contributions, respectively, to the deformation during drawing. $\Delta\varepsilon_r$ is the residual shrinkage.

Source: Andrzej Ziabicki, *Fundamentals of Fiber Formation,* (New York: John Wiley & Sons, 1976) pg. 446.

shrinkage of drawn PET filaments was found to obey the following relationship:

$$log\lambda' = log\lambda'_0 + K[(1-\beta)f_{am}] \tag{2.16}$$

where λ' is the residual extension after a two stage process of drawing and shrinking, f_{am} is the amorphous orientation function and $(1-\beta)$ is the amorphous fraction. The λ'_0 and K are the intercept and slope in the linear relationship. Thus, the residual extension depends upon the amorphous orientation and the level of crystallinity present in the filament before annealing.

The thermal shrinkage in a drawn filament may exhibit a maximum when plotted as a function of draw ratio. This has been observed for polyester [116,150], nylon-6 [151], and acrylic fibers [185,184]. Self-heating and the associated reduction of drawing stress at the higher draw ratio could lead to this type of behavior. Alternately, an increase in crystallinity or a phase transition at the higher draw ratios could be responsible.

Thermal shrinkage of PET fibers spun at high speed goes through a maximum of about 60% at 2000-3000 m/min, then decreases to less than 5% at speeds higher than 5000 m/min [74,167,164,169,133,134]. The amount of thermal shrinkage during annealing is a complex function of the state of amorphous orientation, relaxation time, and the crystallization rate. Nonetheless, several observations can be drawn:

1. Shrinkage can be used as a measure of the amorphous orientation in fibers with little or no crystallinity (below 2000 m/min).

2. The amount of shrinkage is limited by the orientation itself above 2000

m/min due to the increased crystallization kinetics and the development of crystallinity during annealing.

3. Above 5000 m/min, the high crystallinity of the as-spun fiber prevents shrinkage [133,134].

A reduction in crystallite orientation may result from free annealing [143,62,5,43,125]. Annealing at fixed length or under tension reduces the freedom of crystallites and amorphous chains to relax and therefore little reduction in the crystallite orientation can occur [118,140,108,102]. An increase in f_c may even be observed as the result of oriented crystalline growth [62,43]. Annealing at fixed length generally stabilizes the original crystallite orientation unless temperatures close to the melting point are approached [118].

Effect on Crystallinity and Morphology

The degree of crystallinity (in crystallizable polymers) generally increases with annealing temperature if the filament is annealed in an unrestrained state [116,129,151,119]. Annealing at constant length or under tension suppresses the crystallization rate and may even prevent additional crystallization altogether [43,15,224].

The crystallization rate and equilibrium degree of crystallinity depend upon the initial structure. In drawn PET filaments, higher initial crystallinity was shown to lead to slower rates of crystallization during annealing, but all samples reached the same level of crystallinity at high temperatures [116].

Differences in orientation can lead to different crystalline superstructures and lattice structures [88,214,115,90,31,194,189].

Free annealing generally leads to an increase in crystallite dimensions, especially in the direction perpendicular to the chain axes [143,62,5,224], although there are isolated cases in which the crystallite dimensions are reduced [125].

Annealing under tension can cause the crystallite dimensions parallel to the fiber axis to increase considerably. The dimensions perpendicular to the fiber axis may increase only slightly or even decrease [62,224].

The high temperatures that produce an increase in crystallite size also produce an increase in the perfection of the crystal lattice structure. (The two effects are often indistinguishable by WAXD line broadening techniques.) The increase in crystallite size and perfection generally cause an increase in the melting temperature of the polymer.

The long period generally increases in semi-crystalline polymers as the annealing temperature is raised. Higher long periods are observed in free annealed filaments than in those annealed at constant length or under tension. These effects are associated with chain folding and seem to be the result of changes in the dimension of the crystallites that is parallel to the fiber axis.

The fact that the long period increases upon annealing even though the filament undergoes macroscopic shrinkage is puzzling. How can the average distance between crystallite centers increase as the fiber shrinks? Samuels [146] has examined this phenomenon in drawn PET fibers. He suggests that

there is a direct relationship between the amount of shrinkage and the increase in long period. This leads him to believe that the crystallization process is controlled by the relaxation of amorphous chains. He proposes a two-step mechanism in which the amorphous chains first relax, causing a reduction in filament length, followed by crystallization of the relaxed chains. The thickness of the crystallites, and thus the long period, is controlled by the annealing temperature.

Effect on Mechanical and Physical Properties

The mechanical properties are sensitive to the temperature and tension experienced by the filament during annealing. These parameters control the crystallinity and state of orientation developed in the heat set filament.

The modulus may increase or decrease as a result of annealing. Free annealing generally produces a decrease in the modulus as a result of disorientation of amorphous chains and crystallites [143,129,5,43,137]. Annealing under tension may cause only a slight loss in modulus or may even produce an increase [129]. Tensile strength usually decreases when the filament is free annealed, but remains unchanged or even increases if the filament is annealed under tension [143,62,43]. The elongation to break generally increases as a result of annealing, the effect being greater for free annealed filaments than for those annealed under restraint. The residual shrinkage is reduced by annealing as a result of crystallization and shrinkage during annealing. Free annealed filaments, because of their higher shrinkage during annealing, show less residual

shrinkage than fixed annealed filaments.

The total work of deformation usually increases as the annealing temperature is raised. The amount of work is higher for free annealed filaments than for those annealed at fixed length or under tension [62].

CHAPTER 3

CHARACTERIZATION TECHNIQUES

The coplyester-ethers studied in this research were characterized by a number of techniques. In some of the techniques, it was necessary to introduce approximations and modifications in the analysis in order to proceed with the research. A description of the experimental techniques and any modifications or approximations are given in the following sections.

3.1 Wide-Angle X-ray Diffraction (WAXD)

Crystallite orientation and line broadening experiments were performed on a Rigaku X-ray Diffractometer (D/MAX-IA) equipped with a Digital PDP 11/34 computer. The X-ray tube has a copper target. The wavelength of the Cu K_α radiation is 1.5418 Å. Monochromatization of the diffracted radiation was achieved using a graphite crystal mounted on the counter arm. The fiber specimen attachment and stepping motor system were used to mount and orient the filament samples. Intensity measurement were made in symmetric transmission mode.

3.1.1 Orientation Functions

Since the PTMT crystals are triclinic, a minimum of three (hko) planes are necessary for a rigorous determination of the chain axis orientation. Only two suitable (hko) planes are available, however: namely the (100) and the (010). Following the method of Yoshihara et al. [210], a new unit cell is defined such that the angle between the new lattice vectors a' and b' is 90°. This orthorhombic approximation allows an equation to be derived relating the chain axis orientation, $f_{c,Z}$, to $< \cos^2 \phi_{100,Z} >$ and $< \cos^2 \phi_{010,Z} >$, where Z is the reference direction and ϕ is the angle between the normal to the diffraction plane and reference direction. Hall and Pass [73] found that the angle between the normal to the benzene ring lies about 4.4° counter-clockwise from the (010) plane looking down the negative c-direction. Since the obtuse angle between the (100) and (010) planes is 118.7°, the angle between the plane of the benzene ring and the (100) plane is 24.3°:

$$118.7° - 90.0° - 4.4° = 24.3°$$

The new lattice axis b' is picked such that it lies in the plane of the benzene ring. Thus the angle between b and b' is 24.3°. Since a' is selected such that it lies 90° from b' and is perpendicular to the $b' - c$ plane, the angle between a' and the (010) plane is 4.4°. The relationship between these axes are shown in Figure 3.1.

Yoshihara's equation, originally derived for poly(ethylene terephtha-

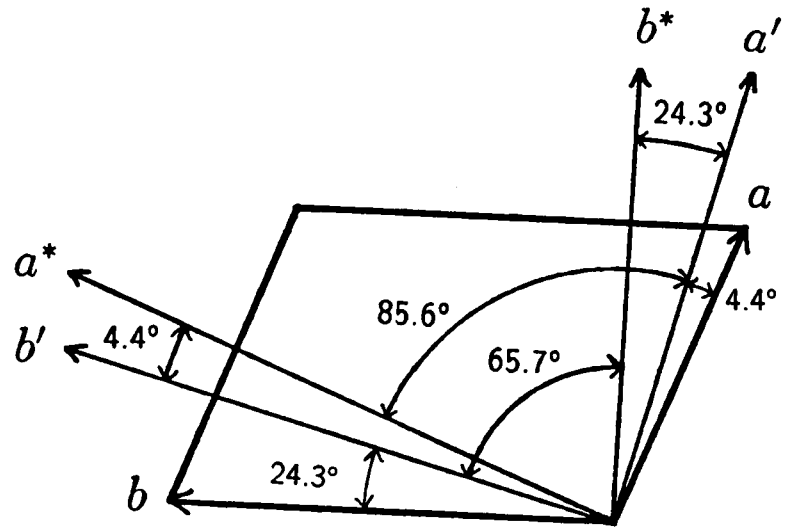


Figure 3.1: Relationship between new and old unit cell axes. The b' axis is selected such that it lies in the plane of the benzene ring. The a' axis is selected such that it lies 90°from the b' axis and perpendicular to the b'–c plane.

late), has the form

$$f_{c,Z} = 2\,\frac{f_{100,Z}\,\cos(2\eta_{010}) - f_{010,Z}\,\cos(2\eta_{100})}{\cos(2\eta_{100}) - \cos(2\eta_{010})} \tag{3.1}$$

where

$$f_{i,Z} = \frac{3 < \cos^2\phi_{i,Z} > -1}{2} \tag{3.2}$$

and η_j are the angles between the reciprocal lattice vectors (a^* and b^*) of the paratropic planes and the b' axis. This same equation can be applied to PTMT once the proper values of η_j are determined. The angles in PTMT between the original reciprocal lattice vectors and the a' and b' axes are summarized below:

	a'	b'
a^*	85.6°	4.4°
b^*	24.3°	65.7°

Substituting in the values of η_j yields

$$f_{c,Z} = 2\,\frac{f_{100,Z}\,\cos[2(4.4°)] - f_{010,Z}\,\cos[2(65.7°)]}{\cos[2(65.7°)] - \cos[2(4.4°)]}$$

which reduces to

$$f_{c,Z} = \frac{1.976\,f_{100,Z} + 1.322\,f_{010,Z}}{-1.65} \tag{3.3}$$

It should be noted that Yoshihara's formula yields values identical to Farrow's method [52] when a' and b' are selected such that the angle between a' and b^* equals that between b' and a^*. This is almost the case for PET when b' is selected such that it lies in the plane of the benzene ring. For PTMT, however

this does not occur:

$$< a' \text{ and } b^* = 4.4°$$

$$< b' \text{ and } a^* = 24.3°$$

3.1.2 Line Broadening

The dimensions of the crystallites were estimated from the broadening of the (100), (010), and ($\bar{1}$04) diffraction peaks using the Scherrer equation [148]:

$$D = \frac{\kappa\lambda}{\beta_0 \cos\theta} \tag{3.4}$$

where D is the mean crystallite dimension in the direction perpendicular to the (hkl) planes, β_0 is the breadth at half maximum intensity of the pure reflection profile in radians, θ is the Bragg angle, and κ is a constant close to unity [4, pg. 423-424]. Since both crystallite size and lattice distortions cause peak broadening, the value of D obtained using the above equation must be regarded as a minimum value.

In practice, the observed breadth of the diffraction peak must be corrected for instrumental broadening and geometric broadening due to the finite sample thickness. Assuming a Gaussian distribution for the component profiles of the observed intensity distribution allows a reasonable estimate to be made of the width of the pure reflection profile, β_0 [4, pg. 217]:

$$\beta_0^2 = B^2 - b^2 - g^2 \tag{3.5}$$

where B is the observed profile, b is the instrumental broadening and g is the geometric broadening.

The geometric broadening can be calculated from the following equation [4, pg. 218]:

$$g = 57.3° \frac{t \sin 2\theta}{d \cos(\theta - \alpha)} \tag{3.6}$$

where t is the sample thickness, d is the specimen to receiving aperture distance, α is the tilt of the sample from the symmetric transmission position, and 2θ is the Bragg angle. For example, the geometrical broadening at $2\theta = 23.3°$ for a 1.75 mm thick sample with $d = 150$ mm and $\alpha = 0$ would be about 0.27°.

The instrumental broadening in symmetric reflection mode was determined using a silicon standard having large, well developed crystallites. It is assumed that all the broadening in this case is from the instrument and not from small crystallite sizes. In order to estimate the instrumental broadening in transmission mode, the crystallite size of two highly crystalline polymer samples were determined in reflection mode. The diffraction profiles of these same samples were then determined in transmission. Since the width of the pure diffraction profile was previously determined, the instrumental broadening in transmission could be estimated. Sample thicknesses were kept approximately the same ($1.75 \pm .05$ mm) to reduce variations in the observed diffraction profile due to geometric broadening. The instrumental and geometric broadening in transmission mode for the three reflections used in this experiment are shown below:

Reflection	2θ	Instrumental and Geometric Broadening
(010)	17.3°	0.01566 rad (0.90°)
(100)	23.3°	0.01653 rad (0.95°)
($\bar{1}04$)	31.5°	0.01710 rad (0.98°)

3.1.3 Crystallite Volume

The volume of the crystallites were estimated from the dimensions determined from the line broadening experiments. The following calculations are based on a model of the crystallites which has surfaces parallel to the (100) and (010) planes of the α–form unit cell.

The angle between the (100) and (010) planes is 61.3°. The area created by a projection of the base of the model crystallite onto a plane perpendicular to the c-axis is given by $XY/(\cos 28.7°)$ where X is the dimension perpendicular to the (010) planes and Y is the dimension perpendicular to the (100) planes (see Figure 3.2). Since the normal to the ($\bar{1}04$) plane lies at about 11.5° to the c-axis, the height of the crystallites is C $(\cos 11.5°)$ where C is the dimension determined from the ($\bar{1}04$) diffraction peak. Thus the crystallite volume can be estimated from the following equation:

$$Vol = XYC\,(\cos\ 11.5°)/(\cos\ 28.7°) = 1.12\,XYC \tag{3.7}$$

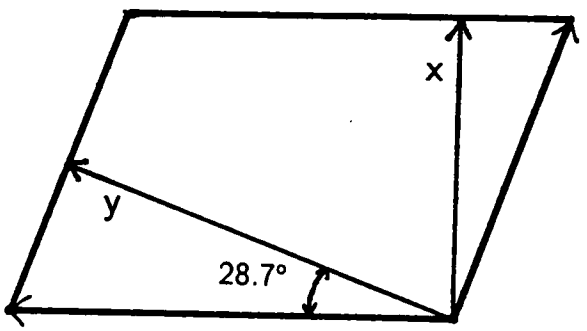


Figure 3.2: Projection of the model crystallite onto the basal plane. "X" is the size in the [010] direction and "Y" is the size in the [100] direction.

3.2 Small Angle X-ray Scattering

3.2.1 Small Angle X-ray Scattering (SAXS)

The SAXS data were obtained using the National Center for Small Angle Scattering Research (NCSASR) 10-m X-ray facilities at the Oak Ridge National Laboratory (ORNL). The two-dimensional position sensitive detector used in this system is particularly useful for acquiring quantitative intensity data on anisotropic samples. For investigations of sample morphology and determination of degree of phase separation, a sample-to-detector distance of 2.126 meters was used. This provides an angular range of dectection from 2.8 mrad to 49 mrad with Cu K_α radiation, corresponding to structures in the range of approximately 5 to 300 Å. In a separate experiment, the morphology of samples in the stretched state was investigated using a sample-to-detector distance of 5.126 meters.

At 40KV and 50ma, exposure times of 30 minutes to two hours were required to produce adequate count statistics. Raw data were corrected for instrumental scattering (due mostly to diffraction from the collimation slits), "dark current" in the detector due to cosmic radiation and electronic noise, detector dead time, and detector sensitivity. NCSASR software was used for data manipulation and graphics.

3.2.2 Long Period

If there is discrete scattering, the long period L can be calculated from the maximum in the intensity distribution $I(s)$ using Bragg's law:

$$L = 1/s \tag{3.8}$$

where $s = 2(\sin\theta)/\lambda$. In SAXS from isotropic or partially oriented samples, the Lorentz correction should be applied to the observed intensity distribution [123]:

$$I(s) = s^2 I_{obs}(s) \tag{3.9}$$

However, this correction is based on the assumption that the widths of the crystallites are substantially larger than the long period L [123]. This is not the case for the copolyester-ether filaments in this project, however, as shown by the WAXD experiments. Therefore, the unaltered intensity distribution will be used in calculating the long period.

3.2.3 Determination of the Degree of Phase Separation

For an isotropic system with pinhole collimation, the invariant has the form $Q = 4\pi \int s^2 I(s)\, ds$ [67]. For an anisotropic system in which the scattered intensity is cylindrically symmetric about s_1 (the fiber axis in this case), the invariant takes the form [123]:

$$Q = 4\pi \int_0^\infty \int_0^\infty I(s_1, s_2)\, s_2\, ds_1\, ds_2 \tag{3.10}$$

The mean square electron density fluctuation defined as $\langle \eta^2 \rangle \equiv \overline{(\rho - \bar{\rho})^2}$ may then be determined from the invariant

$$\overline{(\rho - \bar{\rho})^2} = \frac{4\pi}{\nu\tau} \int_0^\infty s^2 I_a(s)\, ds \qquad \text{(isotropic case)} \qquad (3.11)$$

or

$$\overline{(\rho - \bar{\rho})^2} = \frac{4\pi}{\nu\tau} \int_0^\infty \int_0^\infty I(s_1, s_2) s_2\, ds_1\, ds_2 \qquad \text{(anisotropic case)} \qquad (3.12)$$

where

$d =$ sample thickness in cm

$\rho =$ electron density in $e^-/\mathring{A}^3$

$\bar{\rho} =$ average electron density

$\nu = \lambda^2\, i_e$

$i_e =$ Thompson scattering constant of a free electron

$(7.92 \times 10^{-26} \text{cm}^2)$

$N =$ Avogodro's number $(6.023 \times 10^{23}/\text{mole})$

$I_a =$ scattered intensity in absolute units (I/P_0)

$P_0 =$ intensity of the primary beam

$s = 2(\sin\theta)/\lambda$

$s_1 =$ scattering vector in direction 1 (fiber axis)

$s_2 =$ scattering vector in direction 2 (perpendicular to the fiber axis)

$\tau = d\,\bar{\rho}\,N$ (electrons/cm^2)

This mean square electron density fluctuation can be used to quantitatively characterize the degree of phase separation in a two phase system. For an ideal two phase system (sharp domain boundaries and uniform electron den-

sity within the domain) with known electron densities, ρ_1 and ρ_2, the volume fraction ϕ_1 and ϕ_2 of each phase can be determined from

$$\langle \eta^2 \rangle \equiv \overline{(\rho - \bar{\rho})^2} = \phi_1 \, \phi_2 \, (\rho_1 - \rho_2)^2 \tag{3.13}$$

Applications of this principle to real (nonideal) systems having diffuse phase boundaries and mixing within the phases have been discussed by Bonart and Müller [25] and Koberstein and Stein [103]. In the copolyester-ether system, the parameter η is not a unique determination of the degree of phase separation since η depends on the total hard segment content as well as the degree of phase separation. Also, since the amorphous phase is a mixture of polyether segments and amorphous polyester sequences, the electron density of this phase changes as the DPS changes. This increases the value of η due to an increase in both the $\phi(1-\phi)$ and $(\rho_1 - \rho_2)$ terms.

In order to get around some of these difficulties Bonart and Müller [25] defined an index ε which is the ratio of the experimentally observed electron density fluctuation $\langle \eta^2 \rangle$ to the theoretical value calculated for a given composition assuming total and ideal phase separation $\langle \eta_0^2 \rangle$:

$$\varepsilon = \langle \eta^2 \rangle / \langle \eta_0^2 \rangle \tag{3.14}$$

The quantity ε is not a rigorous determination of the DPS but provides a useful means for comparing the degree of phase separation among samples of the same or different compositions. An index of crystallinity can be roughly estimated by multiplying the degree of phase separation by the volume fraction of hard segments in the copolymer.

3.3 Thermal Analysis

The crystallization kinetics and melting behavior of the copolymers resins were studied using a Perkin-Elmer DSC-2 differential scanning calorimeter (DSC). Subsequent thermal analysis on resins and spun filaments were carried out using a Perkin-Elmer DSC-7. Liquid nitrogen was used to cool the sample chamber during subambient studies. The use of DSC scans to determine crystallinity or morphological features must be done with caution since PTMT and the copolymers crystallize during the scan. The scans may not be representative of the materials at room temperature. A discussion of these problems and an interpretation of the multiple melting behavior of the copolyester-ethers have been presented by Stevenson and Cooper [183] (see Section 2.2.2).

3.4 Birefringence

Fiber diameters d and retardation Γ measurements were made using an Olympus microscope and a 30λ Berek compensator. The diameters were calibrated by means of a Olympus graduated slide marked off in 0.02 mm increments. The birefringence Δ_{tot} is calculated as follows:

$$\Delta_{tot} = \Gamma/d \tag{3.15}$$

The birefringence of an anisotropic two phase system is given by

$$\Delta_{tot} = \beta\Delta_c^\circ f_c + (1-\beta)\Delta_a^\circ f_a + \Delta_{form} \tag{3.16}$$

where

$\Delta_c^\circ =$ intrinsic birefringence of the crystalline phase

$\Delta_a^\circ =$ intrinsic birefringence of the amorphous phase

$\Delta_{form} =$ form birefringence

$f_c =$ crystalline orientation factor

$f_a =$ amorphous orientation factor

$\beta =$ crystalline fraction

$1 - \beta =$ amorphous fraction

If the intrinsic birefringence of each phase and the degree of crystallinity is known, then the birefringence of the system is expressed in terms of the orientation of each phase and the form birefringence. If f_c can be obtained by some independent means, such as from x-ray techniques, and if the contribution from the form birefringence is small, the amorphous orientation function can be determined. However, there are several difficulties associated with the copolyester-ether system. Because of the domain structure and the large differences in refractive indices of the two phases, the contribution of the form birefringence can be quite significant [155,55]. Determination of the form birefringence is experimentally difficult since the size and number of domains is hard to establish. Also, the volume fraction degree of crystallinity β is not known with any great accuracy. The intrinsic birefringence of the crystalline phase can, in theory, be calculated from bond polarizabilities. The intrinsic birefringence of the amorphous phase, however, depends in part on the com-

position of the amorphous phase. Once again, accurate values are difficult to obtain. The composition of the amorphous phase also changes with sample composition and with each processing step.

These experimental problems make quantitative evaluation of orientation functions very difficult. However, if the degree of crystallinity is the same in a series of samples of the same composition, an increase in birefringence with some processing parameter indicates an increase in overall orientation. Conversely, if f_a and f_c are approximately the same in a series of samples, an increase in birefringence indicates an increase in crystallinity.

Birefringence has been used sparingly in this research, and then only as an indicator of trends rather than as a quantitative technique.

3.5 Density

In semi-crystalline homopolymers, density can be used as a measure of the degree of crystallinity x_c:

$$x_c = \frac{\rho_c}{\rho}\left(\frac{\rho - \rho_a}{\rho_c - \rho_a}\right) \tag{3.17}$$

where ρ is the macroscopic density of the sample, and ρ_c and ρ_a are the densities of the 100% crystalline and 100% amorphous phases, respectively.

The density of the copolyester-ether and filaments were measured using a conventional density gradient column prepared from sodium bromide and water. The column was calibrated using glass beads of accurately known densities ($\pm$ 0.0001 g/cm^3). A range of 1.1300 to 1.2750 g/cm^3 could be measured

with a precision of ± 0.0001 g/cm^3. A similar column was prepared for PTMT filaments.

The density of 100% amorphous PTMO is 0.980 g/cm^3 [195,107]. The density of amorphous PTMT is 1.282 g/cm^3 and the density of the α-form crystalline phase is 1.396 g/cm^3 [182].

Since WAXD and DSC techniques show no evidence of a crystalline PTMO phase, it is assumed that only the PTMT segments crystallize. In theory, the degree of crystallinity can be calculated using the additivity of specific volumes and by assuming ideal mixing in the amorphous phase:

$$\frac{1}{\rho_{tot}} = \frac{w_c\,\omega_1}{\rho_c} + \frac{(1-w_c)\,\omega_1}{\rho_{a1}} + \frac{(1-\omega_1)}{\rho_{a2}} \tag{3.18}$$

where the subscripts 1 and 2 refer to the PTMT and PTMO components, respectively, and c and a refer to the crystalline and amorphous phases, respectively. "$\omega 1$" is the weight fraction of the hard segments in the copolymer and "w_c" is the weight fraction of PTMT segments that are crystalline ($w_c\omega_1 = x_c$). The degree of crystallinity in the copolymer system can be calculated if the density of the amorphous phase is known.

In Figure 3.3, the upper and lower limits of density, corresponding to complete phase separation and total phase mixing, are plotted as a function of composition using Equation 3.18. For complete phase mixing, $w_c = 0$, and for complete crystallization of the hard segments, $w_c = 1$. The highest experimentally observed densities for several compositions are also shown on this plot. Several of the compositions have densities higher than the theoretical limit,

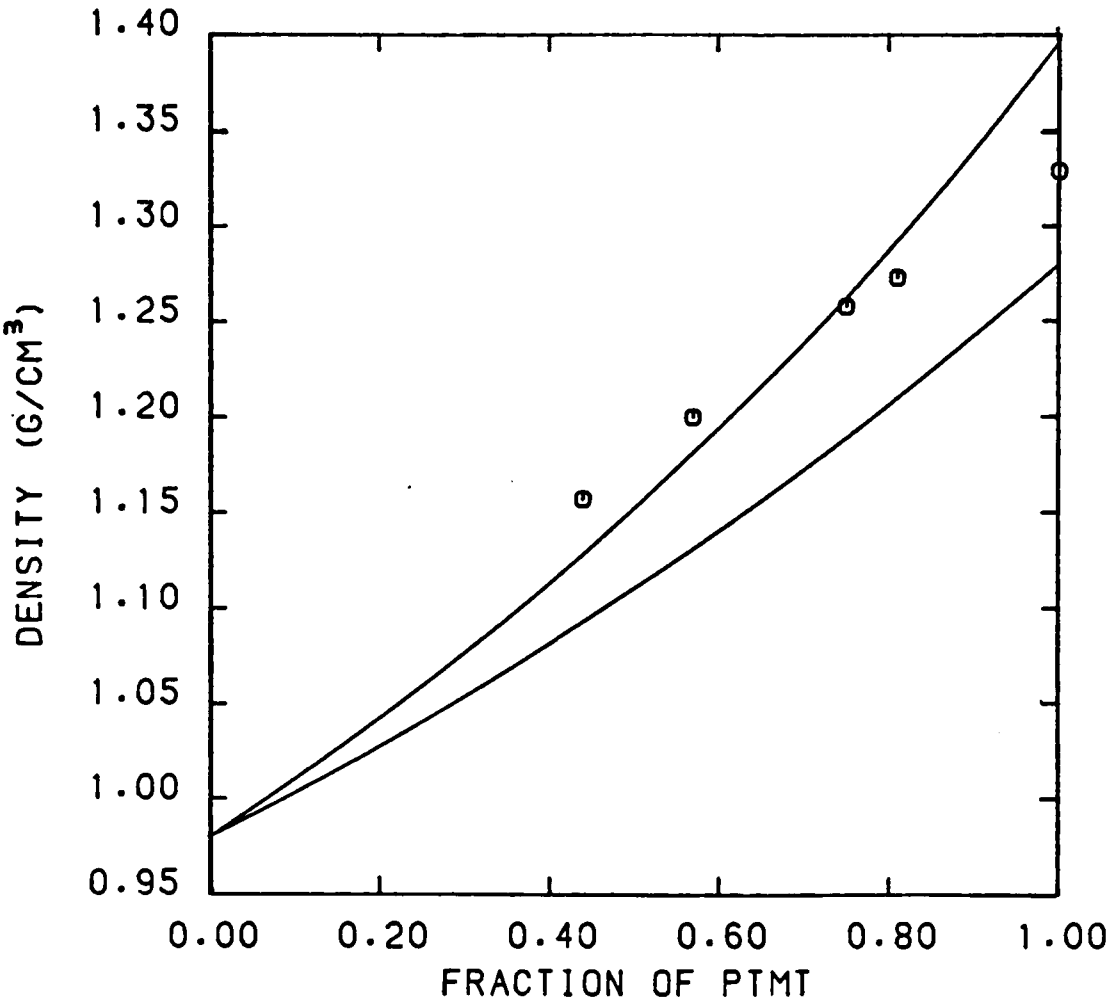


Figure 3.3: Predicted and experimentally observed values of density as a function of composition. The solid lines are the upper and lower limits of density as calculated from Equation 3.18. The data points correspond to the highest densities observed for these compositions in this research.

assuming no crystallization of PTMO segments. As mentioned earlier, there is no evidence in DSC scans or x-ray patterns for crystallization of PTMO segments. Also, these copolymers are based on a PTMO prepolymer of molecular weight 1000 g/mole. There are no reports of PTMO crystallization in the literature in these copolymers until a PTMO prepolymer having a molecular weight of 2000 g/mole is used. The amorphous PTMT and PTMO segments may pack more closely than in an ideal mixture, especially in the domain interfacial boundry layer. Thus, density provides only a qualitative measure of the degree of crystallinity.

3.6 Dynamic Mechanical Data

An Imass Autovibron™ dynamic viscoelastometer was used to determine the glass transition temperatures of selected filaments. This instrument is equipped with a Hewlett-Packard 6940B multiprogrammer for automatic temperature control and data aquisition. A nitrogen purge gas run through a liquid nitrogen bath was used to cool the sample chamber to subambient temperatures. Data were taken at approximately 1° intervals from -100° C to about 100 or 150° C depending on the composition. Data were obtained at three frequencies: 1.1, 11, and 110 Hz. The change in length ΔL, the storage modulus (E'), the loss modulus (E''), and the loss factor ($\tan\delta$) were calculated as a function of temperature. The maximum in the $\tan\delta$ curve is associated with the glass transition temperature.

3.7 Shrinkage in Boiling Water

As discussed in Section 2.6.3, the shrinkage of oriented filaments during free annealing is generally associated with orientation relaxation in the amorphous phase. The amount of shrinkage is a complex function of the state of amorphous orientation, relaxation time and the crystallization rate. Nevertheless, shrinkage provides valuable information about the filaments. A high level of shrinkage can be attributed to contraction of amorphous chains. No shrinkage may mean that either there is little amorphous orientation or that the sample has a high level of crystallinity which prevents shrinkage. Careful interpretation of the results is required to provide meaningful information in the latter case.

The amount of shrinkage (S) is defined as the length before annealing (l_0) minus the length after annealing (l), divided by the original length:

$$\%S = \frac{l_0 - l}{l_0} \times 100\% \tag{3.19}$$

Filaments approximately 300 mm long were placed in boiling water for two minutes (i.e., annealed at 100°C). The filaments were then removed and allowed to cool to room temperature. The lengths before and after annealing were used to calculate the amount of shrinkage.

3.8 Mechanical Properties

3.8.1 Tensile Properties

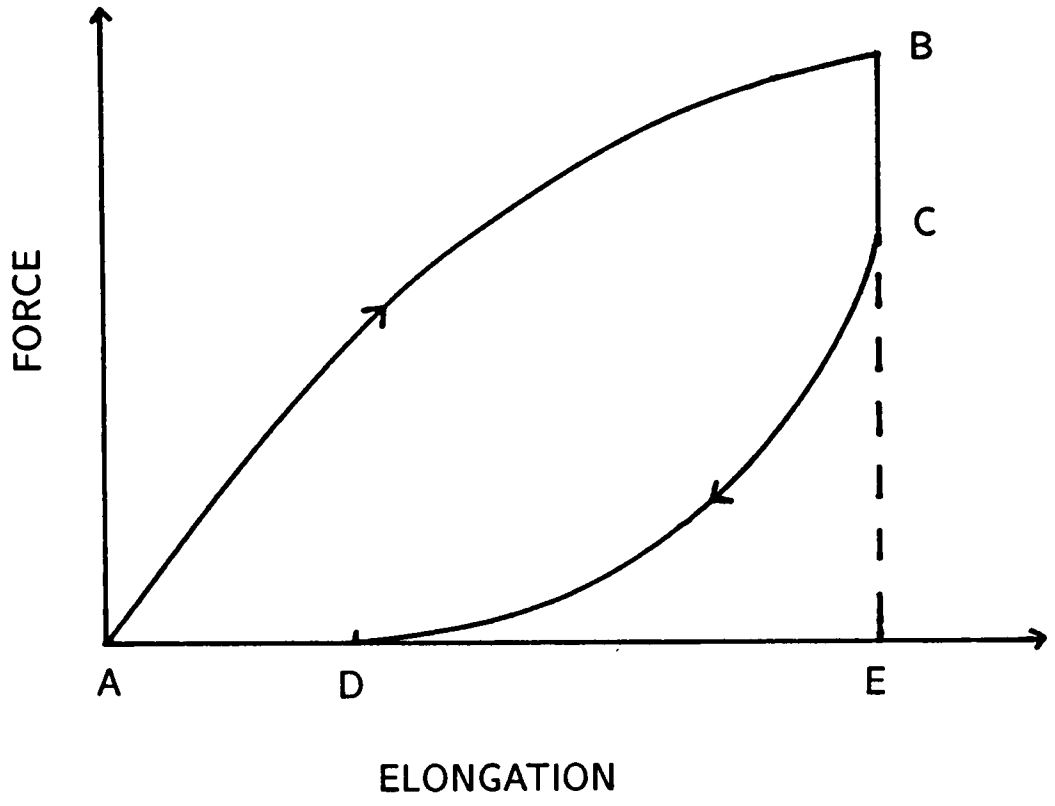
The mechanical properties of the filaments were measured using an Instron tensile tester (Table Model 1122). A short gage length was necessary because of the large elongations to break in some of the more elastic filaments and the limited amount of travel of the crosshead. A gage length of 30mm and a crosshead speed of 50mm/min were selected, giving an initial elongation rate of 167%/min. The elongation was determined from the distance the crosshead had traveled at any given time during the test.

Young's modulus, the elongation to break, and the breaking stress (tenacity) of the filaments were determined from the force–time curves obtained. The modulus was determined from the slope of the initial portion of the curve. The tenacity was defined as the maximum load sustained by the filaments divided by the original cross-sectional area.

3.8.2 Elastic Properties

In order to quantitatively investigate the elastic properties, the filaments were subjected to cyclic testing on the Instron tensile tester. The filaments were stretched to a given elongation and allowed to relax for 30 seconds before reversing the crosshead and allowing the filament to retract to zero stress. The samples were again allowed to relax for 30 seconds and the cycle was repeated at a higher elongation. The stress at strains higher than those previously reached

is fairly independent of the strain history as has been previously shown by Lilaonitkul et al. [114]. The composite stress–strain curve from cyclic testing is almost identical to a curve produced by a single stretch to the final strain (see Figure 2.13, pg. 57). For this reason, the total work recovery from a given elongation can be calculated from the composite extension curve and the retraction curve as shown in Figure 3.4. The values calculated in this manner are not to sensitive to step size and are comparable to the values that would be obtained if the sample had been stretched to those elongations in a single step.



WORK RECOVERY = CDE/ABE X 100%

STRAIN RECOVERY = DE/AE X 100%

Figure 3.4: Schematic diagram showing how strain recovery and work recovery are calculated from cyclic stress-strain curves.

CHAPTER 4

MATERIALS AND CRYSTALLIZATION KINETICS

4.1 Materials

The materials used in this study were kindly synthesized and supplied by E.I. du Pont de Nemours and Company. These copolymers consist of repeatedly alternating polyester and polyether blocks. The hard segment is a crystallizable polyester, poly(tetramethylene terephthalate) (PTMT), while the soft segment is made from poly(tetramethylene ether glycol) terephthalate (PTMEG-T)[37,28,92]. The chemical structure of these copolymers was shown in Chapter 2 (pg. 11). The sequence lengths of the hard and soft segment blocks follow a geometric distribution since the synthesis involves equilibrium ester exchanges. The average hard segment block length and consequently the composition is controlled by selecting the mole ratio of reactants during polymerization [34].

Four copolymers covering a wide range of compositions plus the hard segment homopolymer were investigated in this study. The compositions and approximate transition temperatures of the copolymer resins are shown in Table 4.1. The hard segment content that is reported is based on ^{13}C studies by Jelinski et al. [92] and Bovey [28]. The average degree of polymerization (D.P.) of the hard segment was estimated from the data of Cella [37]. Glass transition

Table 4.1: Composition and approximate phase transition temperatures of the copolyester-ethers used in this study.

POLYMER	WT.-% HARD SEGMENT[a]	AVERAGE D.P. of HARD SEGMENT[b]	T_m (°C)	T_g [c] (°C)
PTMT	100	>150	221°	+40°
H7246	81	22	217°	-18°
H6346	75	17	202°	-33°
H5556	57	8	203°	-55°
H4056	44	6	152°	-65°
PTMEG[d]	0	-	38°	-84°

Sources:

[a] F.A. Bovey, *Pure Appl. Chem.*, **54(3)**, 559-568 (1982).
L.W. Jelinski, F.C. Schilling, and F.A. Bovey, *Macromolecules*, **14**, 581-586 (1981).

[b] R.J. Cella, *J. Polym. Sci.*, **42**, 727-740 (1973) and *Encycl. Polym. Sci. Technol., Suppl. Vol.2*, 485-510 (1977).

[c] J.W. Van Bogart, A. Lilaonitkul, and S.L. Cooper, *Adv. in Chem. Series*, **176**, 4-29 (1979).

[d] R.E. Wetton and G. Allen, *Polymer*, **7**, 331-365 (1966).

temperatures were estimated from the data of Van Bogart et al. [21]. It should be noted that T_g varies with the DPS, and thus varies to some extent on the thermal history of sample. The PTMEG data were reported by Wetton and Allen [199]. The melting temperatures of the copolymers were determined by the author, and represent the temperature at the peak maximum.

4.2 Quiescent Crystallization Behavior

Before trying to melt spin filaments from these copolymers, the crystallization kinetics under quiescent, isothermal conditions were studied as well as the crystallization behavior while cooling at constant rate. These experiments should provide basic information on the nature of the crystallization behavior and the relative crystallization rates of the various compositions. Comparison of these results to commercially spun materials such as poly(ethylene terephthalate) and polypropylene should be useful in determining what sort of spinline behavior to expect from the copolymers.

Zhu, Wegner, and Bandara [223] studied the crystallization kinetics of copolyester-ether films using light microscopy. Spherulitic structures were produced by isothermal crystallization at low degrees of supercooling. As the supercooling was increased, the nucleation density increased dramatically. Zhu and Wegner [222] report that clear films were produced by quenching from the melt. Upon annealing, these samples remained clear, indicating that the nucleation density was very high and that crystallites much smaller than the

wavelength of light were produced. They report that the morphology changed from spherulitic in samples crystallized isothermally to a continuous network of lamellae in samples quenched rapidly to room temperature from the melt.

4.2.1 Isothermal Crystallization

Samples of 10–15 mg were melted in the DSC at temperatures about 25° C above their highest melting point for 5 minutes to eliminate all traces of crystallinity. These samples were then rapidly cooled to the desired crystallization temperature and allowed to crystallize isothermally. Temperatures were selected such that crystallization was essentially complete in 2–30 minutes. The crystallization temperatures are given in Table 4.2.

In order to determine whether these materials behave in the manner described by Gornick and Mandelkern [70] for random copolymers (see Section 2.5), the relative degree of conversion θ_{rel} (defined as the degree of crystallinity at time t (x_t) to the crystallinity at infinite times x_∞) was plotted as a function of time. Isothermal curves for H4056, H7246, and PTMT are shown in Figures 4.1–4.3. The copolyester-ether isotherms did not show the "fanning out" behavior at low degrees of supercooling or at high degrees of conversion that was observed by Gornick and Mandelkern for random copolymers. Instead they are mutually superimposable as would be expected from a simple Avrami type crystallization behavior.

Table 4.2: Crystallization half-times, Avrami exponents and crystallization rate constants.

	T_c (°C)	$t_{\frac{1}{2}}$ (mins)	n	K (mins^{-n})
H4056	84.0	2.67	3.89	0.0152
	90.0	3.36	3.81	0.00685
	94.0	3.99	3.66	0.00438
	98.0	4.57	3.60	0.00293
	104.0	5.76	2.90	0.00432
	112.0	11.76	2.97	0.000459
H5556	155.0	3.62	3.39	0.00885
	159.0	5.35	3.09	0.00389
	163.0	7.46	3.17	0.00119
	165.0	8.63	2.96	0.00118
	169.0	16.75	2.39	0.000823
H6346	155.0	2.98	3.22	0.0206
	159.0	4.49	3.03	0.00732
	161.0	5.56	2.98	0.00417
	163.0	7.10	–	–
	165.0	9.00	3.04	0.000871
	167.0	9.69	2.72	0.00144
H7246	174.5	1.89	3.25	0.0876
	180.5	4.46	2.97	0.00817
	182.5	5.27	2.62	0.00891
	184.5	6.17	2.94	0.00329
	186.5	7.29	3.05	0.00162
	188.5	7.29	3.05	0.00162
PTMT	188.2	2.93	2.83	0.0331
	191.2	3.76	2.79	0.0172
	192.7	4.78	2.61	0.0117
	194.2	5.67	2.66	0.00686
	195.7	5.96	–	–
	197.2	8.55	2.31	0.00488
	199.8	13.8	–	–

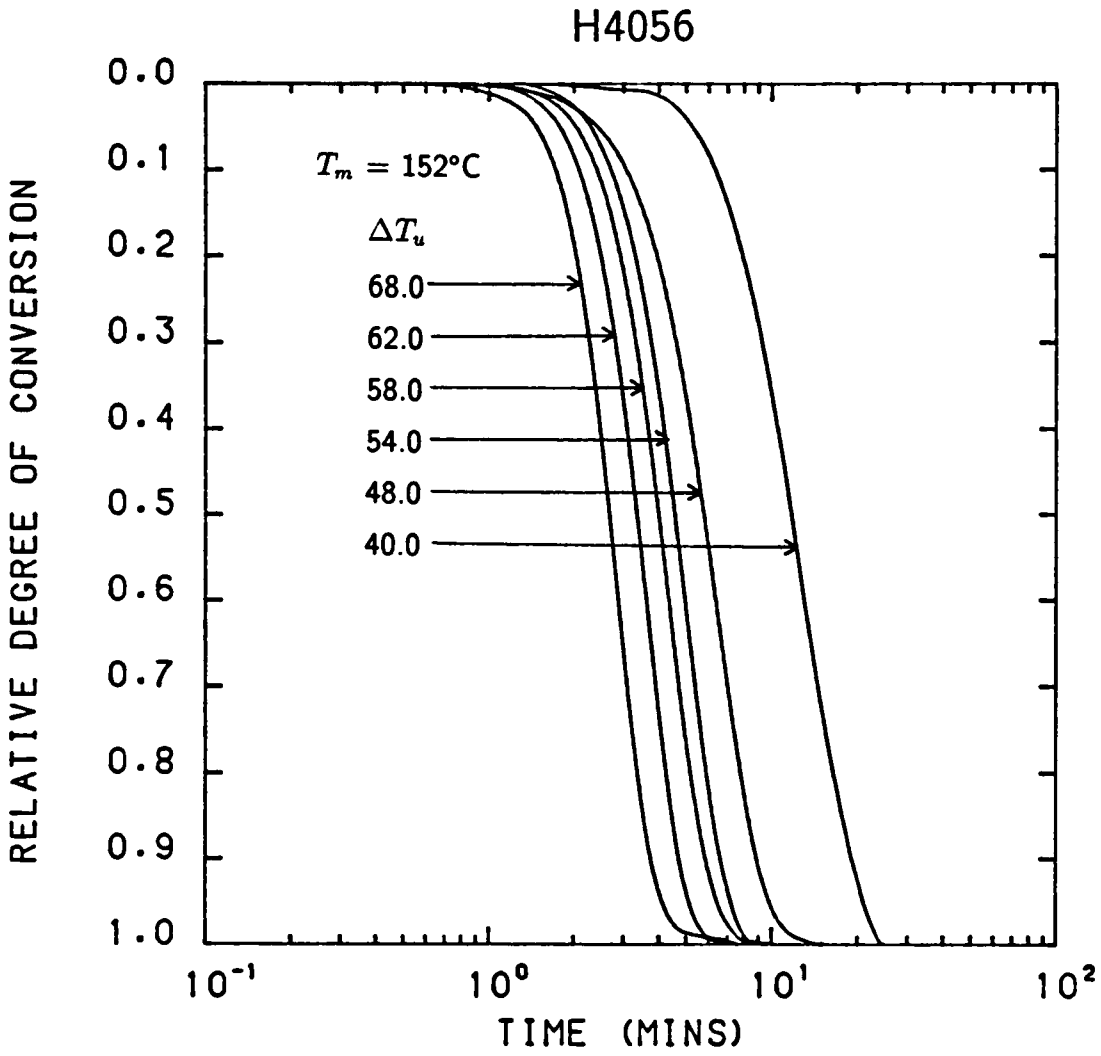


Figure 4.1: Relative degree of conversion as a function of time for H4056.

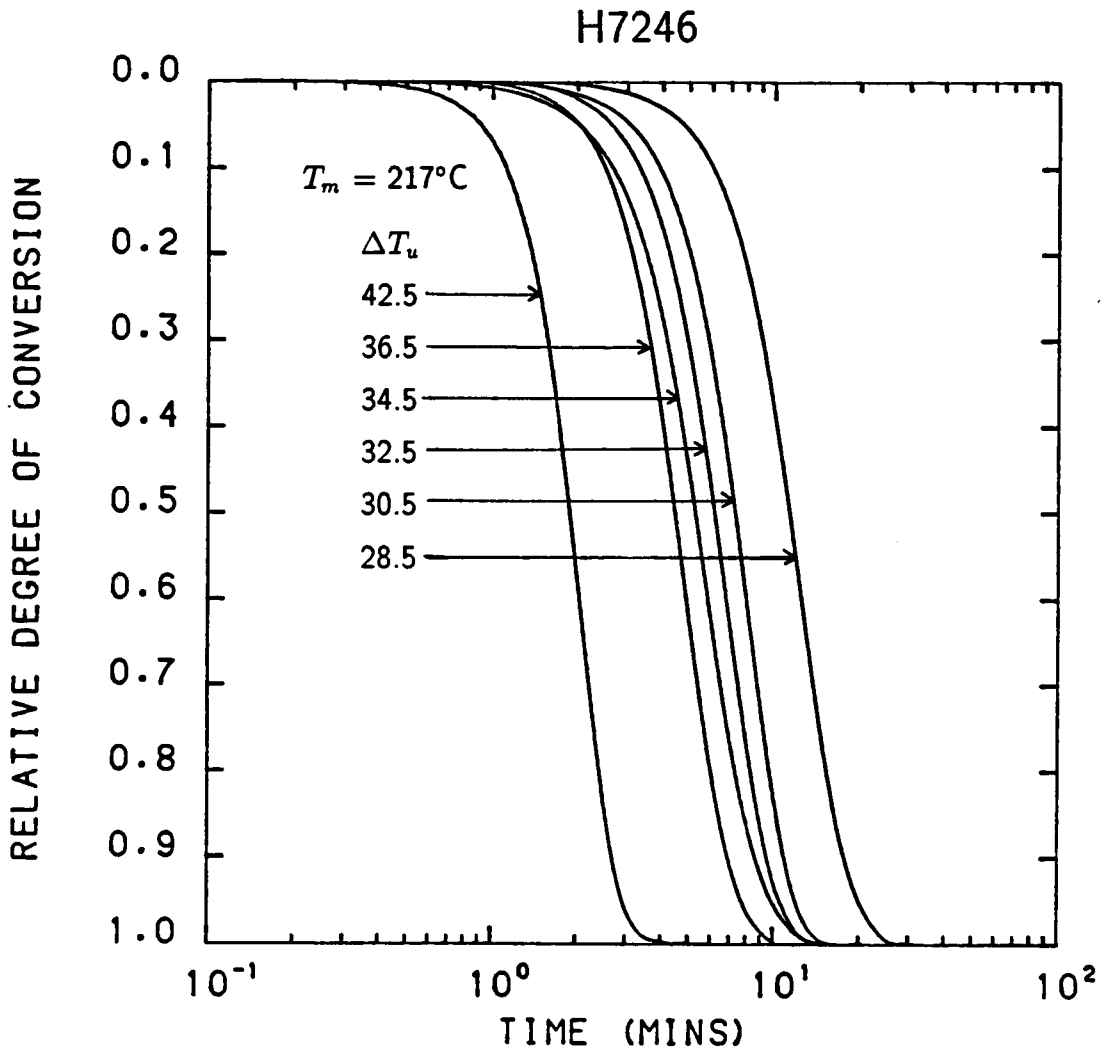


Figure 4.2: Relative degree of conversion as a function of time for H7246.

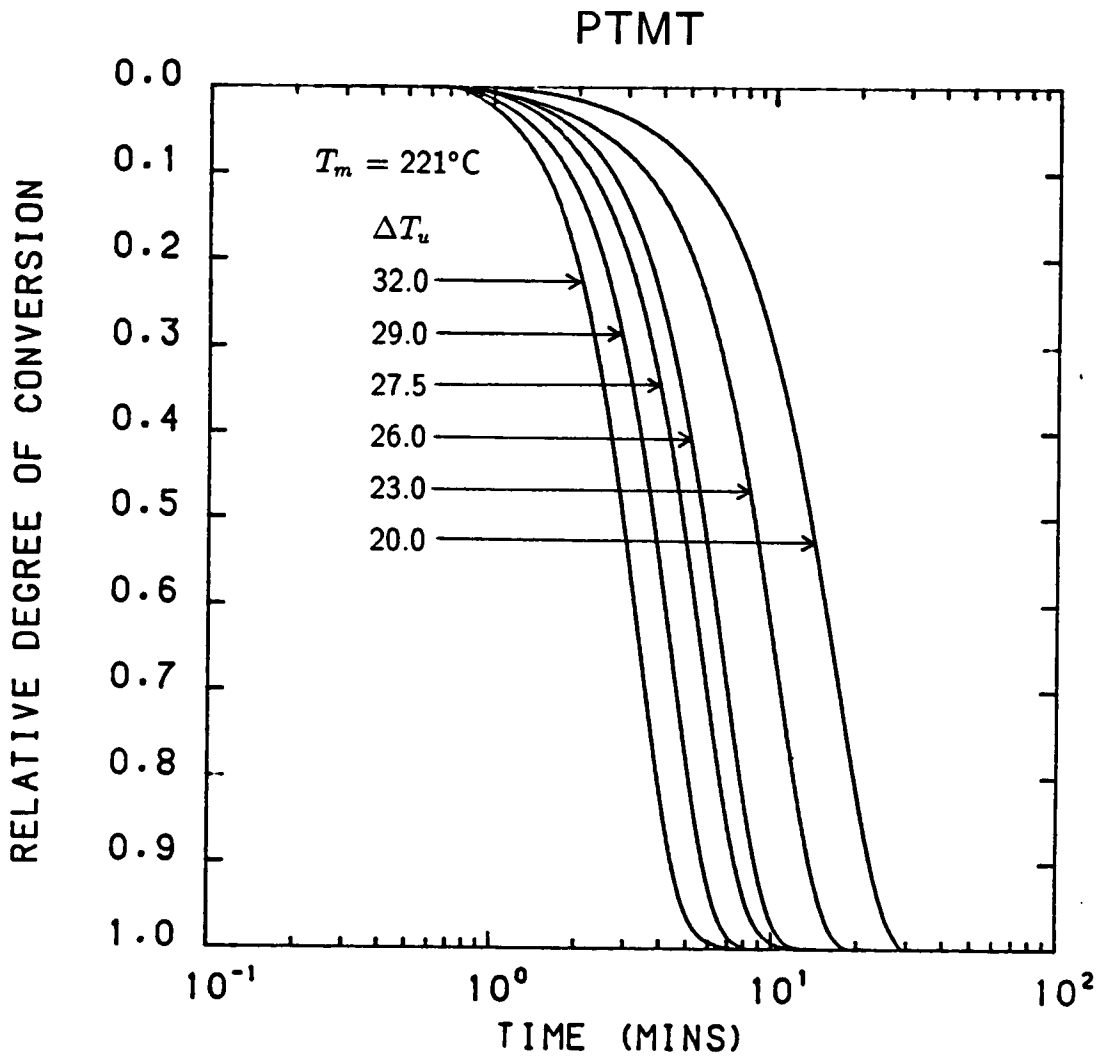


Figure 4.3: Relative degree of conversion as a function of time for PTMT.

The Avrami equation for polymers can be expressed as:

$$\frac{x_t}{x_\infty} = 1 - exp(Kt^n) \tag{4.1}$$

The Avrami exponent "n" can be determined from a plot of $ln(-ln(1-x(t)))$ versus $ln(t)$. This should yield a straight line with slope "n" and intercept "K". The values of "n" obtained in this way have been given in Table 4.2. The value of "n" increases as HSC and degree of supercooling decrease. This is in contrast to the results obtained by Zhu and Wegner [222] who report that "n" did not change with degree of supercooling but did change dramatically with composition. They also found a maximum in "n" with composition: The 54 wt.-% composition had a higher value of "n" than either the 45 or 72 wt.-% composition. The non-integer values of "n" in their samples were attributed to the non-geometrical shape of the growing crystals. The growth was, however, approximately three-dimensional in all compositions.

In this analysis, time t was measured from the moment the sample began to cool to T_c. It takes approximately 30 seconds to one minute, depending on ΔT, for the samples to cool to and equilibrate at the crystallization temperature. The cooling time should be subtracted from the measured time, but it is difficult to establish the exact time it takes the sample to reach T_c. The sample apparently cools quite rapidly ($\sim$360°C/min) to a temperature near T_c, but then some time is required for equilibration at T_c. The shape of the isotherms and the values of "n" are not dependent on the absolute value of t, but "K" is. The value of "K" is also very sensitive to the slope of the line in

the plot of $ln(-ln(1-x(t)))$ versus $ln(t)$. It may be better to determine "K" using the half-time of crystallization data. Substituting 0.5 for the relative degree of conversion in Equation 4.1 leads to:

$$K = \ln 2 \,/(t_{\frac{1}{2}})^n \tag{4.2}$$

Using the values of "n" and the half-times of crystallizations $t_{\frac{1}{2}}$, the values of "K" can be determined. They have been reported in Table 4.2.

A plot of the half time of crystallization as a function of crystallization temperature and composition is shown in Figure 4.4. For a given half-time of crystallization, the crystallization temperature of the copolyesters decreases, in general, as hard segment content decreases within the range of temperatures investigated. Polypropylene (PP) crystallizes at temperatures between those of H5556 and H4056. All the copolymers crystallize at lower temperatures than poly(ethylene terephthalate) (PET).

The crystallization rate is of primary importance in this study. A plot of the half time of crystallization as a function of supercooling and composition is shown in Figure 4.5. As hard segment content (HSC) is reduced the crystallization rate decreases and much higher degrees of supercooling are required for crystallization. The H4056 composition crystallizes even more slowly than poly(ethylene terephthalate)(PET), which is considered to have sluggish crystallization kinetics. Since PET crystallizes in the spinline only under conditions of high stress, the compositions low in HSC may not crystallize on the spinline.

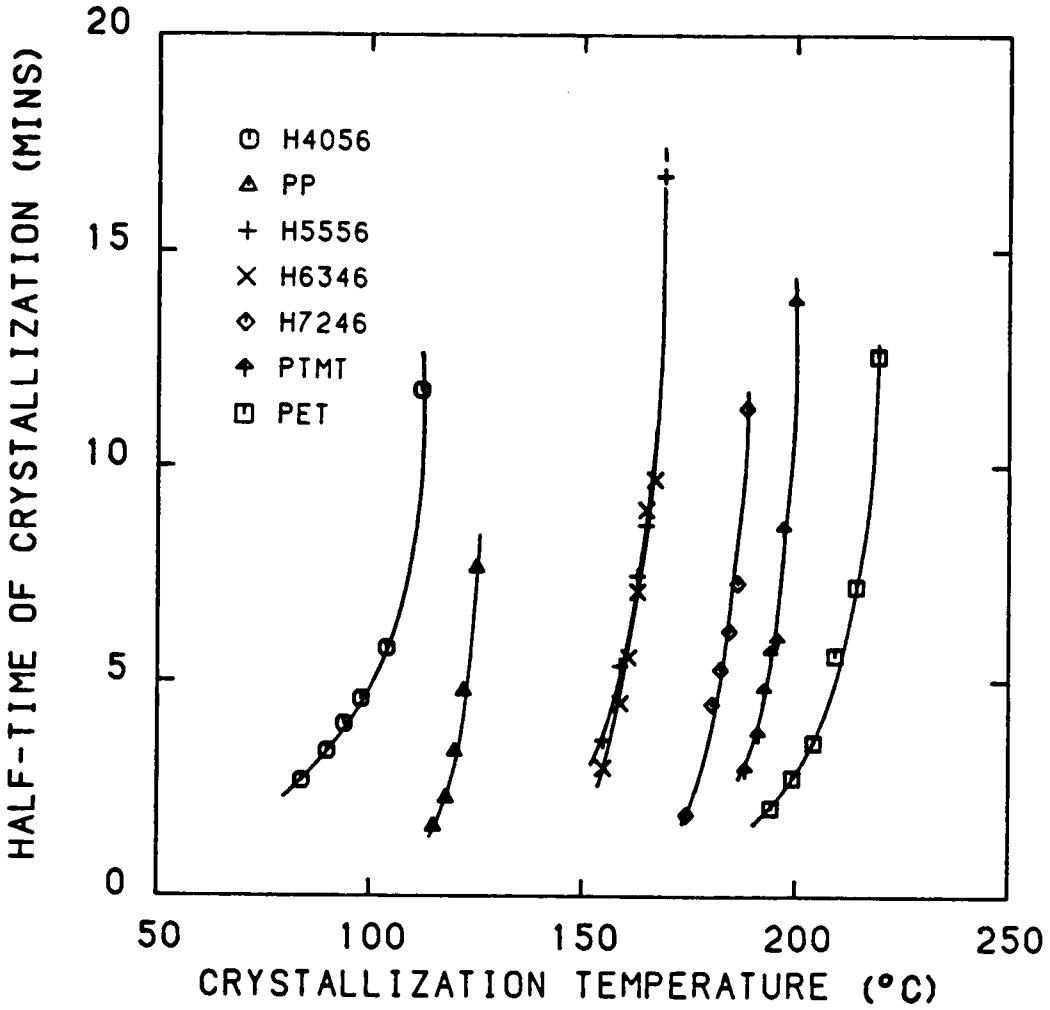


Figure 4.4: Half-times of crystallization for the copolyesters as a function of the crystallization temperature. The results for PET and PP are shown for comparison.

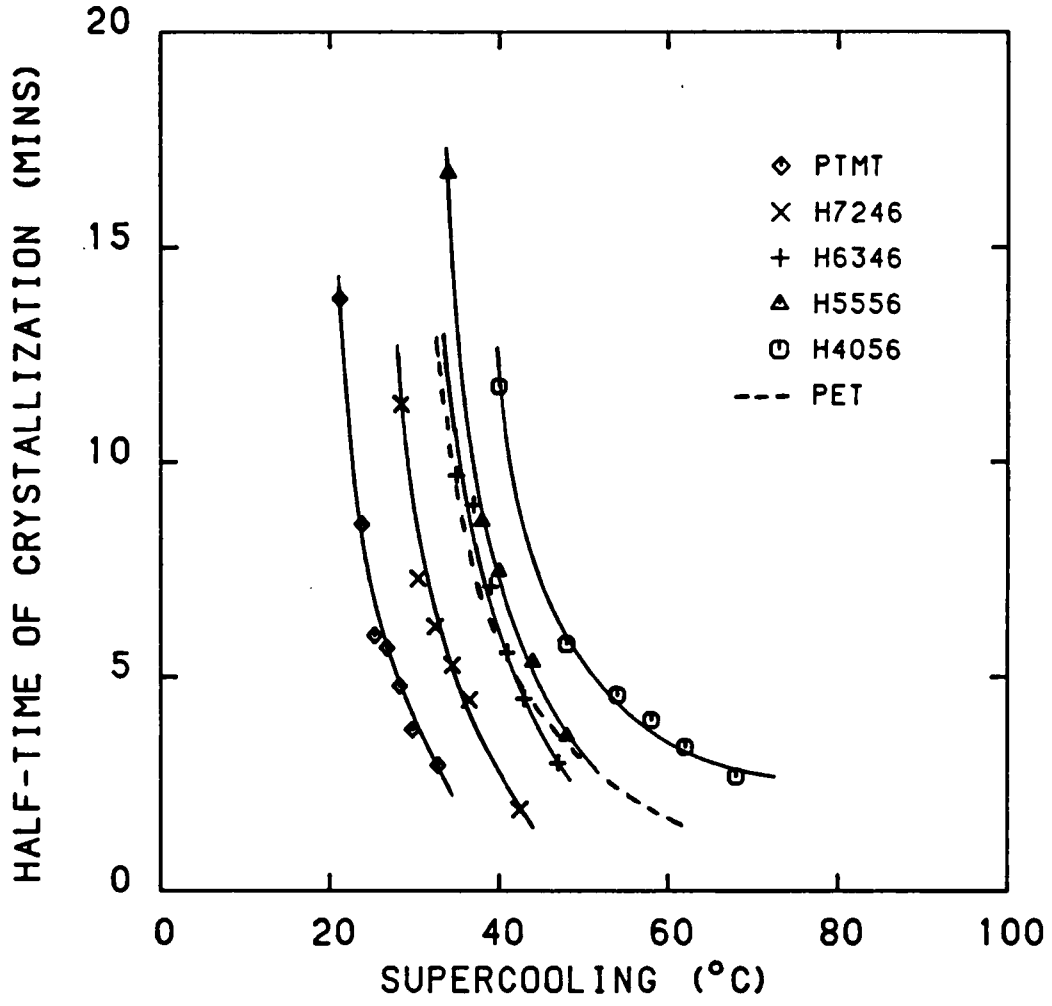


Figure 4.5: Half-times of crystallization as a function of the degree of undercooling for the copolyesters. The results for PET are shown for comparison.

4.2.2 Non-isothermal Crystallization

Studies of the crystallization behavior while cooling at constant rate show that the crystallization temperature drops with decreasing HSC and increasing cooling rate (see Figure 4.6). At the higher cooling rates, the compositions high in HSC crystallize well above room temperature (>90°C), while the H4056 composition must cool to almost 25°C before it crystallizes. Since the cooling rates during melt spinning are probably much higher than those produced in the DSC, much higher degrees of supercooling may be needed before crystallization takes place.

4.2.3 Crystallization from the Glassy State

Since the copolymers are above their respective Tg's at room temperature, it may be possible for water-quenched filaments to crystallize after spinning. In order to study the crystallization behavior of these copolymers from the glassy state, samples were quenched from the melt in liquid nitrogen. The samples produced in this manner were clear. These samples were transferred in liquid nitrogen to the DSC, which was being held at -100°C. Upon heating at 5 or 10° C/min, a crystallization exotherm was produced. In H4056, it occurs at about -12°C. The crystallization temperature increases as HSC increases as shown in Figure 4.7. The copolymer highest in HSC crystallizes at about 18°C, while the PTMT homopolymer crystallizes at about 40°C. It is evident from this experiment that crystallization can take place at room temperature in all the copolymers. Pure PTMT is below its T_g at 25°C and does not crystallize.

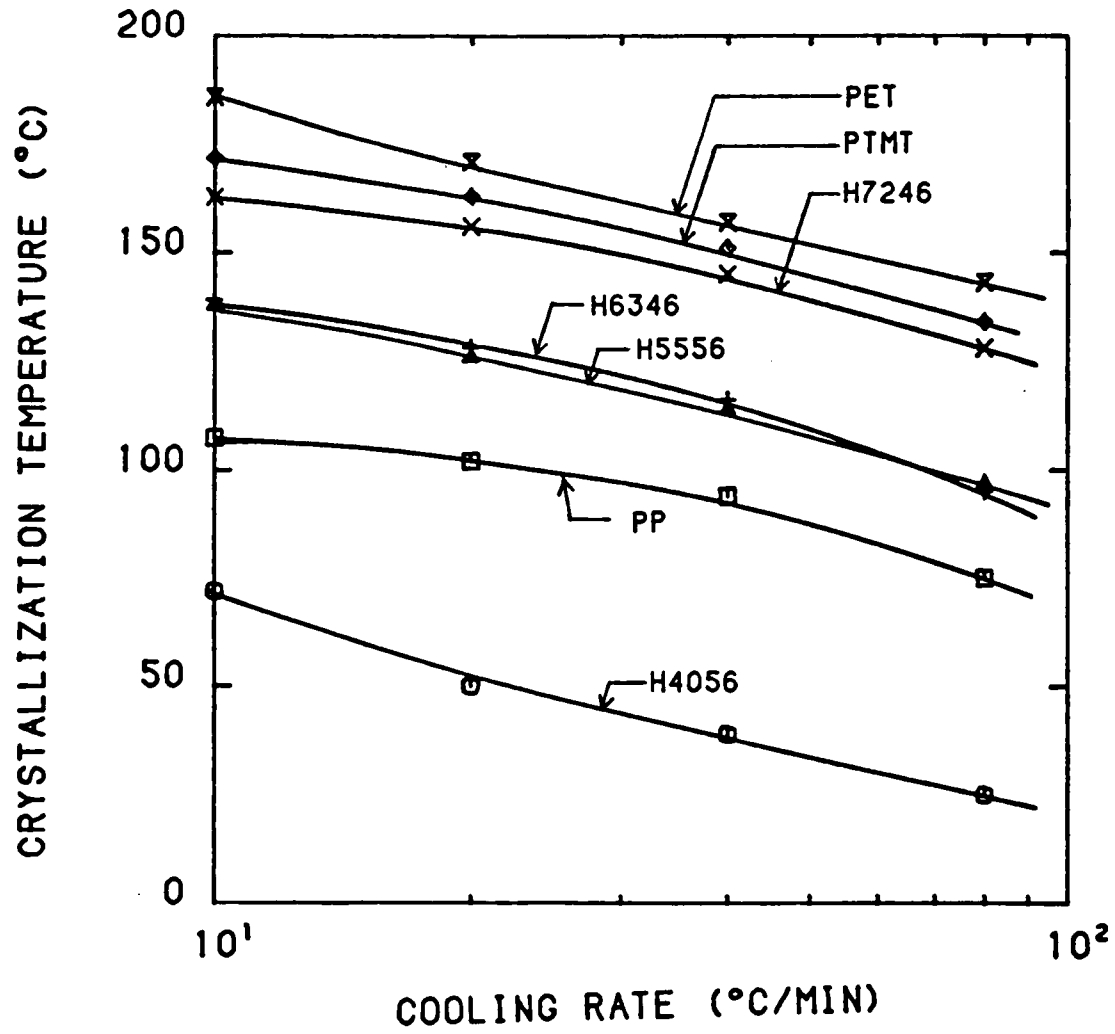


Figure 4.6: Crystallization temperature of the copolyester-ethers as a function of composition and cooling rate. Polypropylene (PP) and poly(ethylene terephthalate) are shown for comparison.

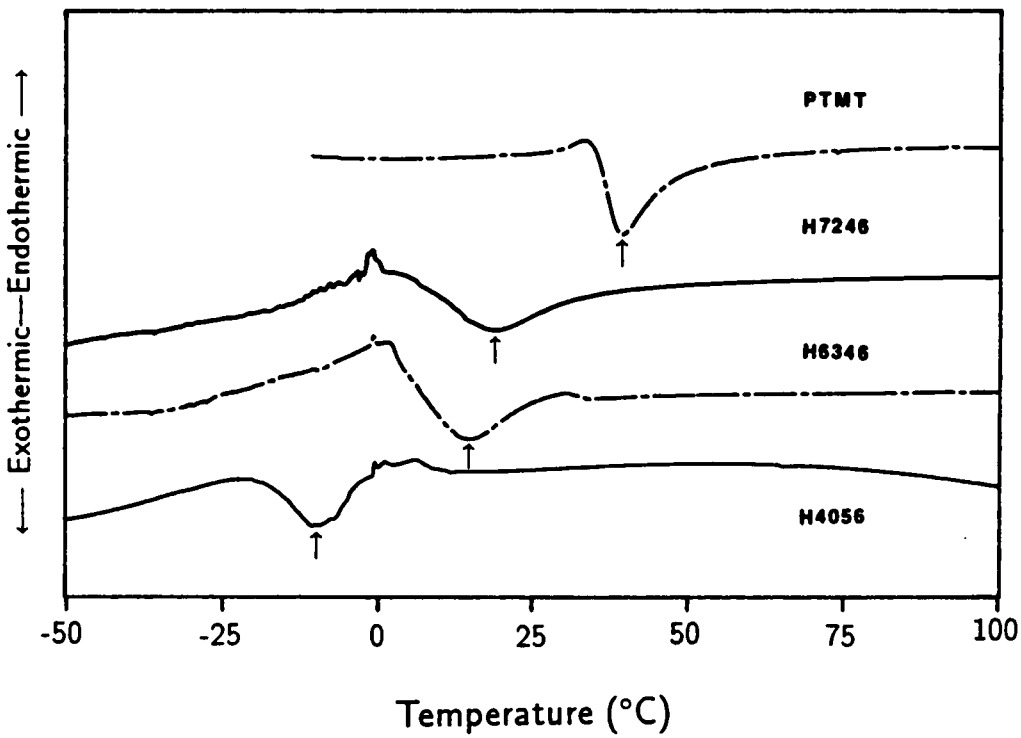


Figure 4.7: DSC curves showing crystallization from the glassy state. The crystallization peaks for H4056, H6346, H7246, and H7246 are at -12°, 14°, 18°, and 40°C, respectively.

Briber and Thomas [32] have also studied the crystallization behavior of the copolyester-ethers. They found that after cooling isothermally crystallized samples to room temperature, some of the short hard segment sequences remaining in the matrix crystallize. This new growth could form at the edge of existing crystallites or as smaller crystallites scattered through the matrix. The new crystallites took weeks to form at room temperature. These results imply that fractionation according to sequence length can occur. The authors explain that the fractionation occurs not as a result of incompatibility, but due to a coupling of the sequence length with the stable crystallite size at a given crystallization temperature. Thus, shorter segments can crystallize at low temperatures, albeit at very slow rates.

CHAPTER 5

FIBER FORMATION AND HEAT TREATMENT

5.1 Melt Spinning Techniques

The filaments were produced by melt spinning from a Fourné screw extruder equipped with a Zenith metering pump. Several different take-up methods were tried. The sluggish crystallization kinetics of the compositions low in HSC caused sticking and stretching problems during take-up if the filaments were spun into air. In an effort to solve these problems, a water quench bath was used. The bath was equipped with motorized rollers to prevent stretching of the filament between the bath and the constant tension take-up device. This apparatus is shown in Figure 5.1. The water bath was kept at 26.5± 1.5°C. After much experimentation, the air gap was set at 16± 1cm to minimize draw resonance. A polyester carrier yarn introduced into the spinline at the second godet prevented the copolyester filament from drawing in the winding device. With this set-up, all compositions could be spun under controlled and reproducible conditions. Filaments could be taken up at speeds up to 275 to 450 m/min depending on the composition.

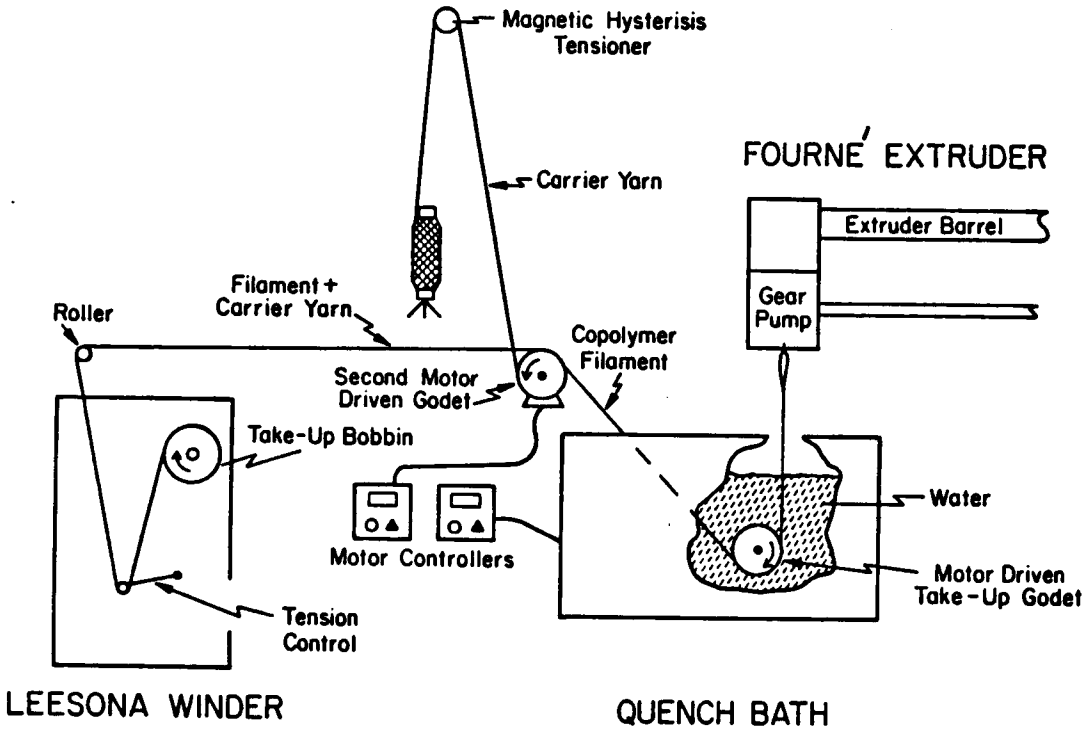


Figure 5.1: Schematic diagram of the spinline, water bath, and winder.

5.2 Crystallization Behavior During Spinning

During spinning without a quench bath, the filaments become increasingly tacky and difficult to handle as HSC decreases. This is easily explained by the crystallization kinetics of the copolymers from the melt. The amount of time and the degree of supercooling required for crystallization increases as HSC decreases.

When using a quench bath, the pure PTMT filaments are still no problem to spin although density measurements indicate they are amorphous. Of the copolymers, however, the H5556 filaments are the easiest to handle. Next easiest are the H7246 and H6346 filaments. H4056 is the hardest to take up. It stretches quite easily in a taffy-like manner and a carrier yarn must be used to prevent it from drawing in the winder.

In order to investigate this interesting behavior further, filaments were spun from an Instron capillary rheometer into a water bath, and the birefringence was measured as a function of time after initial contact with the water. The first data point was taken on-line just as the filament emerged from the bath. The elapsed time at this point was approximately 3 seconds. The filament was then cut and subsequent measurements were made off-line.

The results of this experiment are shown in Figure 5.2. H5556 has a fairly high birefringence coming out of the bath. Little or no change in birefringence occurs after spinning. Thus, considerable phase separation has already taken place in the bath and little or no further crystallization takes place at

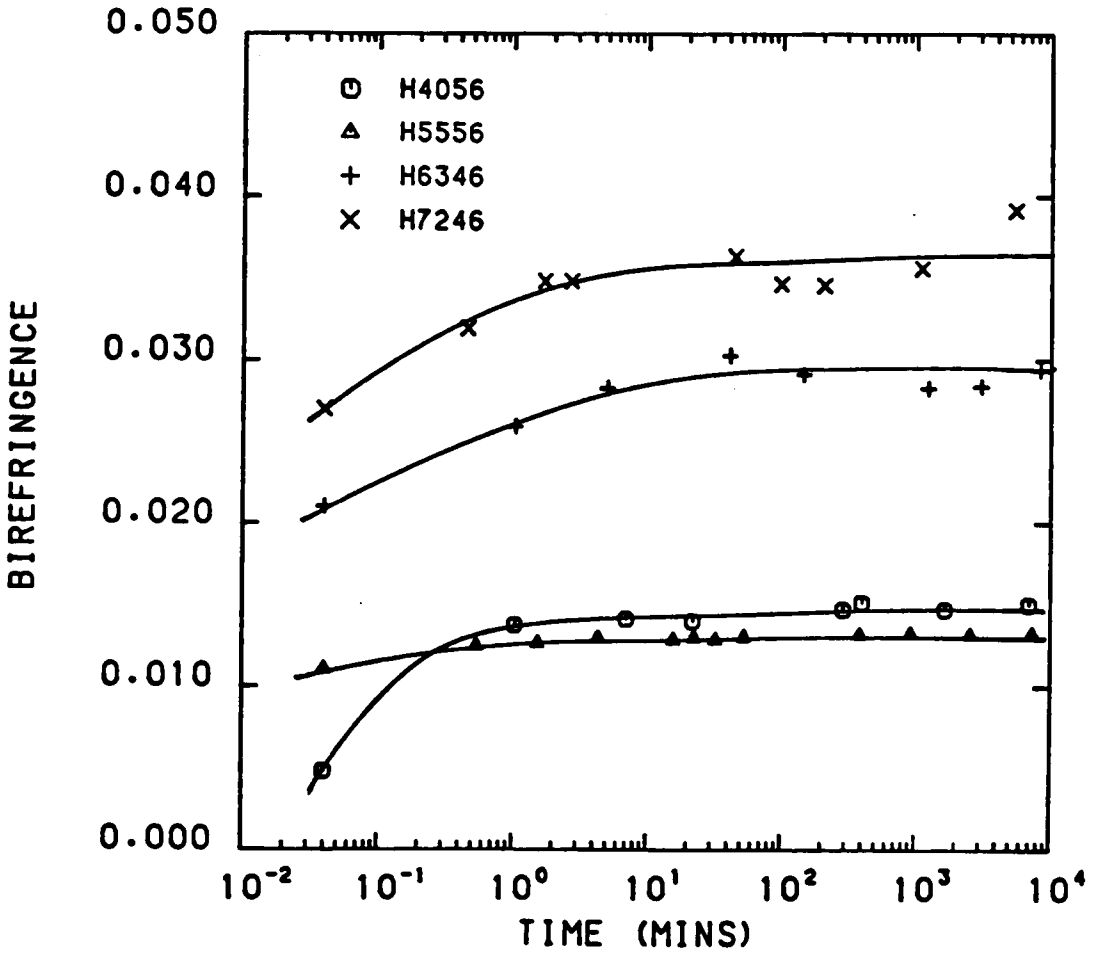


Figure 5.2: Birefringence of the water quenched filaments as a function of time.

room temperature. The birefringence of the H7246 and H6346 filaments is high coming out of the bath and increases slowly for several minutes. This indicates that these compositions partially crystallize in the bath and that further crystallization takes place during take-up. The birefringence of H4056 is quite low coming out of the bath, but it increases greatly during the first minute and more slowly for several more minutes. This means that very little crystallization takes place in the bath and that appreciable crystallization probably does not occur until the filament is on the bobbin.

Equatorial WAXD scans of the spun fibers taken immediately after spinning show that little or no additional primary crystallization occurs after the first ten minutes but that some secondary growth or crystallite perfection may take place. This effect is most pronounced for H4056.

The crystallization kinetics of these copolymers from the glassy state are not well understood. Apart from orientation effects, however, two factors would seem to control the crystallization behavior. The maximum crystallization rate in the range of temperatures from T_g to T_m is determined by the composition and the sequence length distribution. For a given composition, the crystallization rate at a particular temperature is determined by the degree of supercooling experienced by the composition; that is, the proximity of the actual crystallization temperature to the optimum crystallization temperature for that composition. The degree of supercooling may also determine the maximum degree of crystallinity that can be achieved at that temperature.

Filaments spun from the PTMT homopolymer are apparently quenched

to below their T_g (40°C) so rapidly that there is not enough time for appreciable crystallization to take place. Since the copolymers are quenched under similar conditions, one would expect little or no crystallization to occur in them until they are at or near the quench temperature ($\sim$ 26°C). (Remember that the crystallization rate and temperature drop as HSC decreases.) The H5556, H6346, and H7246 compositions all crystallize fairly rapidly near the quench temperature judging by their high birefringence upon emergence from the water bath. Crystallization of the H5556 filament seems to have stopped at this point while the H7246 and H6346 filaments continue to crystallize for several more minutes. It may be that H5556 is closer to its optimum crystallization temperature than either H7246 or H6346 and crystallizes more rapidly in the bath. The sluggish crystallization kinetics of the H4056 composition allows relatively little crystallization to occur in the bath, but since this copolymer is well above T_g at room temperature, it continues to crystallize after spinning.

5.3 Annealing Treatment

After spinning, portions of the filaments were annealed at constant length under a nitrogen atmosphere at temperatures of 100°, 141°, and 180°C for four hours. Great care was taken to exclude oxygen from the annealing chamber to prevent oxidative degradation at the elevated temperatures.

The annealing chamber consists of a glass tube about $1\frac{3}{8}$ inches in diameter and about 10 inches long. The tube is closed on one end and has a ground

glass fitting on the other end. A removable end piece allows the samples to be inserted or removed. A four-way stop cock attached to this piece can be opened or closed to allow the chamber to be purged. A schematic diagram of the annealing chamber is shown in Figure 5.3.

Free annealed filaments were simply wound into loose loops and placed in the annealing chamber. The fixed annealed filaments were wound onto aluminum frames about 10 cm long and the ends tied off, before placing them in the chamber. A drawing of the frame is also shown in Figure 5.3. The chamber was evacuated to less than 10^{-5} torr and then partially refilled with 99.998% pure N_2. The annealing chamber with the samples in it were then placed in an oil bath at the desired temperature and annealed for the specified time.

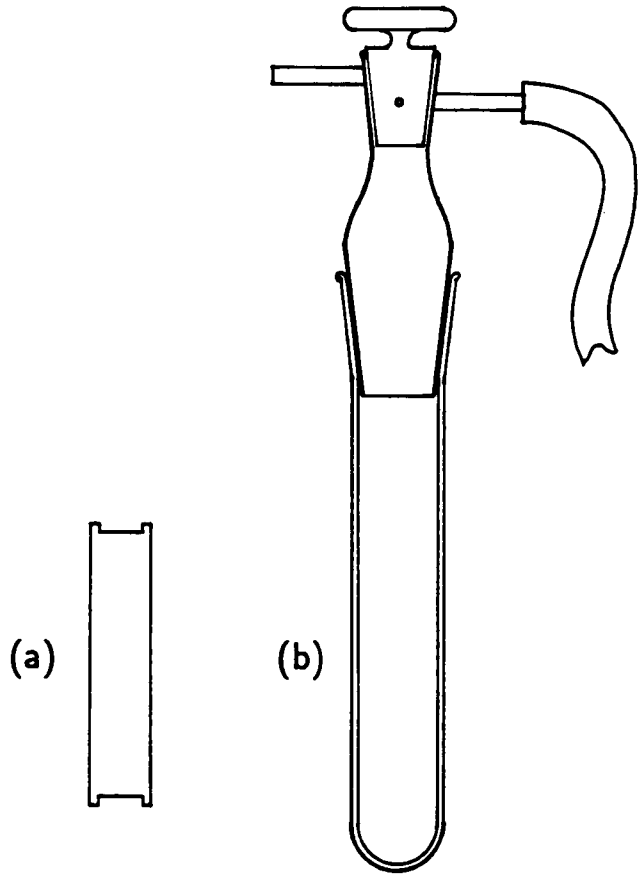


Figure 5.3: Schematic diagram of (a) an aluminum frame used to hold the filaments at fixed length and (b) the annealing chamber.

CHAPTER 6

STRUCTURE DEVELOPMENT IN MELT SPUN FILAMENTS

6.1 Structural Features

Air quenching produced opaque or translucent filaments depending on the composition and take-up velocity. Spinning into a quench bath produced translucent filaments under all the conditions investigated. It is believed that rapid quenching produces a higher nucleation density and thus smaller crystallites than in more slowly cooled samples [222]. Filaments spun from the PTMT homopolymer were essentially amorphous. As-spun samples were conditioned at room temperature for several months prior to their characterization.

These filaments are believed to have a two phase structure as has been reported for other copolyester samples processed in different ways by other investigators [34,37,205]. WAXD patterns of H4056 and PTMT filaments are compared in Figure 6.1. The only difference between the patterns of the two materials is the strong amorphous halo that appears in the H4056 pattern. WAXD patterns of all the copolymers show a diffuse halo from an amorphous phase and diffraction peaks that correspond to PTMT crystallites. There is no evidence of a crystalline PTMEG phase in any of the compositions studied. Rheovibron curves of the copolymers, shown in Figure 6.2, exhibit a single, broad glass transition region that is intermediate to the glass transition tem-

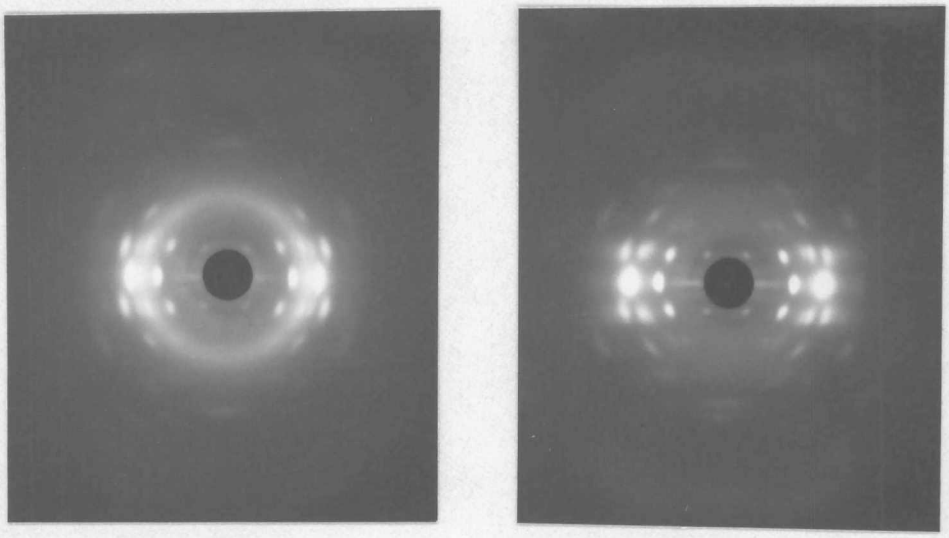


Figure 6.1: WAXD patterns of highly oriented filaments of (a) H4056 and (b) PTMT. The copolymer pattern is very similar to that of the homopolymer. There does not appear to be a crystalline PTMO phase in H4056.

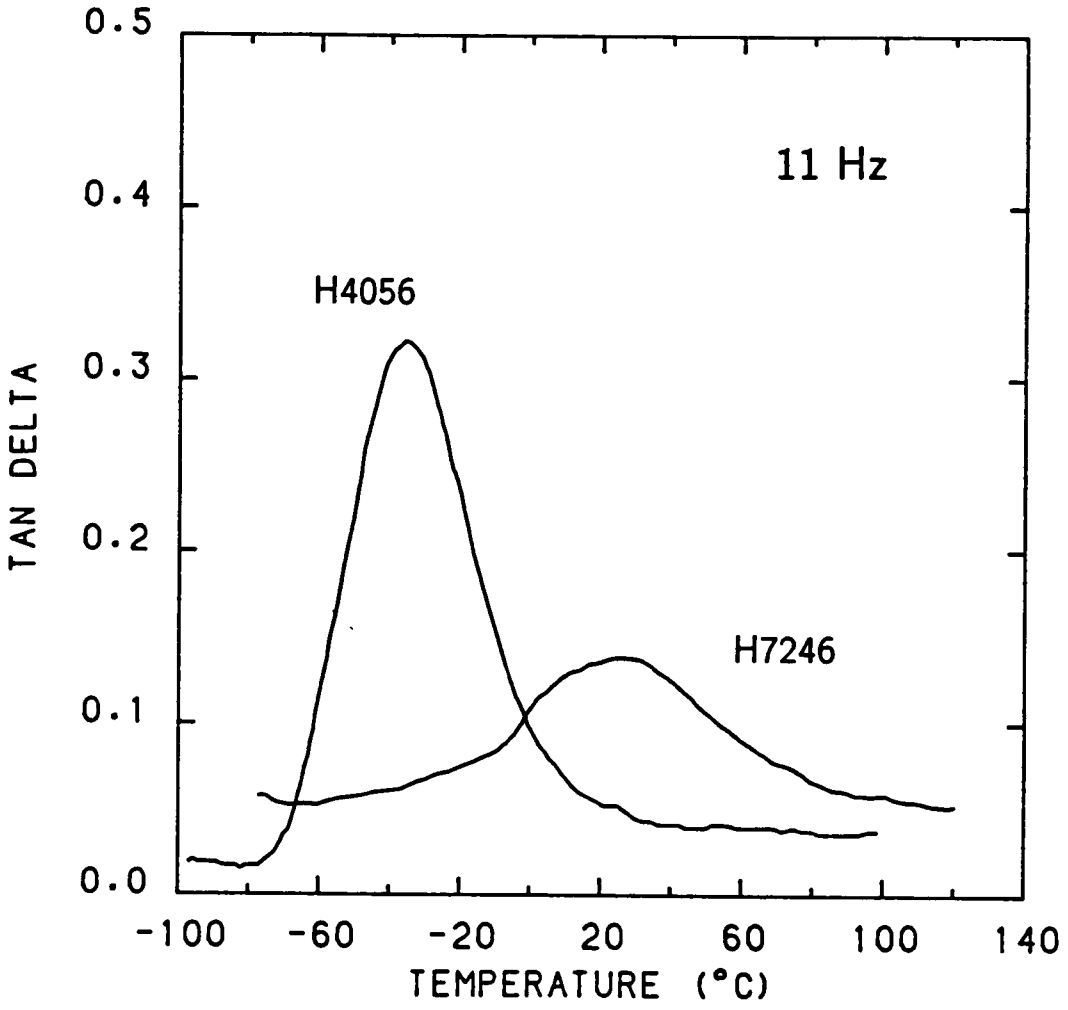


Figure 6.2: Result of dynamic mechanical testing on H4056 and H7246 filaments that have been drawn and free annealed.

peratures of the two homopolymers. Two separate peaks would be expected if there were an amorphous PTMT phase in addition to the amorphous PTMEG phase. Thus, one phase is made up entirely of crystalline PTMT segments, while the other phase consists of the remaining uncrystallized PTMT segments and all of the PTMEG segments.

A general overview of the domain structure of the filaments is provided by an inspection of their SAXS patterns. Scattering patterns of the as-spun filaments are shown in Figure 6.3 as a function of composition and take-up velocity. Patterns from an unoriented film of each compositon are shown for comparison. Two main features should be noted. First, the two point patterns indicate a lamellar structure with some degree of preferred orientation. As SDR is increased, the lamellae become increasingly aligned with their long axis perpendicular to the fiber axis. The orientation changes from almost isotropic at take-up speeds of 50m/min to highly anisotropic at speeds of 200m/min and greater. As will be shown in the next section, the chain axes of the crystalline hard segments become preferentially aligned parallel to the fiber axis at high SDR's, so the chain stems must traverse the short dimension of the lamellae. Secondly, the intensity of the peaks increases as HSC decreases. This suggests there may be an increase in the mean square electron density difference of the phases as HSC decreases. As discussed in Chapter 3, this can result from changes in either the volume fraction of each phase or the electron density difference between the phases or both. These results will be analyzed more quantitatively in Section 6.1.2.

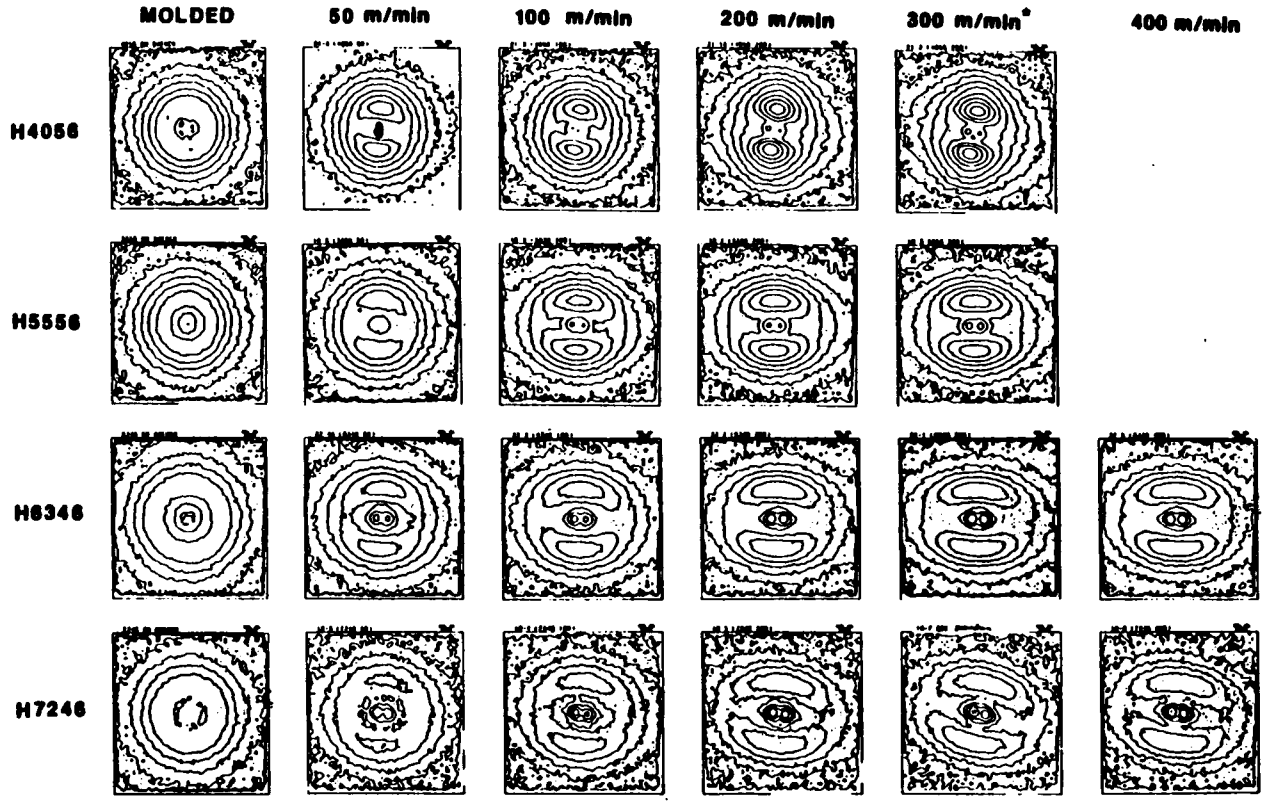


Figure 6.3: Small angle x-ray scattering patterns of the as-spun filaments.

Filaments spun at 250 or 300m/min were subjected to an annealing treatment at several elevated temperatures. Figure 6.4 shows the SAXS patterns of these filaments as a function of composition and annealing temperature. As annealing temperature increases, the SAXS peak increases in intensity and its width in the direction perpendicular to the fiber axis decreases. This phenomenon becomes more pronounced as HSC increases. The growth in peak intensity may indicate an increase in the electron density difference of the phases as would be expected in the case of increasing phase separation. These results will also be analyzed in Section 6.1.2. The narrowing of the peaks in the transverse direction may indicate that the lamellae are growing in a direction perpendicular to the fiber axis. The amount of growth that occurs during annealing appears to increase as HSC increases. This will be discussed in more detail in Section 6.1.3.

The microstructure of the various filaments were further characterized using birefringence, density, DSC, WAXD, and SAXS techniques. The degree of orientation, degree of phase separation, and the details of the morphology were determined as a function of composition, SDR, and annealing conditions. Details of the characterization techniques are described in Chapter 3.

6.1.1 Orientation

A high level of crystalline orientation is desired for maximum strength and elasticity [1]. WAXD techniques show that the degree of preferred orientation of the crystalline hard segments in these filaments increases rapidly up to a

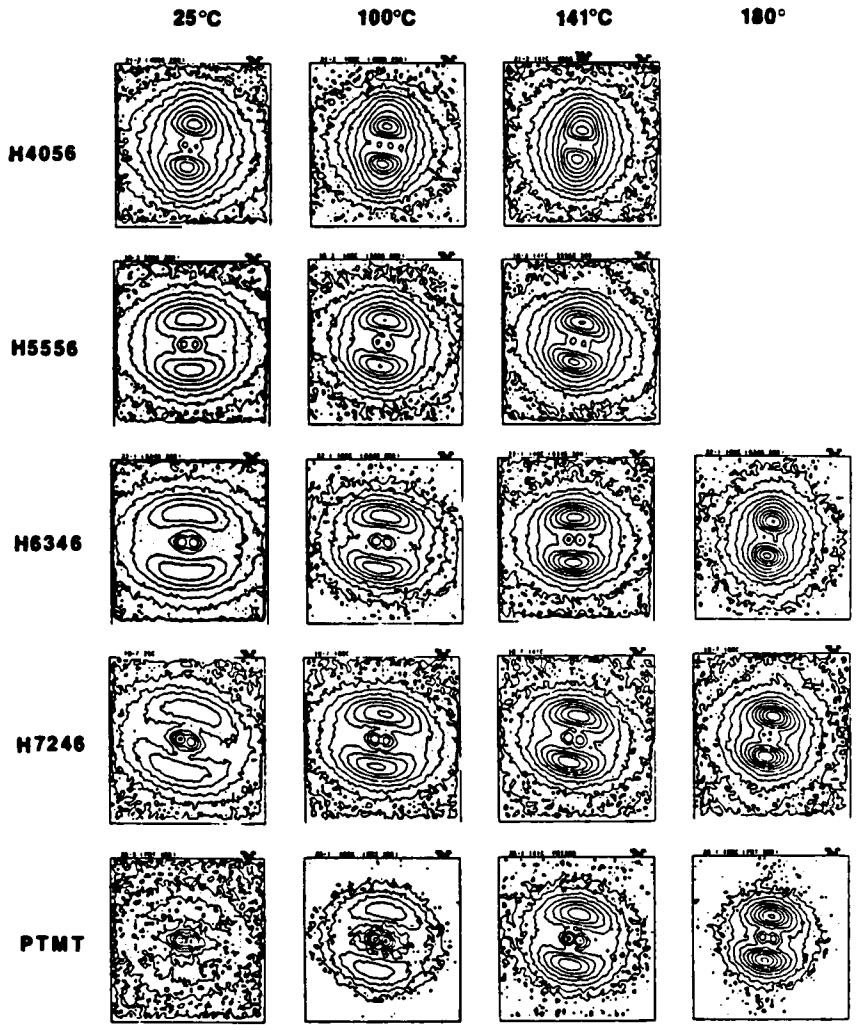


Figure 6.4: Small angle x-ray scattering patterns of annealed filaments. All filaments were spun at 300m/min.

point and then levels off as spin draw ratio (SDR) is increased. These results are shown in Figure 6.5. The birefringence increases in a similar manner with SDR as shown in Figure 6.6. Spinning speeds higher than about 400m/min were not possible with the water bath due to filament breakage. However, higher spinning speeds probably would not produce appreciably higher levels of orientation judging from the way f_c and the birefringence begin to level off at take-up velocities of around 300 to 400m/min. Similar copolyester-ether filaments spun by Abhiraman et al. [1] using a water bath showed no significant increase in birefrigence upon increasing the take-up velocity from 500 to 1000 m/min (SDR's of about 50 to 110).

As shown in Figure 6.2, the quenched filaments from compositions low in HSC may not be completely above their T_g at room temperature (25°C), because of the broad transition zone. As HSC increases, the transition moves to even higher temperatures. Thus, any amorphous orientation created during spinning may be partially "frozen in". Immersion in boiling water would be expected to raise all these samples to a point well above their T_g, allowing the amorphous regions to relax. The shrinkage in boiling water was used as a measure of the amorphous orientation.

The results of this experiment are shown in Table 6.1. The samples spun at 50m/min show no shrinkage. In fact, they expand by 1 or 2%, probably as a result of crystallization. None of the as-spun filaments show any significant shrinkage, except those spun from H4056 at 200 and 250m/min. These show 8% and 14% shrinkage, respectively. The H4056 filaments spun at

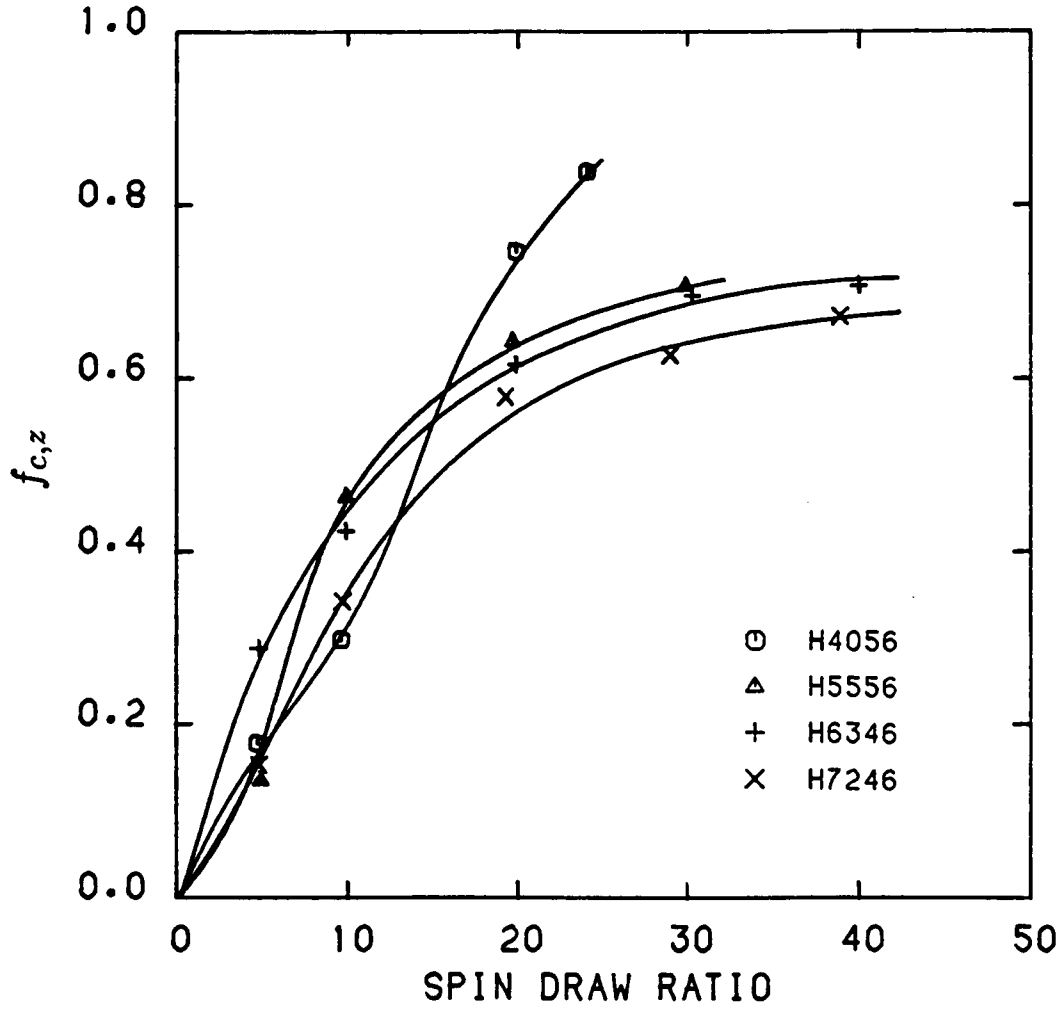


Figure 6.5: Crystalline orientation functions $f_{c,z}$ of the as-spun filaments as a function of spin draw ratio.

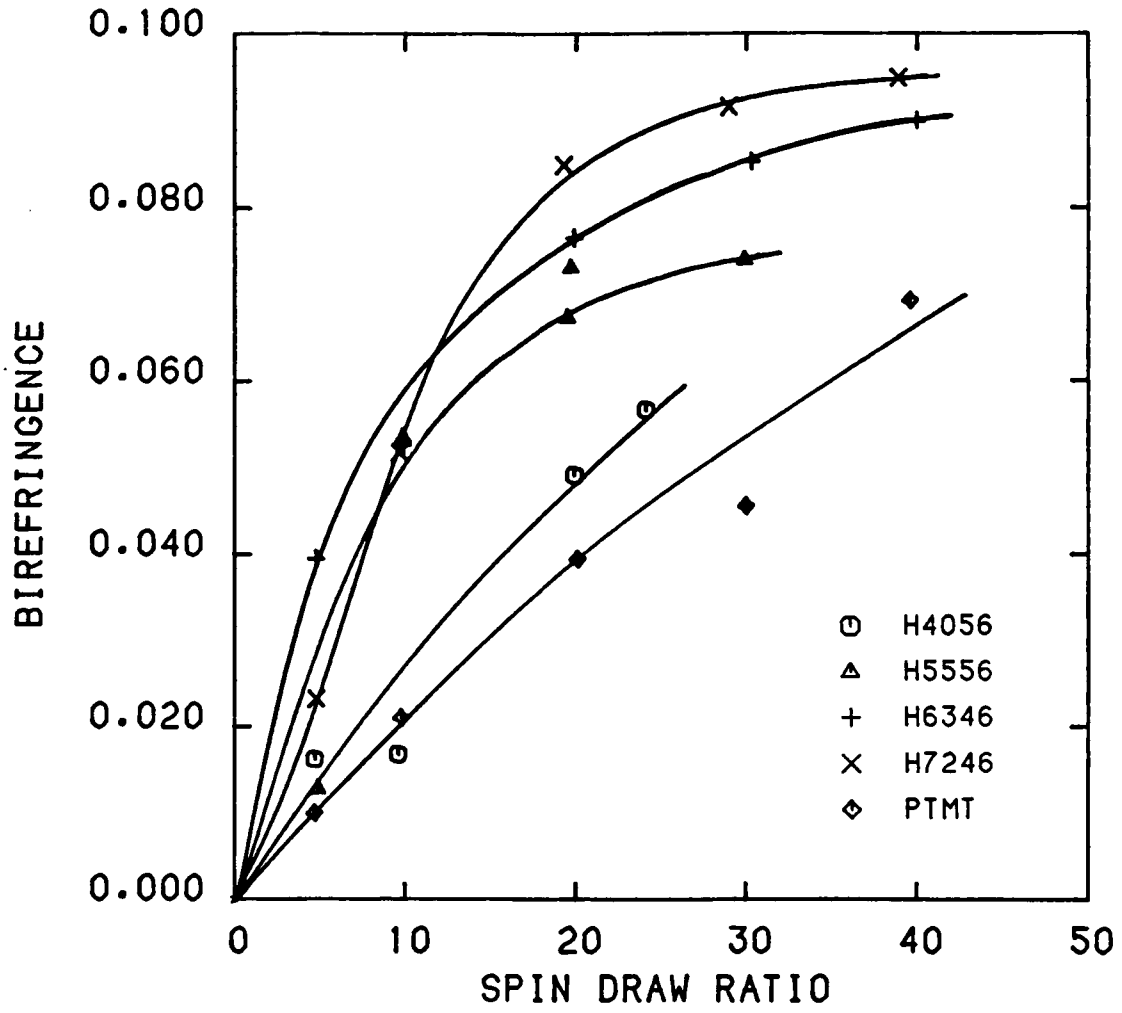


Figure 6.6: Birefringence of the as-spun filaments as a function of spin draw ratio.

Table 6.1: Percent shrinkage of as-spun filaments after immersion in boiling water.

SAMPLE	50	100	200	250	300
H4056	-0.9	-0.5	8	14	–
H5556	-0.1	–	–	–	0.9
H6346	-2.6	–	–	–	0.4
H7246	-1.6	–	–	–	-2.0
PTMT	-1.8	–	–	–	-2.2

Note: The take-up velocity in m/min is shown at the top of each column. Negative values reflect an increase in length.

200 and 250m/min were drawn 18% and 32%, respectively, between the two take-up godets during spinning to prevent sagging and tangling of the spinline. This may have created a strain in the amorphous phase as the sample was crystallizing.

These results show that, except for the two H4056 filaments that were drawn slightly, little orientation of the amorphous phase results from the spinning process itself, regardless of composition or spin draw ratio.

Samples spun at 300m/min (250m/min for H4056) were annealed at several temperatures. Annealing produces a moderate increase in hard segment orientation as shown in Figure 6.7. This is a result of oriented crystal growth as will be shown in Section 6.1.3.

The results of the shrinkage experiment on annealed filaments are shown in Table 6.2. Annealing at 100°C or higher at fixed length substantially reduces the shrinkage of H4056 filaments spun 250m/min. This is due to crystallization and stress relaxation during fixed annealing [212]. The relaxation may result from a reduction in amorphous entanglements or partial melting and subsequent rearrangement of chain segments. Annealing has very little effect on the shrinkage of the other filaments, since it was so small originally. Any orientation remaining in the amorphous phase after the boiling water treatment must result from segments whose motion is somehow restricted by the crystalline domains.

In summary, the water quench melt spinning procedure can be used to produce filaments having a high level of crystalline orientation while maintain-

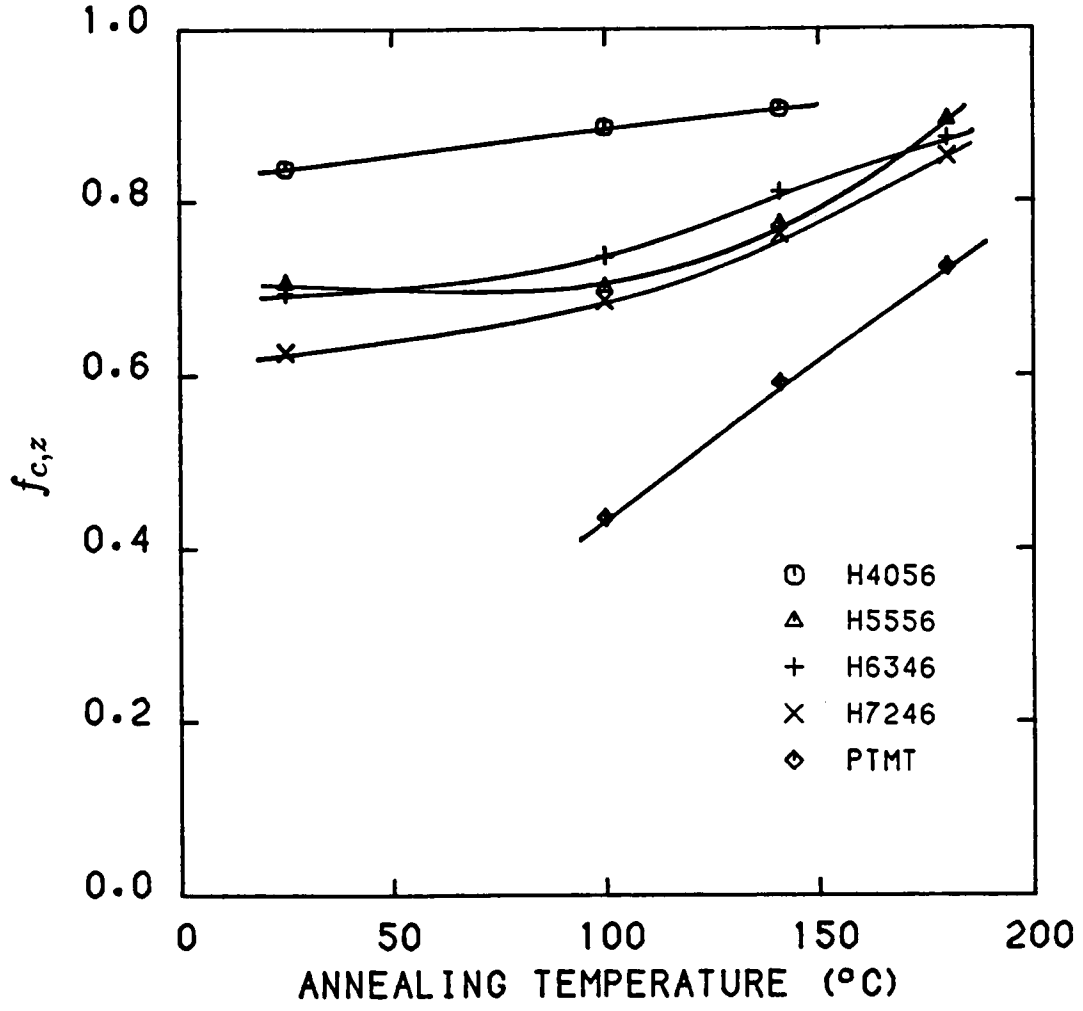


Figure 6.7: Effect of annealing on the crystalline orientation functions $f_{c,z}$ of the filaments spun at 300m/min.

Table 6.2: Percent shrinkage of annealed filaments after immersion in boiling water.

SAMPLE	25°C	100°C	141°C	180°C
H4056 250	14	3.2	1.6	–
H5556 300	0.9	0.7	–	2.1
H6346 300	0.4	0.0	–	1.4
H7246 300	-2.0	-0.2	–	-0.7
PTMT 300	-2.2	-0.8	–	-1.0

Note: Annealing temperature is shown at the top of each column. Negative values reflect an increase in length.

ing a low level of amorphous orientation. Fixed annealing can enhance the crystalline orientation while further reducing stresses in the amorphous phase.

6.1.2 Degree of Phase Separation

The degree of phase separation is one of the most important parameters in determining the physical and mechanical behavior of these copolymers since it determines the degree of physical crosslinking and the glass transition temperature for a given sample. Changes in the amount of phase separation were followed by measuring bulk density and through SAXS techniques. The quantity ε defined by Bonart and Müller [25] is used in comparing the relative degree of phase separation among the different copolymer samples. The results of the density and SAXS experiments for as-spun filaments are shown in Table 6.3 and Figure 6.8, respectively.

Except for H4056 spun at 250m/min, neither the density or ε show much change with SDR, indicating that the DPS is virtually independent of this parameter. There is, however, a large effect of composition on the DPS, as shown in Figure 6.8. The DPS decreases as HSC increases, despite the fact that the crystallization kinetics studies show the crystallization rate increases as HSC increases (at a given degree of supercooling).

The density and DPS are shown as a function of composition and annealing temperature in Figures 6.9 and 6.10. Both the density and ε increase significantly in all compositions, except H4056. The increases become larger as HSC increases. From these data, it is apparent that annealing below T_m

Table 6.3: Density (grams/cm^3) of as-spun filaments as a function of composition and spinning speed.

SAMPLE	50	100	200	250	300	400
H4056	1.1543	1.1541	1.1543	1.1544	–	–
H5556	1.1922	–	–	–	1.1922	–
H6346	1.2380	–	–	–	1.2380	–
H7246	1.2494	1.2489	1.2492	–	1.2486	1.2486
PTMT	1.2795	–	–	–	1.2801	–

Note: The take-up velocity in m/min is shown at the top of each column.

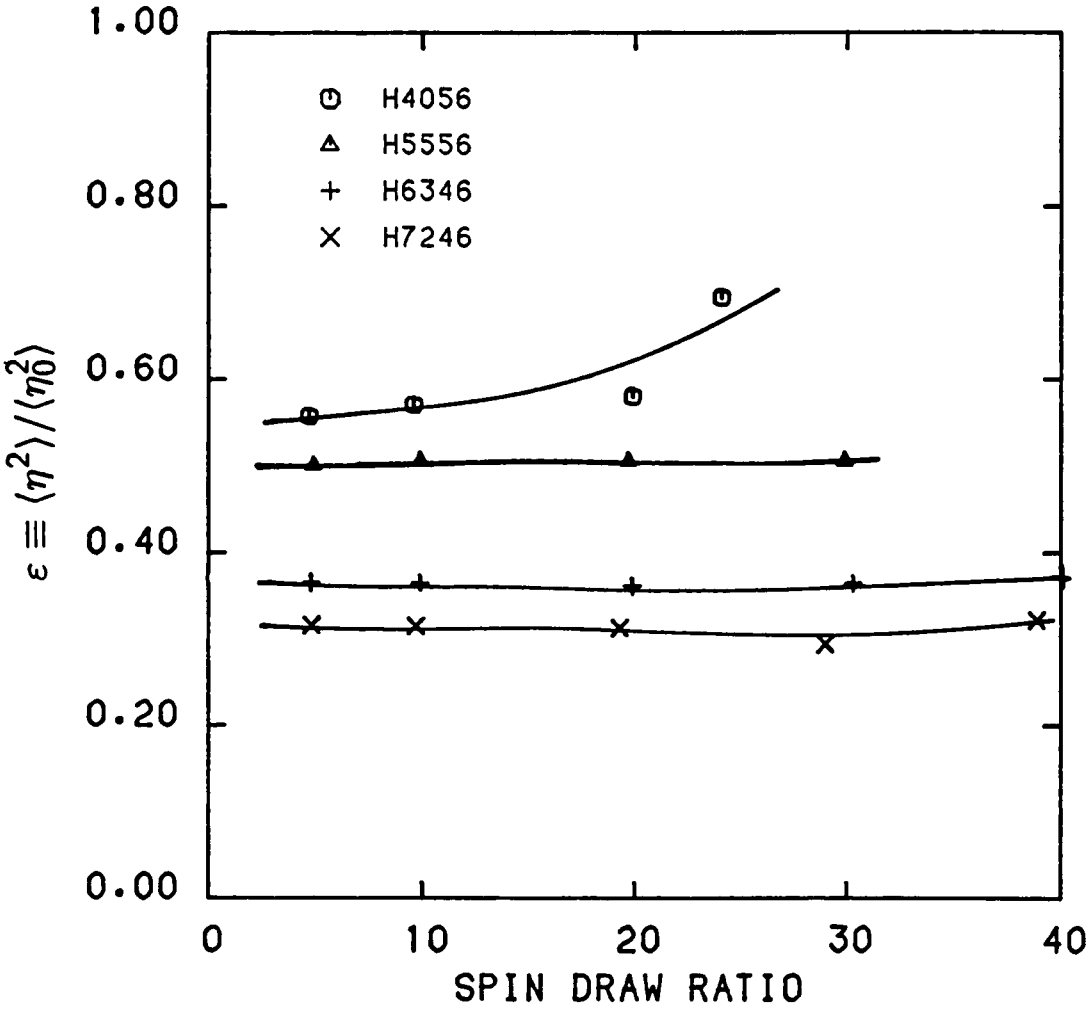


Figure 6.8: Relative degree of phase separation ε for each composition as a function of spin draw ratio.

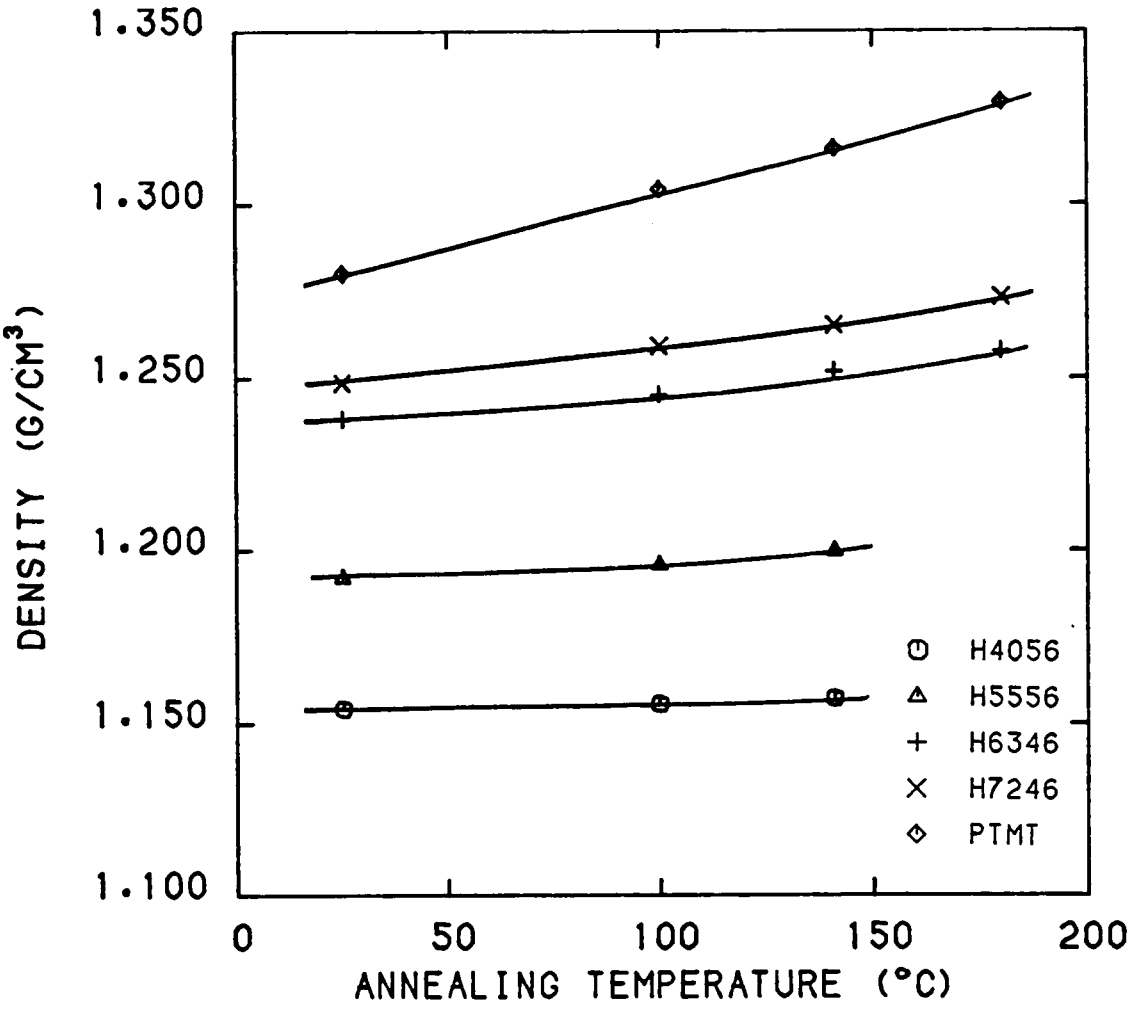


Figure 6.9: Density of the filaments spun at 300m/min as a function of annealing temperature.

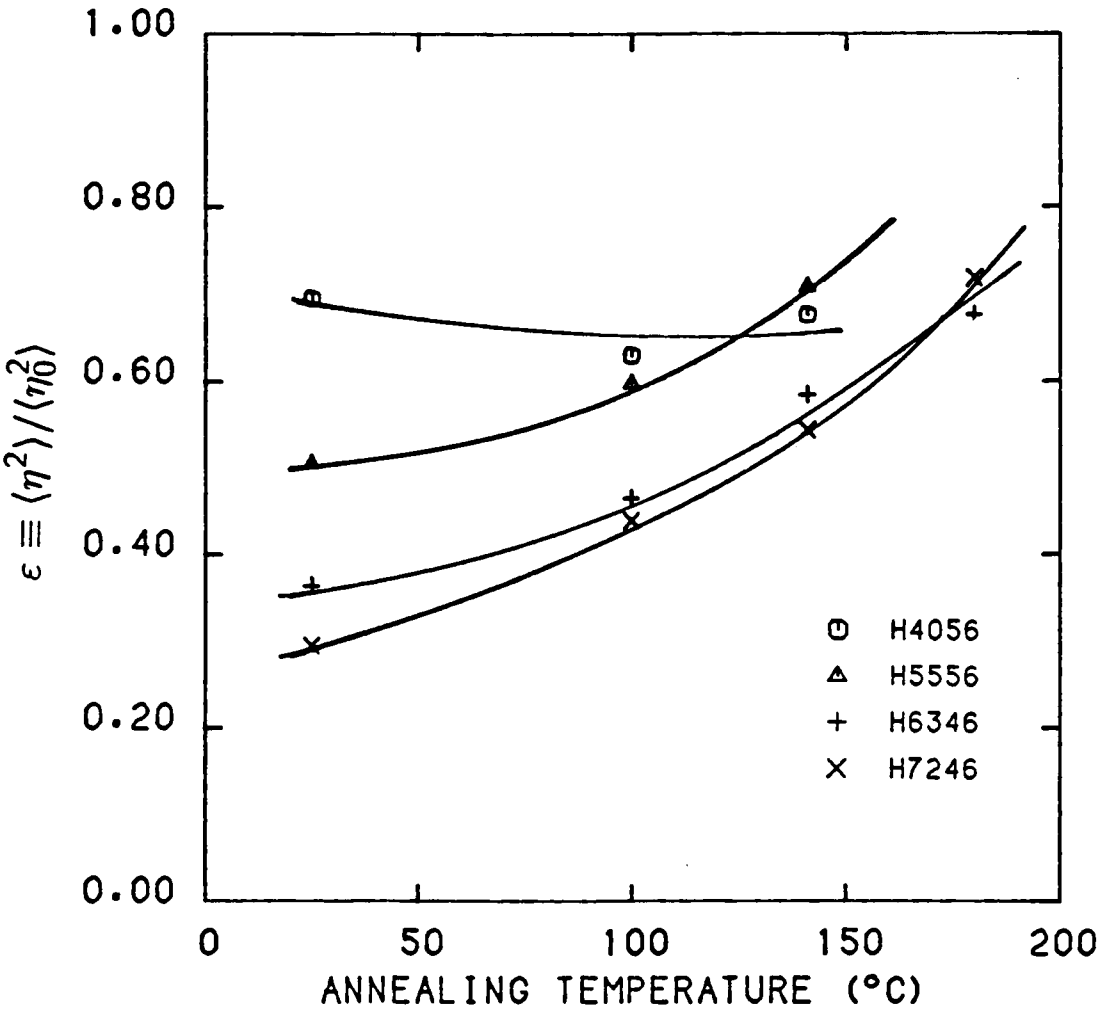


Figure 6.10: Effect of annealing temperature on the relative degree of phase separation of filaments spun at 300m/min.

promotes phase separation. Figure 6.10 shows H4056 already has a high level of phase separation after conditioning at room temperature and that annealing does not change the DPS appreciably. There is some scatter in the SAXS data for H4056, but the density results indicate that there is little or no increase in DPS upon annealing. The compositions higher in HSC are at lower levels of phase separation after spinning. Filaments from these compositions show significant increases in the DPS upon annealing. As HSC increases, higher and higher annealing temperatures are required to attain a given DPS. Comparable results were reported by Bandara and Droscher [16] for compression molded sheets made from copolyester-ethers quenched from the melt in ice water and subsequently annealed at several temperatures between 80°and 186°C.

The results reported above suggest that the DPS may be related to the degree of undercooling ($T_m - T_a$) a particular sample experiences during annealing. If this is the case, a plot of DPS as a function of undercooling should produce a single master curve upon which all samples would fall. As shown in Figure 6.11, only a partial fit is acheived by this method. The curves tend to merge around 50°–75°C of undercooling, but at higher undercoolings they are still widely separated. These results will be discussed in more detail in Section 6.2.

6.1.3 Morphology

Crystallite size and spacing as well as other morphological features may be of considerable importance in determining the mechanical properties of these

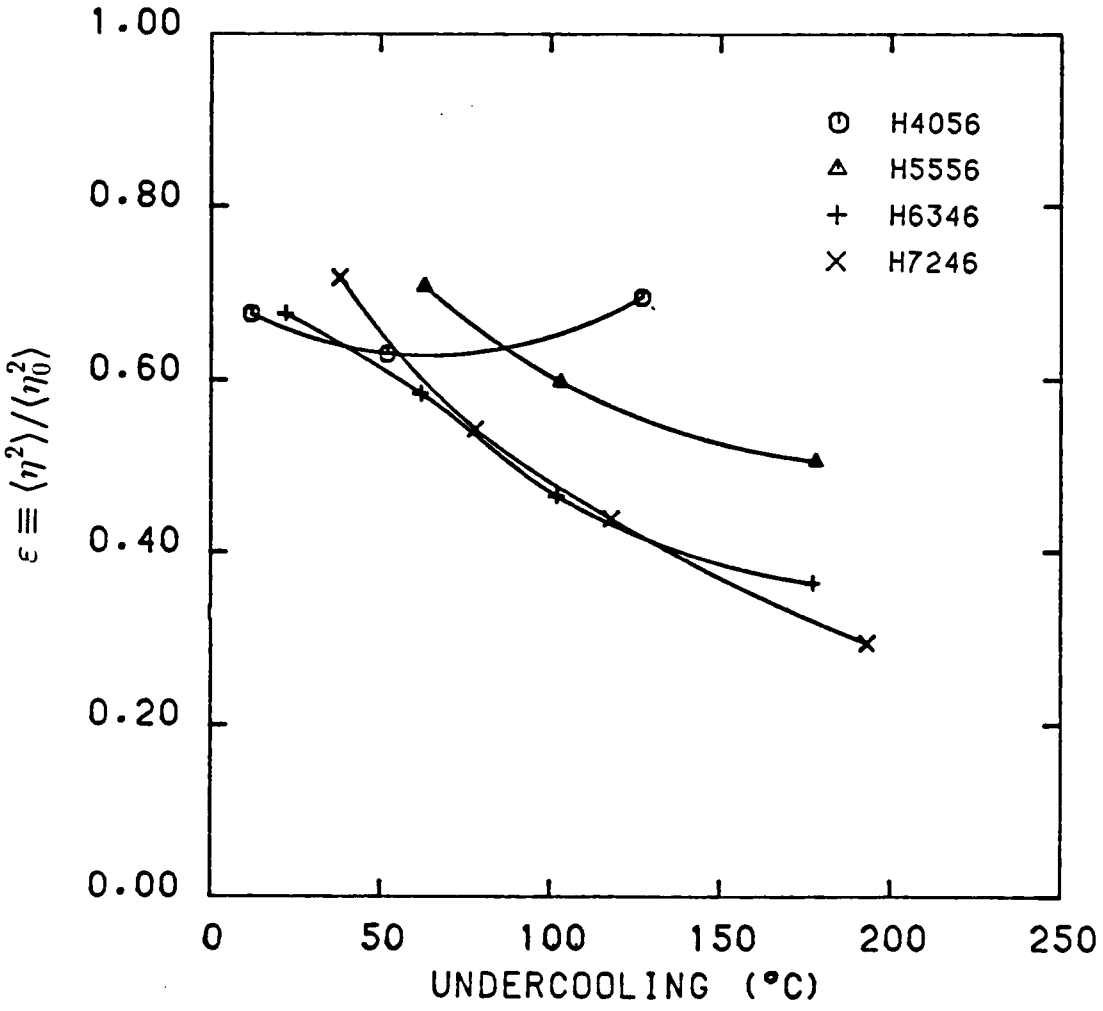


Figure 6.11: Relative degree of phase separation as a function of the degree of undercooling experienced by the filaments during annealing. These filaments were all spun at 300m/min.

filaments. Details of the morphology were investigated as a function of SDR and annealing temperature using WAXD, DSC, and SAXS techniques.

The DSC curves of some of the as-spun filaments are shown in Figure 6.12. These curves exhibit a broad melting peak at higher temperatures and a second, smaller endotherm around 50–60° C. DSC curves of filaments annealed at 141° C are shown in Figure 6.13. The higher temperature endotherm sharpens and grows in size upon annealing, while the second endotherm shifts to about 150° C. Since H4056 is annealed at a temperature close to its melting temperature, the annealing peak and the primary melting peak merge. This behavior has been observed for other compositions as well [195]. The lower temperature endotherm appears at the same place in all the materials including PTMT. DSC curves of samples annealed at other temperatures indicate that the second endotherm always appears at a temperature just above T_a. Similar behavior has also been observed for poly(ethylene terephthalate) (PET) samples as well [141]. For these reasons, the lower temperature peak is attributed to the PTMT phase in the copolymer samples and does not appear to be associated with a crystalline PTMEG phase. These results are consistent with the idea that small hard segment crystallites with a melting temperature just above T_a are formed during annealing.

Estimates of the crystallite size were obtained by measuring the broadening of the (100), (010), and ($\bar{1}$04) WAXD peaks produced by the PTMT phase. The 2θ scans used in this analysis are shown in the Appendix (Figures A-1 through A-8).

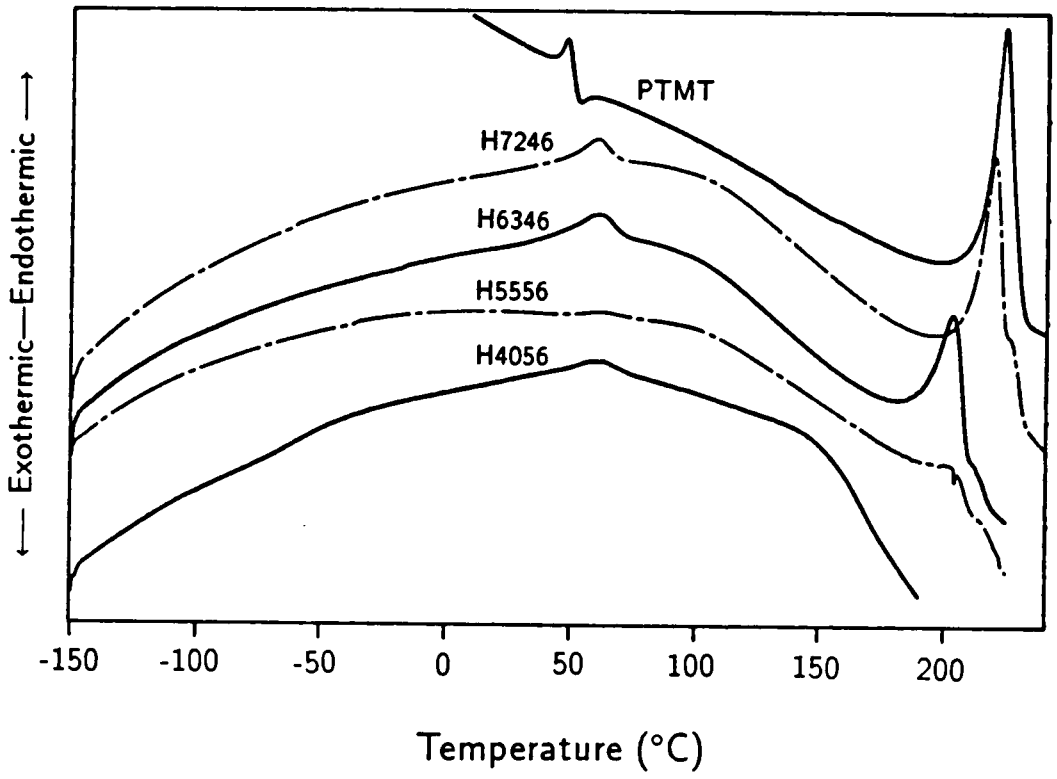


Figure 6.12: DSC traces of filaments spun at 50m/min. There is an endotherm at about 50–60°C in addition to the primary melting peak.

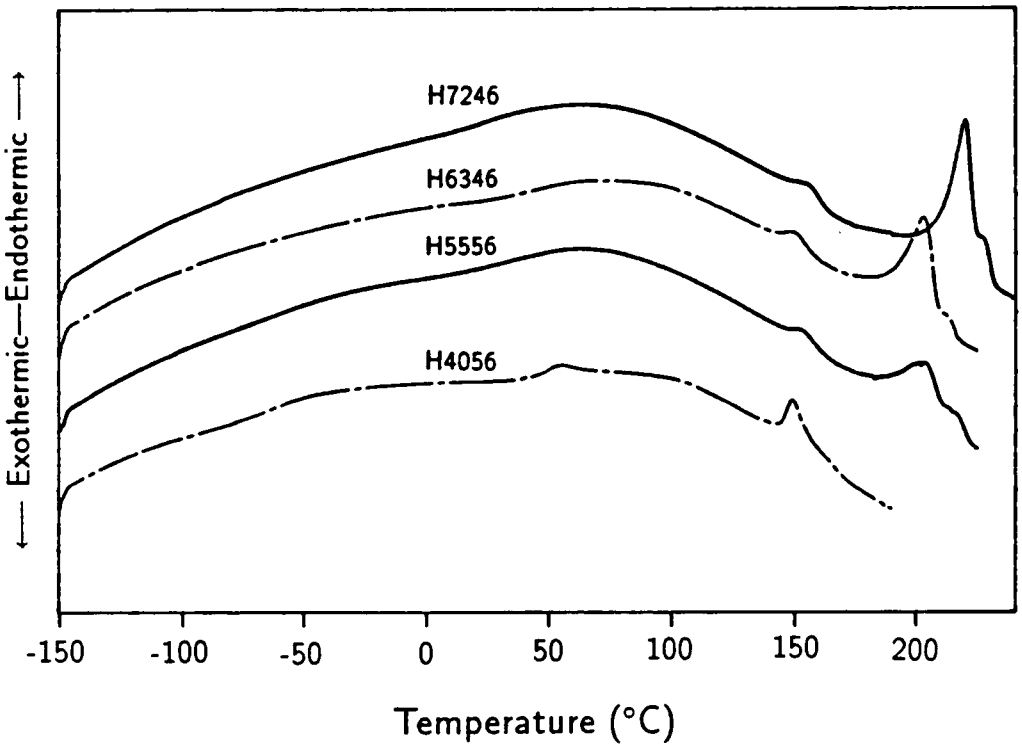


Figure 6.13: DSC traces of filaments spun at 50m/min and annealed at 141°C. The smaller endotherm now appears at about 150°C.

The width of the crystallites in the (100) and (010) crystallographic directions in each composition are shown as a function of annealing temperature in Figures 6.14 and 6.15. These figures show that there is not a great difference between the widths in the directions normal to the (100) and (010) planes. The filaments from H4056 show some increase in crystallite size and perfection as annealing temperature is raised, but seem to be limited to some upper value. The other compositions show much larger changes. In unannealed samples, the dimensions calculated from the (100) and (010) diffraction peaks range from 57Å and 86Å, respectively, in H4056 to 31Å and 26Å in H7246. These dimensions grow to 90Å and 102Å in H4056 after annealing at 141°C, and to 149Å and 109Å in H7246 after annealing at 180°C. Thus, the H7246 crystallites are initially smaller than the ones in H4056, but are able to grow to a larger size upon annealing.

The lateral dimensions of the crystallites are shown as a function of composition at each annealing temperature in Figures 6.16 and 6.17. At 25°and 100°C, the width decreases, in general, as HSC increases. At 25°C, for instance, the widths drop from about 80Å in H4056 to around 30Å in H7246. At the higher annealing temperatures, there appears to be a maximum with respect to composition in the lateral dimensions at about 70 to 80 wt.-% PTMT. This probably results from the different degrees of undercooling experienced by each composition and constraints on the crystallite size. Zhu et al. [222,223] crystallized similar copolyesters from the melt and observed that the spherulites

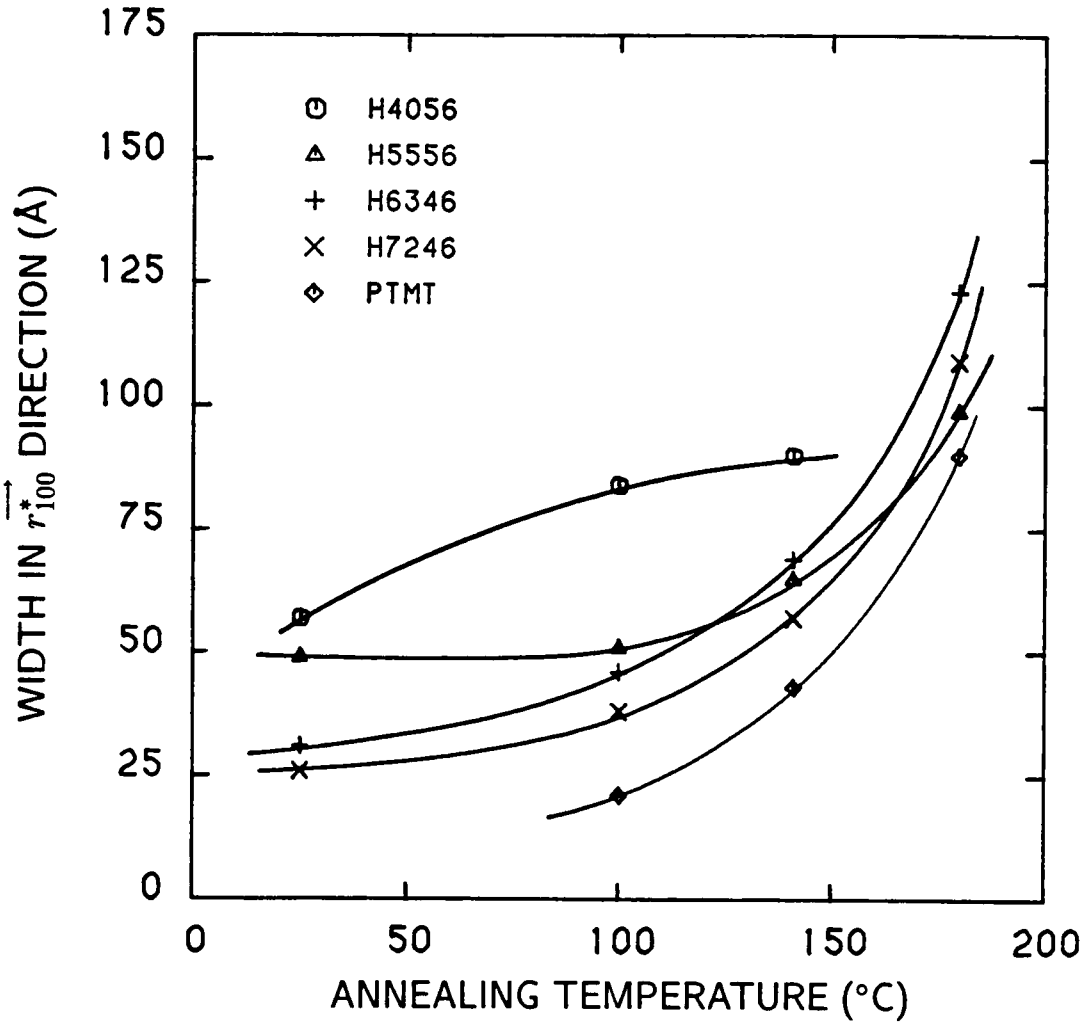


Figure 6.14: Apparent width of the crystallites in the direction normal to the (100) crystallographic planes as a function of annealing temperature. These filaments were spun at 300m/min.

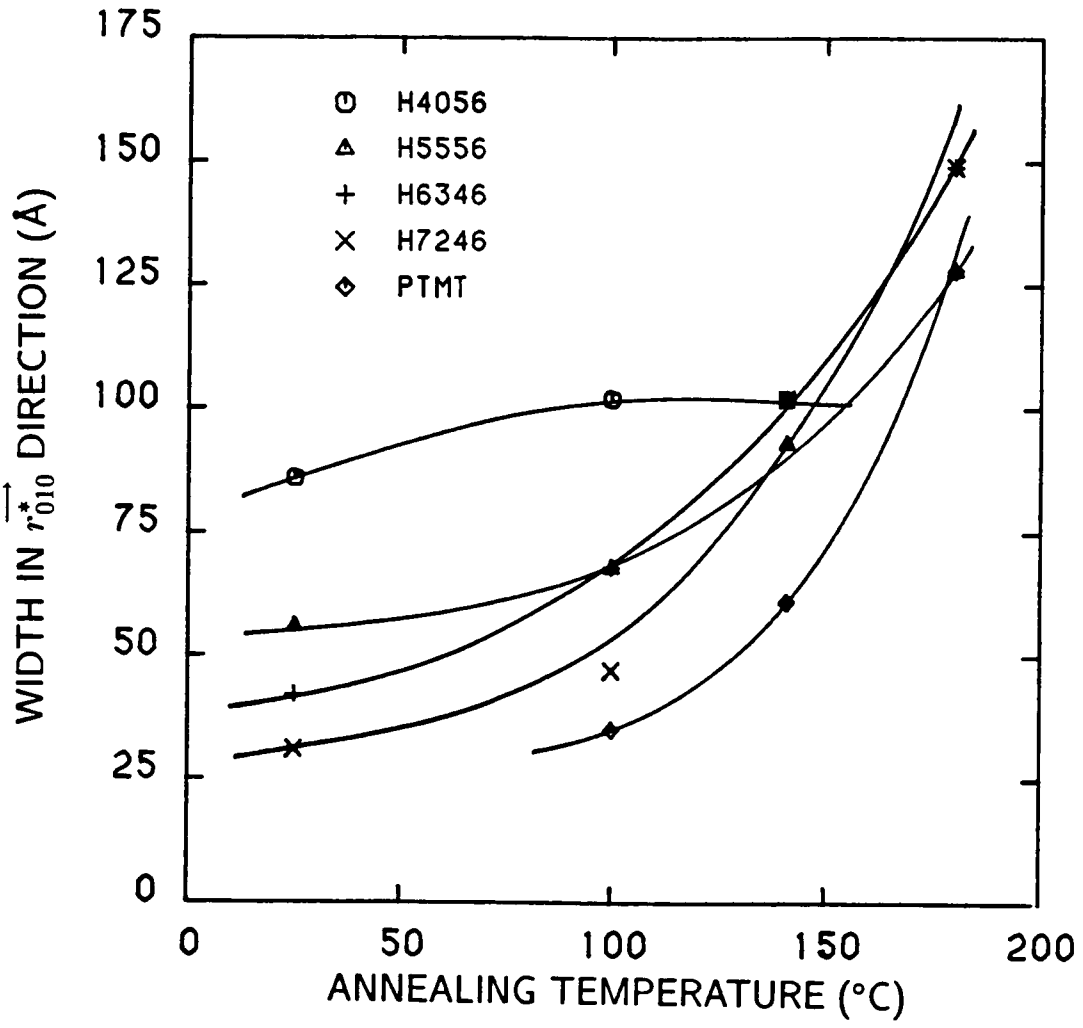


Figure 6.15: Apparent width of the crystallites in the direction normal to the (010) crystallographic planes as a function of annealing temperature.

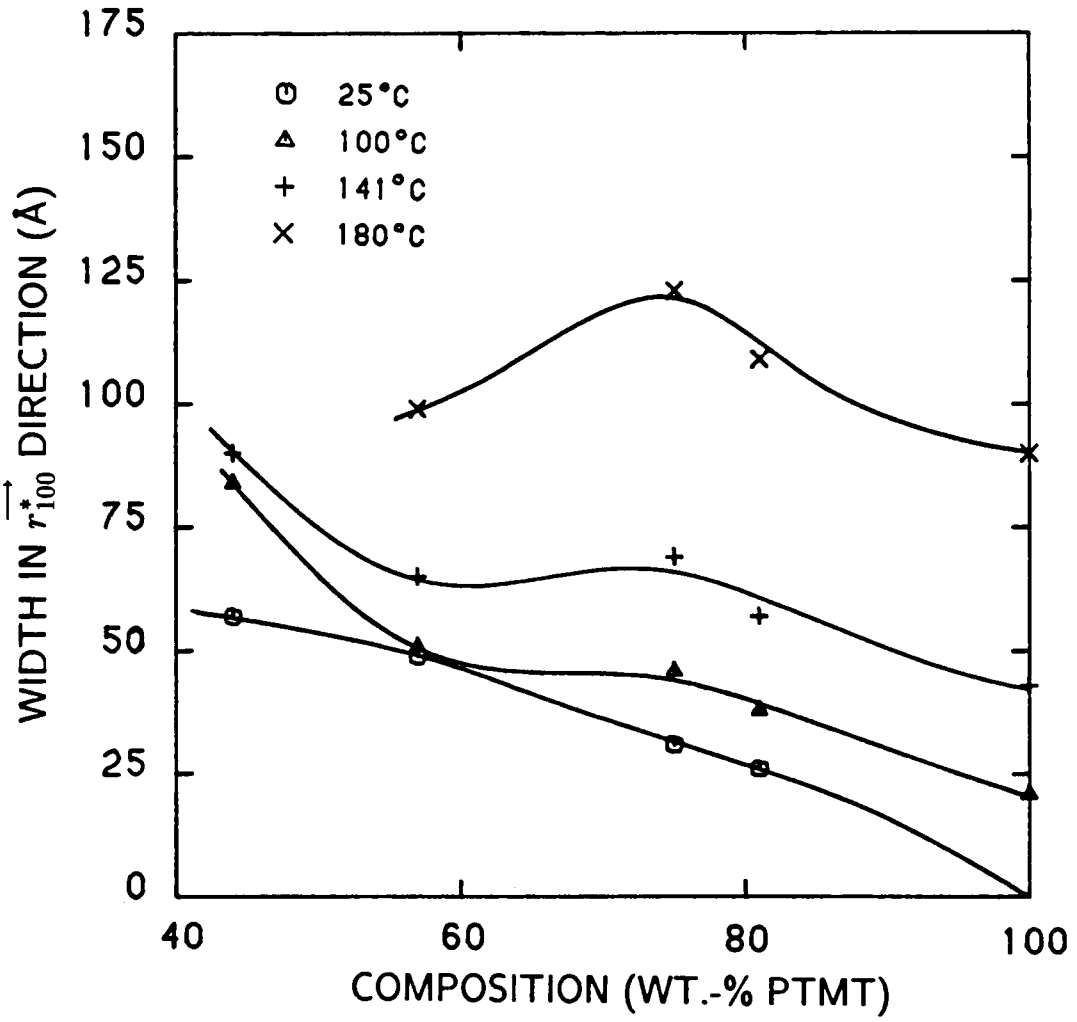


Figure 6.16: Apparent width of the crystallites in the direction normal to the (100) crystallographic planes as a function of composition.

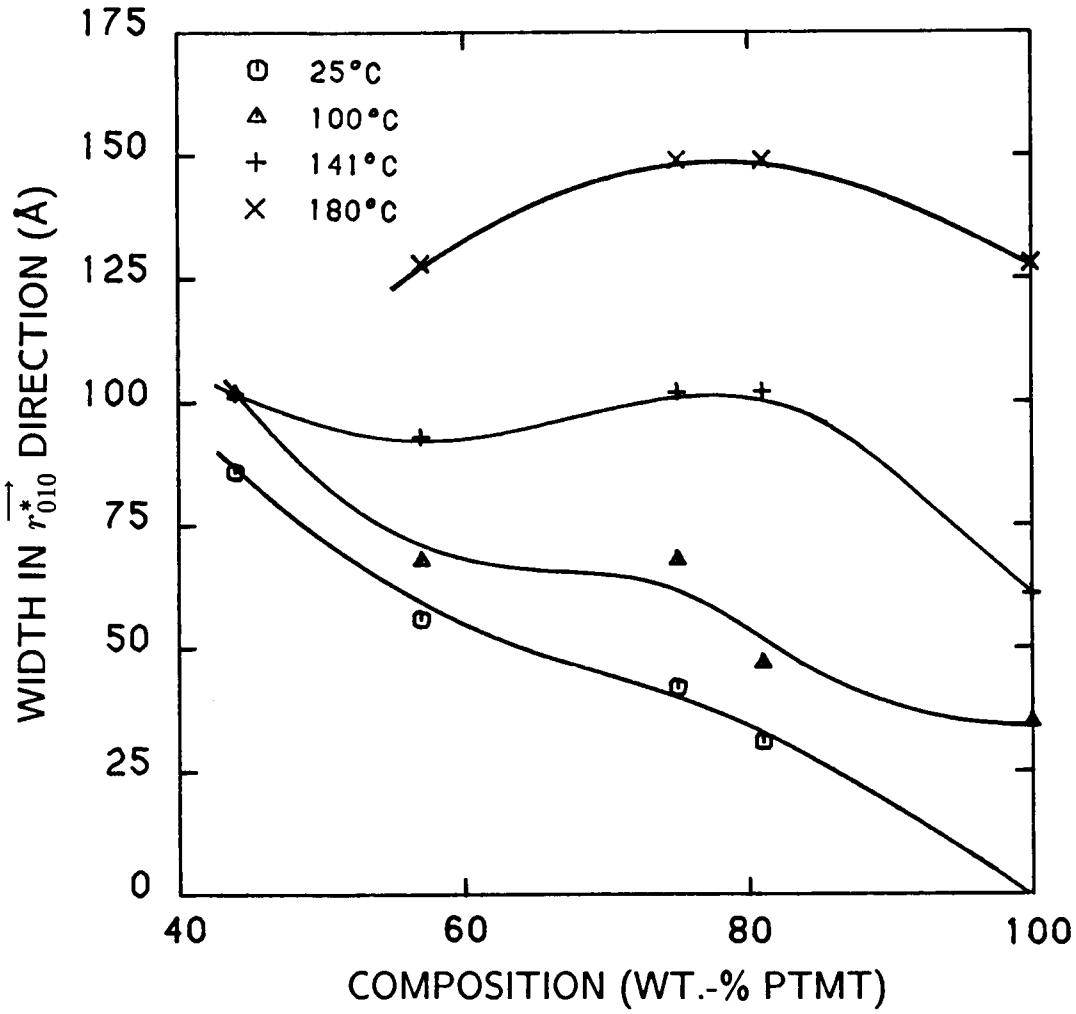


Figure 6.17: Apparent width of the crystallites in the direction normal to the (010) crystallographic planes as a function of composition.

never impinge, but reach a constant size with time that depends on the crystallization temperature.

The thickness of the crystallites is shown as a function of annealing temperature in Figure 6.18. In filaments conditioned at room temperature, the crystallites are around 40Å thick in H4056, H5556, and H6346, and about 32Å in H7246. The PTMT filaments are initially amorphous but crystallize upon annealing. Both homopolymer and copolymer crystallites gradually thicken as annealing temperature is raised. The increases range from about 10Å in H4056 to around 25 or 30Å in the other copolymer samples. Lamellae about 60–75Å thick are produced at 180°C in filaments from all compositions except H4056, which melts. These increases are small compared to those in the direction perpendicular to the chain axis. There is little effect of composition on the thickness at each annealing temperature. At 25°C, the thickness becomes immeasurable at high HSC due to reduced crystallinity. At 100°and 141°C, the thickness is insensitive to composition. At the highest annealing temperature, the thickness decreases slightly as HSC increases. One might expect that the crystallite thickness depends on the degree of undercooling it experiences during annealing as it does for homopolymers [17]. Figure 6.19 shows that when the data are plotted in this manner, the thicknesses of the crystallites from all compositions, except H4056 can be fitted reasonably well to a single master curve. The H4056 seems to be limited in thickness at small undercoolings.

The crystallite dimensions determined in this work are comparable to those reported by others. Buck et al. [34], using transmission electron mi-

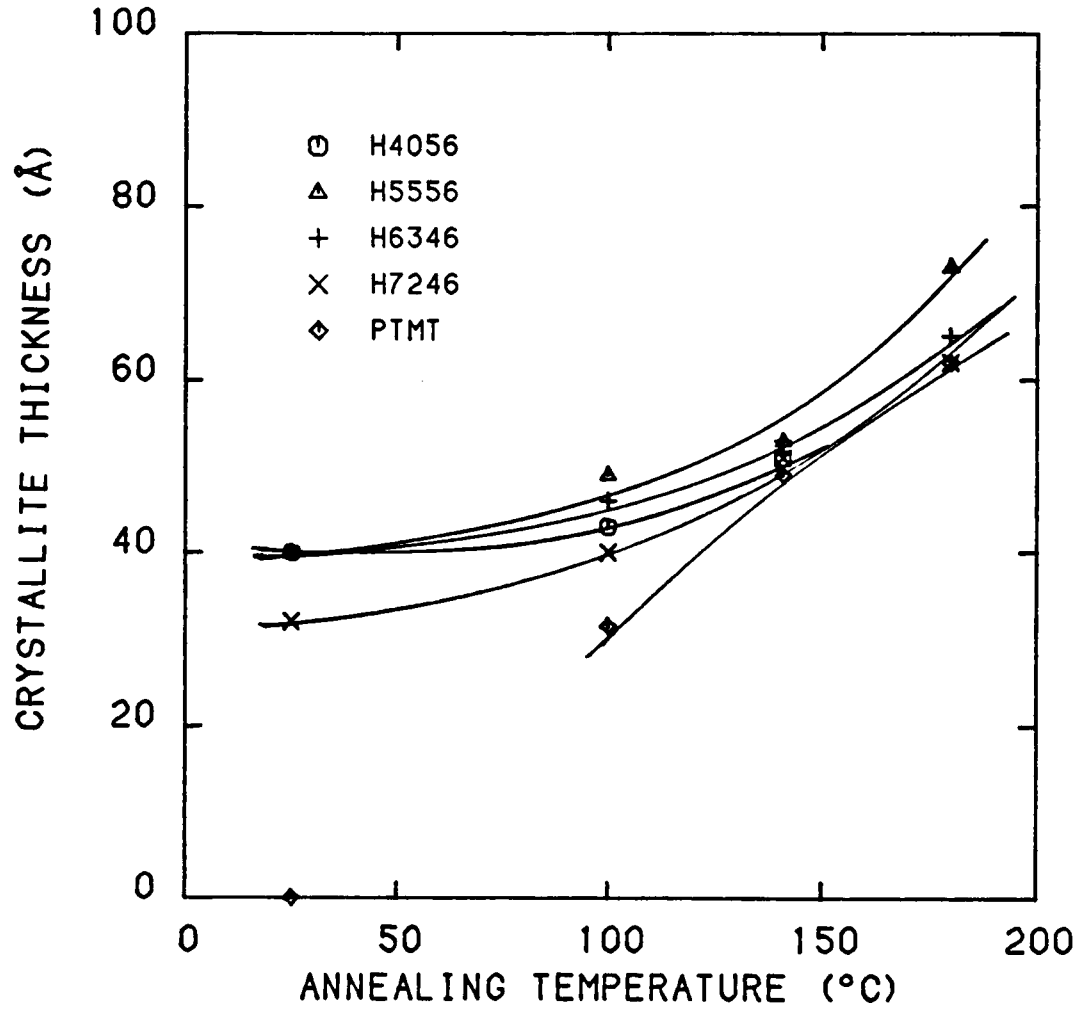


Figure 6.18: Apparent thickness of the crystallites as a function of temperature. The normal to the $(\bar{1}04)$ reflection, which was used to determine the thickness, lies approximately 11.5° from the c-axis direction.

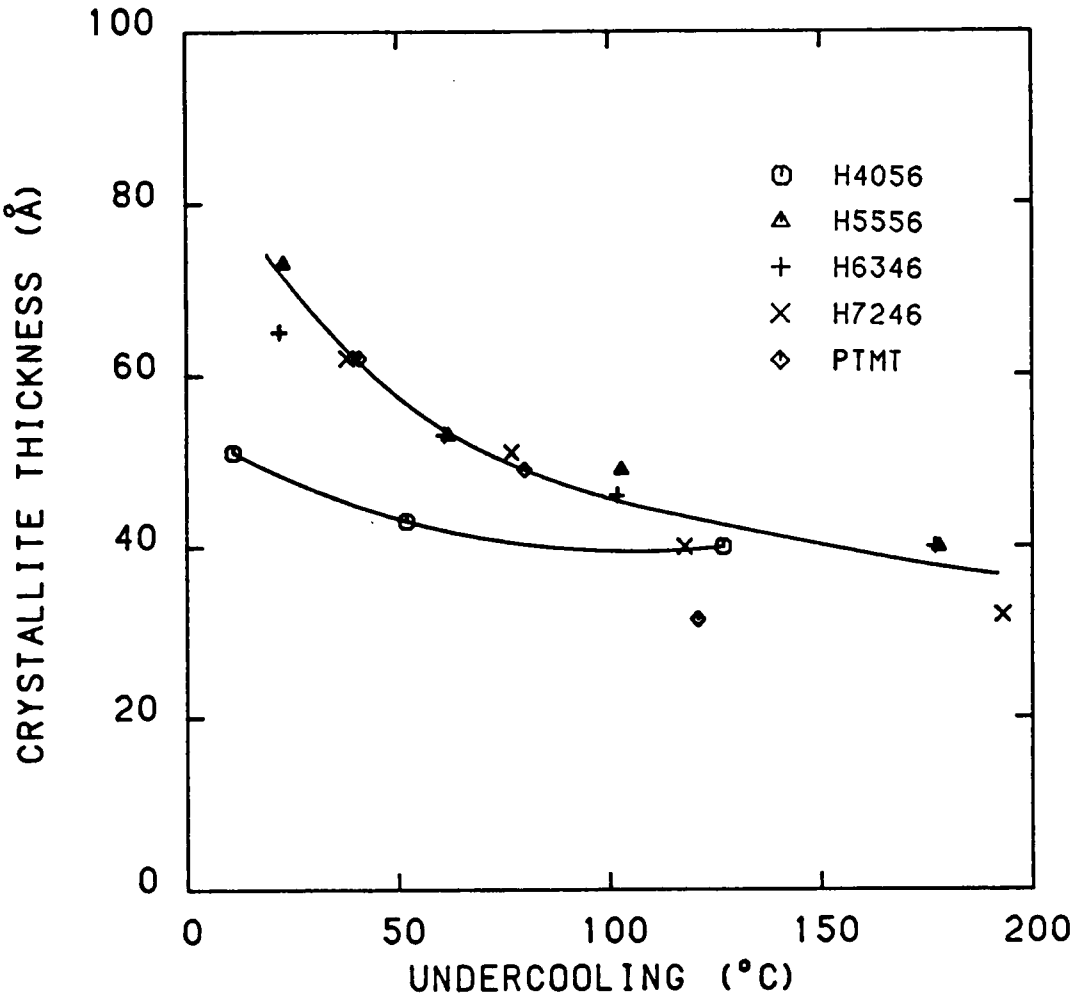


Figure 6.19: Apparent thickness of the crystallites as a function of the degree of undercooling ΔT_u. The thickness of the H4056 crystallites appears to be limited by the short hard segment sequence lengths.

croscopy, report seeing lamellar structures 15–25Å thick by 100–300Å wide in isotropic samples quenched from the melt. In oriented, annealed samples, they calculate an average crystallite size of 55Å in the fiber direction using WAXD data. Bandara and Droscher [16], using SAXS techniques, calculate crystallite thicknesses of around 35 to 45Å in copolyester-ether sheets quenched from the melt and subsequently annealed.

A volume index for the crystallites can be calculated using Equation 3.7 from Chapter 3. This technique does not provide absolute values but is useful for following changes in the average crystallite size. Figure 6.20 is a plot of the crystallite size index as a function of undercooling. Annealing at undercoolings less than 100°C causes a dramatic increase in the crystallite size/perfection in filaments from all the compositions except H4056. The increases in size result primarily from growth in the equatorial directions of the crystallites rather than from a thickening process. Figure 6.21 shows that the total crystallite size index decreases, in general, at the lower temperatures as HSC increases. In filaments annealed at 180°C there is a distinct maximum in size at about the composition of H6346.

The long period in these samples ranged from 88 to 177Å depending on the composition and annealing temperature. In as-spun filaments, the long period is virtually independent of SDR as shown in Figure 6.22. Samples spun at 250 or 300m/min were annealed at several temperatures. The long period in filaments from all compositions increases upon annealing, as shown in Figure 6.23. The change becomes more pronounced as HSC decreases. The

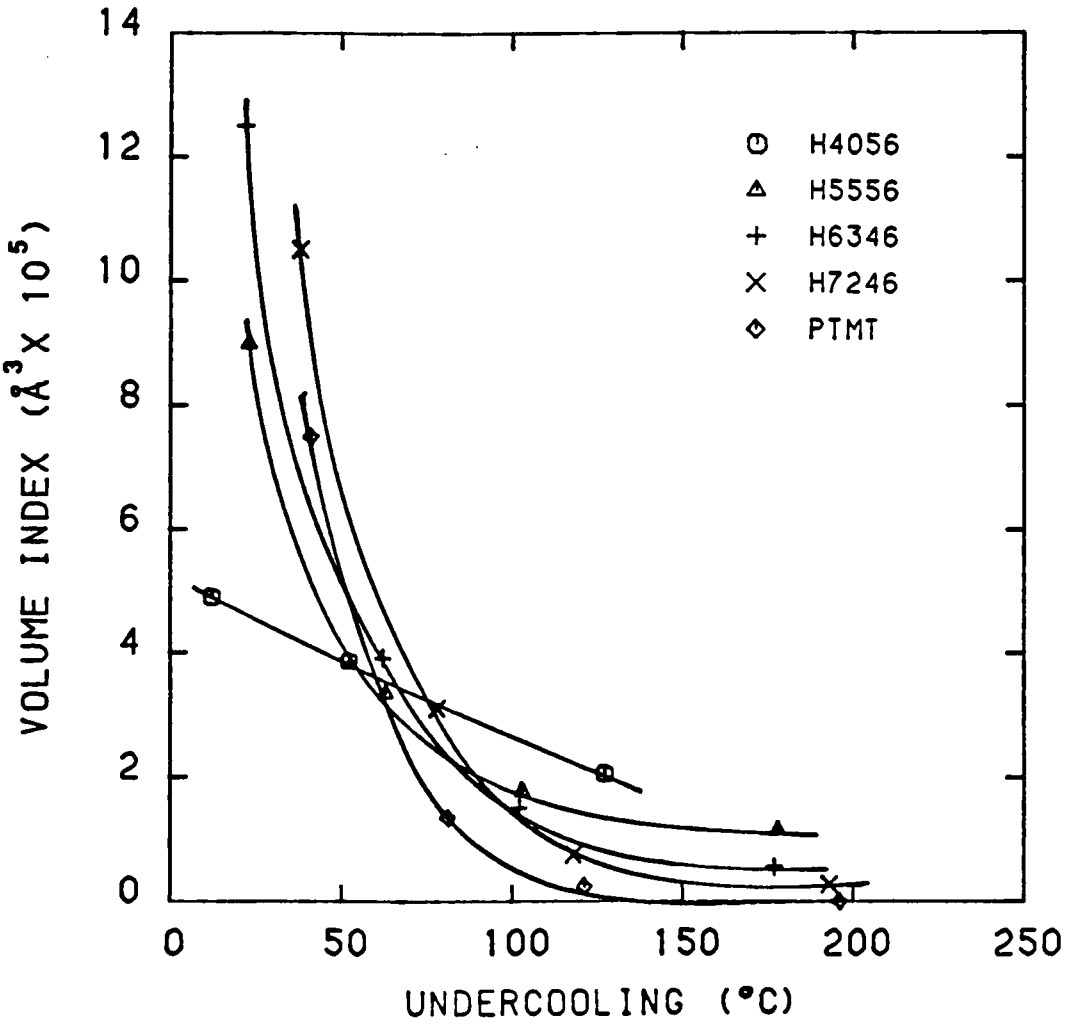


Figure 6.20: Apparent size of the crystallites as a function of the degree of undercooling ΔT_u.

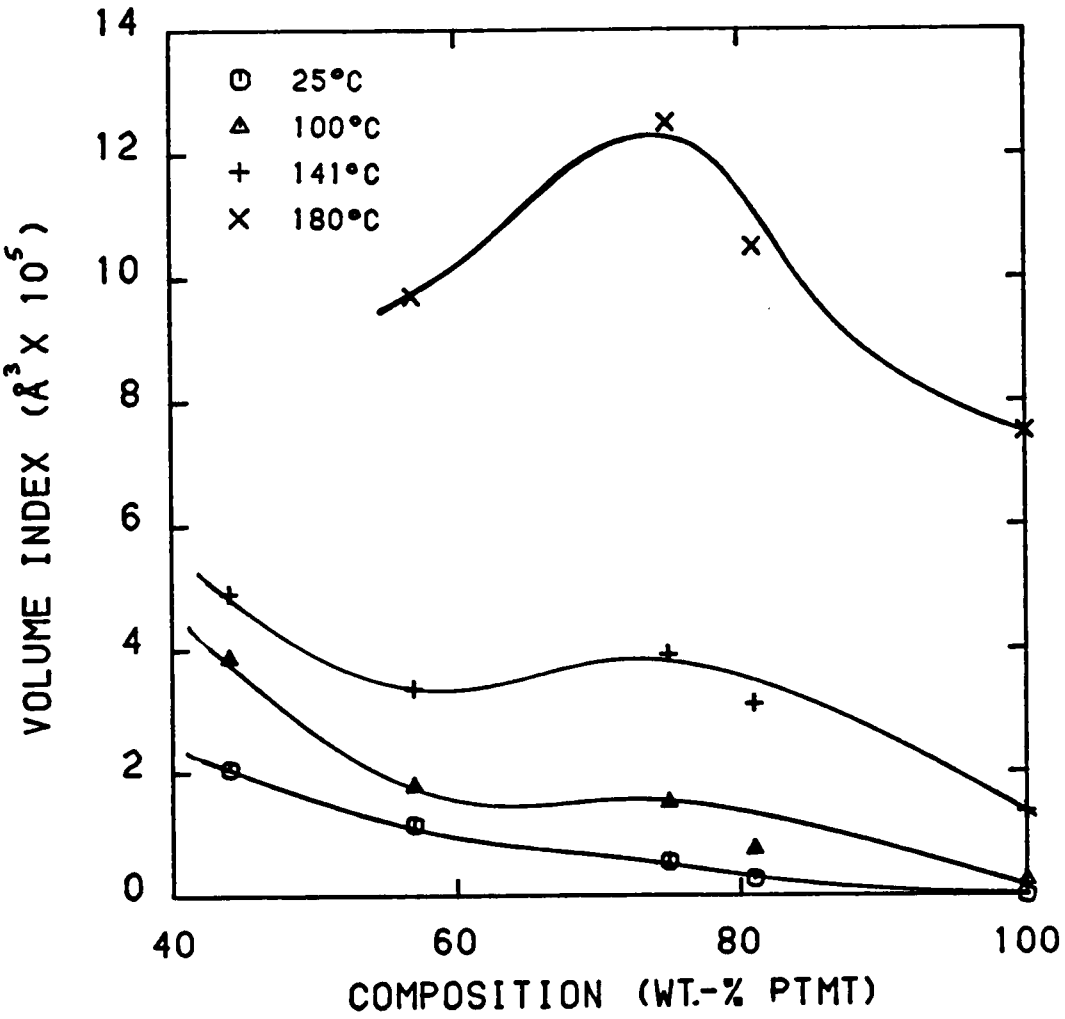


Figure 6.21: Apparent size of the crystallites as a function of composition at each annealing temperature.

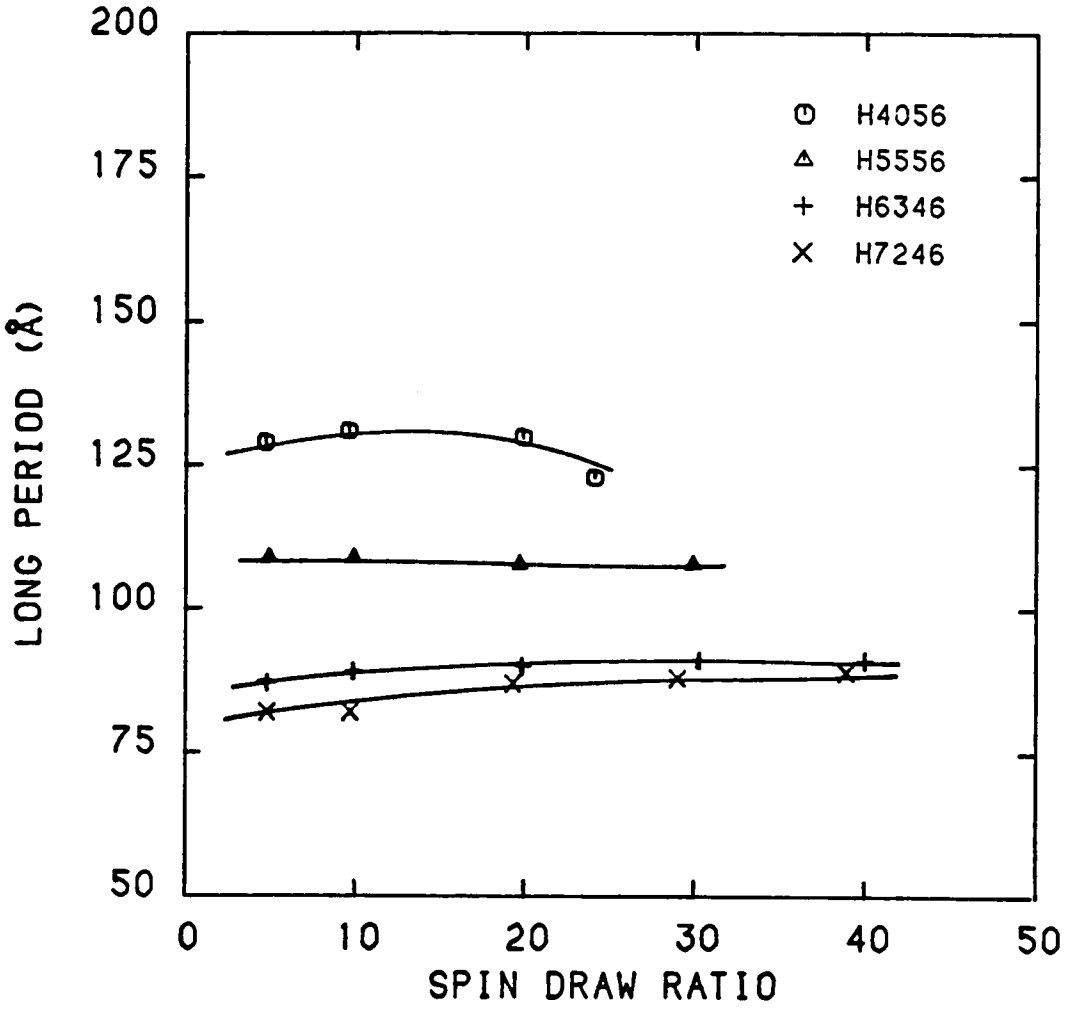


Figure 6.22: Long period of the as-spun filaments as a function of the spin draw ratio.

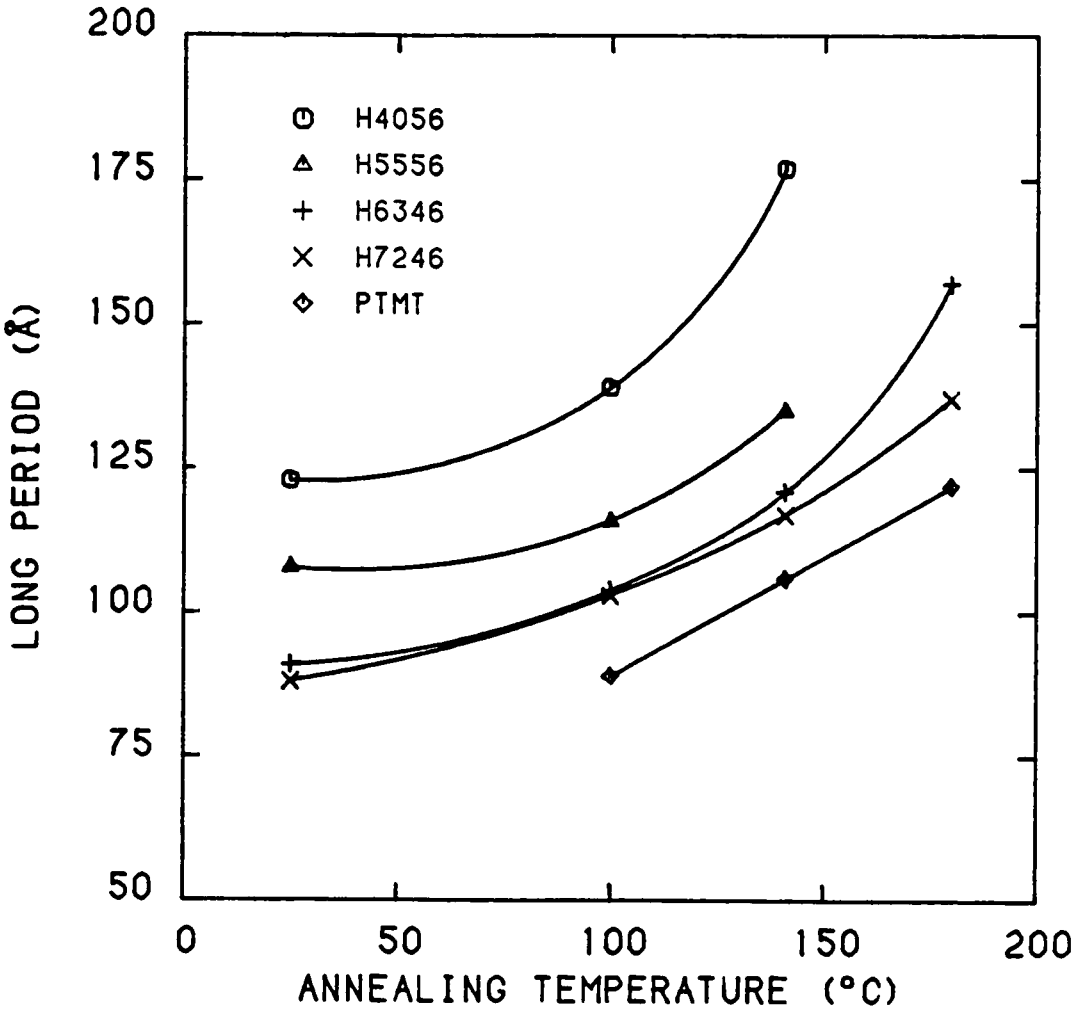


Figure 6.23: Long period of the filaments spun at 300m/min as a function of annealing temperature.

long period in the H4056 filament increases from 123Å at room temperature to 177Å after annealing at 141°C, a difference of 54Å. The long period in the H7246 filament increases from 88Å to 117Å upon annealing at the same temperature; a change of only 29Å. The as-spun PTMT filament is amorphous, but develops a long period of 89Å at 100°C. This increases to 122Å after annealing at 180°C.

The effect of composition on long period is shown more clearly in Figure 6.24. The long period decreases as HSC increases, with the change becoming more pronounced as the annealing temperature is raised. At 25°C, the long period decreases from about 123Å in H4056 (44 wt.-%) to about 88Å in H7246 (72 wt.-%); a substantial change. After annealing at 141°C, long periods range from 177Å in H4056 to 106Å in the PTMT homopolymer.

If the data are plotted as a function of undercooling as shown in Figure 6.25, there is still a strong effect of composition. The copolymers lowest in HSC still exhibit the highest long period. Thus, the long period is not affected much by the SDR, but increases in general with either decreasing HSC or undercooling.

The increase in long period with annealing temperature was previously noted by Buck et al. [34] who report long period spacings of 98Å to 168Å in a 57.5 wt.-% composition annealed at several temperatures between 25°and 167°C. They attribute the increase in spacing upon annealing to a thickening of the lamellae. Wegner et al.[195] report long periods of 100Å to 275Å in compression molded films from several compositions which were quenched from the

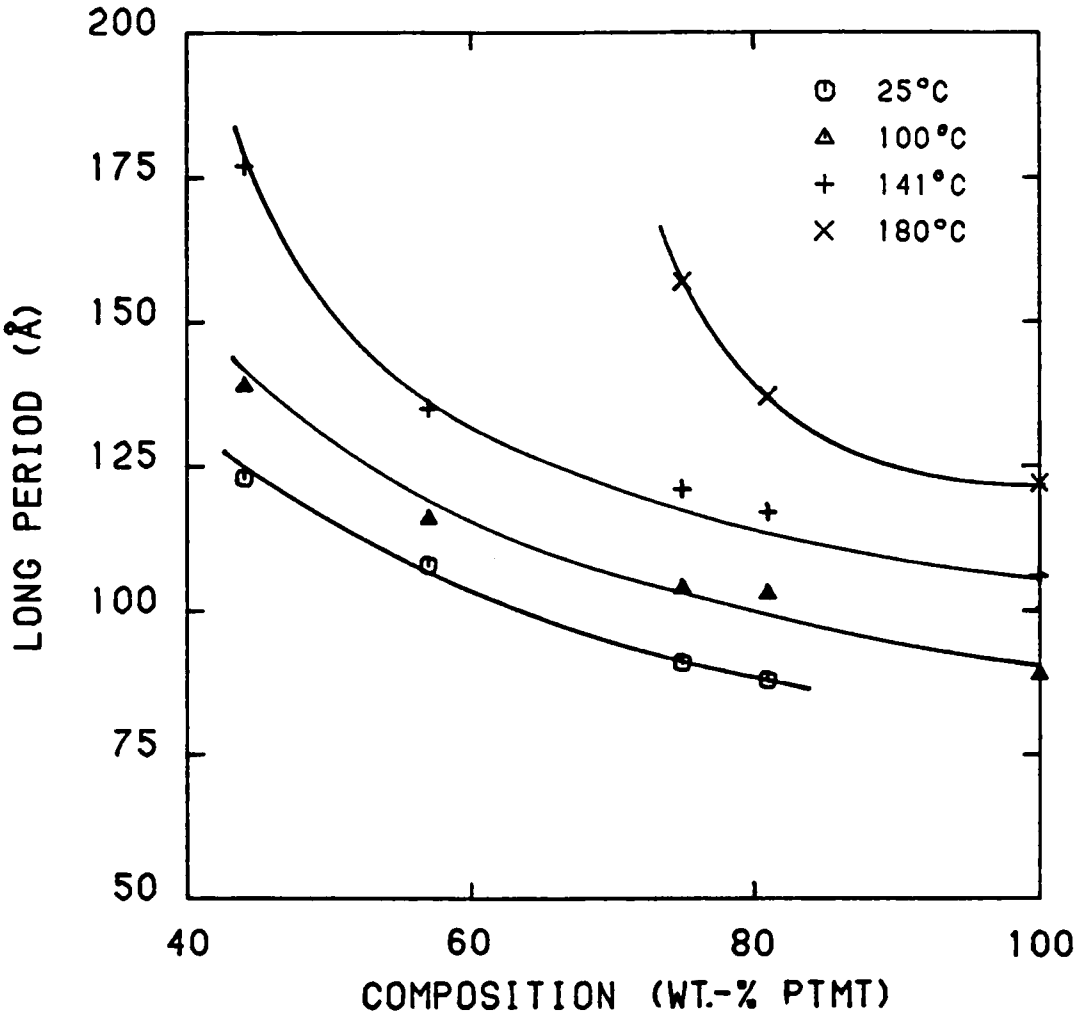


Figure 6.24: Long period of the filaments spun at 300m/min as a function of composition at each annealing temperature.

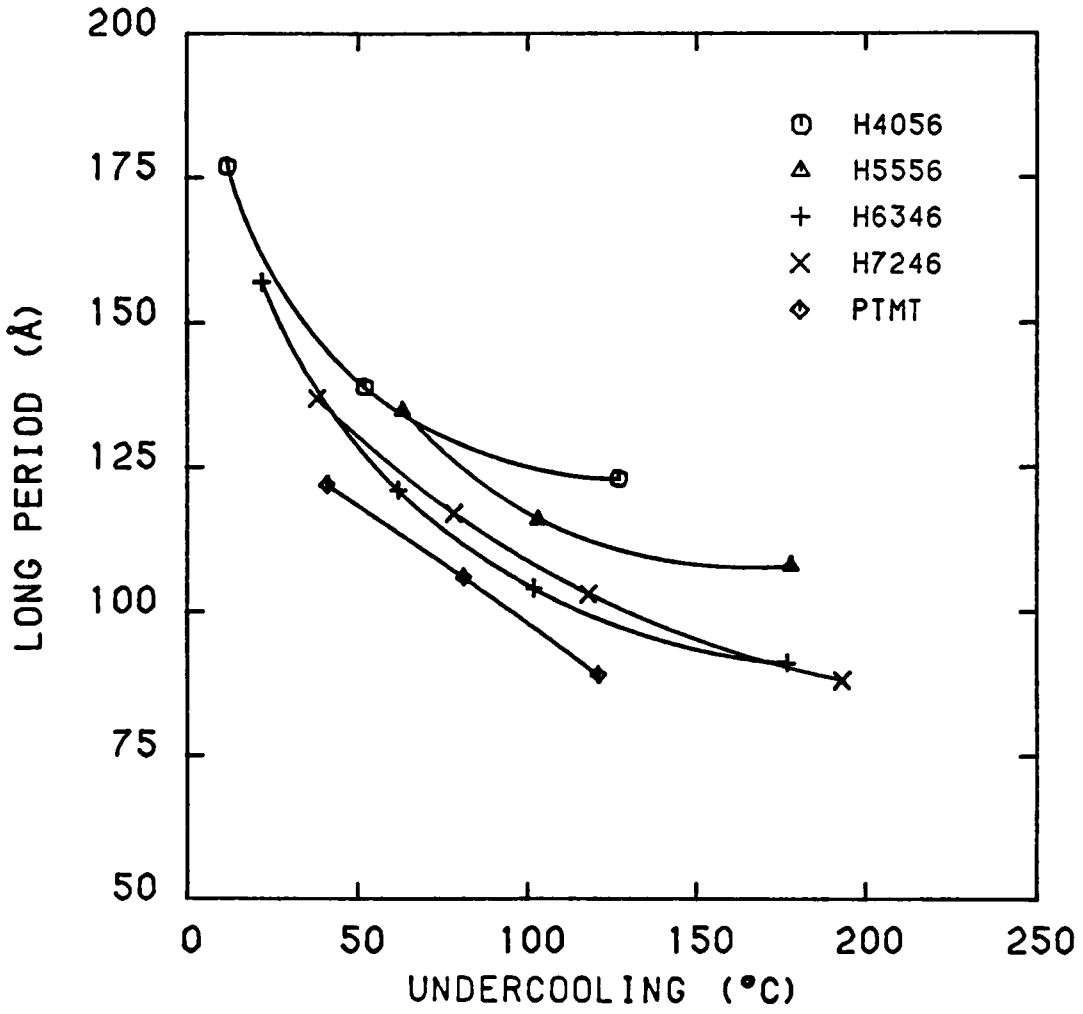


Figure 6.25: Long period of the filaments spun at 300m/min as a function of the degree of undercooling ΔT_u.

melt in ice water and annealed at temperatures between 150 and 210°C. They are surprised to see a long period of 250Å in a sample having an average hard segment length of only about 4 units, even though it has been annealed very close to its melting temperature. Neither hard nor soft segment length seemed to have much effect on the long period if it was plotted as a function of undercooling. They report a large increase in the long period upon annealing but are unable to reconcile this with the microstructure. They don't believe chain folding and thickening are enough to explain the observed increase. They point out that several sequences of hard and soft blocks are necessary to bridge the gap between adjacent lamellae. Zhu and Wegner [223] conclude from their studies that the crystallites remain at constant thickness during annealing while the space between the lamellae increases in inverse proportion to the undercooling. However, they do not propose a mechanism for this behavior.

6.2 Discussion of Structure

The PTMT filaments obtained by spinning into water are amorphous. The copolymer filaments are quenched under the same conditions, and since the crystallization rate has been shown to decrease as HSC decreases, it is unlikely that much crystallization of the PTMT segments can occur before the filaments reach the quench temperature. Since the long period and the degree of phase separation are virtually independent of SDR for a given composition, crystallization appears to occur at the same temperature and to the same

extent regardless of SDR. For these reasons it is believed that most if not all of the crystallization takes place after quenching. "Stress induced crystallization" does not appear to play a significant role in the crystallization behavior of these filaments.

The degree of phase separation in the quenched filaments decreases as HSC increases. This may be explained by the broad glass transition region of these copolymers. Rheovibron curves for two compositions were shown in Figure 6.2. It is believed that the higher temperature portion of the transition region is due to the longer sequences. The longer hard segments are quenched to a point below their individual T_g in the water bath and are unable to crystallize. The fraction of sequences with T_g less than the quench temperature increases as hard segment content decreases, thus increasing the amount of crystallization that can occur at this temperature.

Annealing produces large increases in the DPS and the size of the crystallites in all compositions except H4056, which shows only moderate increases. WAXD experiments show that growth takes place primarily by the addition of chain stems to the equatorial surfaces of the crystallites. The H4056 composition reaches a relatively high level of phase separation and has fairly well developed crystallites after aging at room temperature. Further crystallization is apparently limited by the low concentration of crystallizable hard segments in the amorphous phase. As the HSC (and sequence length) of the other compositions increases, the fraction of segments short enough to crystallize at the quench temperature goes down and as a result, the DPS decreases as HSC

increases. Therefore, annealing is necessary to produce high levels of phase separation in these filaments. The higher the HSC and average sequence length, the higher the annealing temperature required to reach a given DPS.

These results suggest that the phase separation behavior of different compositions may be tied together by the degree of undercooling each composition experiences during annealing. However, when the DPS of different compositions is plotted as a function of ΔT_u as previously shown in Figure 6.11, the data do not all fall on a single line as would be expected. The data points tend to converge at low undercoolings, but at high undercoolings, the DPS still decreases as HSC increases. It is believed that only the shorter sequences are able to diffuse to the growth front and crystallize at high undercoolings [16]. Since the compositions low in HSC contain a greater fraction of shorter PTMT sequences and a lower T_g, a greater proportion of the hard seqments are able to crystallize at high undercoolings.

The crystallites formed upon quenching are able to thicken upon annealing just as the homopolymer does. The variation with composition seems to be related to an undercooling effect. When plotted as a function of ΔT_u (refer to Figure 6.20), the thickness of crystallites in all compositions, except H4056, can be described reasonably well by a single line. The thickness increases smoothly as ΔT_u decreases, just as in the case of homopolymers. The PTMT crystallites, however, are somewhat smaller than those of the other compositions at high undercooling due to low crystallinity. The comparatively

high glass transition temperature of PTMT does not allow much crystallization to occur at the low temperatures.

The H4056 crystallites do not thicken at low ΔT_u as much as the other compositions. This may be explained by the short average hard segment length in this composition, which is around 4–6 units [37]. Since the PTMT repeat distance is about 11Å, the corresponding crystallite thickness would be about 44 to 66Å. This is about the size achieved by the H4056 crystallites at 11°of undercooling as was shown in Figure 6.20. Judging from the other compositions, a thickness of about 75Å would be expected at this undercooling. Apparently, there are not enough sequences of sufficient length in H4056 to form many crystals of this thickness.

These results show that the thickness depends primarily on the degree of undercooling and is not too sensitive to composition except when the sequence length is shorter than the optimum needed by the growing crystal or when the composition is close to its glass transition temperature.

In those compositions with hard segments long enough for chain folding to occur, existing crystallites may thicken in much the same manner as homopolymers. But, it is more likely that the increase results from longer chain stems being added to the growth front. Since H4056 has relatively short hard segments one would expect its thickness in the c-axis direction to be limited as was shown to be the case above. As hard segment length increases, the upper limit of crystallite thickness increases accordingly.

The WAXD experiment shows the crystallite thickness in annealed sam-

ples does not vary greatly with HSC, while SAXS shows a decrease in the long period as HSC increases. Since the changes in the crystallite thickness alone cannot account for the change in long period, the thickness of the amorphous phase must vary with HSC. If one assumes a model of the structure in which the lamellae are stacked parallel to one another, then $L = L_a + L_c$ and the thickness of the amorphous layer is merely the long period minus the crystallite thickness. The variation in thickness of the amorphous layer with composition is shown in Figure 6.26. In general, the distance between lamellae increases as as HSC decreases. Thus, the large long periods observed for compositions low in HSC are a result of the thick amorphous layer. A model of the structure consistent with the observed results is shown in Figure 6.27.

The long period increases greatly in these materials upon annealing. WAXD shows some increase in the crystallite thickness upon annealing, but in most compositions, this is not enough to account for the large increase in long period. As shown in Figure 6.28, the thickness of the amorphous layer in the copolymers must increase as the degree of undercooling is reduced. The amount of the increase grows larger as HSC increases. One may wonder by what mechanism the amorphous regions are able to thicken by such large amounts.

There is some evidence to suggest that some of the crystallites formed at the quench temperature may melt during annealing. Figures 6.12 and 6.13 showed the DSC curves of H4056 samples before and after annealing at 141°C. The as-spun filament has a broad melting peak starting at about 100°C and

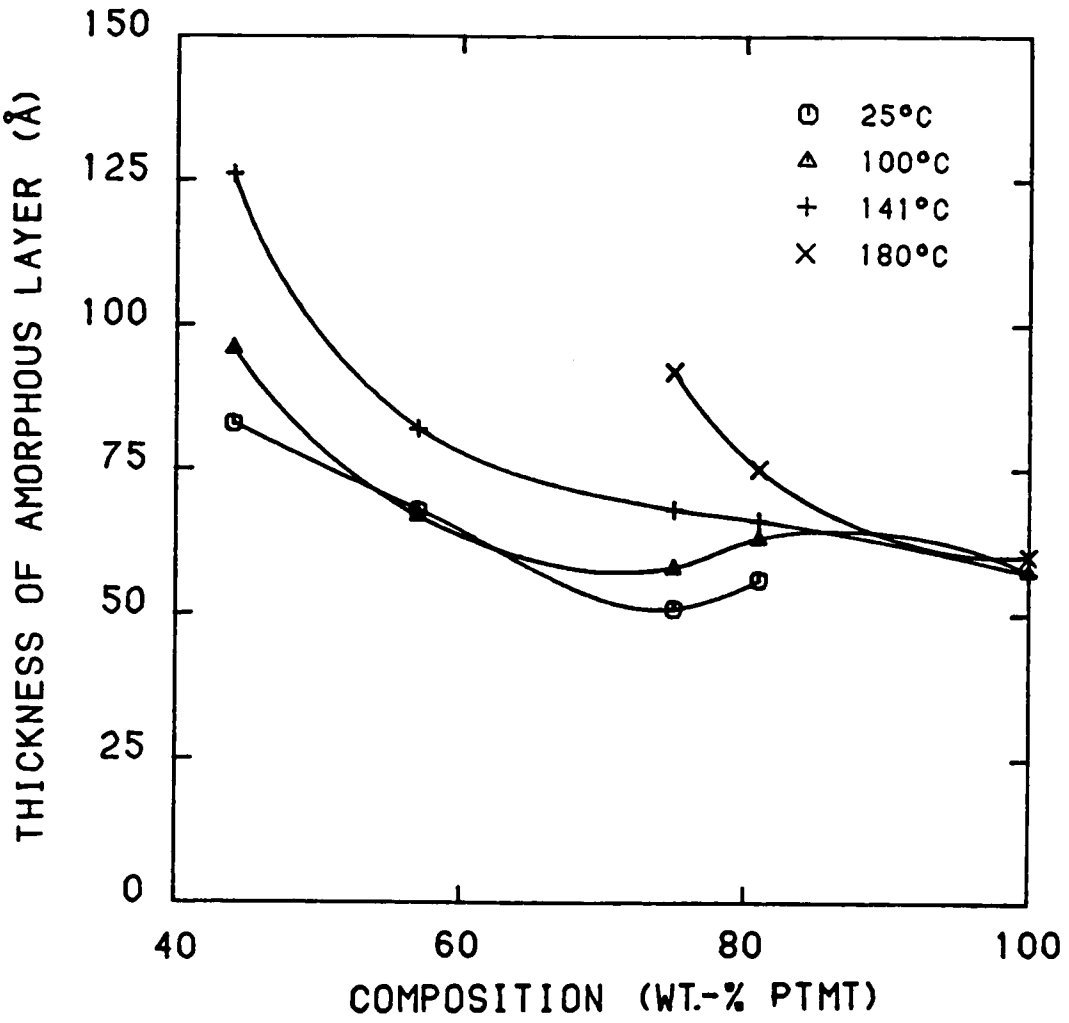


Figure 6.26: Thickness of the amorphous layer as a function of composition and annealing temperature.

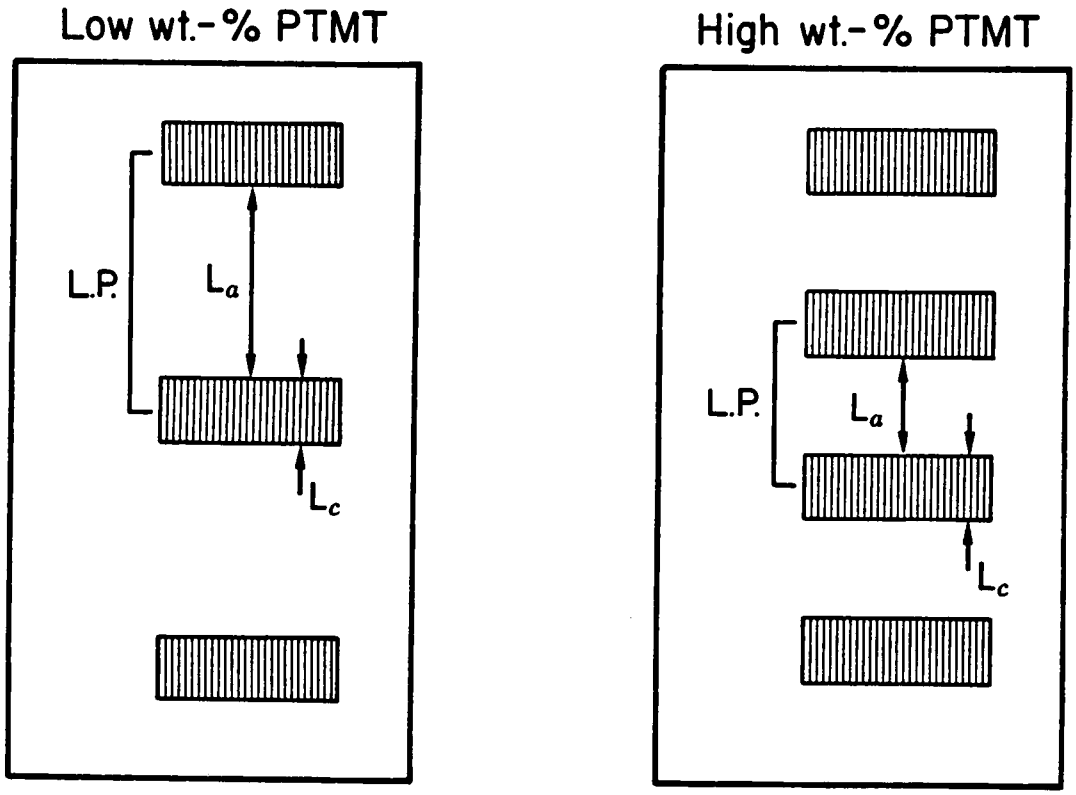


Figure 6.27: Model of the domain structure explaining the effect of composition on the long period.

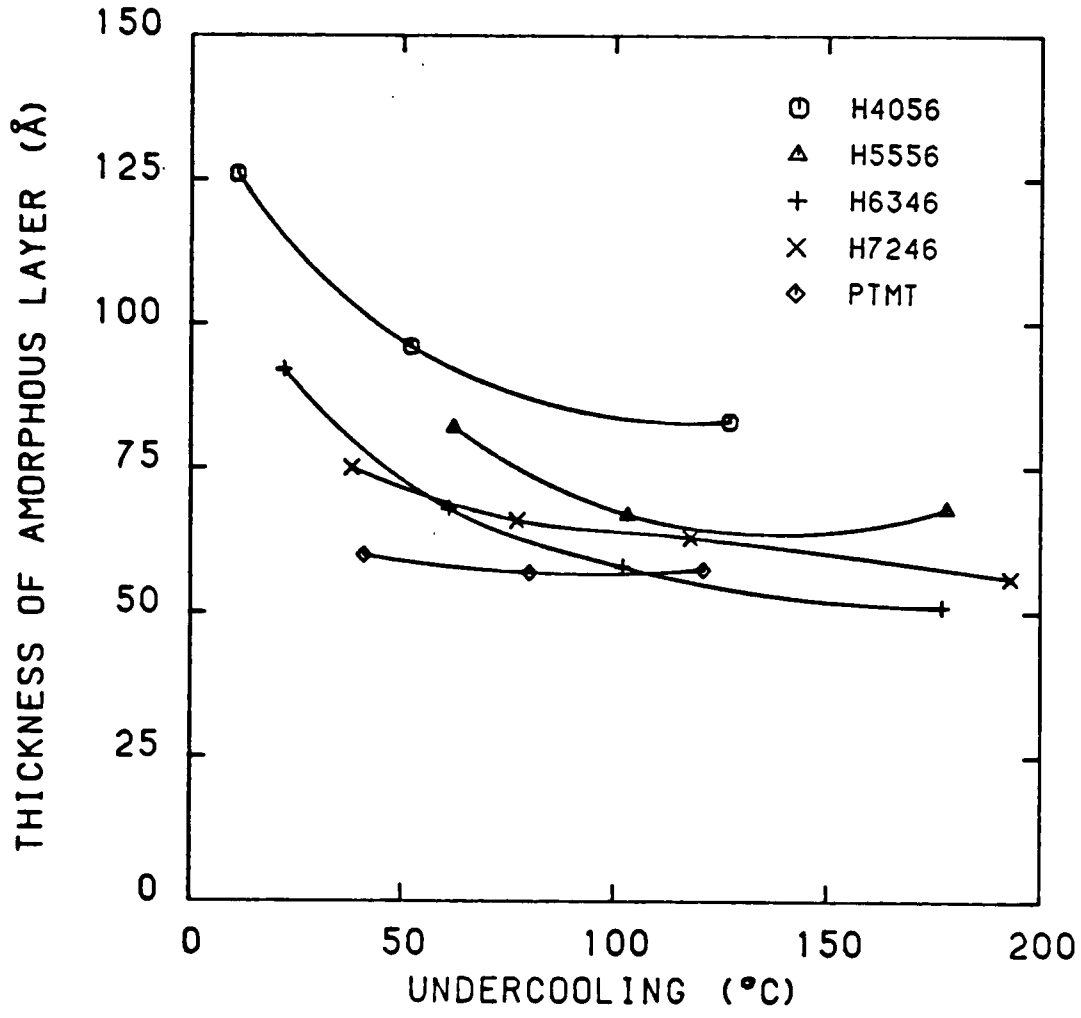


Figure 6.28: Thickness of the amorphous layer in filaments spun at 300m/min as a function of the degree of undercooling ΔT_u.

ending around 175°C; an indication that there is a broad distribution of crystallite shapes and sizes. After annealing, the part of the melting peak below T_a disappears while the part above T_a intensifies. Apparently, there is a population of crystallites with $T_m < T_a$ that melts upon annealing. The population with $T_m > T_a$ grows during annealing at 141° C, producing the sharp peak observed around 150°C. The low melting crystallites are probably made up of the shorter hard segments, while the higher melting crystallites consist of longer segments.

Since the remaining crystallites are larger and further apart, the amorphous layer is, in effect, thicker. A model of the structural changes which occur upon annealing is shown in Figure 6.29 for a composition low in HSC. As HSC increases, more of the increase in long period can be attributed to a thickening of the lamellae.

6.3 Conclusions

The filament microstructure consists of small lamellar-like crystallites dispersed in an amorphous matrix. The crystallites become more closely spaced as HSC increases, and more highly oriented as SDR increases. No appreciable orientation of the amorphous phase could be detected in the as-spun filaments.

The degree of phase separation in the quenched filaments decreases as HSC increases. Only the shorter sequences are believed to crystallize at the bath temperature (~26.5°) because of the high degree of undercooling. An-

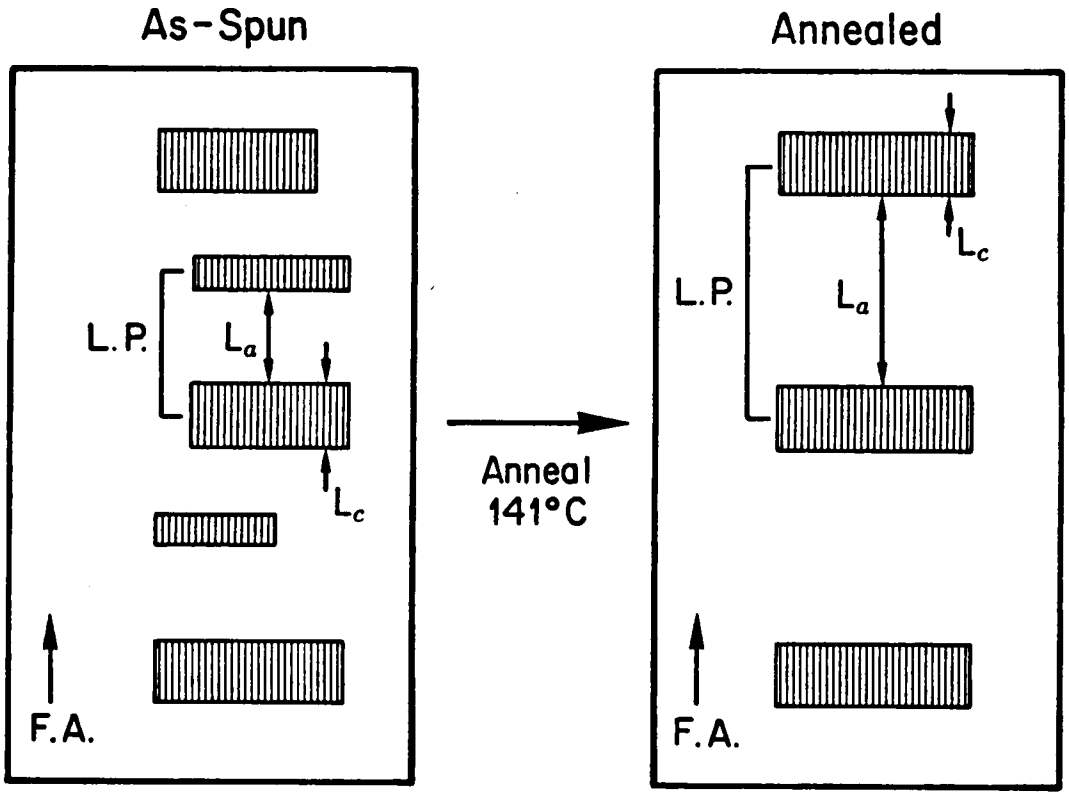


Figure 6.29: The smaller crystallites which form at room temperature are believed to melt at the higher annealing temperature.

nealing produces large increases in the DPS and the size of the crystallites in all compositions except H4056, which reaches a relatively high level of phase separation and has fairly well developed crystallites after aging at room temperature. During annealing at small ΔT_u, the longer sequences are able to diffuse to the growth front and crystallize.

In compositions high in HSC, the crystallites are able to thicken upon annealing just as in the homopolymer. The thickness depends primarily on the degree of undercooling and is not too sensitive to composition except when the sequence length is shorter than the optimum needed by the growing crystal. The crystallites grow primarily by the addition of chain stems to their equatorial surfaces.

The large increase in the long period of some of the copolymers upon annealing can not be explained by an increase in the thickness of the crystallites alone. The thickness of the amorphous layer in the copolymers must also increase as the degree of undercooling is reduced. There is evidence that the smaller crystallites, which probably form from shorter sequences, melt during annealing. The net effect is that only larger more widely spaced crystallites are left after annealing.

Thus, fractionation according to sequence length may occur during crystallization and annealing. Only a portion of the sequences are able to crystallize at any given degree of undercooling. Long hard segments diffuse very slowly at high undercooling, while crystallites composed of short sequences are thermodynamically unstable at low undercoolings. The highest DPS may be achieved

by crystallizing or annealing at low ΔT_u, and then cooling the sample slowly to the end use temperature. Both long and short segments would be crystallized in this manner.

CHAPTER 7

MODULUS-STRUCTURE RELATIONSHIPS

In this chapter, the moduli of the various filaments are presented followed by an analysis of modulus–structure relations. A model of the structure is presented that is consistent with the observed mechanical properties.

7.1 Modulus Results

The moduli of the as–spun filaments are shown as a function of SDR and composition in Figure 7.1. The modulus increases slightly with increasing SDR as a result of the higher levels of hard segment orientation, but this appears to be a second order effect. The modulus increases greatly, however, as the HSC increases. This is not surprising considering the modulus of PTMT is much higher than that of PTMEG. The exact mechanism for the increase is not clear from these results alone. The increase could be due to a greater degree of cross-linking of the soft segments or it could signify a change in morphology from a continuous amorphous phase to a continuous crystalline phase.

The effects of annealing on the modulus of filaments spun at 250 to 300 m/min are shown in Figure 7.2. The modulus of filaments spun from the PTMT homopolymer increases as the annealing temperature is raised. This is common for semi-crystalline homopolymers and is explained by the transfor-

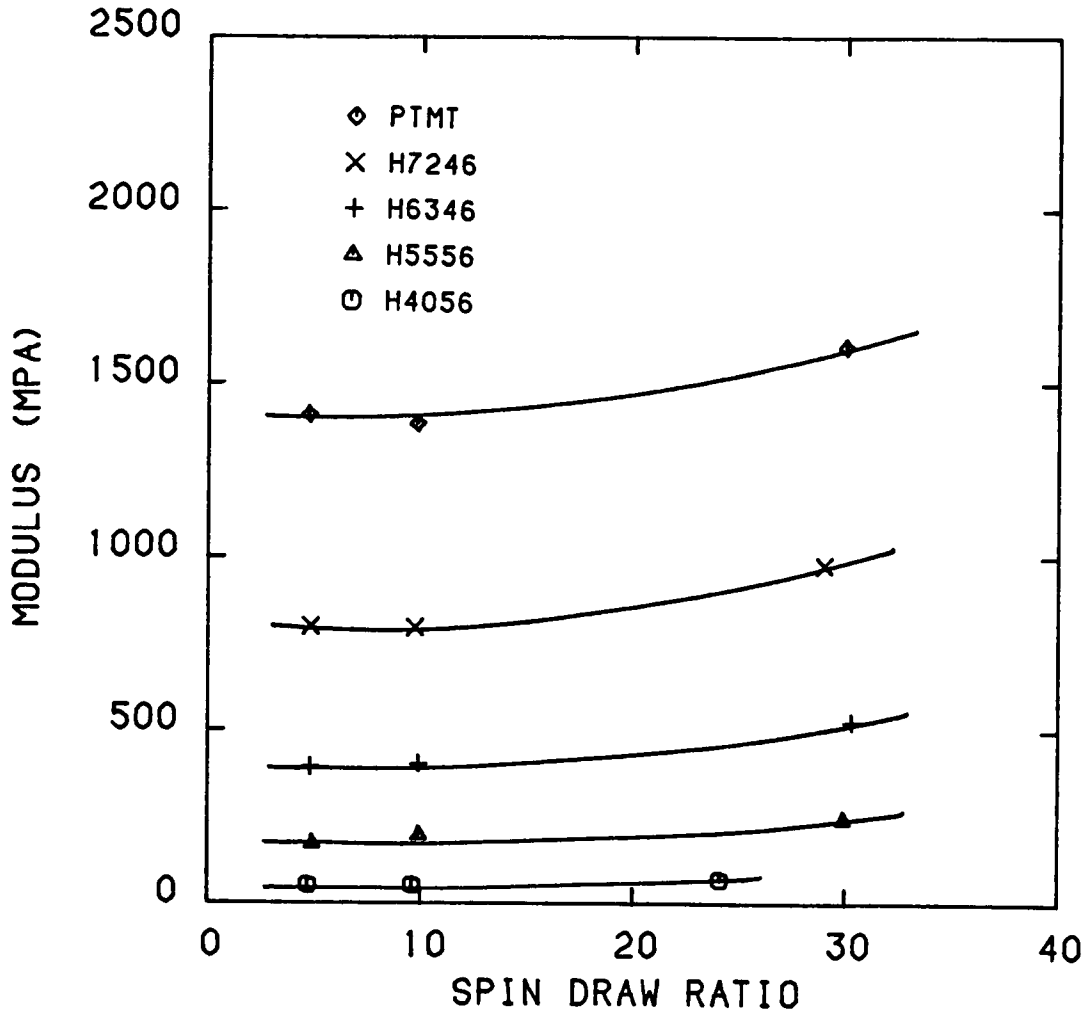


Figure 7.1: Modulus of the as-spun filaments as a function of SDR and composition.

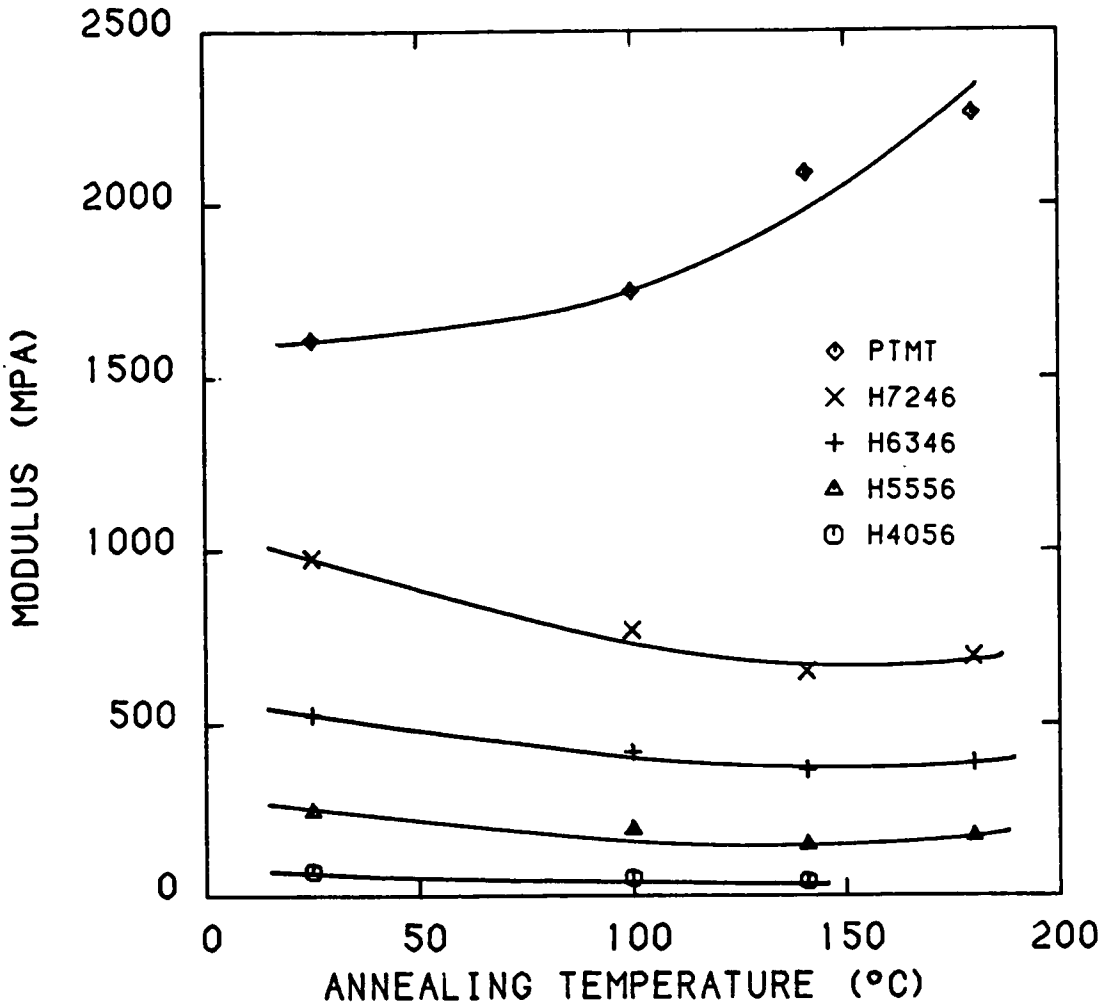


Figure 7.2: Effect of annealing temperature on the modulus of filaments spun at 300m/min.

mation of material from an amorphous to crystalline state. The copolymers, however, show a drop in modulus despite an increase in crystallinity. This may be related to changes in the composition of the amorphous phase and to changes in crystallite size and spacing. These possibilities will be explored in the next section.

7.2 Analysis

By developing a reasonable morphological model that explains how the modulus changes with composition and annealing temperature, more may be learned about the details of the structure and how they influence the macroscopic modulus. Such an analysis may help answer such questions as: What is the origin of the high modulus as compared to typical cross-linked elastomers? Is it due to the "psuedo-elastic" deformation of the crystalline phase as Cella hypothesized or is there another plausible explanation? Is the crystalline phase continuous or are the crystallites dispersed in an elastomeric matrix? What effect do crystallite size and spacing and DPS have on the modulus? What causes the decrease in modulus upon annealing?

Several equations have been developed to describe the mechanical response of multi-phase systems to changes in composition and microstructure [100,76,187,9,53]. Takayanagi and coworkers [186,187,117] and others following his technique [77,104], have used simple models to understand the modulus-structure relationships in semi-crystalline polymers. The "Takayanagi model"

is based on the volume fractions of the crystalline and amorphous phases and a reasonable approximation of the the modulus of each phase. The composite modulus of a complex system can be calculated using a combination of basic series and parallel elements. The exact combination depends on whether one assumes equal stress or equal strain in the different phases. Takayanagi [186,187] has found the equal stress assumption works well for interpreting the behavior of semi-crystalline polymers and incompatible polymer blends. The modulus of simple two-phase systems can be calculated from the following equations:

Series:

$$E_s = \left(\frac{\nu_a}{E_a} + \frac{\nu_c}{E_c}\right)^{-1} \tag{7.1}$$

Parallel:

$$E_p = \nu_a E_a + \nu_c E_a \tag{7.2}$$

Composite (assuming equal stress):

$$E_{comp} = \left(\frac{\beta}{\gamma^2 E_a + (1-\gamma^2)E_c} + \frac{1-\beta}{E_c}\right)^{-1} \tag{7.3}$$

where ν_a and ν_c are volume fractions of the amorphous and crystalline phases, and E_a and E_c are the moduli of the amorphous and crystalline fractions. The parameter β expresses the degree of parallelism and γ the degree of series connection.

The moduli of various phases have been approximated by Takayanagi [187] to within an order of magnitude for conventional thermoplastics:

$$E_c(\|) \approx 10^{11} Pa$$

$$E_c(\perp) \approx 10^{9} Pa$$

$$E_a(< T_g) \approx 10^{9} Pa$$

$$E_a(> T_g) \approx 10^{7} Pa$$

where $E_c(\|)$ is the modulus along the chain axis direction of the crystal and $E_c(\perp)$ is the modulus perpendicular to the chain axis direction. The modulus of the amorphous phase (E_a) below T_g is about two orders of magnitude higher than it is above T_g.

Simple models based on the work of Takayanagi may be useful in further analyzing the relationship between the modulus of the copolyester filaments and structural parameters such as composition, DPS, crystallite size and spacing, and orientation. In applying this type of analysis to the copolyester system, three criteria must be met.

1. The model must be a reasonable approximation of observed structural features. The degree of phase separation, the crystallite size and spacing, and the orientation of lamellae must be considered.

2. The model must be able to explain the variation of modulus with composition. (In general, the modulus increases as HSC increases.)

3. The model must be able to explain the effect of annealing on the modulus. As shown earlier, the modulus decreases upon annealing at large

undercooling, but increases in some compositions when the filaments are annealed at small undercooling.

The filaments for which this analysis is carried out were all spun at a high enough rate to produce a high level of crystallite orientation. The shrinkage experiments indicate there is very little preferred orientation of the amorphous chains. In order to simplify the analysis, the crystalline chains will be modelled as though they are all aligned parallel to the fiber axis ($f_c = 1$) and the chains in the amorphous phase will be considered to be randomly oriented ($f_a = 0$). Thus, the value of $E_c(\|)$ will be used to represent the modulus of the crystalline phase in the direction of the fiber axis. The value of $E_a(> T_g)$ will be used as an approximation of the modulus of PTMEG chains, while $E_a(< T_g)$ will be used to represent the modulus of amorphous PTMT chains.

Pertinent mechanical and structural data for the copolyester filaments are shown in Table 7.1. The parameters needed for the Takayanagi analysis can be calculated from these data.

The dimension β_c representing the relative thickness of the crystalline domain is calculated directly from the long period and the crystallite thickness:

$$\beta_c = t_{104}/L \tag{7.4}$$

where t_{104} is the thickness of the crystallite and L is the long period. The parameter γ_c, representing the relative width of the crystalline domain, is estimated from the approximate degree of crystallinity (ν_c) and β_c:

$$\beta_c \gamma_c^2 = \nu_c \tag{7.5}$$

Table 7.1: Experimental data used in the Takayanagi analysis.

SAMPLE	T_a (°C)	E_{obs} ($\times 10^{-8} Pa$)	LONG PERIOD (Å)	t_{104} (Å)	f_c	EST. CRYST. (%)
4056	25	0.70	123	40	0.75	16
250	100	0.51	139	43	0.89	14
	141	0.42	177	51	0.91	15
5556	25	2.46	108	40	0.71	14
300	100	1.93	116	49	0.70	17
	141	1.48	135	53	0.77	20
6346	25	5.26	91	40	0.70	13
300	100	4.16	104	46	0.74	17
	141	3.65	121	53	0.81	22
	180	3.86	157	65	0.87	26
7246	25	9.78	88	32	0.63	11
300	100	7.70	103	40	0.69	18
	141	6.51	117	51	0.76	22
	180	6.94	137	62	0.85	29

The square of γ_c is used to represent the three dimensional nature of the microstructure.

There are two approaches that can be taken initially in developing a model for the copolyesters. One can assume that the crystalline phase is continuous or that the amorphous phase is continous. There is no way of knowing *a priori* which will work better. That is one of the questions we are trying to resolve.

7.2.1 Continous Crystalline Phase

In this model the crystalline phase is assumed to be continuous. Physically, this means the lamellae are considered to impinge upon each other in the radial direction and are linked together in the axial direction by some means. The axial linkage can represent the intersection of two or more lamellae in the type of morphological model proposed by Cella [37] or it can represent taut tie molecules between lamellae. The crystalline matrix type model has been used successfully to simulate the mechanical response of drawn filaments of polyethylene [187].

A schematic diagram of this model is shown in Figure 7.3. The modulus of the crystalline phase is approximated as $10^{11}Pa$. The amorphous phase is assumed to be above T_g, so its modulus is approximated as 10^7Pa. The composite modulus is calculated from E_a and E_c using a form of Equation 7.3:

$$E_{comp} = \left(\frac{\beta_a}{\gamma_a^2 E_a + (1-\gamma_a^2)E_c} + \frac{1-\beta_a}{E_c} \right)^{-1} \tag{7.6}$$

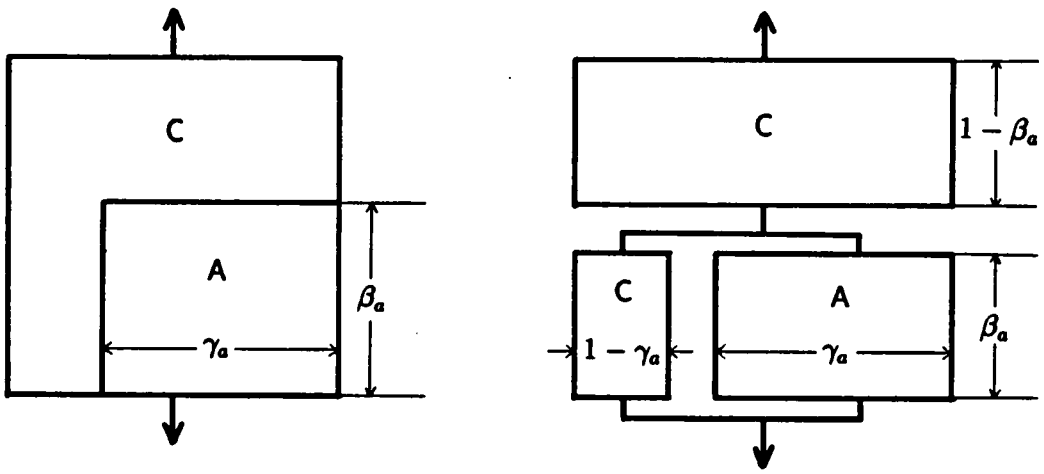


Figure 7.3: Model of the structure based on a continuous crystalline phase (C). The width γ_a and thickness β_a of the amorphous phase (A) are variable.

The parameter β_a represents the relative thickness of the amorphous phase, where $\beta_a = 1 - \beta_c$. The value chosen for the parameter γ_a determines the volume fraction of the amorphous phase, where $\nu_a = \beta_a \gamma_a^2$.

E_{comp} decreases as β_a and γ_a increase. Calculations based on a wide range of values of β_a and γ_a show that the the macroscopic modulus decreases rapidly as γ_a approaches one, as long as β_a is greater than zero, and that it increases dramatically as β_a approaches zero when γ_a is greater than about 0.9. This model is not very sensitive to the values of β_a and γ_a when $\beta_a > 0.1$ and $\gamma_a < 0.9$.

The predicted modulus does not vary much with β_a within the range of experimentally observed values. Using the data for β_a, values of γ_a close to one are required to obtain reasonable values of the modulus. Even at such high values of γ_a, the degree of crystallinity predicted by the model seems to be too high. The data in Table 7.2 show the results of this analysis.

This model indicates that it is the small amount of crystalline material tying the crystallites together that gives the copolyesters their high modulus. The increase in modulus as HSC increases results from an increase in the amount of the connecting material. But what is the nature of this material? Considering the small size of the crystallites in the copolyester filaments, the lamellae probably do not impinge upon each other to a significant degree. For this reason, the connecting material is believed to consist of taut tie molecules.

In summary, this model can predict reasonable values of the modulus, but there are a couple of problems with modeling the crystalline phase

Table 7.2: Values of γ_a^2 predicted by the "crystalline matrix" model using the observed values of the modulus and the data for β_a.

SAMPLE	T_a (°C)	E_{obs} ($\times 10^{-8} Pa$)	β_a	Predicted γ_a^2	$1 - \beta_a \gamma_a^2$
4056	25	0.70	0.67	0.9996	0.33
250	100	0.51	0.69	0.9997	0.31
	141	0.42	0.71	0.9998	0.29
5556	25	2.46	0.63	0.9985	0.37
300	100	1.93	0.58	0.9989	0.42
	141	1.43	0.61	0.9992	0.39
6346	25	5.26	0.56	0.9971	0.44
300	100	4.16	0.56	0.9978	0.44
	141	3.65	0.56	0.9981	0.44
	180	3.86	0.59	0.9978	0.41
7246	25	9.78	0.64	0.9938	0.36
300	100	7.70	0.61	0.9954	0.30
	141	6.51	0.56	0.9964	0.44
	180	6.94	0.55	0.9963	0.45

Note: The volume fraction degree of crystallinity predicted by the model is equal to $1 - \beta_a \gamma_a^2$.

as though it is continuous in the radial direction. First of all, the degree of crystallinity predicted by the model seems much too high. Secondly, this assumption makes it difficult to model the lateral growth of the crystallites upon annealing. Both these problems could be solved by eliminating the requirement that the crystalline phase be continuous in the radial direction.

7.2.2 Tie Molecule Model

In this model, the crystallites will no longer be considered continuous in the radial direction. This allows the width of the crystallites to be adjusted to more accurately represent the observed degree of crystallinity. The schematic diagram for this model is shown in Figure 7.4. The new model becomes identical to the "crystalline matrix" model in the case of $\gamma_c = 1$.

The modulus can be modelled as two parallel parts coupled in series. The moduli of the parallel parts are given by

$$E_{P1} = \gamma_c^2 E_c + (1 - \gamma_c^2) E_a$$

and

$$E_{P2} = \gamma_t^2 E_c + (1 - \gamma_t^2) E_a$$

The composite modulus is then given by

$$E_{comp} = \left(\frac{\beta_c}{E_{P1}} + \frac{1 - \beta_c}{E_{P2}} \right)^{-1} \tag{7.7}$$

Once again E_c is approximated as $10^{11} Pa$ and E_a as $10^7 Pa$. γ_t^2 is defined as the relative fraction of tie molecules. In order for the definition of γ_t to make sense, γ_c must be much greater than γ_t.

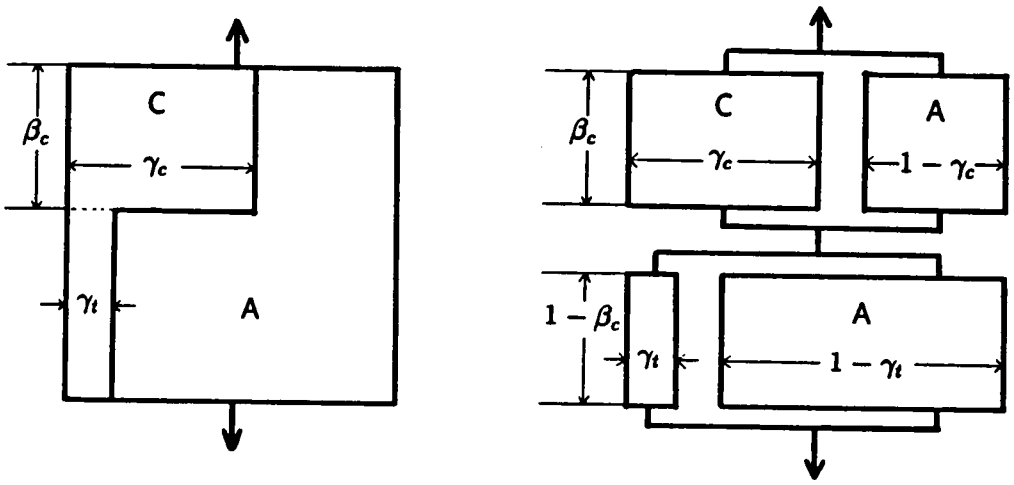


Figure 7.4: Model of the structure assuming the crystallites are dispersed within the amorphous matrix but connected by tie molecules. γ_c and β_c are the width and thickness of the crystalline phase, respectively. γ_t^2 represents the portion of tie molecules.

The value of E_{comp} increases as β_c, γ_c, or γ_t increase. The dimension γ_c has only a small effect on E_{comp} when β_c is less than about 0.95 (provided γ_c is not close to zero). E_{comp} increases rapidly as β_c approaches values close to one. Under these circumstances, the value of γ_c becomes important. The variation of the macroscopic modulus with the parameter γ_t^2 is shown in Figure 7.5 for various values of β_c at $\gamma_c = 0.6$. At very low values of γ_t^2 the modulus increases very little as γ_t^2 increases. Above values of about 10^{-4}, the parameter γ_t^2, has a strong influence on the macroscopic modulus.

The macroscopic modulus is not very sensitive to the value of β_c, except at high values of β_c. As β_c approaches one, the modulus increases sharply. Since experimental values of β_c were found to lie between about 0.29 and 0.45, the thickness and separation of the crystallites has only a small effect on the macroscopic modulus and the radial dimensions of the crystallites have almost no effect. Using the experimental value of β_c, γ_c can be adjusted to reflect the degree of crystallinity. (The increase in crystallinity caused by annealing can be modeled as an increase in γ_c.) The critical determination of the modulus is the number of tie molecules as represented by γ_t^2. By adjusting the parameter γ_t, values of E_{comp} can be obtained that are close to observed moduli. Thus, the model satisfies most of the morphological requirements while predicting approximate values of the observed moduli.

The value of γ_t^2 can be calculated if E_{comp}, E_c, E_a, β_c, and γ_c are known. Solving Equation 7.7 for γ_t^2 leads to the following equation :

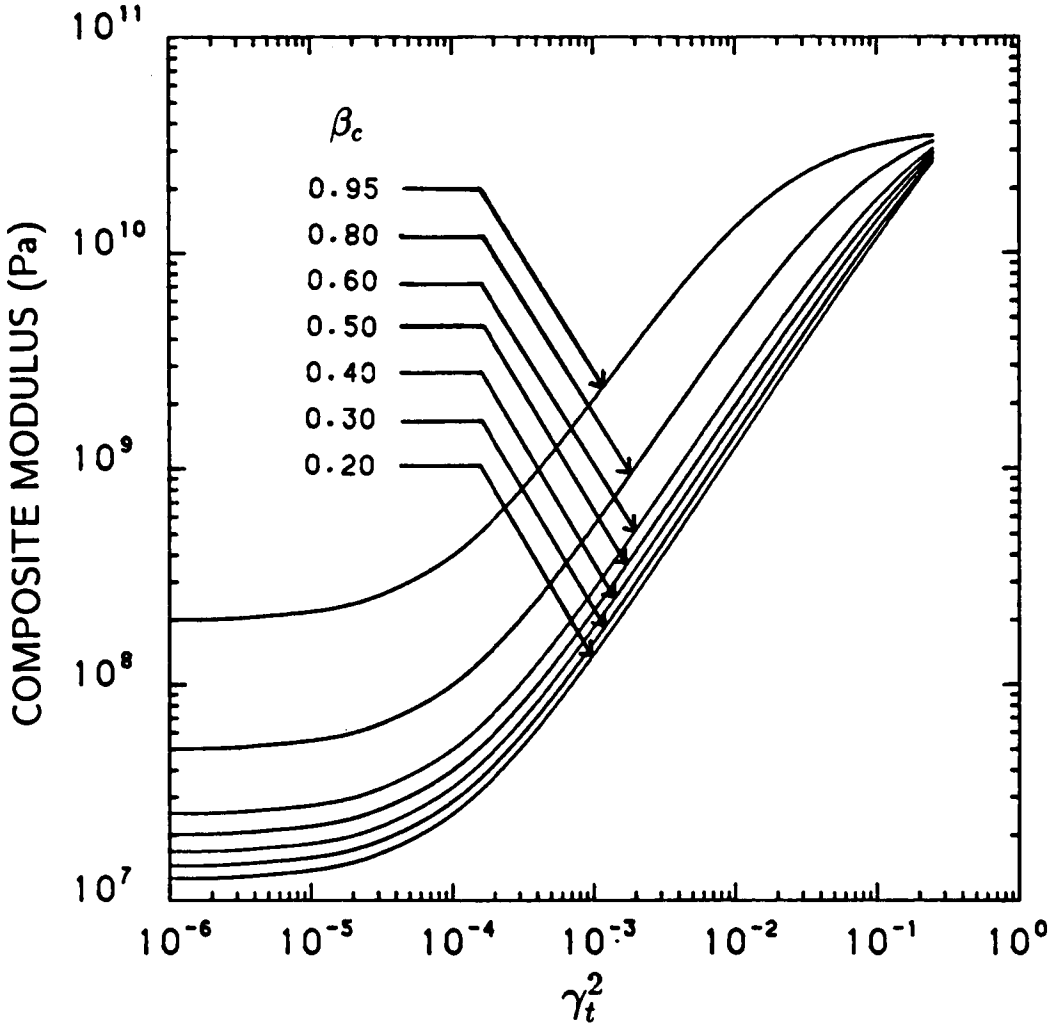


Figure 7.5: Variation of the composite modulus with the relative fraction of tie molecules γ_t^2. These results were calculated using Equation 7.7.

$$\gamma_t^2 = \frac{X/Y - E_a}{Z} \tag{7.8}$$

where

$$X = E_{P1}E_{comp}(1 - \beta_c)$$

$$Y = E_{P1} - \beta_c E_{comp}$$

$$Z = E_c - E_a$$

Using the experimentally determined values of E_{comp} and β_c, and reasonable estimates of γ_c, the value of γ_t^2 for each sample was calculated. The data are summarized in Table 7.3. The calculated values of γ_t^2 are plotted as a function of the observed modulus in Figure 7.6. The values calculated for different compositions and annealing temperatures all fall very nearly on a single curve.

These results show that the macroscopic modulus predicted by this model is directly dependent on the number of tie molecules, rather than the composition or degree of crystallinity *per se*. Changes in crystallite size and spacing have only a secondary effect. Thus, the increase in modulus as HSC increases can be explained as being the result of an increase in the number of tie molecules, rather than from changes in crystallite size and spacing, or some fundamental change in morphology as the composition changes.

In order to satisfy the third criteria, the model must predict the behavior of the copolymers upon annealing. Assuming that the degree of crystallinity increases during annealing and that the number of tie molecules remains the

Table 7.3: Fraction of taut tie molecules (γ_t^2) predicted by the "tie molecule" model using the experimental data shown.

SAMPLE	T_a (°C)	E_{obs} ($\times 10^{-8} Pa$)	β_c	γ_c	Predicted $\gamma_t^2 (\times 10^4)$
4056	25	0.70	0.33	0.70	3.69
250	100	0.51	0.31	0.67	2.52
	141	0.42	0.29	0.72	1.98
5556	25	2.46	0.37	0.62	14.54
300	100	1.93	0.42	0.64	10.21
	141	1.48	0.39	0.72	8.04
6346	25	5.26	0.44	0.54	28.69
300	100	4.16	0.44	0.63	22.41
	141	3.65	0.44	0.71	19.51
	180	3.86	0.41	0.80	21.83
7246	25	9.78	0.36	0.55	62.33
300	100	7.70	0.39	0.68	46.28
	141	6.51	0.44	0.71	35.67
	180	6.94	0.45	0.80	37.36

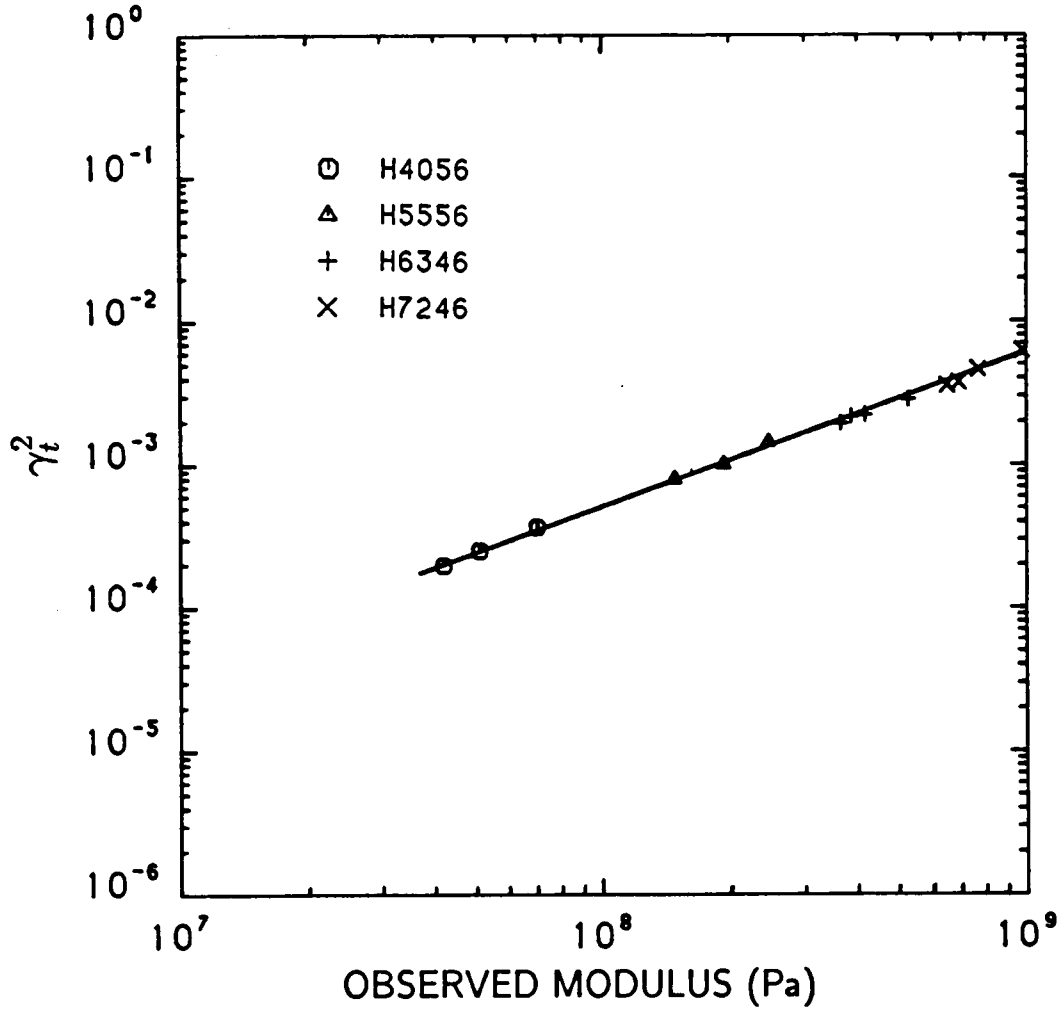


Figure 7.6: Variation of γ_t^2 with observed values of modulus. Values of γ_t^2 were calculated using experimentally determined values of modulus and β_c, and reasonable estimates of γ_c. Note the smooth variation in γ_t^2 with modulus despite the variation in composition.

same, the product $\beta_c\gamma_c$ grows larger and the model predicts a slight increase in modulus. This increase would be expected for homopolymers, and is observed for PTMT, but the modulus of the copolymers decreases upon annealing at large to moderate undercooling. The drop in modulus could be explained by a decrease in the dimension γ_t as shown in Figure 7.7. Physically, this would mean that the number of tie molecules decreases as the filaments are annealed. In H4056 this could result from the melting of the smaller crystallites and an increase in the distance between crystalline domains, but in H6346 and H7246 this distance remains about the same. In their case, the number of taut tie molecules would be expected to increase due to either an increase in the actual number of tie molecules as the crystallites become larger, or due to a tightening of existing loose tie molecules as the crystallites thicken. The slight increase in modulus observed at small ΔT_u may be a result of this phenomenon.

Thus, this model does a good job of satisfying the first two criteria mentioned in the introduction. It fails, however, in predicting the decrease in modulus upon annealing. Perhaps a model in which the amorphous phase is considered continuous would do a better job of handling this problem.

7.2.3 Continous Amorphous Phase

In this model we assume that the crystallites are imbedded in a continuous elastomeric phase. A schematic diagram of this model is shown in Figure 7.8. The macroscopic modulus is calculated from a form of Equation 7.3:

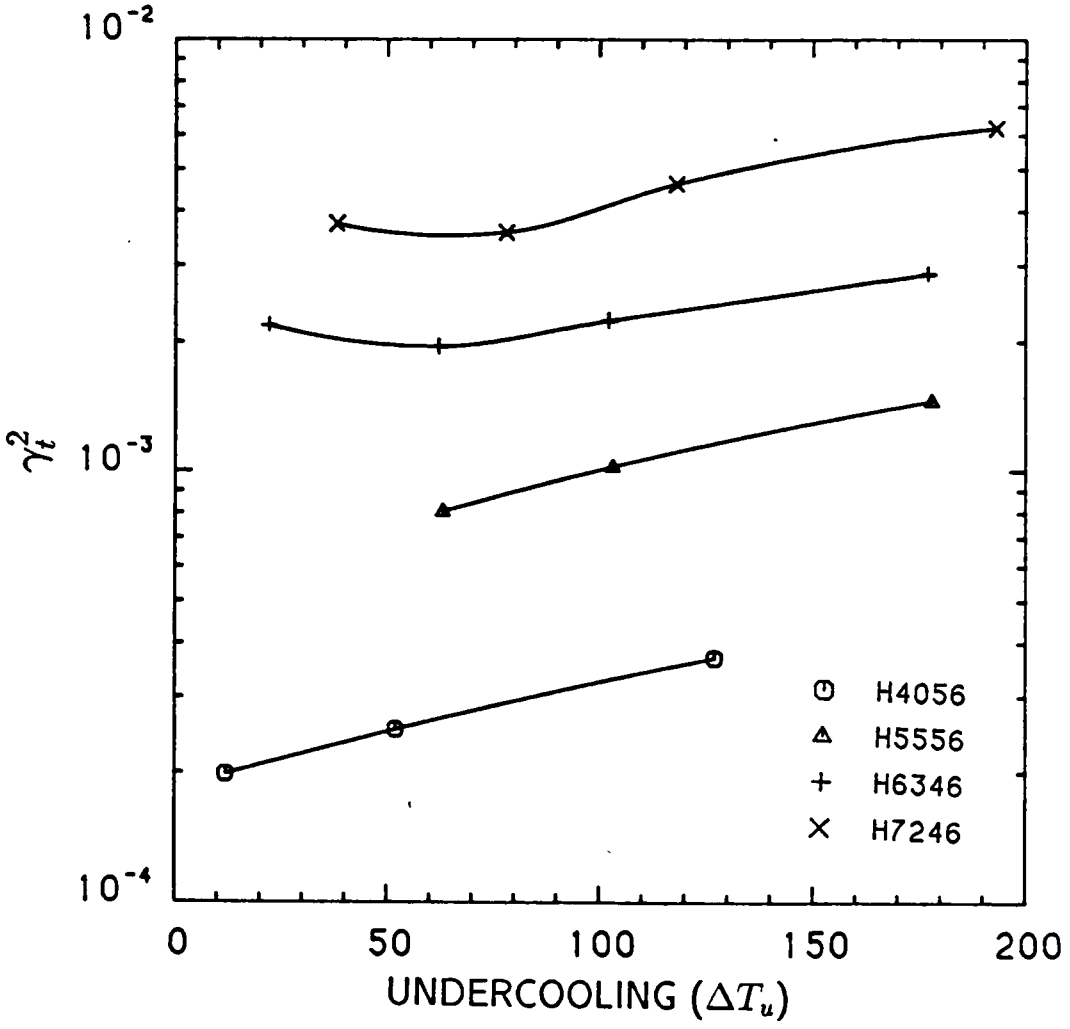


Figure 7.7: Calculated values of γ_t^2 needed to explain the decrease in modulus upon annealing. The indicated decrease in γ_t^2 as ΔT_u grows smaller seems unlikely.

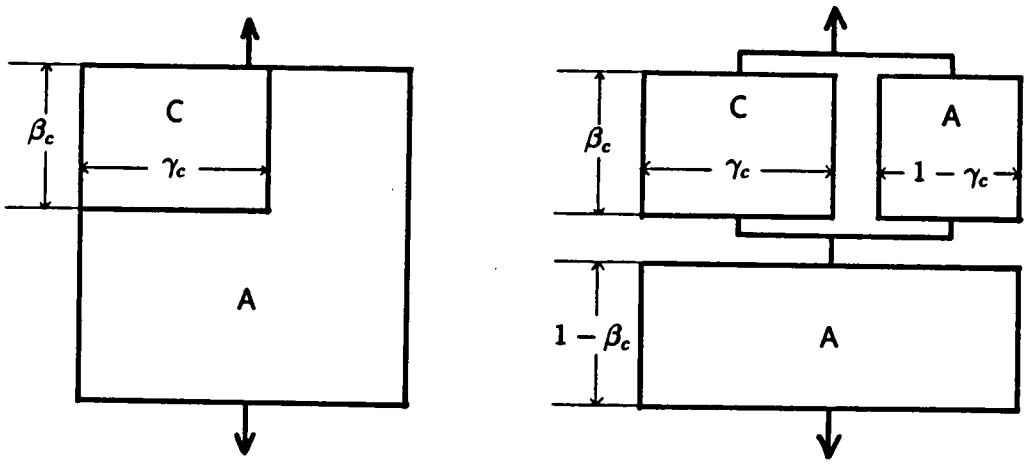


Figure 7.8: Morphological model based on a continuous amorphous phase. The size of the crystalline region C and the modulus of the amorphous phase E_a can vary with composition and annealing treatment.

$$E_{comp} = \left(\frac{\beta_c}{\gamma_c^2 E_a + (1 - \gamma_c^2) E_c} + \frac{1 - \beta_c}{E_c} \right)^{-1} \tag{7.9}$$

where β_c and γ_c represent the dimensions of the crystalline fraction.

The amorphous phase is assumed to be above T_g, so E_a is approximated as $10^7 Pa$. The modulus increases as γ_c and β_c increase, but remains near $10^7 Pa$ unless $\gamma_c > 0.01$ and $\beta_c > 0.9$. As a result, the model is not too sensitive to the value chosen for E_c when $\beta_c < 0.9$. Since the experimental values of β_c were found to lie between 0.29 and 0.45, the value of $10^{11} Pa$ chosen for E_c should be adequate for our purpose.

The predicted values of E_{comp} based on the available data for β_c and γ_c are shown in Table 7.4 for the unannealed filaments. The model is not very sensitive to changes in β_c and γ_c, and underpredicts the modulus by a factor of about 5 to 100 (the error grows worse as HSC content increases). In order to produce values of the moduli close to those observed experimentally, β_c would need to be around 0.8 to 0.995 depending on the composition.

The values of β_c determined experimentally increase as the annealing temperature is raised in all the compositions except H4056. Since the crystallites grow in the radial direction during annealing and since the DPS increases during annealing, it is reasonable to expect that γ_c also increases. Assuming that β_c and γ_c increase continuously as ΔT_u decreases, the modulus predicted by the model increases slightly as the filaments are annealed. This behavior is opposite from that which is observed. The predicted modulus can decrease as γ_c grows, but only if β_c decreases. (In H4056, β_c decreases slightly upon

Table 7.4: Macroscopic modulus E_{comp} predicted by the "amorphous matrix" model using experimental data for β_c and γ_c.

SAMPLE	T_a (°C)	E_{obs} ($\times 10^{-8} Pa$)	β_c	γ_c	Predicted E_{comp}($\times 10^{-8} Pa$)
4056 250	25	0.70	0.33	0.70	0.12
5556 300	25	2.46	0.37	0.62	0.12
6346 300	25	5.26	0.44	0.54	0.13
7246 300	25	9.78	0.36	0.55	0.12

annealing, but this is not the case for the other compositions.)

In summary, this model can be adjusted to take into account the observed long period, crystallite thickness, and degree of crystallinity, but does not predict reasonable values of the modulus based on the observed morphology. This model of the structure is unable to predict either the change in modulus with composition or annealing with any degree of success.

The modulus in this model is determined primarily by the modulus of the amorphous phase. The value of $10^7 Pa$ used for E_a seems to be too low. This model does not take into account the effect of dissolved hard segments on the modulus of the amorphous phase. These hard segments may act to raise E_a and produce higher values of E_{comp}. This hypothesis leads to the solution model discussed next.

7.2.4 Solution Model

None of the previous models consider the effect of HSC and DPS on the composition and modulus of the amorphous phase. The modulus of the amorphous phase would be expected to increase as the fraction of dissolved hard segments increase. In order to take these effects into consideration, E_a must be allowed to vary as its composition changes. The lower limit of E_a will be the same as the modulus of pure PTMEG, while the upper limit can not be greater than the modulus of amorphous PTMT. Since pure PTMEG is above its T_g at room temperature, its modulus will be approximated as $10^7 Pa$. Amorphous PTMT is below its T_g at room temperature so its modulus will be approxi-

mated as $10^9 Pa$. The actual value of E_a probably lies somewhere between the two extremes depending upon the composition of the amorphous phase.

We would like to see how E_{comp} varies with E_a and whether or not reasonable values of E_{comp} are predicted. Equation 7.9 is still used to make the calculations. As in the simple amorphous matrix model, the modulus is not very sensitive to the value chosen for E_c or to the values of β_c and γ_c unless β_c is large (> 0.9). In the following calculations, E_c is approximated as $10^{11} Pa$, and for the purpose of illustration, γ_c is selected to be 0.6. This value is close to those calculated from experimental data. The variation of the macroscopic modulus with E_a is shown in Figure 7.9 for several different values of β_c. At constant β_c and γ_c, E_{comp} increases in direct proportion to E_a. Just as in the "tie molecule model", the macroscopic modulus is not very sensitive to the value of β_c, until β_c starts to approach a value of "one".

The experimentally determined values of β_c were found to range from 0.29 to 0.45. Within this range, β_c has only a small effect on E_{comp} as shown in Figure 7.9. The effect of γ_c is almost negligible in this range. For this reason, values of γ_c can be chosen to reflect the degree of crystallinity. Thus the macroscopic modulus is determined less by the size and spacing of the crystallites and more by the modulus of the amorphous phase.

The amorphous modulus E_a can be calculated if E_{comp}, E_c, β_c, and γ_c are known. Equation 7.9 can be re-expressed as a quadratic equation in terms of E_a:

$$aE_a^2 + bE_a + c = 0 \tag{7.10}$$

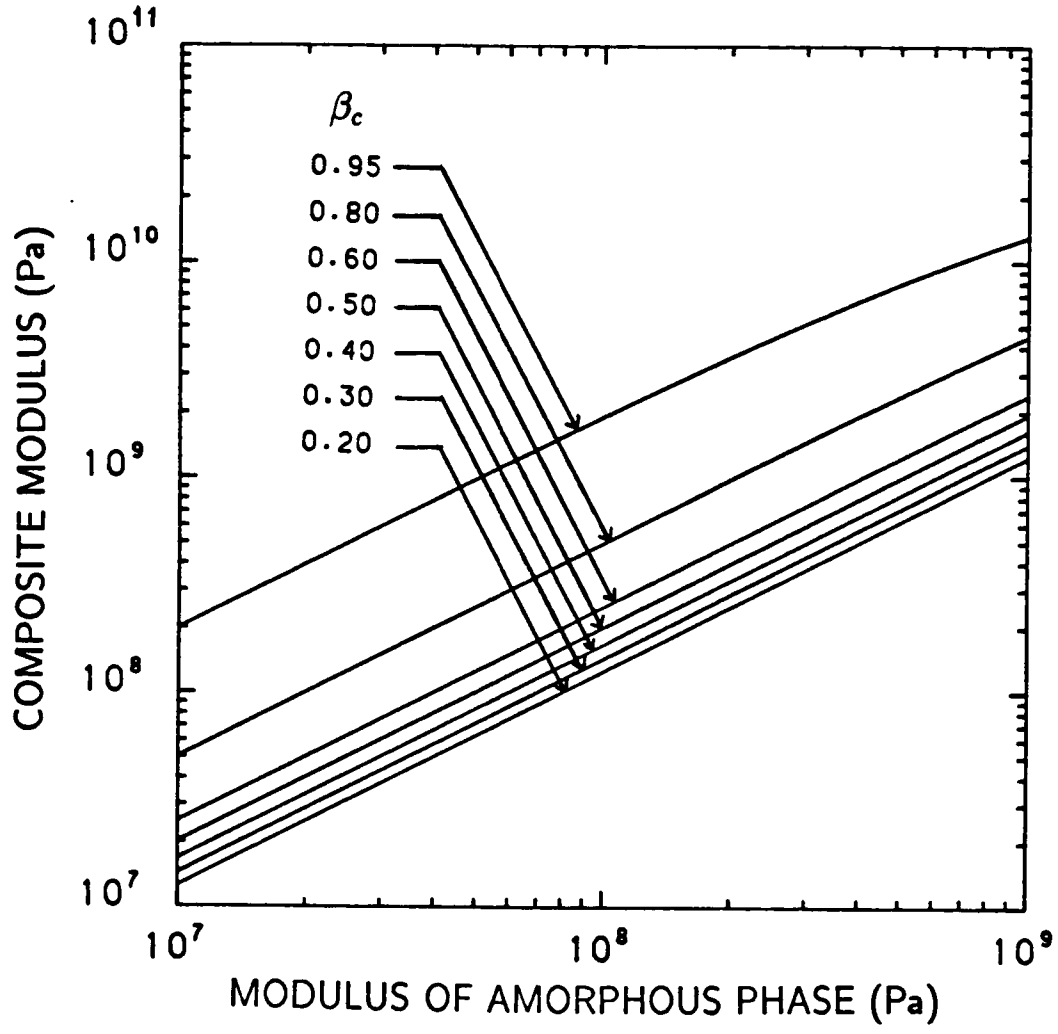


Figure 7.9: Variation of the composite modulus with the modulus of the amorphous phase and the crystallite thickness (β_c). The results were calculated using Equation 7.9 and letting $\gamma_c = 0.6$.

where

$$a = 1 - \gamma_c^2$$

$$b = \gamma_c^2 E_c - E_{comp}[\beta_c + (1 - \beta_c)(1 - \gamma_c^2)]$$

$$c = -E_{comp}(1 - \beta_c)\gamma_c^2 E_c$$

Using the experimental values of E_{comp} and β_c and reasonable estimates of γ_c, the modulus of the amorphous phase was back calculated from the model. The data are shown in Table 7.5. E_a is plotted as a function of E_{comp} in Figure 7.10. All the values fall very nearly on a single curve. These results indicate that the modulus of the filament is determined primarily by the modulus of the amorphous region. The overall composition and degree of crystallinity influence the macroscopic modulus almost solely by their effect on E_a.

The general increase in modulus with increasing HSC is the result of an increase in E_a caused by an increase in the fraction of hard segments dissolved in the amorphous phase. The decrease in modulus upon annealing can now be explained. As the samples are annealed, the DPS increases and the number of hard segments dissolved in the amorphous phase is reduced. As the hard segments are driven out of the amorphous phase, a greater percentage of the chain segments are above their T_g, and the modulus drops.

Thus, this model is able to simulate the pertinent observed structural features and can explain both the effect of composition on the modulus and the decrease in modulus upon annealing. Almost all of the criteria established in the introduction are met. The only thing the model is unable to explain

Table 7.5: Modulus of the amorphous phase predicted by the "solution" model using the experimental data shown.

SAMPLE	T_a (°C)	E_{obs} ($\times 10^{-8} Pa$)	β_c	γ_c	E_a ($\times 10^{8} Pa$)
4056	25	0.70	0 .33	0.70	0.47
250	100	0.51	0.31	0.67	0.35
	141	0.42	0.29	0.72	0.30
5556	25	2.46	0.37	0.62	1.55
300	100	1.93	0.42	0.64	1.12
	141	1.48	0.39	0.72	0.90
6346	25	5.26	0.44	0.54	2.97
300	100	4.16	0.44	0.63	2.34
	141	3.65	0.44	0.71	2.05
	180	3.86	0.41	0.80	2.28
7246	25	9.78	0.36	0.55	6.33
300	100	7.70	0.39	0.68	4.73
	141	6.51	0.44	0.71	3.67
	180	6.94	0.45	0.80	3.84

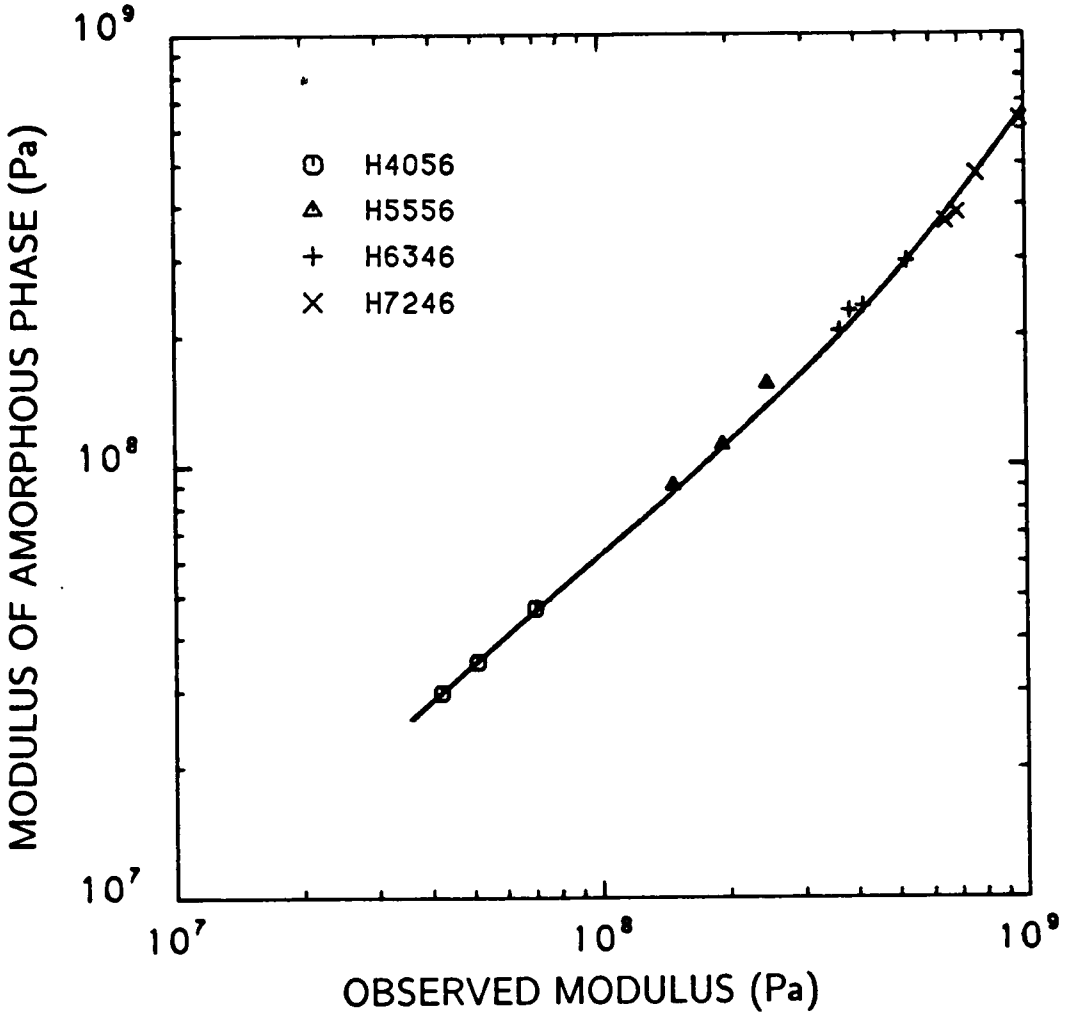


Figure 7.10: Modulus of the amorphous phase (E_a) as a function of the macroscopic modulus. Values of E_a were calculated using Equation 7.10 and experimentally determined values for the macroscopic modulus and crystalline fraction. These data are given in Table 7.5.

is the upturn in macroscopic modulus at low ΔT_u. As shown in Figure 7.11, the amorphous modulus of H7246 and H6346 would have to increase upon annealing at small ΔT_u in order to explain this behavior. If it is assumed that DPS continues to increase as ΔT_u decreases, E_a would be expected to decrease. An additional refinement of the model is needed to explain the annealing behavior.

7.2.5 Solution Model with Tie Molecules

Both the solution model and the tie molecule model are able to explain the effect of composition on the modulus, but neither are able to completely describe the behavior upon annealing. Perhaps a combination of both will solve this problem. In this model the amorphous phase is considered to be continuous and there are tie molecules between the crystallites. The modulus of the amorphous phase is allowed to vary between that of pure PTMEG which is above T_g (about 10^7Pa) and that glassy crystalline PTMT which is below T_g (about 10^9Pa). The modulus of the crystalline phase and the taut tie molecules are estimated to be about $10^{11}Pa$. The model does not require the modulus of the tie molecules to be equal to $E_c(\|)$, but since they are considered to be taut crystalline chains, this value seems appropriate.

An increase in the macroscopic modulus can be easily explained by an increase in the relative number of taut tie molecules, whereas a decrease may be explained by a drop in the modulus of the amorphous phase as the DPS increases. E_a is expected to drop continuously as the DPS increases and the

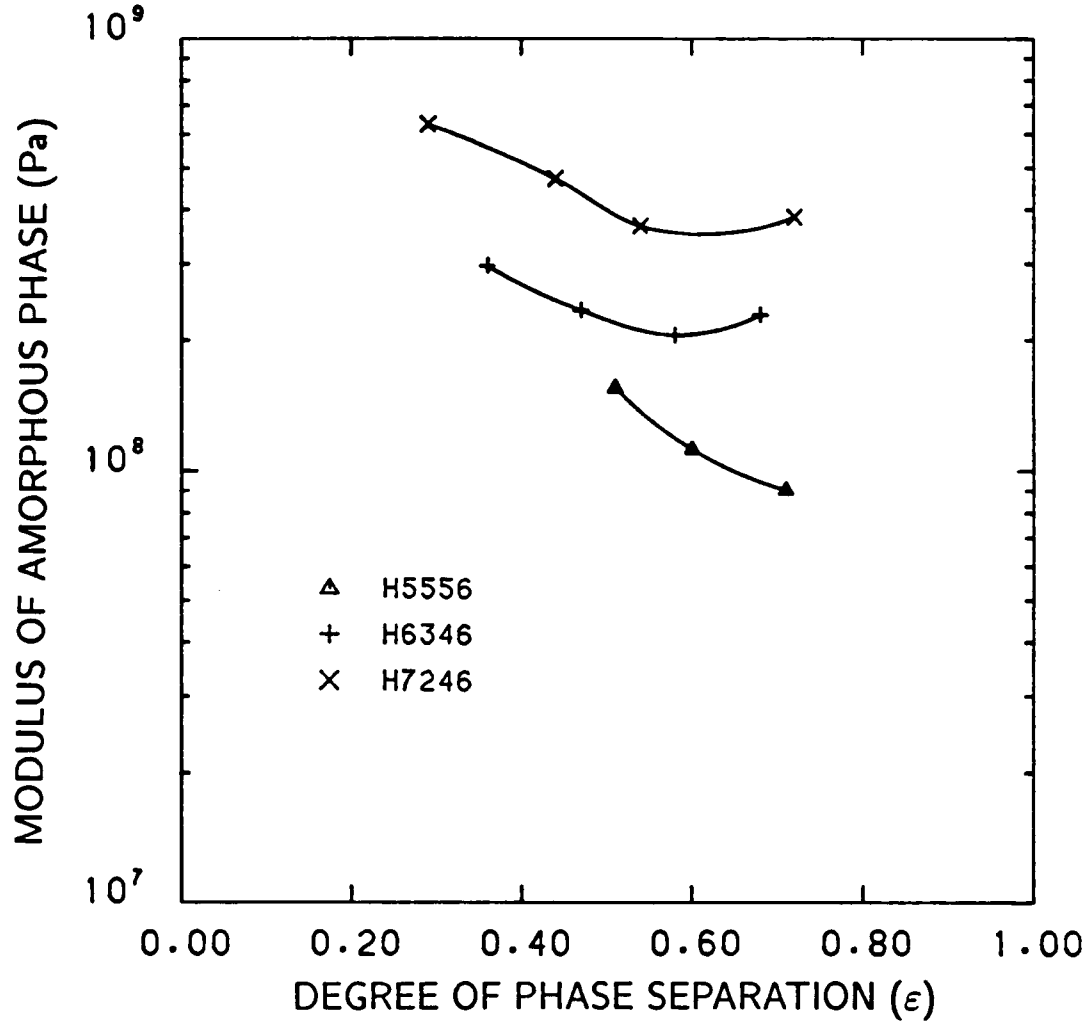


Figure 7.11: Plot of the amorphous modulus (E_a) as a function of the observed DPS. The increase in E_a at high DPS seems unlikely. The results were calculated using Equation 7.10.

number of taut tie molecules are expected to increase as the degree of crystallinity increases. Can the observed behavior be explained by a combination of the two effects? Is it possible for the overall modulus to drop as the number of tie molecules increase or to increase as E_a decreases?

We need to know how the interaction of E_a and γ_t affect the macroscopic modulus. At constant E_{comp}, the number of taut tie molecules must increase as the modulus E_a decreases. The maximum number of these tie molecules will be observed at the lower limit of E_a, which has been assumed to be $10^7 Pa$. This fraction of tie molecules (γ_t^2) was calculated in the "tie molecule" model. The results of this calculation were shown in Table 7.3. For a given E_{comp}, the model predicts the maximum E_a to occur when γ_t^2 is zero. These maximum values of E_a were calculated previously in the the "solution" model and were shown in Table 7.2.4. The intermediate combinations of E_a and γ_t can be determined from Equation 7.7. Solving for E_a leads to a quadratic equation:

$$AE_a^2 + BE_a + C = 0 \tag{7.11}$$

where

$$A = (1 - \gamma_c^2)(1 - \gamma_t^2)$$

$$B = \gamma_c^2 E_c(1 - \gamma_t^2) + \gamma_t^2 E_c(1 - \gamma_c^2)$$

$$C = (\gamma_c \gamma_t E_c)^2 - E_{comp}[\beta_c \gamma_t^2 E_c + (1 - \beta_c)\gamma_c^2 E_c]$$

To roughly approximate the experimental values, let $\beta_c = 0.4$ and $\gamma_c = 0.6$. E_c is still assumed to be about $10^{11} Pa$. By solving the quadratic equation for E_a at numerous values of γ_t, the relationship between E_a and γ_t^2

at a given E_{comp} can be determined. Theoretical values of E_a have been plotted as a function of γ_t^2 in Figure 7.12 for various values of E_{comp}. The solid lines are "iso-macroscopic moduli" contours. Each contour varies by a factor of two from its neighbor. In general both E_a and γ_t increase as E_{comp} increases.

At small fractions of tie molecules, the amorphous modulus must drop only very slightly to maintain constant E_{comp} as γ_t^2 increases. The effect of γ_t^2 on the overall modulus is very small in this region and E_{comp} is determined primarily by E_a. As γ_t^2 increases further it begins to have a substantial influence on the macroscopic modulus and E_a must drop quickly to compensate for the increase caused by γ_t^2. In this region the overall modulus is dominated by the effect of tie molecules.

The key question, however, is whether or not the model can explain the effects of annealing on the observed modulus. The assumption has been made that E_a decreases continuously and that γ_t increases continuously as the degree of undercooling becomes smaller. Can E_{comp} decrease as both these events occur? Looking at Figure 7.12, it can be seen that a curve starting in the upper left half of the plot and ending in the lower right half would represent both decreasing E_a and increasing γ_t^2. Initially this line crosses the contours in the direction of decreasing E_{comp}, but must eventually cross lines of increasing E_{comp}. So, the answer to the question is "yes, under certain conditions".

Plugging the experimental data E_{obs}, β_c, and γ_c into the model, the possible combinations of E_a and γ_t^2 for each sample were calculated. The contour lines for each composition are shown in Figures 7.13 thru 7.16. The

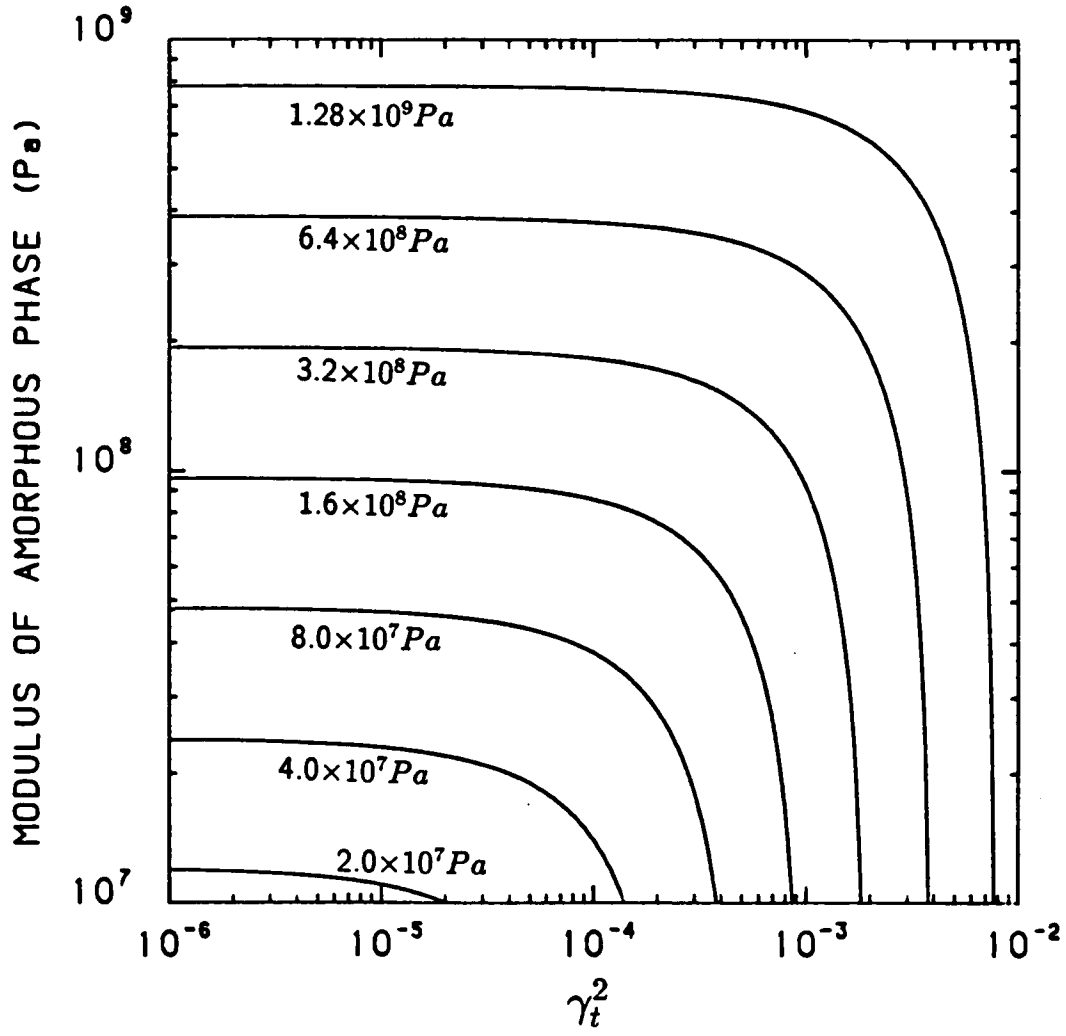


Figure 7.12: Values of E_a as a function of the fraction of tie molecules (γ_t^2) for several values of E_{comp} (shown next to each curve). E_a was calculated using Equation 7.11, letting $\beta_c = 0.4$ and $\gamma_c = 0.6$.

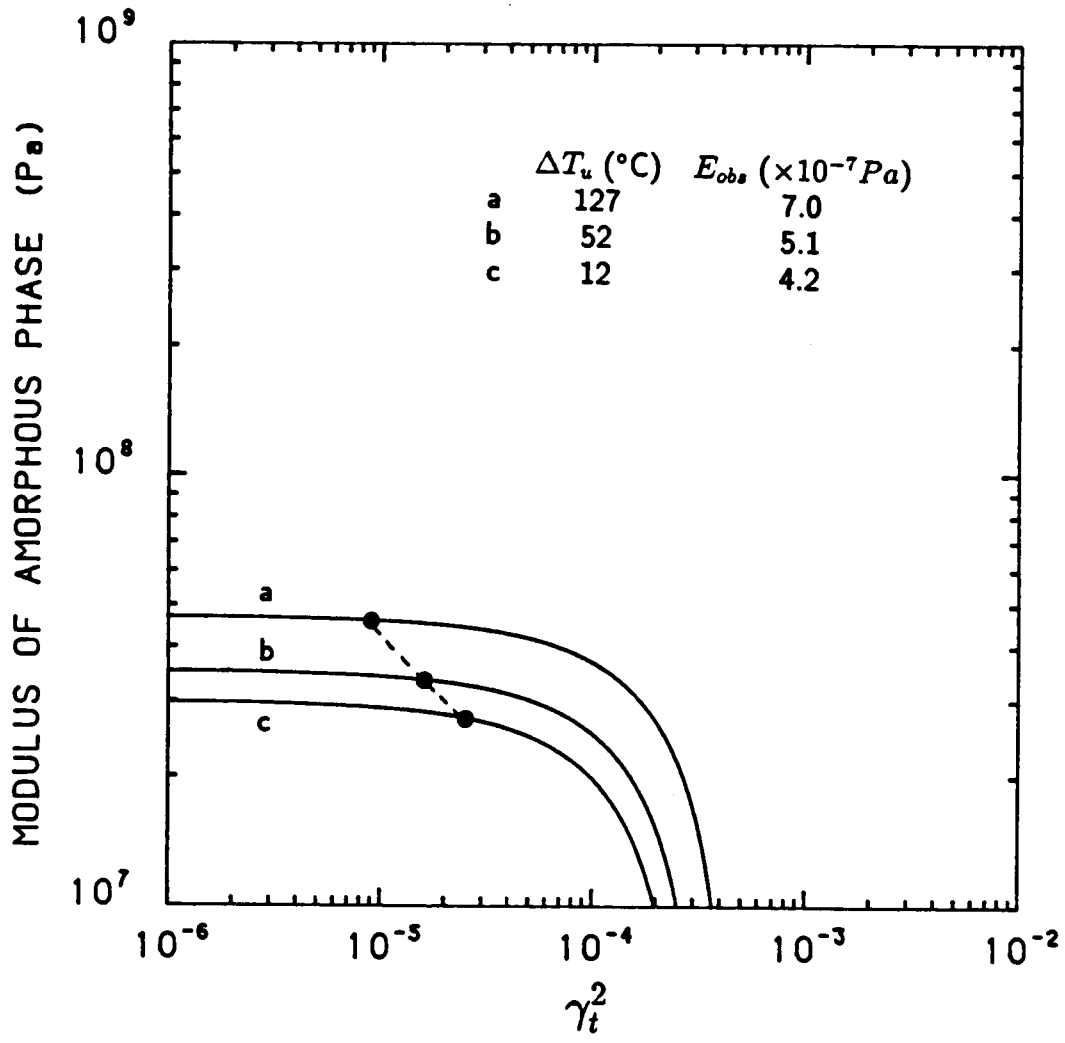


Figure 7.13: Possible combinations of E_a and γ_t^2 that would result in the observed macroscopic modulus (E_{obs}) in H4056 at each annealing temperature. E_a is expected to drop and γ_t^2 is expected to increase during annealing. The dotted line refers to possible changes in E_a and γ_t^2 that would explain the decrease in modulus observed upon annealing.

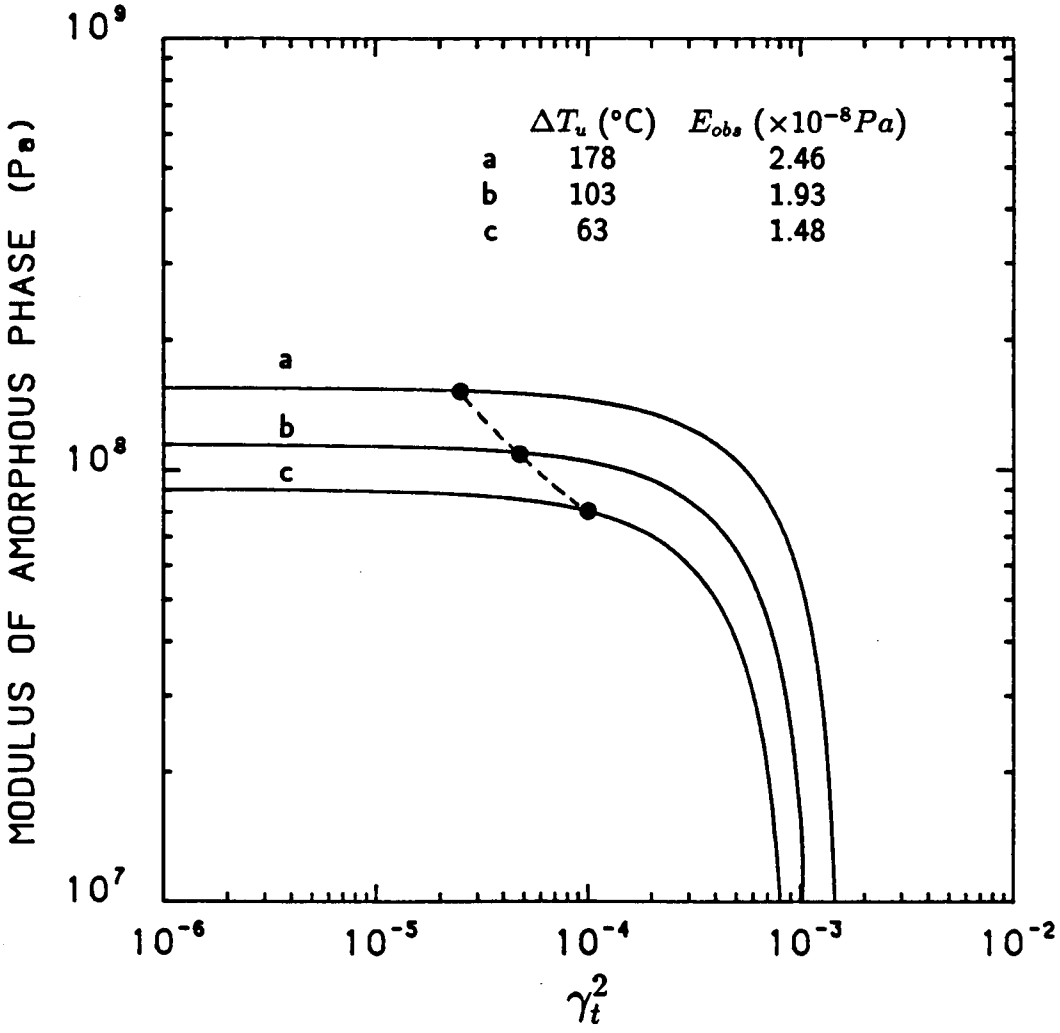


Figure 7.14: Possible combinations of E_a and γ_t^2 that would result in the observed macroscopic modulus (E_{obs}) in H5556 at each annealing temperature. The dotted line refers to possible changes in E_a and γ_t^2 that would explain the decrease in modulus observed upon annealing.

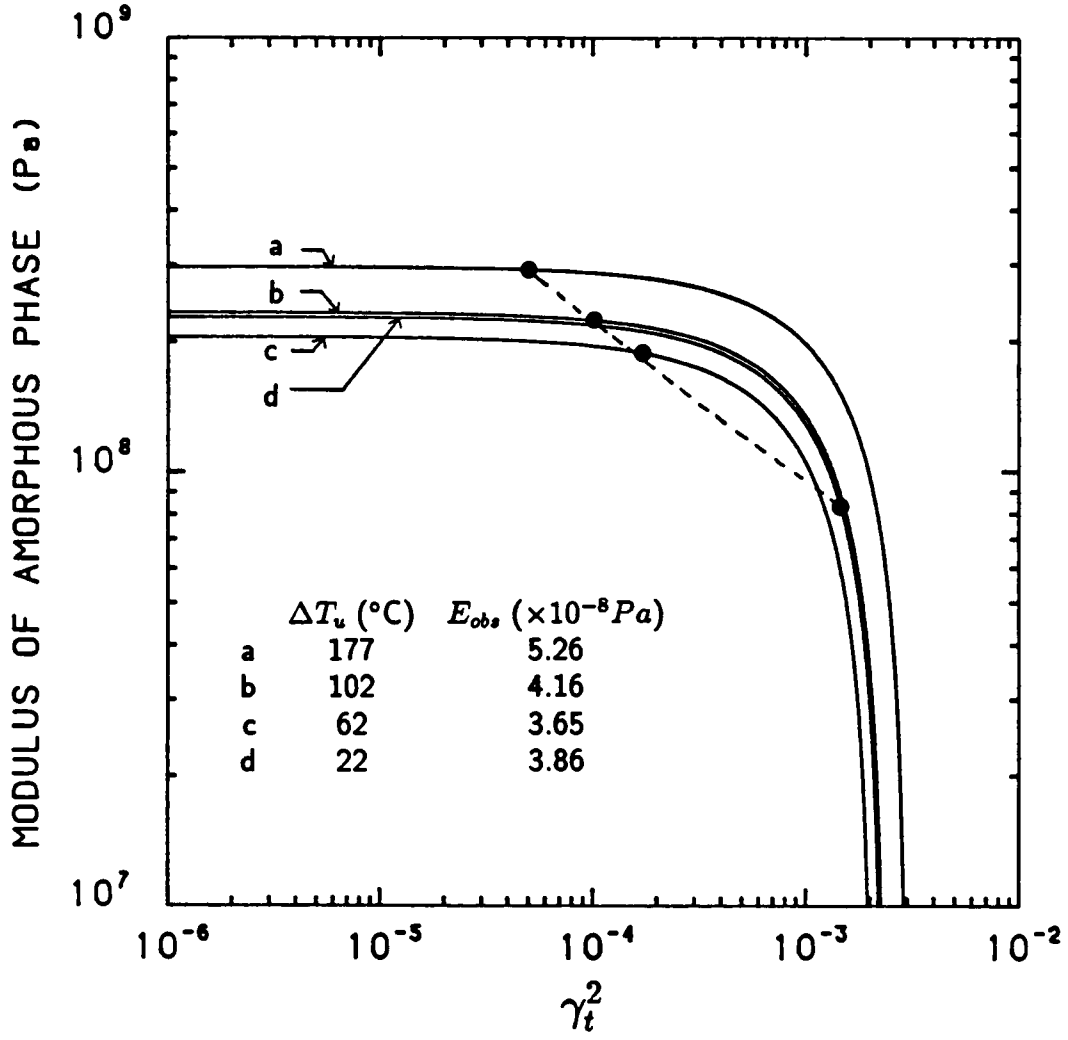


Figure 7.15: Possible combinations of E_a and γ_t^2 that would result in the observed macroscopic modulus (E_{obs}) in H6346 at each annealing temperature. E_{obs} decreases at high ΔT_u, but then increases at low ΔT_u. The dotted line refers to possible changes in E_a and γ_t^2 that would explain these changes in modulus.

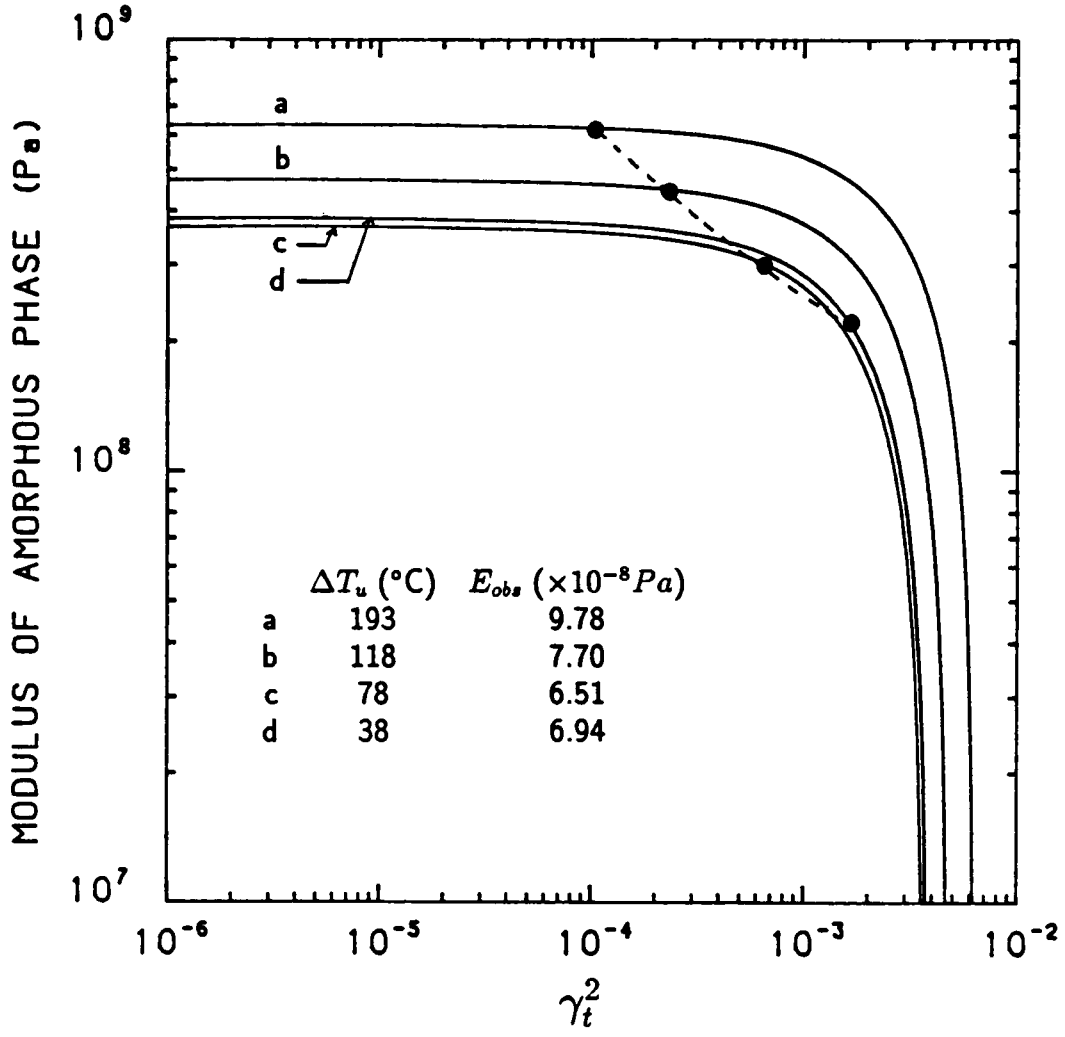


Figure 7.16: Possible combinations of E_a and γ_t^2 that would result in the observed macroscopic modulus (E_{obs}) in H7246 at each annealing temperature. E_{obs} decreases at high ΔT_u, but then increases at low ΔT_u. The dotted line refers to possible changes in E_a and γ_t^2 that would explain these changes in modulus.

dashed curves represent possible changes in E_a and γ_t consistent with the above assumptions and the observed behavior of the modulus. These curves are not uniquely determined. Additional information on how E_a varies with composition or an independent determination of the number of tie molecules would be needed to determine the exact curves.

The data can be interpreted as follows. In the as-spun samples there are relatively few tie molecules and their contribution to the modulus is almost negligible. As the samples are annealed, the DPS increases and the modulus of the amorphous phase drops considerably resulting in a decrease in the macroscopic modulus. At low annealing temperatures, the number of tie molecules increases, but not enough to make much difference in the modulus. At higher annealing temperatures, the degree of crystallinity increases greatly and the number of taut tie molecules becomes large enough to have a considerable influence on the modulus. At some point, the increase in E_{comp} caused by γ_t^2 outweights the decrease caused by a drop in E_a. This results in the increase in the macroscopic modulus at small ΔT_u noted for the compositions high in HSC. The general increase in modulus with increasing HSC is likely to be the result of an increase in both E_a and γ_t.

This model meets all the criteria established at the beginning of this section. It is able to model the pertinent morphological features such as crystallite size and spacing, degree of crystallinity, changes in DPS with composition and annealing temperature and predict their effect on the overall modulus. Both

the changes in modulus with composition and with annealing treatment can be satisfactorily explained with this model.

7.2.6 Effects of Orientation

In all the calculations, we have assumed perfect orientation of the crystalline chains ($f_c = 1$) and totally random orientation of the amorphous chains. Most of the samples used in this analysis have a fairly high level of crystalline orientation ($f_c > 0.7$) and virtually no amorphous orientation. Thus, the assumption made in the model regarding orientation is a fair approximation of the orientation in the actual samples.

The effects of crystalline and amorphous orientation on the macroscopic modulus could be calculated, however, by refining the model to take into account the variation of E_c and E_a with chain orientation. The modulus of the crystalline phase has been estimated to be around $10^{11}Pa$ when the chains are parallel to the stretch direction ($f_c = 1.0$) and 10^9Pa when they are perpendicular to the applied deformation ($f_c = -0.5$). The modulus of the amorphous phase ranges from about 10^9Pa when the chains are randomly oriented ($f_a = 0$) to no more than $10^{11}Pa$ in the unlikely case of perfect alignment with the stretch direction ($f_a = 1.0$). Once the upper and lower limits of E_c and E_a are known, rough estimates of the modulus of each phase can be made at intermediate values of f_c or f_a. In order to do a more rigorous analysis, one would need functions that describe how the modulus of each phase varies with orientation: $E_c = F(f_c)$ and $E_a = G(f_a)$. Thus, the effects of orientation on

the modulus can be examined in the context of the present modelling approach, but it was not deemed necessary for the present analysis of filament moduli.

7.3 Conclusions

These results show that the crystalline and amorphous phases in the copolyester filaments should be considered to be co-continuous. The crystallites are dispersed in an amorphous matrix, but are connected by tie molecules in the axial direction. Calculations of γ_c based on β_c and the estimated degree of crystallinity in these samples suggest that the crystallites do not impinge upon one another in the radial direction.

The model suggests that the number of tie molecules increases, in general, as the HSC increases; probably as a result of the longer hard segments and the shorter distance between crystallites. The number of tie molecules also increases as the degree of crystallinity increases. This is a result of the larger size of the crystallites and the greater number of physically cross-linked hard segments. The number of taut tie molecules may increase during annealing as a result of new crystal growth or as a result of a tightening of loose tie molecules as the crystallites thicken.

The modulus of the amorphous phase is raised by the presence of dissolved hard segments. The increase in the macroscopic modulus observed as HSC increases is probably the result of both an increase in the number of taut tie molecules and an increase in E_a as the fraction of hard segments dissolved

in the amorphous phase increases. The amorphous modulus decreases in any given composition as the DPS increases. This results from the increase in the weight fraction of soft segments in the amorphous phase as the dissolved hard segments crystallize.

Thus, the relationship between modulus and annealing temperature can be understood. The as-spun filaments have a relatively low DPS and only a few tie molecules. Upon annealing, the DPS and the number of tie molecules both increase. At large ΔT_u, there are too few taut tie molecules to have much effect on the modulus. The increase in DPS, however, causes the modulus of the amorphous phase to drop significantly resulting in a reduction of the macroscopic modulus. At small ΔT_u, the number of tie molecules has grown large enough to have a considerable influence on the macroscopic modulus. At some point, the increase in modulus caused by the tie molecules begins to outweigh the decrease caused by the drop in E_a. An increase in the macroscopic modulus is then observed.

CHAPTER 8

DEFORMATION BEHAVIOR AND MECHANICAL PROPERTIES OF THE MELT-SPUN FILAMENTS

8.1 Structural Changes During Deformation

The elastic behavior of these filaments are of primary concern. In order to gain more insight into their elastic behavior, one needs to understand how the microstructure reacts to externally applied deformations. Several fundamental questions about the elastic behavior arise. What part of the structure deforms during stretching? Does the microstructure deform in an affine manner? Is the original microstructure recovered upon release of the tension or are there permanent changes in the structure? In order to answer these questions, the deformation of the microstructure was studied using SAXS techniques. A highly phase separated filament of H4056 spun at 50 m/min was selected for this experiment. SAXS patterns were taken of the filament at various levels of strain and again after removal of the stress. The patterns taken in this manner are shown in Figure 8.1. The approximate elongations during stretching and the residual strains after allowing the filament to relax are given below each pattern.

At low elongations, the meridional reflection is in the form of an arc due to the orientation distribution of the lamellae. During stretching to low

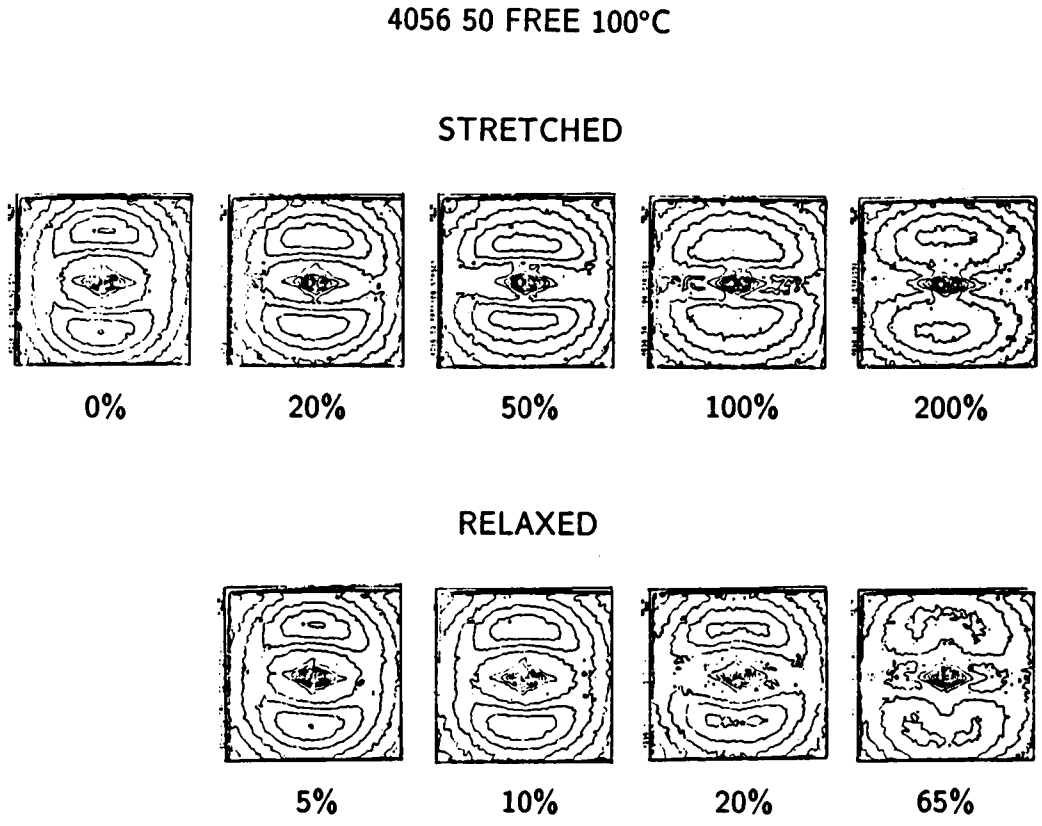


Figure 8.1: SAXS patterns of stretched (top row) and stretched and relaxed H4056 filaments (bottom row). The patterns of the relaxed filaments are shown directly below the corresponding patterns of the stretched filament. The residual strain of the relaxed filament is shown below the pattern.

elongations, the SAXS peak moves to lower angles, but the basic shape of the scattering pattern is retained. After allowing the sample to relax, patterns almost identical to the one from the original unstretched filament are obtained. Macroscopically, the filaments show a high degree of strain recovery from these low elongations.

Upon stretching to about 200%, the form of the reflection changes from an arc to a horizontal streak. This indicates that a major reorganization of the microstructure is taking place. The horizontal streak may arise from lamellae stacked parallel to one another, but having small lateral dimensions [181,78]. The original lamellae are apparently broken up into smaller chunks during large deformations. These lamellar fragments are aligned so that the chain axes are preferentially oriented toward the fiber axis. Scattering patterns obtained from the relaxed filaments are no longer identical to the original unstretched pattern so the change in the microstructure is irreversible. The horizontal streak produced at 200% elongation changes into an arc when the filament is allowed to relax, indicating that the lamellar chunks disorient upon release of the stress.

The mean square electron density fluctuations were calculated from the available intensity data. Due to the limited angular range of dectection in the 5 meter geometry used for the stretching experiment, a significant portion of the scattered intensity could not be measured. For this reason, the values of $\overline{(\rho - \bar{\rho})^2}$ are probably lower than they should be, but may be useful in showing trends. The results are reported as the ratio of the value for the stretched

filament to the value for the unstretched filament. The results are shown in Table 8.1. The ratio drops as the sample is stretched, but some of the loss is recovered when the filament is allowed to retract. The permanent loss in scattering power indicates an increase in phase mixing. There appears to be a strong correlation between the ratios calulated for the relaxed samples and the strain recovery measured during tensile testing. The higher the strain recovery the higher the scattering power of the relaxed sample. The results of the cyclic testing are reported in Section 8.3.

The patterns were further analyzed by taking one-dimensional data slices of the intensity in the meridional direction. The data slices corresponding to the stretched filaments and to the same filaments after retraction are shown in Figure 8.2. Long periods calculated from the peak maxima using Bragg's law are given in Tables 8.1 and 8.2.

At low elongations, the long period increases in almost direct proportion to the macroscopic deformation. There is little change in the shape of the peak, but there is a significant drop in intensity. This may indicate the DPS has been slightly reduced. When the filament is allowed to retract, the peaks move back close to their original position with only a small permanent loss of intensity. Thus, the changes in microstructure are largely reversible. This reversibility is the source of the good elastic recovery observed at low elongations.

As the strain is increased, the shape of the SAXS peak changes considerably. At 100% elongation, there is no longer a distinct periodicity and the intensity has dropped considerably. At 200%, the long period decreases

Table 8.1: Ratios of mean square electron density fluctuations.

INITIAL STRAIN	$\frac{<\eta^2>_s}{<\eta^2>_0}$	RESIDUAL STRAIN	$\frac{<\eta^2>_r}{<\eta^2>_0}$
20%	0.92	5%	0.98
50%	0.78	10%	0.91
100%	0.66	20%	0.82
200%	0.57	65%	0.68

Note: Values of $<\eta^2>$ for strained and relaxed filaments are expessed as a fraction of the value for the unstretched filament.

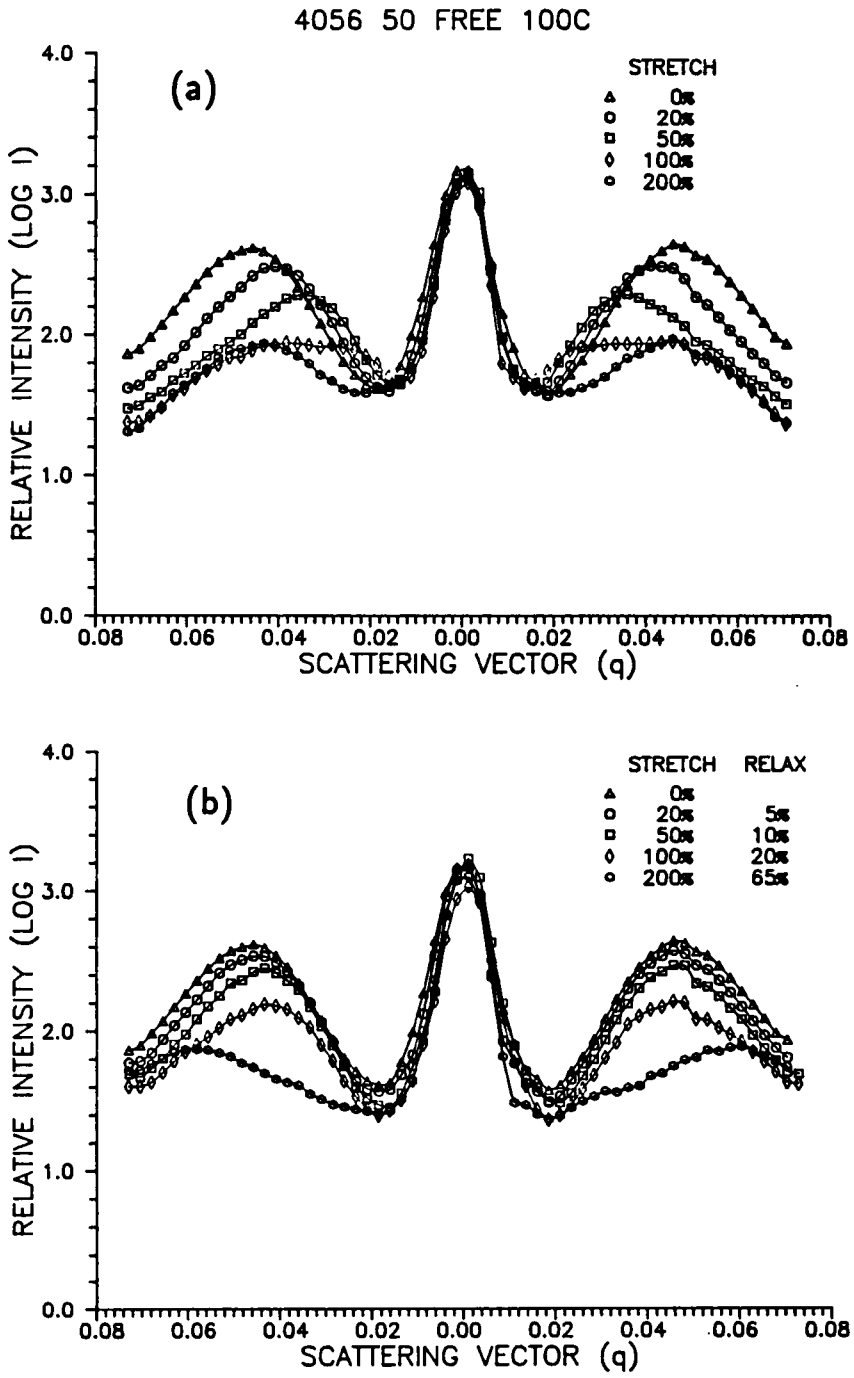


Figure 8.2: One-dimensional data slices in the meridional (fiber axis) direction corresponding to the SAXS patterns shown in Figure 8.1. (a) stretched filaments; (b) stretched and relaxed filaments. The scattering vector q is defined as $4\pi(\sin\theta)/\lambda$.

Table 8.2: Long periods observed for the H4056 filament in the strained state.

STRAIN	OBSERVED L.P. (Å)	EXPECTED L.P. IF AFFINE (Å)
0%	136	136
20%	151	163
50%	177	204
100%	~ 133–266	272
200%	~ 142	408

Table 8.3: Long periods observed for the H4056 filament after retraction.

INITIAL STRAIN	RESIDUAL STRAIN	OBSERVED L.P. (Å)	EXPECTED L.P. IF AFFINE (Å)
0%	0%	136	136
20%	5%	139	143
50%	10%	140	150
100%	20%	~ 141	163
200%	65%	~ 121	224

instead of increasing. Upon removal of the stress, the long period decreases further and some of the scattering power is recovered, but the basic shape of the curves is much different from that of the unstretched filament. The long period is much shorter than would be predicted from the residual strain in the filament assuming an affine deformation and recovery.

The stress-strain curve associated with the deformation of this H4056 filament is show in Figure 8.3. In the region below the yield point there is a rapid build-up in stress as the crystalline superstructure is deformed. The deformation of the microstructure is largely reversible in this region as shown by the SAXS experiment, and the filament exhibits good elastic recovery. In the region beyond the yield point, the stress builds up slowly with strain. This is associated with the irreversible deformation or "drawing" of the crystalline phase and poor elastic recovery.

These results show that at low elongations ($< 50\%$ in H4056), the crystalline domains are separated in an approximately affine manner. As the filament is stretched, the tie molecules and bridge segments begin to exert a force on the crystallites. This may cause translation, rotation, or bending of the lamellae, but with little permanent deformation at these low elongations. Lilaonitkul, West, and Cooper [114] have shown that in cast films both the hard and soft segments orient toward the stretch direction as the samples are deformed. The extension of the amorphous chains must account for most of the change in filament length, since the crystallites appear to remain fairly intact at these small deformations. When the stress is removed, the soft segments

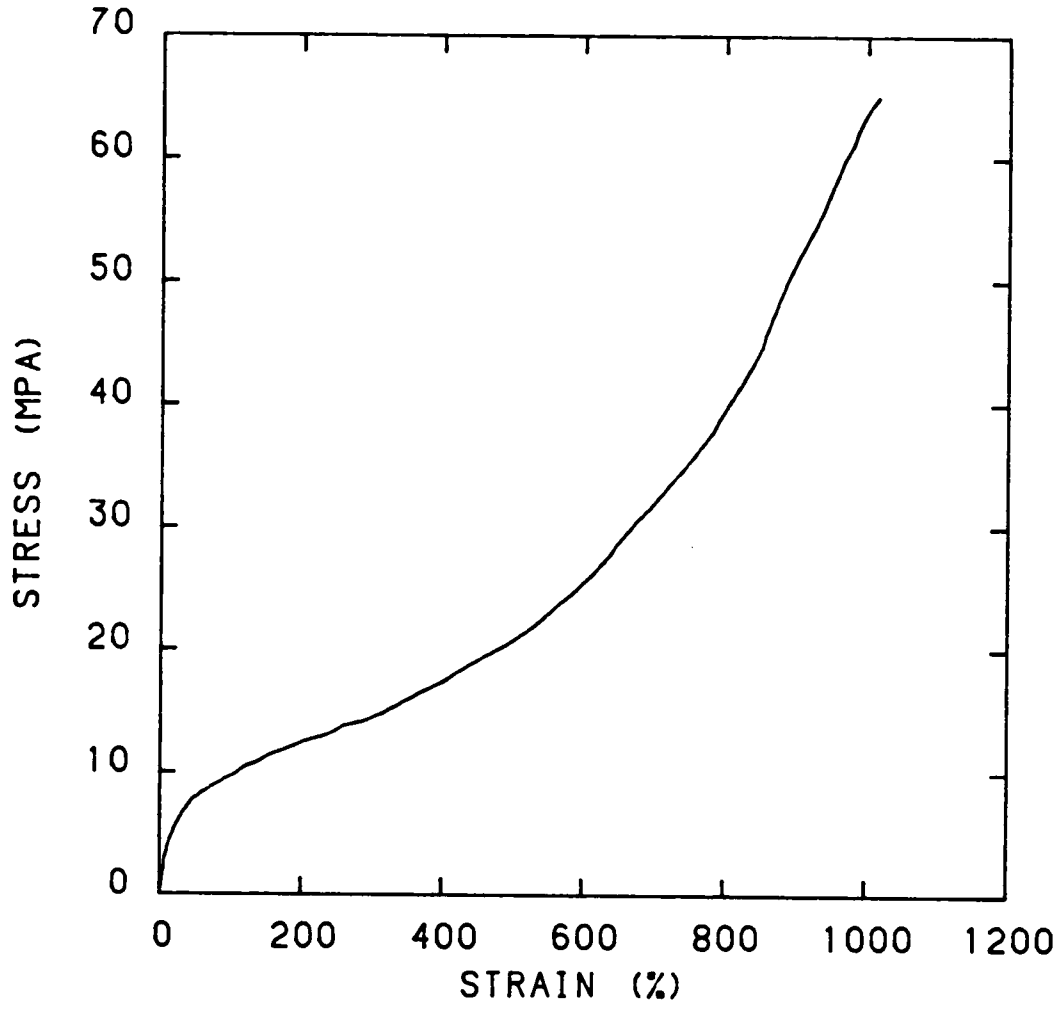


Figure 8.3: Stress-strain curve for a H4056 filament spun at 50m/min and free annealed.

quickly disorient and pull the crystallites back toward their original positions. Thus the deformation is largely reversible and good elastic properties are observed.

At higher elongations, the lamellae can no longer withstand the forces exerted on them by the tie molecules and taut bridge segments and they begin to tear apart as shown by the radial broadening of the SAXS peak at 100% elongation. As the crystallites are pulled apart from one another, the hard segments try to line up parallel to the stretch direction. At 200% elongation the original lamellae has been broken apart and a new microstructure consisting of smaller, more closely spaced crystallites has been produced as shown by the horizontal streak and the shorter long period. The small chunks are preferentially aligned with the hard segments parallel to the stretch direction, as shown by the lack of circumferential spread in the SAXS pattern.

Upon release of the stress, the amorphous chains quickly relax and the lamellar chunks are able to partially disorient. The permanent drop in scattering power is evidence that some phase mixing occurs as part of the irreversible deformation. Some of the hard segments apparently pull out of the crystallites and remain mixed with the amorphous phase. Energy lost to plastic deformation of the crystalline phase prevents the filament from fully recovering its original microstructure, and poor elastic properties are observed.

Void formation and bending of the lamellae, as proposed for elastic polypropylene filaments [145], does not appear to be a major part of the deformation mechanism in these filaments. There are no strong meridional streaks

in the SAXS patterns of these filaments that would indicate void formation between the lamellae.

The strong equatorial streaks in the SAXS patterns of cold drawn PTMT filaments are evidence of void formation and a fibrillar type structure. The weak equatorial streaks seen in the patterns of the copolymer filaments are most likely the result of reflection from the fiber surfaces rather than an indication of void formation.

8.2 Stress at Large Deformations

As the filaments are stretched past the yield point, the crystallites are being torn apart and extensive structural reorganization takes place. The drawing region extends from approximately 25% up to about 250% or higher depending on the sample. In this region of deformation, the level of stress in the annealed samples surpasses and remains higher than that of unannealed samples, except for H4056. In Figure 8.4, the stress at 150% strain is shown as a function of crystallite separation and annealing temperature. Two effects are noted. First, the stress goes down as the initial separation of the crystallites increases. This may be due to a decrease in the number of tie molecules which traverse the amorphous region between crystallites. This would be expected because of the decrease in the number and length of the hard segments as the HSC decreases (the HSC decreases in the figure from left to right along the curves). Also, the number of PTMT hard segments dissolved in the amorphous

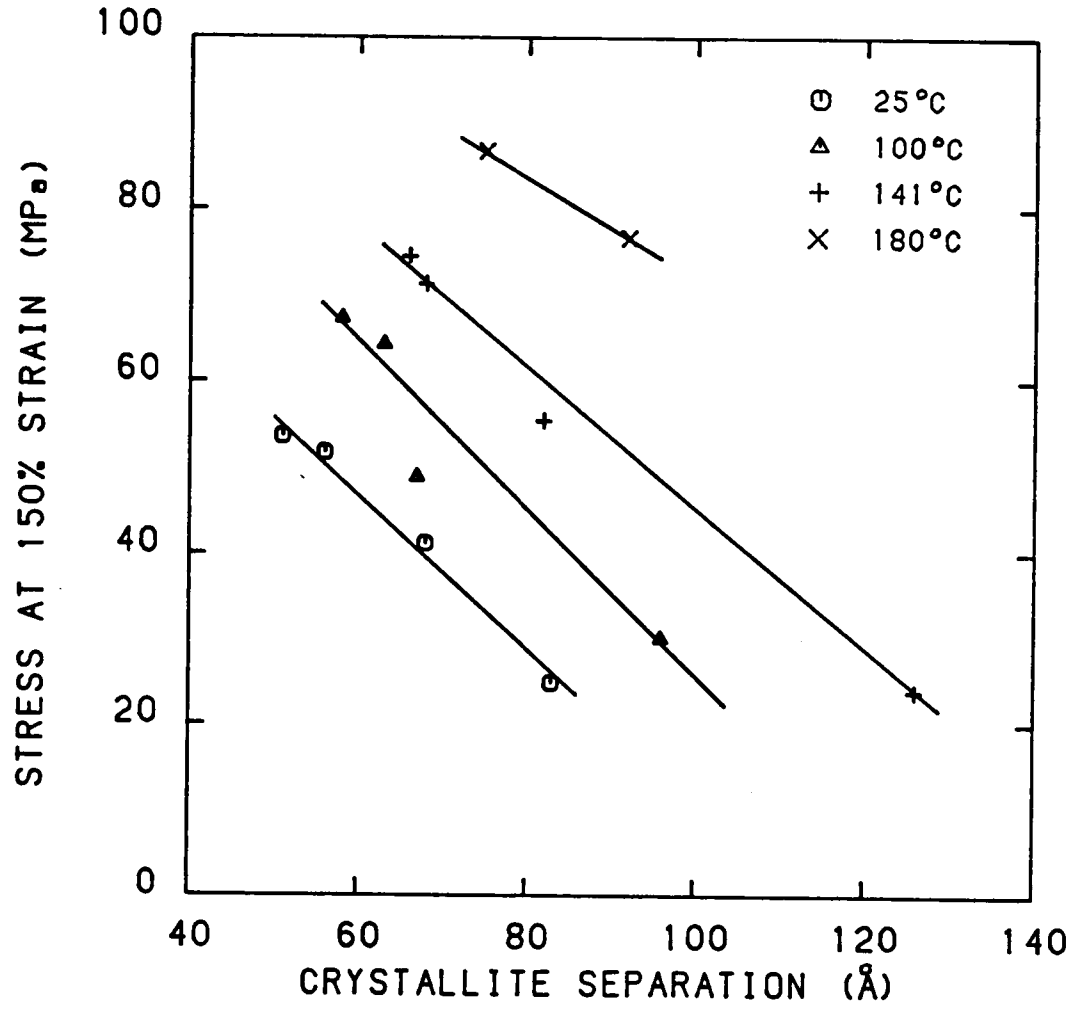


Figure 8.4: Stress at 150% strain as a function of crystallite separation. These filaments were spun at 300m/min and annealed at the indicated temperatures.

phase decreases as HSC is lowered as shown by the decrease in the glass transition temperature. Thus, the modulus of the amorphous phase decreases as HSC decreases. The second effect is that the stress increases as the annealing temperature goes up. (This trend is opposite to that noted for the modulus.) This might be expected due to the large increase in the size of the crystallites that occurs during annealing. The number of hard segment tie molecules would be expected to increase as the crystallites grow larger. Also the higher degree of crystallinity means a greater number of physically cross-linked soft segments (bridge segments). Both the increased number of tie molecules and bridge segments would result in a higher stress level as the filaments are stretched to large deformations. This interpretation of the behavior is consistent with the "solution-tie molecule model" discussed in Chapter 7.

8.3 Elastic Properties

In order to quantitatively investigate the elastic properties, the filaments were subjected to cyclic testing on an Instron tensile tester. The procedure was described in Section 3.8.2. The cyclic stress-strain behavior of the H4056 sample on which the SAXS experiment was performed is shown in Figure 8.5. The strain recovery and work recovery at each elongation were calculated from the extension and retraction curves as previously described. The strain recovery and work recovery are shown as a function of elongation in Figure 8.6. High strain recovery ($> 90\%$) is obtained at elongations up to 50%. The high

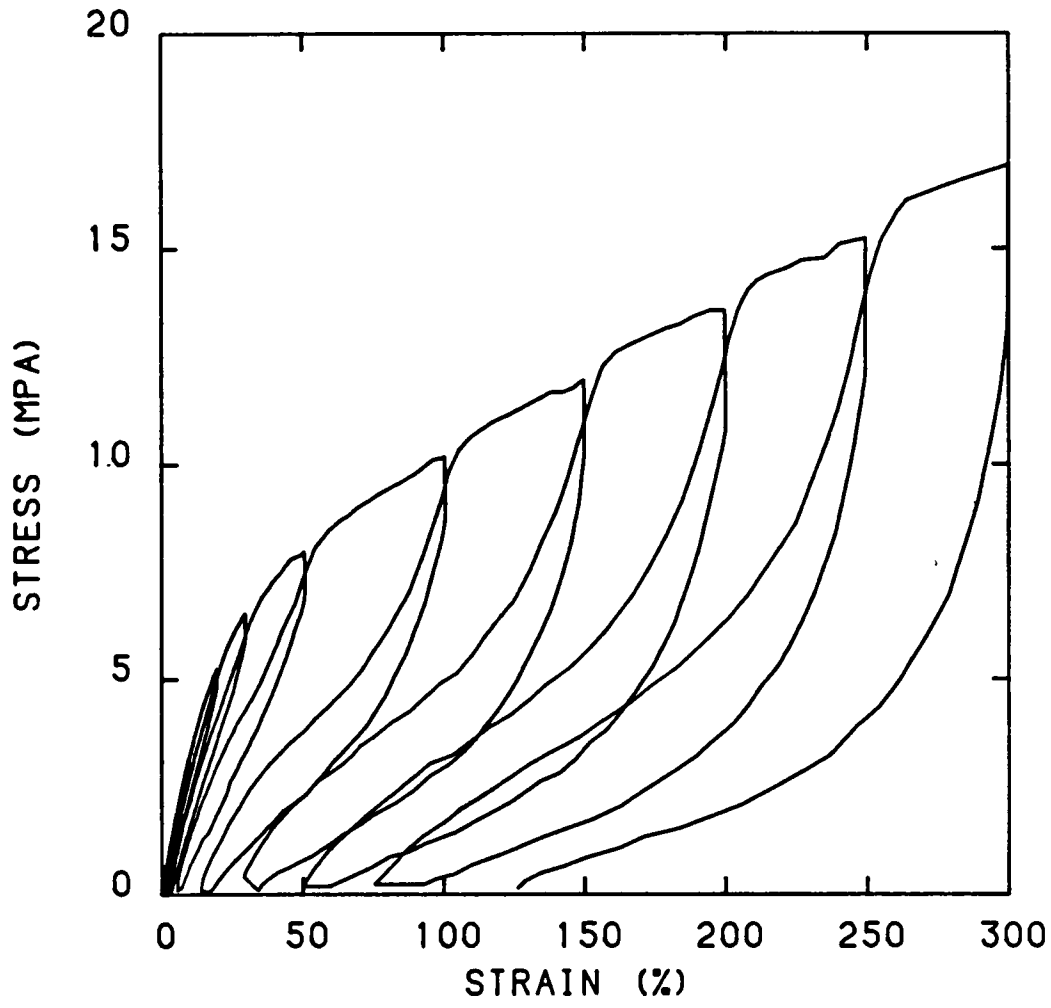


Figure 8.5: Cyclic stress-strain behavior of an H4056 filament. The filament was spun at 50m/min and free annealed at 100°C.

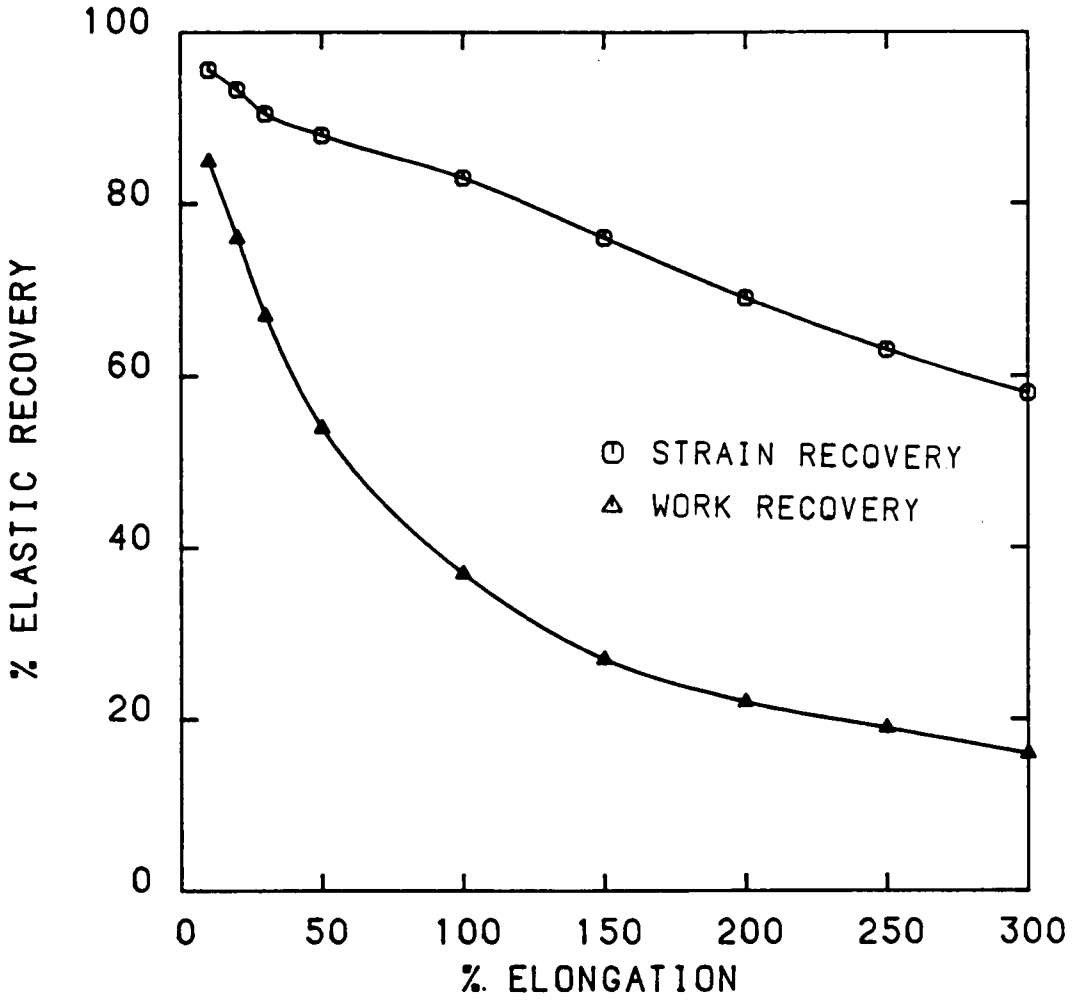


Figure 8.6: Strain recovery and work recovery calculated from the cyclic data shown in Figure 8.5.

strain recovery is associated with the reversible deformation of the microstructure discussed in Section 8.1. The strain recovery gradually decreases as the filament is stretched to higher elongations. The work recovery is high at very low elongations ($< 10\%$), but drops rapidly as elongations are increased. The energy losses are associated with plastic deformation of the crystalline regions and hysteresis. The hysteresis may be due to reorientation of crystallites and viscoelastic effects in the amorphous phase.

The work recovery is always lower than the strain recovery, since the latter is only a measure of dimensional changes and does not take into account the retractive force. The H4056 sample can exhibit a high level of elastic recovery even when there is only a low level of work recovery. Apparently, a relatively small portion of highly strained elastic chains are enough to allow the filament to recover a large portion of its original dimensions, albeit with only a low retractive force.

The effect of SDR and annealing treatment on the elastic properties of H4056 can be seen in Figures 8.7 and 8.8. An increase in SDR from 50 to 250 m/min produces a small increase in the strain recovery due to the higher orientation of the hard segments. The work recovery is less for the sample spun at 250m/min than for the one spun at 50m/min. This behavior is not typical of the copolyester filaments in general. The filament spun at 250m/min has a much steeper stress-strain curve than the 50m/min sample, and breaks at a much lower elongation. If the work recovery is plotted as a function of the relative or normalized strain (elongation/ultimate elongation) (not shown), the

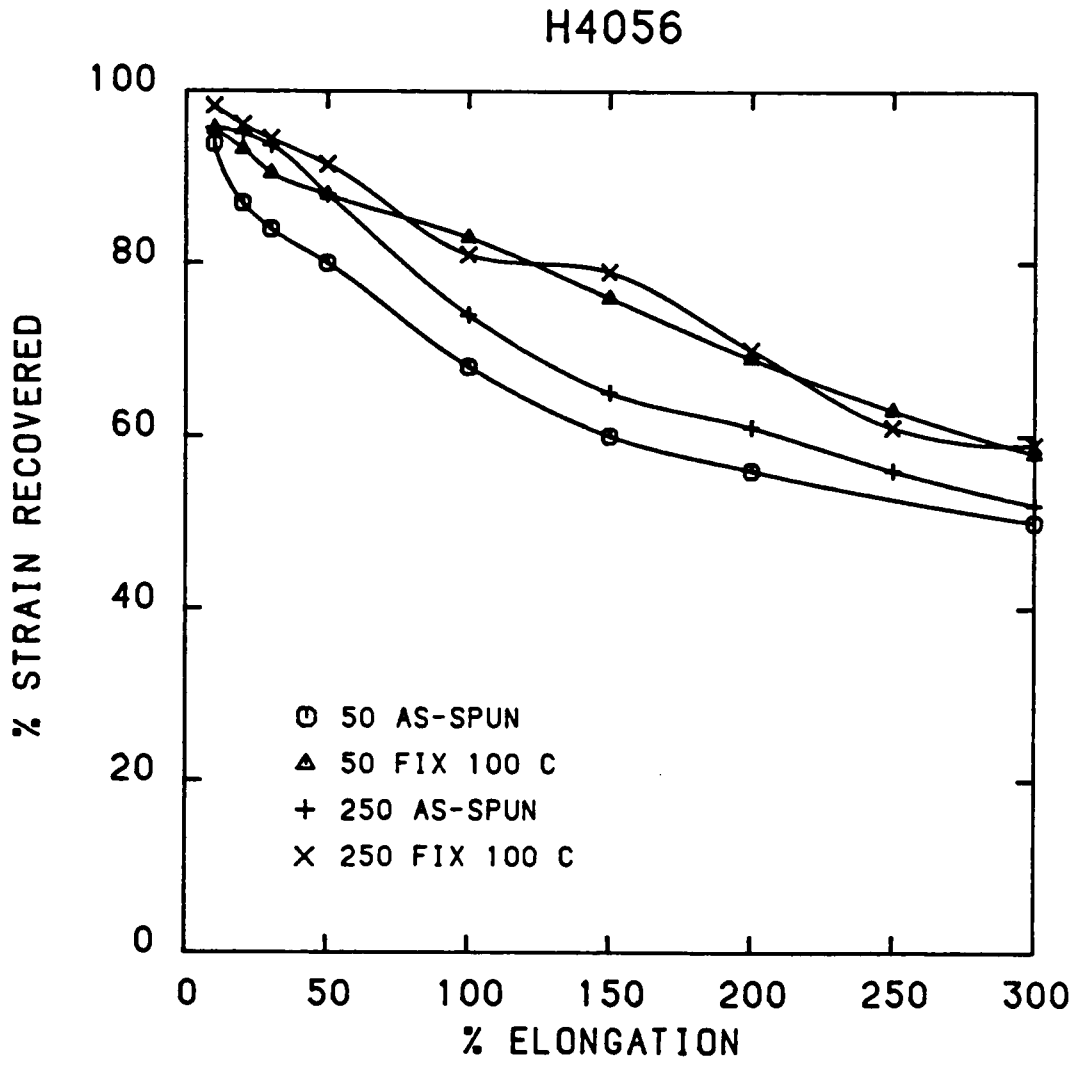


Figure 8.7: Strain recovery of H4056 filaments of different SDRs before and after fixed annealing at 100°C.

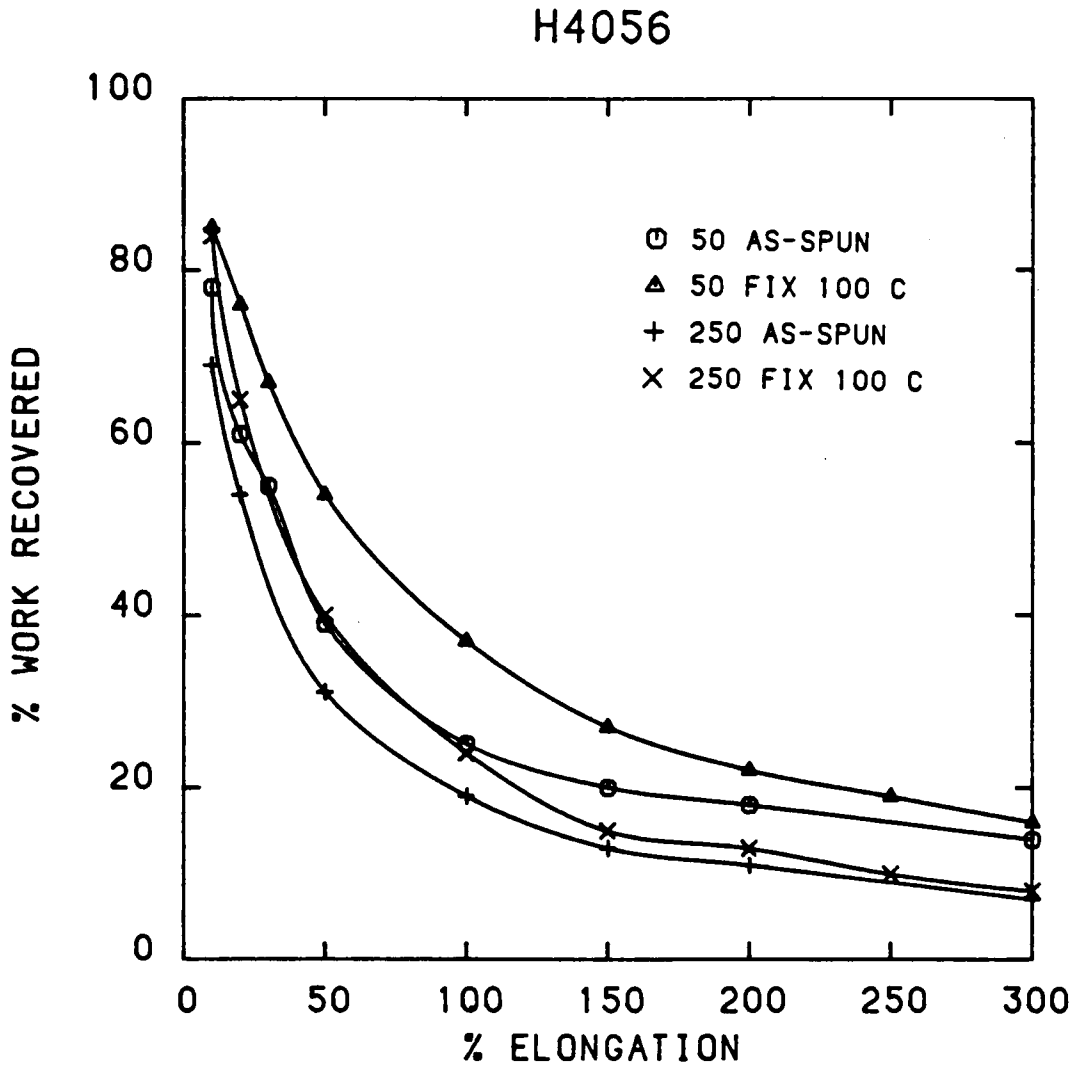


Figure 8.8: Work recovery of H4056 filaments of different SDRs before and after fixed annealing at 100°C.

two filaments show about the same work recovery.

Annealing produces gains in both the strain and work recovery of each filament by reducing the number of hard segments dissolved in the elastomeric phase. This reduces the modulus of the amorphous phase as discussed in Chapter 7. Also, the reduction in the number of small crystallites and the increase in the size and perfection of the larger crystallites may serve to lower plastic deformation.

The elastic properties of H7246 filaments are shown in Figures 8.9 and 8.10. The unannealed filaments have a very low DPS and exhibit poor elastic properties. Increasing the SDR produces higher levels of crystallite orientation and results in higher strain recovery and work recovery at low elongations. As f_c is increased, there is less tendency for the crystallites to reorient at low elongations and they are more resistant to shear. Annealing greatly increases both the strain and work recovery of these filaments due to the large increase in the DPS.

The effect of composition can be readily seen by comparing Figures 8.7 and 8.9 or Figures 8.8 and 8.10. The greater fraction of PTMEG and fewer tie molecules in the H4056 filaments results in superior elastic properties compared to the H7246 filaments. The H7246 filaments can be made to approach the elastic performance of H4056 at very low elongations, but plastic deformation of the crystallites at higher elongations causes the elastic recovery of H7246 to drop off much more rapidly than in H4056.

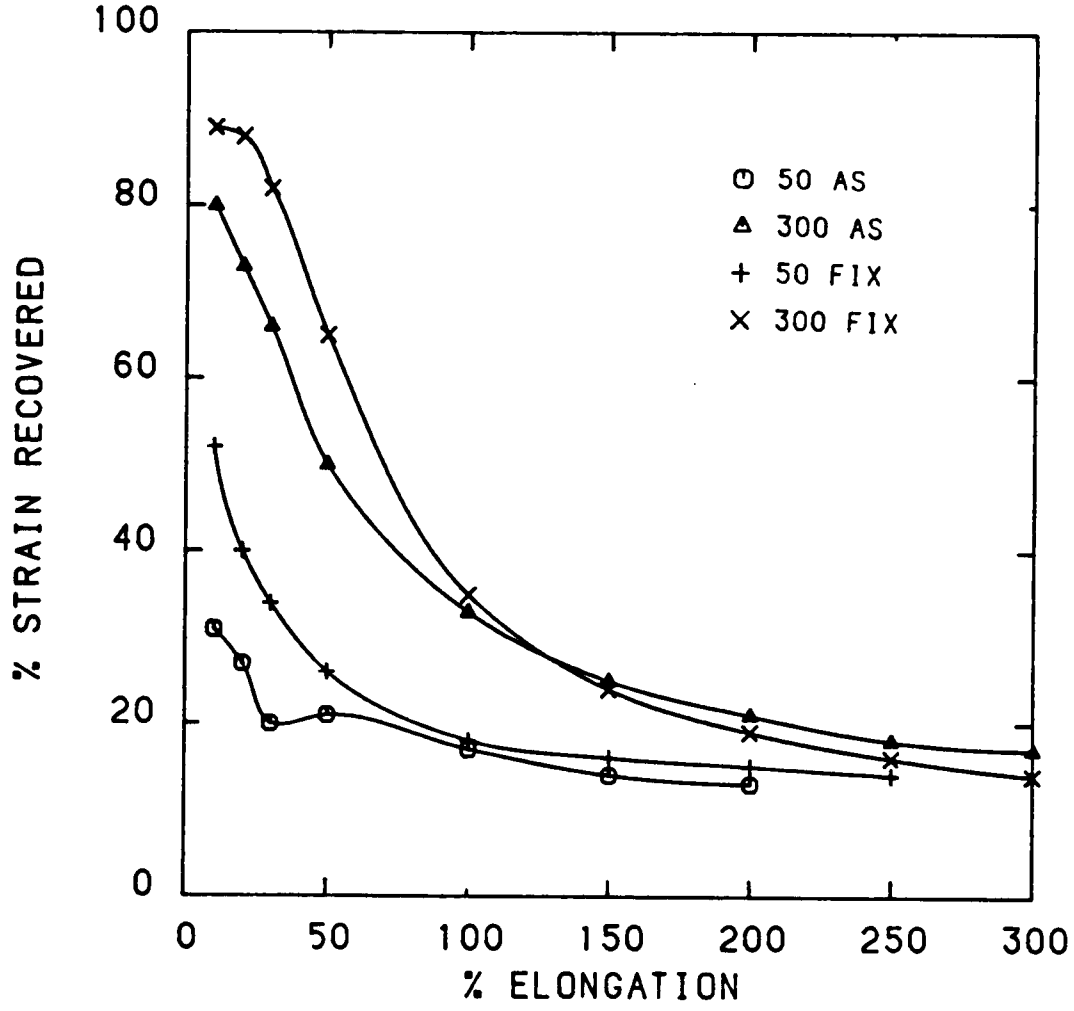


Figure 8.9: Strain recovery of H7246 filaments of different SDRs before and after fixed annealing at 180°C.

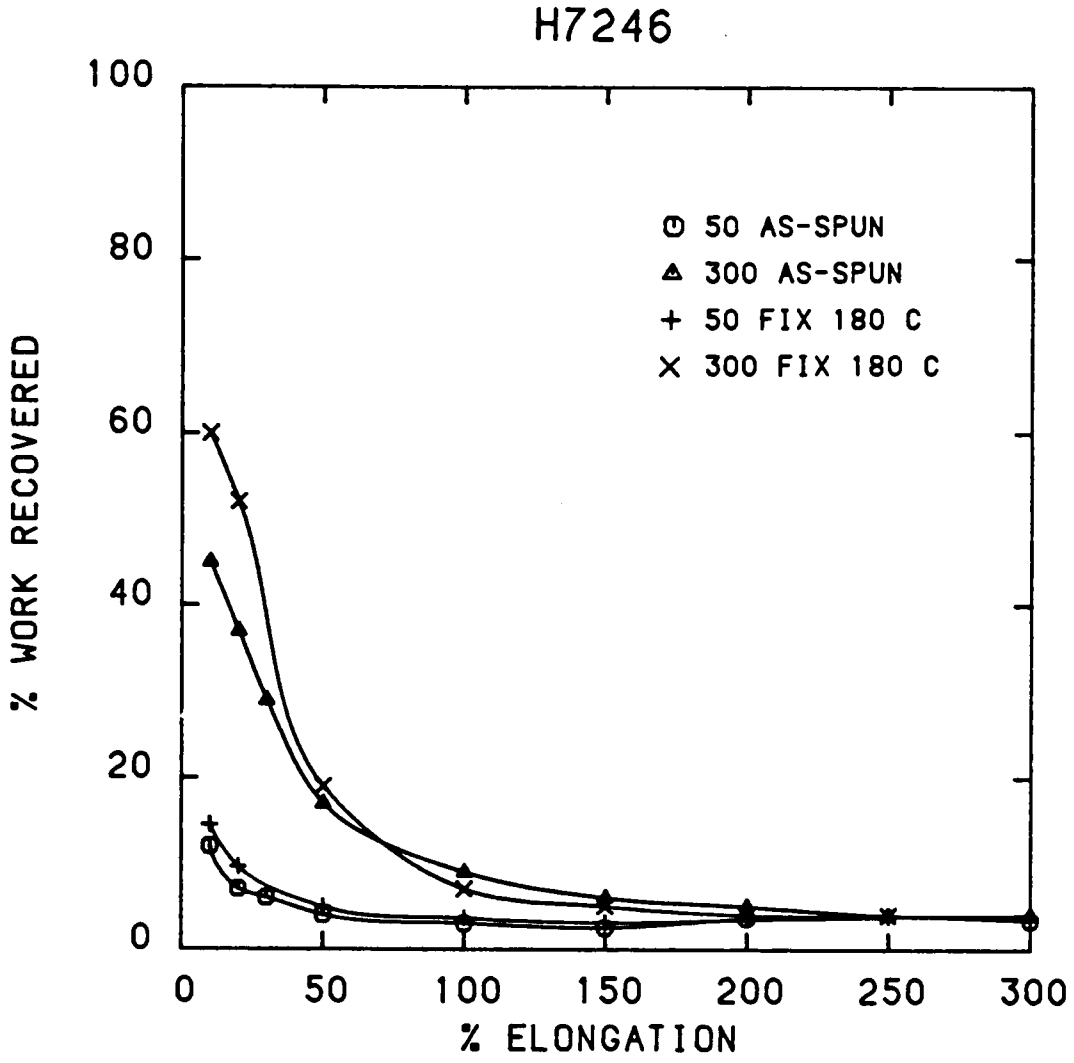


Figure 8.10: Work recovery of H7246 filaments of different SDRs before and after fixed annealing at 180°C.

8.4 Ultimate Properties

8.4.1 Elongation to Break

Elongations to break from about 7 to 9.5× were observed, depending on the composition, for filaments spun at low speed. These compare with values of 3.5 to 5.5× reported for films [211]. The ultimate elongation of the as-spun filaments drops as SDR increases. This is directly related to the increase in f_c as shown in Figure 8.11. The PTMT filaments remain amorphous and show less dependence on SDR. Stress-strain curves of PTMT filaments at all SDR's show a considerable amount of necking and drawing behavior. Figure 8.11 also shows that the ultimate elongation increases as HSC decreases for a given value of f_c. This is due to the increase in the number of highly coiled amorphous chains as HSC decreases.

Filaments low in HSC show an increase in ultimate strain upon annealing, while those from the PTMT homopolymer show a decrease. This is illustrated in Figure 8.12. Filaments from the intermediate compositions show little change. Both the amount of hard segment drawing and soft segment stretching play a role in determining the ultimate elongation. In H4056, stretching of the elastomeric phase appears to be the dominant factor. Since annealing reduces the number of hard segments dissolved in the amorphous phase and increases the distance between physical cross-links, the PTMEG chains are more free to stretch. In the PTMT homopolymer, the increase in crystallinity upon annealing causes the filament to be less ductile. In the intermediate compositions,

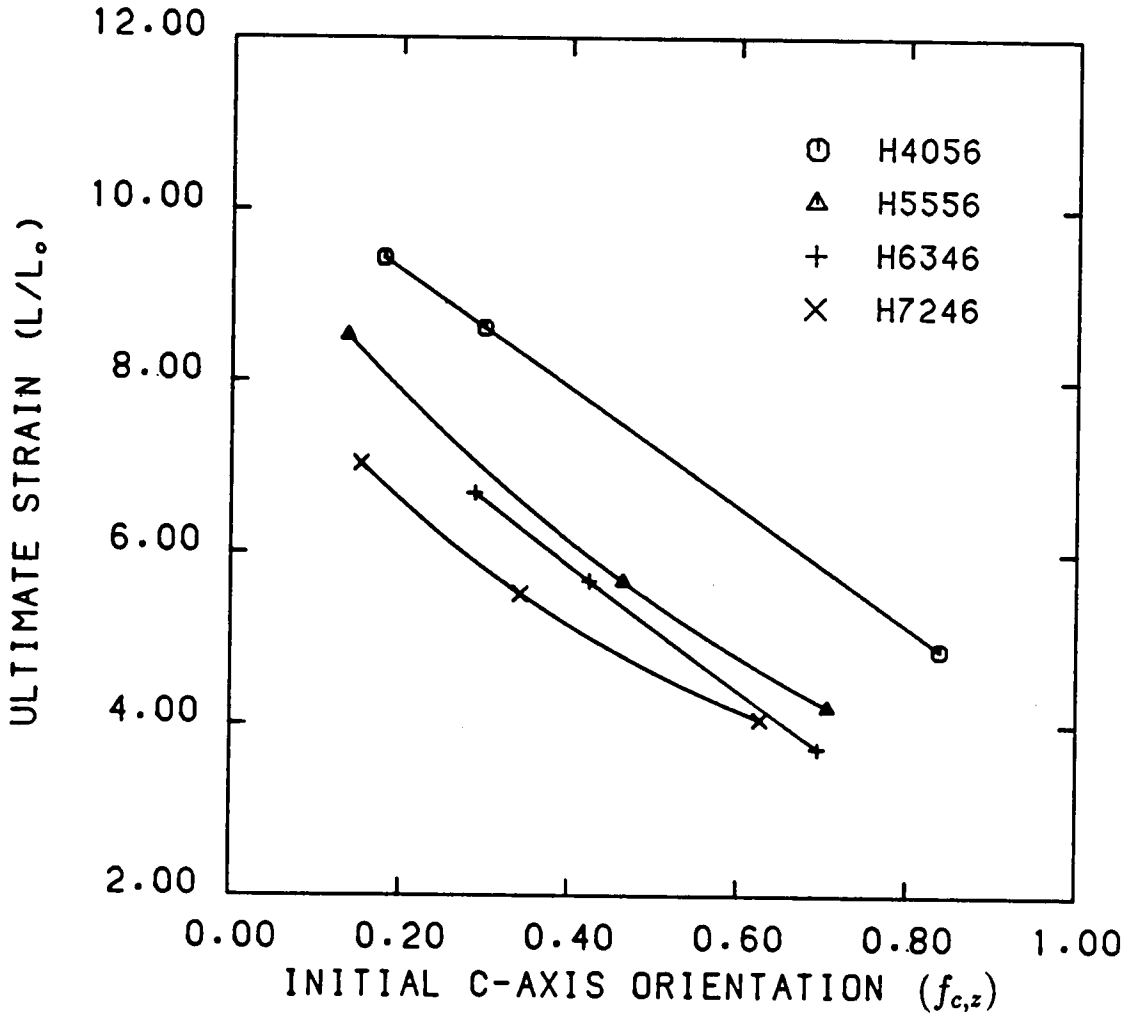


Figure 8.11: Relationship of ultimate elongation to composition and crystalline orientation.

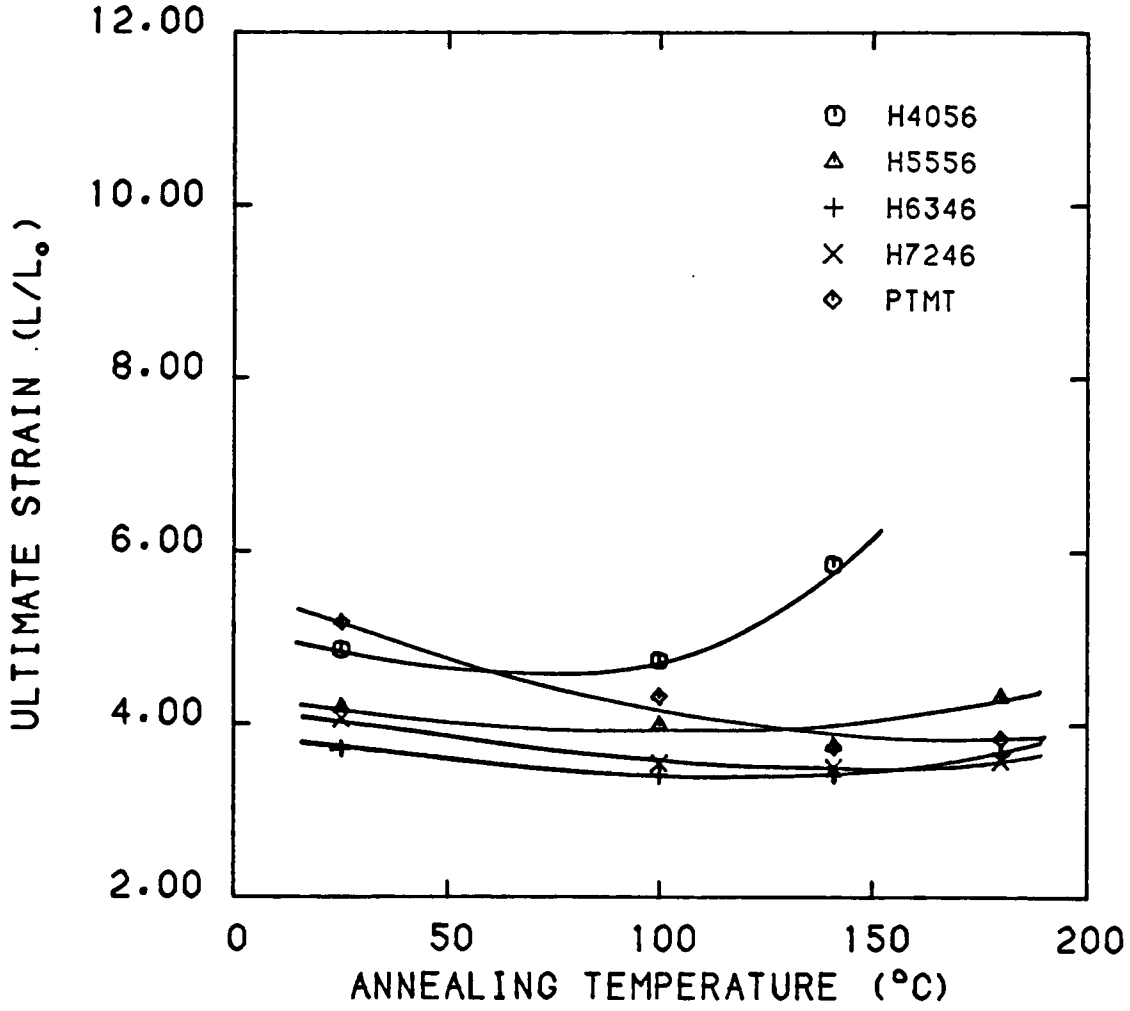


Figure 8.12: Relationship of ultimate strain to composition and annealing temperature.

these two factors seem to balance each other and little change in the maximum elongation is observed. Also, much of the domain structure is destroyed during testing so that the initial DPS has only a secondary effect on ultimate properties. Thus, the the elongation to break depends more on the initial degree of orientation than on the degree of phase separation in a given sample.

8.4.2 Tenacity

Tenacities in the range of about 70 to 150 MPa were measured for the copolymer filaments depending on composition. Abhiraman [1] has reported values of around 50 to 125 MPa for PTMT/PEO filaments that were 45-50 wt-% PTMT. Unoriented films of PTMT/PTMEG have tenacities of only about 25–40 MPa [211]. For comparison, elastic filaments of polypropylene have been reported with tenacities of 100–450 MPa [145]. Polyester fibers produced by high speed spinning have tenacities in the range of 100 to 600 MPa [169].

The tenacity of the unannealed copolymer samples increases with increasing HSC and increasing initial crystallite orientation as shown in Figure 8.13. The higher initial orientation results in more chains being aligned in the fiber axis direction at high elongations, increasing the fiber strength. The increase in tenacity with HSC results from the higher tenacity of the PTMT phase.

The filaments spun at 250 to 300m/min were annealed at several elevated temperatures. Figure 8.14 shows that annealing does not change the tenacity of the filaments very much, except in H4056. This is in contrast to

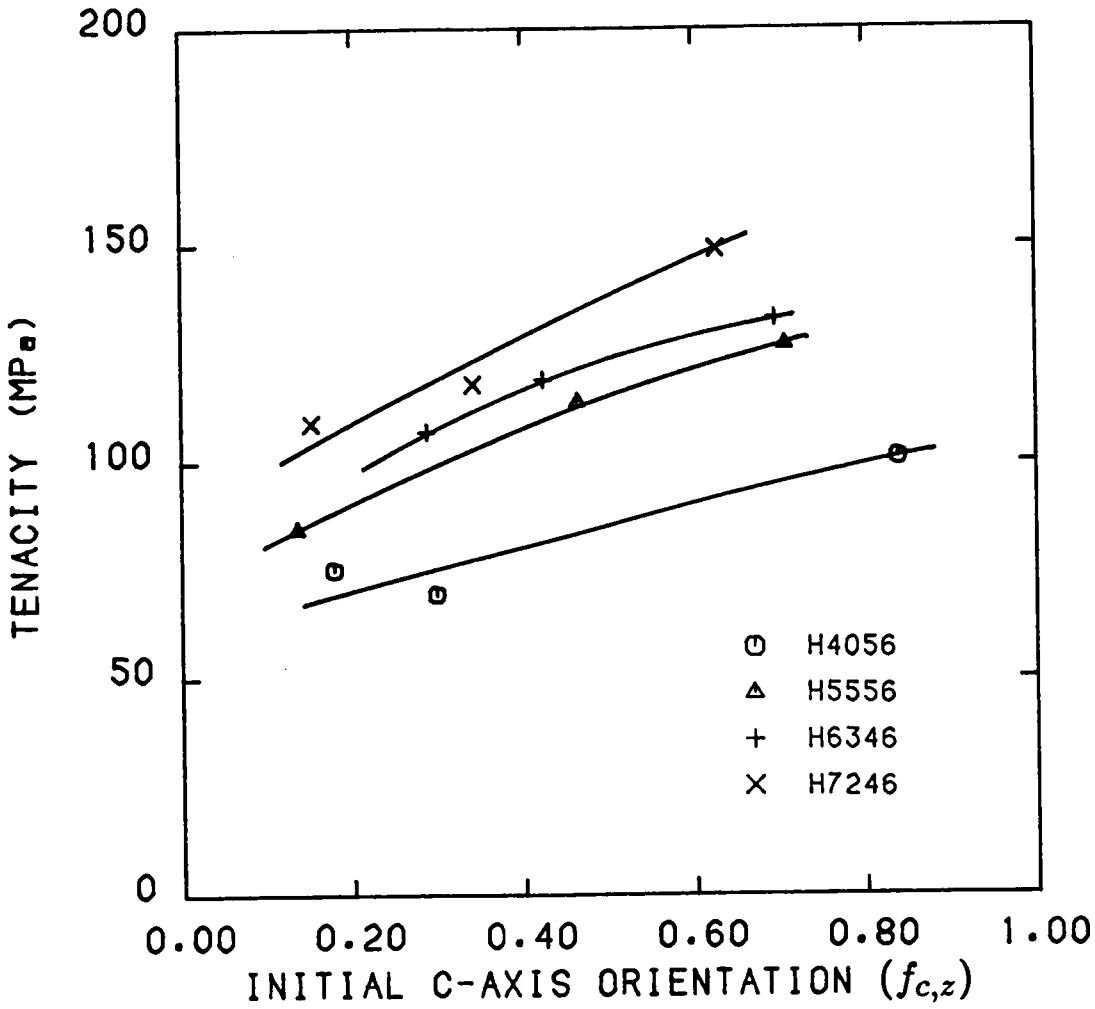


Figure 8.13: Tenacity as a function of crystalline orientation.

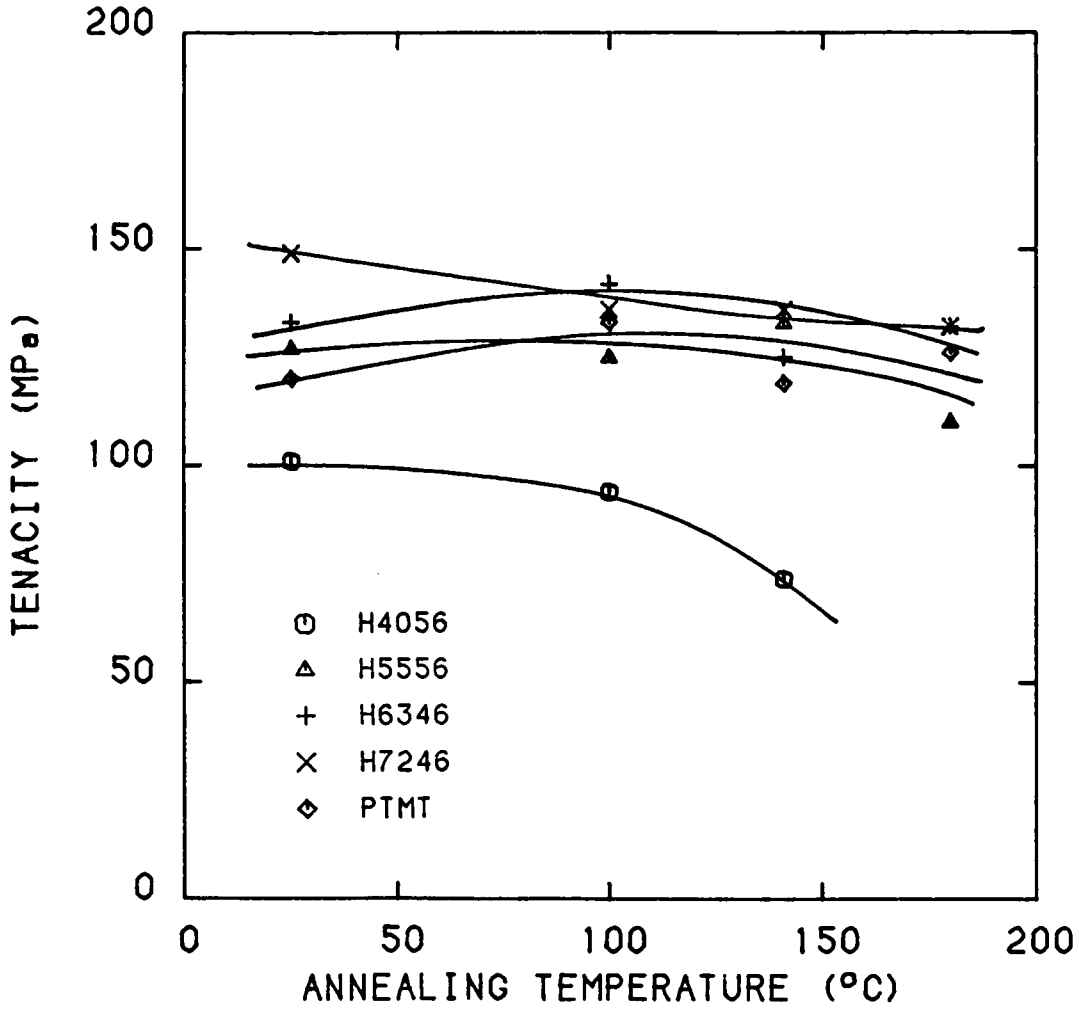


Figure 8.14: Tenacity as a function of annealing temperature for each composition.

the effect of annealing on other mechanical properties such as drawing stress. However, since much of the domain structure is destroyed by drawing to high elongations, the initial degree of phase separation within a particular composition has only a minor effect on ultimate strength. The tenacities of the H6346 and H7246 filaments are in several cases equal to or greater than those of the undrawn PTMT filaments. The PTMT filament would be expected to have the highest tenacity, but the higher c-axis orientation developed in the copolymers may override the effect of composition. Also, the compositions high in HSC may be thought of as "rubber-modified" PTMT. The better energy dissipation mechanism afforded by the domain structure of the copolymers may contribute to the higher tenacity of these filaments [21].

8.5 Conclusions

SAXS experiments show that the microstructure deforms in a nearly affine manner at low elongations and that the original microstructure is recovered upon release of the stress. At low elongations (below the yield point), the crystalline network is distorted but little permanent deformation of the crystalline domains takes place. Most of the deformation takes place in the elastomeric phase. Upon removal of the macroscopically applied strain, the elastomeric chains retract and pull the crystallites back close to their original positions.

At elongations past the yield point, the stresses exerted on the crystal-

lites by the tie molecules and taut bridge segments exceed the cohesive forces within the crystallites and plastic deformation takes place. This is the source of the "permanent set" observed macroscopically.

The stress at large deformations increases as HSC increases because of more dissolved hard segments in the amorphous phase and an increase in the number of tie molecules between crystallites. The stress increases upon annealing as the crystallites grow larger. This is believed to result from an increase in the number of tie molecules and physically cross-linked elastomeric chains. The bridge segments seem to play a more important role in determining the stress at large elongations than they do in determining the modulus.

The elastic properties are influenced greatly by the microstructure of the filaments. The relative amounts of each phase, the size and spacing of the crystallites, the degree of phase separation, the number and configuration of the tie molecules, and the orientation of the crystalline and amorphous chains all influence the elastic behavior. The composition determines the relative amounts of each phase and to some extent the number of tie molecules. As HSC decreases, the crystallites are spaced further apart and the hard segments become shorter. Both effects make it more difficult for a PTMT segment to bridge the amorphous region between crystallites. Fewer hard segment tie molecules mean less plastic deformation. Thus, much better elastic properties are observed in H4056 than H7246. Annealing promotes phase separation and reduces stresses in the amorphous phase. A greater DPS results in higher elastic recovery by increasing the number of amorphous chains that are cross-linked and by driv-

ing dissolved hard segments out of the elastomeric phase. Increasing the SDR increases the orientation of the crystalline chains and produces lamellae that are preferentially aligned with their long axis perpendicular to the fiber axis. This reduces rotation and shearing of the lamellae during stretching since the crystalline chains are aligned in the direction of the applied force.

In the copolyester filaments, tenacity increases as HSC and crystalline chain orientation increase. Filaments high in HSC may, in some cases, exhibit higher breaking stresses than pure PTMT filaments as a result of the energy dissipation mechanism provided by the domain structure. The elongation to break is reduced as HSC and orientation increase. Much of the domain structure is destroyed during very large deformations, and as a result, the initial DPS has only a secondary effect on these properties. Thus, the HSC and orientation of the hard segments play a significant role in determining the fracture behavior, while the DPS has only a minor effect.

CHAPTER 9

DRAWN FILAMENTS

9.1 Introduction

In the previous chapter it was shown that there is a large amount of plastic deformation in the copolyester filaments during stretching. It is desirable to reduce the amount of plastic deformation for several reasons. The ratio of stretching force to retractive force would be reduced, producing an increase in work recovery. "Permanent set" of the filament would be reduced, resulting in an increase in elastic recovery. Also, the filaments would have a greater strength at lower elongations.

Cyclic loading to a given elongation has been shown to reduce the stress during extension in polyurethane filaments [44]. Perhaps the same results can be achieved with the copolyester filaments. Figure 9.1 shows the stress-strain behavior of a filament of H4056 during cycling to 250% elongation. The second extension curve is at a much lower force level than the first, while the second retraction curve coincides almost exactly with the first. In subsequent cycles, the force during extension is reduced further by small increments. After about five cycles the reduction becomes insignificant. The retraction curve follows the same path in every cycle.

The area under the initial extension curve can be divided into three

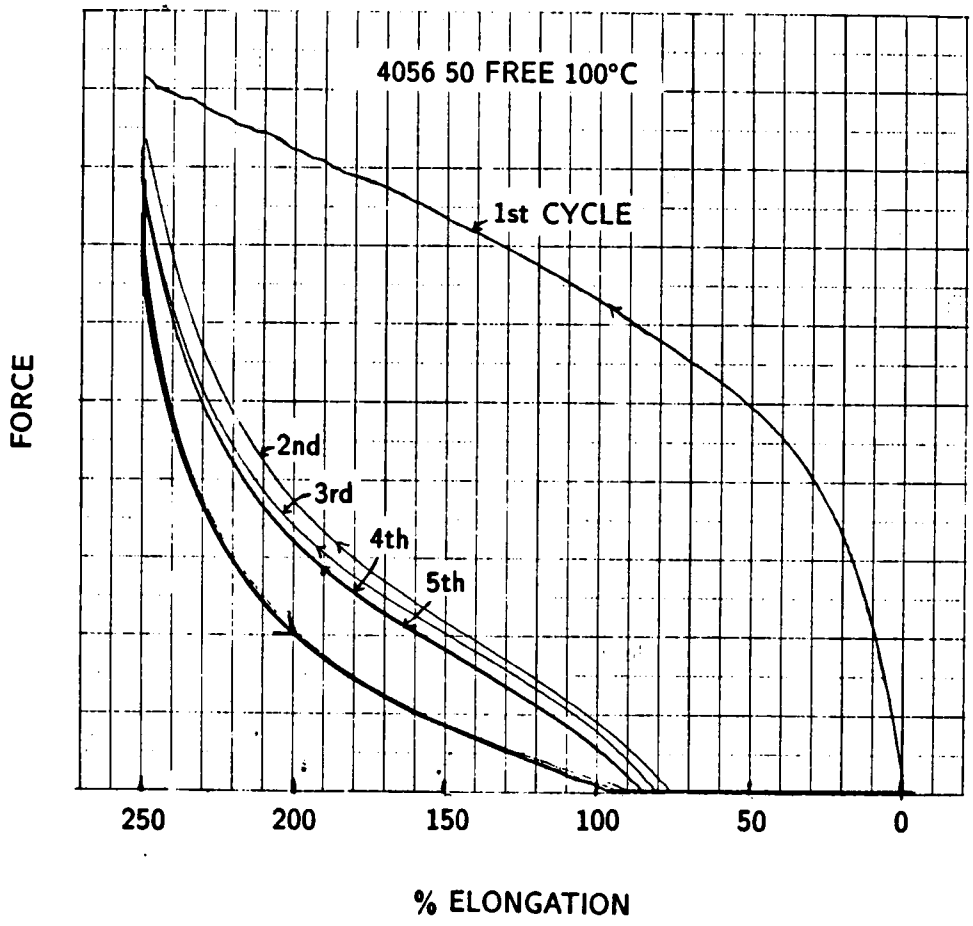


Figure 9.1: Stress-strain behavior of a H4056 filament during cycling to 250% elongation. The filament was spun at 50m/min and then annealed at 100°C to insure a high DPS.

regions. The area between the initial extension curve and the fifth extension curve is proportional to the work lost as plastic deformation. The area between the fifth extension curve and the retraction curve is proportional to the work lost to hysterisis, and the area under the retraction curve represents the work recovered due to elastic retraction.

Although five cycles are required to produce the maximum reduction in plastic deformation, most of the reduction occurs in the first cycle. These results suggest that drawing may be a viable path to enhanced elastic properties by reducing plastic deformation. Drawing may also provide a means of producing high strength elastic fibers, such as those needed for medical sutures.

9.2 Drawing and Annealing Treatment

Both the effects of spin draw ratio and draw temperature on the drawing behavior and final structure of the filaments need to be determined. For this reason, filaments spun at both low and high spinning speeds (50 and 300 m/min) were drawn. The low SDR filaments were drawn at two temperatures: one set at 25°C, and the second set at an elevated temperature. There was some debate as to what the higher temperature should be, but 100°C was finally selected for the following reasons. First, it is well above the T_g of all the compositions, but not so high as to cause partial melting and sticking of the filaments on the hotplate. This temperature is low enough to avoid degradation of the sample during drawing. The second reason for selecting 100°C is

that all the compositions could be drawn at this temperature, eliminating the the variable of different draw temperatures for different compositions.

The apparatus used to draw the samples is shown in Figure 9.2. The equipment includes two godets and speed controllers, a one meter long hot-plate and temperature controller, and a Leesona winder to take-up the drawn filament. The hotplate was removed for cold-drawing. With this set-up, filaments could be drawn continuously. The feed velocity (V_1) of the filaments was 10m/min in all cases. The velocity at the second godet (V_2) determines the nominal draw ratio (V_2/V_1). The residence time on the hot plate can be closely estimated from the final velocity since the draw zone tends to be very close to the front edge of the hotplate. The approximate residence times would then range from about 1.5 sec at V_2 = 40m/min to about 1.0 sec at 60m/min.

The 50 m/min samples were selected for cold drawing rather than the 300 m/min samples because of their greater load bearing capacity and their resistance to breakage in the drawing apparatus. At low draw ratios the H7246 filaments would not draw evenly, leaving lengths of completely undrawn material. Filaments from all compositions were drawn to their natural draw ratio to ensure complete and even drawing. A distinct neck was observed in H7246 and PTMT. The PTMT filaments could not be fully drawn using the drawing apparatus. The filaments would partially neck then break before completely drawing. These filaments had to be drawn manually at a slower rate to remove all undrawn portions.

Both "50 m/min" and "300 m/min" samples could be easily hot drawn.

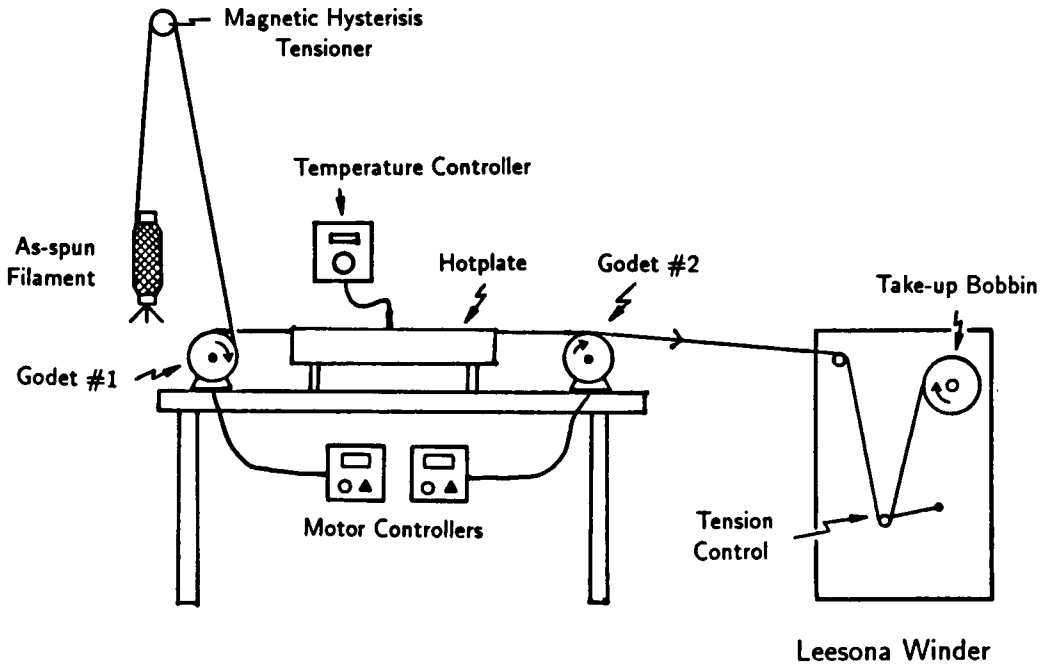


Figure 9.2: Schematic of continuous drawing apparatus.

At this temperature the neck in H7246 and PTMT is much less prominent and the draw ratio needed for even drawing is much less critical. Thus, the same draw ratio could be used for all compositions. The "50m/min" filaments were drawn 5×, while the "300m/min" filaments were drawn 3×.

A Zimmer© diameter monitor and an IBM personal computer were used to collect and statistically analyze diameter data. A description of this equipment has been given in a dissertation by Jayendra Bheda [19] of our laboratories.

The diameters of the filaments were measured before drawing (D_1), during drawing (D_2), and after drawing and relaxation at room temperature (D_3). The diameter ratio $(D_1/D_2)^2$ is a measure of the applied draw ratio and should be approximately equal to the velocity ratio V_2/V_1 during drawing:

$$(\frac{D_1}{D_2})^2 = \frac{L_2}{L_1} = \frac{V_2}{V_1} \tag{9.1}$$

where L_1 is the length of a given mass of filament before drawing and L_2 is the length of the same mass during drawing. The diamenter ratio $(D_1/D_3)^2$ represents the residual draw ratio after the filaments elastically contract:

$$(\frac{D_1}{D_3})^2 = \frac{L_3}{L_1} \tag{9.2}$$

where L_3 is the length of a given mass of filament after drawing and subsequent relaxation under no stress at room temperature. L_3 is significantly smaller than L_2 due to elastic retraction of the filaments after the drawing stress is removed. The applied draw ratios and residual draw ratios of the drawn filaments are shown in Table 9.1.

Table 9.1: Draw ratios and diamenters of drawn filaments.

	V_2/V_1	D_1	D_2	D_3	$(D_1/D_2)^2$	$(D_1/D_3)^2$
Cold Drawn (25°C)						
H4056 50	6.0	301	119	158	6.4±0.5	3.6±0.3
H5556 50	5.5	325	139	157	5.5±0.4	4.3±0.3
H6346 50	4.2	305	150	162	4.1±0.6	3.5±0.5
H7246 50	5.0	313	143	157	4.8±0.6	4.0±0.4
PTMT 50	–	290	–	151	–	3.7±0.3
Hot Drawn (100°C)						
H4056 50	5.0	301	140	163	4.6±0.5	3.4±0.3
H5556 50	5.0	325	–	144	–	4.1±0.3
H6346 50	5.0	305	138	160	4.9±0.6	4.1±0.5
H7246 50	5.0	313	153	150	4.2±0.4	3.8±0.5
PTMT 50	5.0	290	137	143	4.4±0.5	4.1±0.6
Hot Drawn (100°C)						
H4056 250	3.0	123	64	70	3.7±1.7	3.1±1.6
H5556 300	3.0	132	68	81	3.8±1.1	2.7±0.6
H6346 300	3.0	135	69	78	3.8±1.0	3.0±1.0
H7246 300	3.0	124	71	78	3.1±0.6	2.5±0.5
PTMT 300	3.0	131	71	82	3.4±0.7	2.6±0.6

Note: The D_i are the diameters in microns of the filaments before, during, and after drawing.The ratio $(D_1/D_3)^2$ represents the residual draw ratio.

After drawing, selected filaments were subjected to a heat treatment at an elevated temperature for 4 hours, using the apparatus described in Chapter 5. Filaments were annealed in two ways: (1) at fixed length and (2) without restraints (free annealed). Considerable shrinkage occurred during free annealing. By measuring the diameter before and after annealing, the amount of shrinkage can be determined assuming there is an insignificant change in volume:

$$shrinkage = \frac{L_3 - L_4}{L_3} = 1 - (\frac{D_3}{D_4})^2 \tag{9.3}$$

where L_4 is the length of a unit mass of filament after free annealing. The diameter ratio $(D_1/D_4)^2$ is equal to the final strain (L_4/L_1) of the drawn and free annealed filament. The results of these calculations are shown in Table 9.2. Among the filaments annealed at 180°C, the amount of shrinkage tends to decrease as HSC increases. The H5556 filaments shrink as much as 56%, while the PTMT filaments shrink only about 15%.

9.3 Structure

In drawing the filaments, it is desirable to develop crystalline domains in which the PTMT segments are fully extended and oriented in the fiber axis direction. At the same time, one would like to minimize the amount of orientation in the amorphous phase to maximize elastic extension and recovery. A high degree of phase separation produces good physical crosslinking and reduces the viscosity of the elastic phase. A filament with such a structure

Table 9.2: Final strain ratio and shrinkage of cold drawn filaments during free annealing.

	D_4	shrinkage (%)	$(D_1/D_4)^2$
H4056 50	298	-2	1.01
H4056 50 6.0X	213	45	2.16
H5556 50 5.5X	235	56	1.91
H6346 50 4.2X	222	46	1.89
H7246 50 5.0X	197	37	2.52
PTMT 50 5.0X	163	15	3.16

Note: H4056 was annealed at 100°C while the other compositions were annealed at 180°C. D_4 is the diameter in microns of the filament after free annealing.

should have low modulus, high strength, high elongation to break and good elastic properties. There is, however, a trade-off between high strength and high elongations. The best combination will depend on the desired application. In medical sutures for instance, there is a premium on high strength but only small extensions are needed ($< 20\%$). Other applications may require high elongations and high elastic recovery as in an elastic filament used in a "stretch" fabric.

Details of the microstructure of the drawn filaments are presented in the following sections. The effects of the various processing conditions on the structure will be described.

9.3.1 Orientation

The orientation and extension of the chains are of prime importance in determining the mechanical behavior of the drawn filaments. Measurements of f_c, shrinkage at elevated temperature, and elongation at break provide valuable information on the state of orientation of the chains.

As shown in Table 9.3, high levels of crystalline orientation are developed in the fully drawn filaments regardless of initial SDR or composition. The draw temperature has little effect on the crystalline orientation. High levels of crystalline orientation remain after annealing, in both fixed and free annealed filaments. The values of f_c after free annealing are only slightly lower than those produced after fixed annealing even though the free annealed samples may shrink as much as 56% during annealing.

Table 9.3: Crystalline chain orientation functions for the drawn filaments.

PROCESSING CONDITION	H4056	H5556	H6346	H7246	PTMT
50 AS-SPUN	0.18	0.14	0.29	0.15	–
50 COLD DRAWN	0.90	0.88	0.84	0.86	0.87
50 HOT DRAWN	0.91	–	–	0.87	–
50 CD & FREE	0.87	0.89	0.87	0.88	0.84
50 CD & FIX	0.90	0.92	0.89	0.89	0.87
50 HD & FIX	0.91	–	–	0.89	–
300 AS-SPUN	0.84	0.71	0.70	0.63	–
300 & FIX	0.89	0.89	0.88	0.85	0.72
300 HOT DRAWN	0.91	–	–	0.87	–

Note: Annealing of H4056 samples occurred at 100°C – other samples at 180°C.

The shrinkage of these filaments in boiling water and during free annealing at higher temperatures provides some clues as to the orientation of the amorphous chains in these filaments. As shown in Table 9.4, the cold drawn samples may shrink as much as 55% in boiling water depending on the composition. The amount of shrinkage is even higher at the 180°C temperature experienced during free annealing. The amount of shrinkage decreases as HSC increases. Slightly lower shrinkage is noted for hot drawn samples. After fixed or free annealing, the samples show negligible shrinkage in boiling water, except for H4056, because of either stress or strain relaxation and increased crystallinity.

The diffuse halo present in the WAXD patterns gives a more direct indication of the orientation of the amorphous chains. In both as-drawn and drawn and fixed annealed filaments there appears to be slightly less intensity in this ring at the meridion than at the equatorial position. In undrawn and in drawn and free annealed filaments, the intensity appears to be uniform around the ring. These results indicate that there may be a low level of amorphous orientation in the drawn filament and that this orientation is retained during fixed annealing. In undrawn or free annealed filaments there appears to be little or no preferred orientation of the amorphous segments.

Lilaonitkul and Cooper [112] have studied the crystalline and amorphous orientation of similar copolyesters using infrared dichroism. For a cast film stretched to 250% elongation and held under tension, they calculate an f_a

Table 9.4: Percent shrinkage of as-spun and drawn filaments after two minutes in boiling water.

PROCESSING CONDITION	H4056	H5556	H6346	H7246	PTMT
50 AS-SPUN	-1	0	-3	-2	-2
50 COLD DRAWN	55	34	29	21	13
50 HOT DRAWN	42	24	22	15	14
50 CD & FREE	1	0	-1	-1	-1
50 CD & FIX	36	3	2	1	2
50 HD & FIX	31	–	–	1	–
300 AS-SPUN	14	1	0	-2	-2
300 & FIX	3	2	1	0	–
300 HOT DRAWN	40	22	17	12	13

Note: Annealing of H4056 samples occurred at 100°C – other samples at 180°C.

equal to about 0.2. It is doubtful that amorphous orientation of any of the unrestrained drawn filaments in the present study is higher than this.

9.3.2 Degree of Phase Separation

In order to get good elastic properties it is necessary to achieve a high level of phase separation. Figure 9.3 shows how the DPS, as determined by SAXS techniques, varies with composition and processing conditions. (A list of the DPS values used to produce Figure 9.3 are given in Table A.1 in the Appendix.) Both cold and hot drawing tend to reduce the DPS of as-spun samples. This is apparently caused by a break-up of the crystalline structure and mixing of PTMT segments into the amorphous phase as they are pulled out of the crystalline structure. DPS is greatly enhanced by annealing and the level of phase separation can be brought back up to levels close to that of an undrawn and annealed filament. Free annealing produces a higher DPS than fixed annealing.

The loss tangent at 11 Hz as a function of temperature for both fixed and free annealed filaments of H4056 and H7246 are shown in Figures 9.4 and 9.5. The α-transition temperatures at 1.1, 11, and 110 Hz, which are related to the glass transition temperatures, are shown below:

	1.1 Hz	11 Hz	110 Hz
H4056 FIX	-33.0	-26.4	-18.7
H4056 FREE	-41.8	-35.5	-27.5
H7246 FIX	–	36.0	42.6
H7246 FREE	–	25.0	36.3

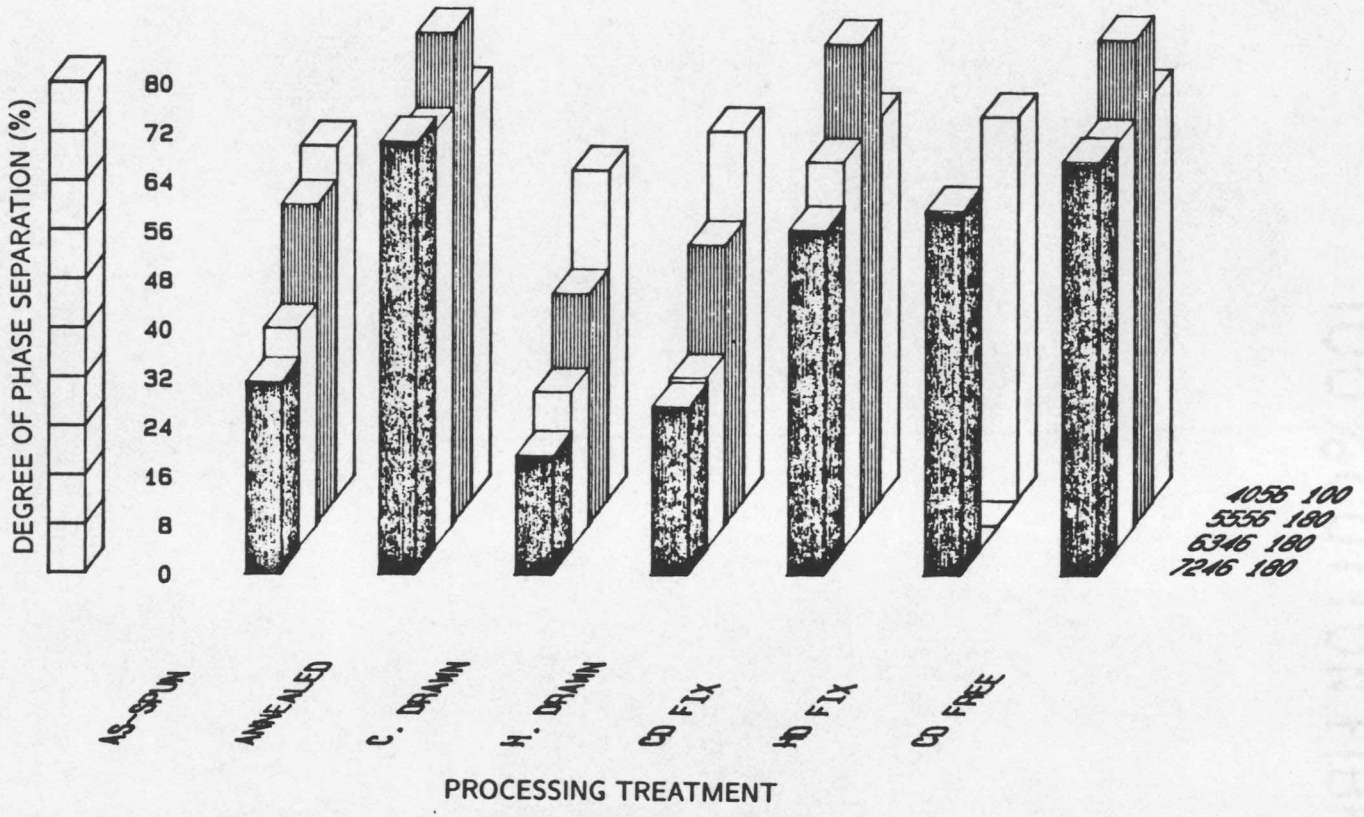


Figure 9.3: Degree of phase separation as a function of composition and processing conditions. All the filaments were initially spun at 50m/min. The annealing temperature was 100°C for H4056 and 180°C for the other compositions.

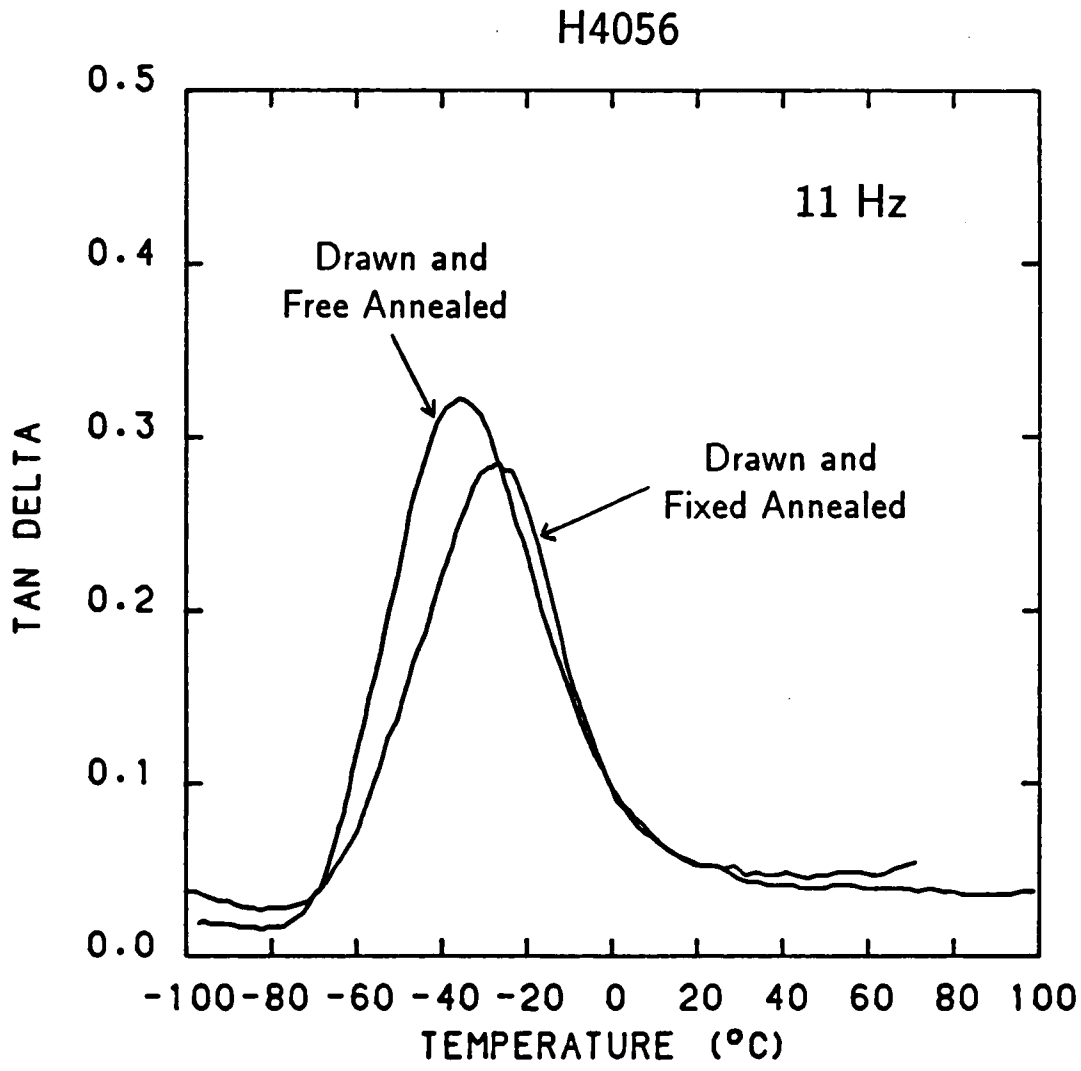


Figure 9.4: Rheovibron data showing the difference in T_g between free and fixed annealed drawn filaments of H4056.

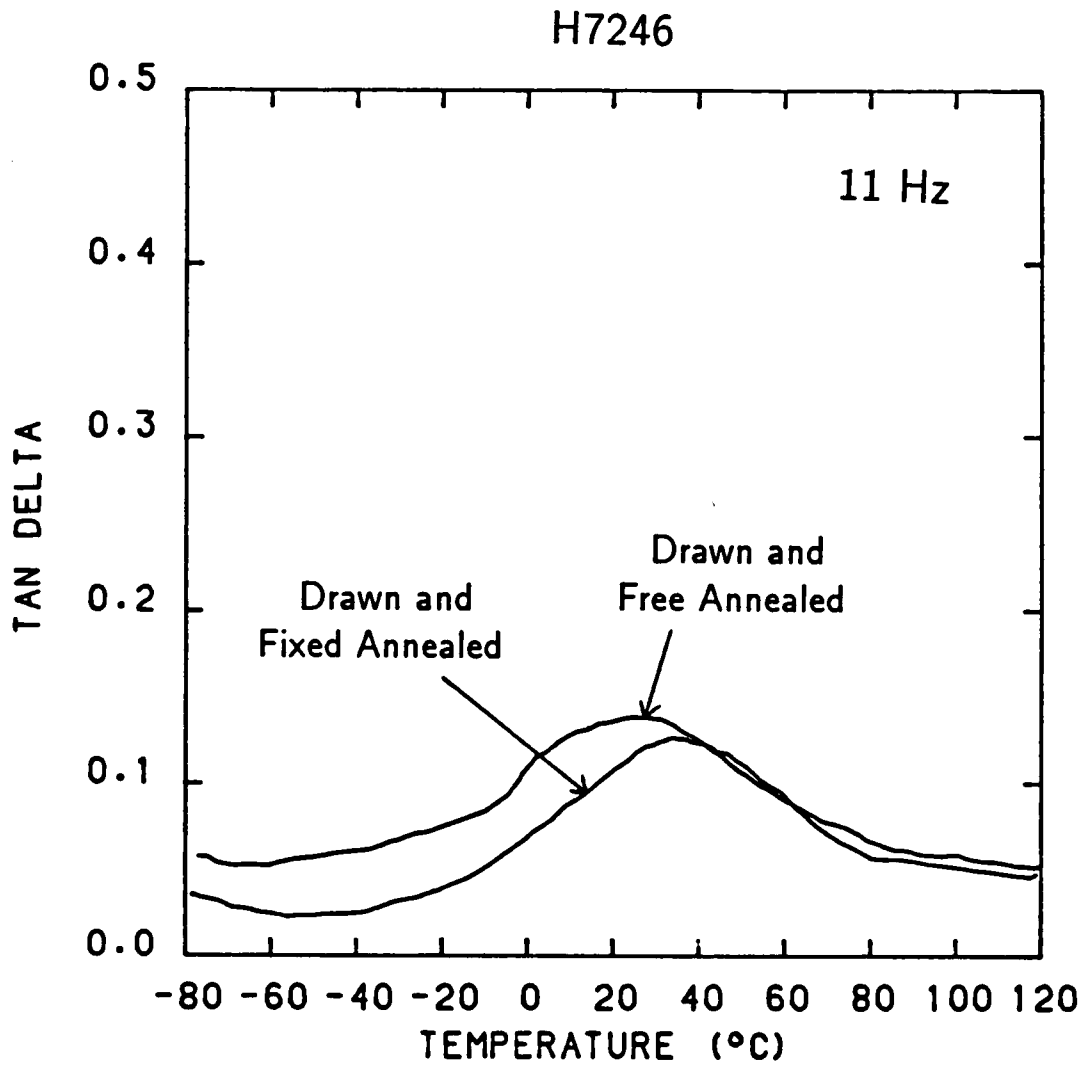


Figure 9.5: Rheovibron data showing the difference in T_g between free and fixed annealed drawn filaments of H7246.

These data show that the free annealed samples have a significantly higher T_g than fix annealed filaments, which could be due to either higher DPS or to greater tension on the chains, or both.

9.3.3 Morphology

The SAXS patterns of selected drawn filaments are shown in Figures 9.6 and 9.7. Patterns for the other compositions are shown in the Appendix (Figure A.9). Interpretation of these patterns provide a general overview of the morphology created by the various drawing and annealing treatments. Upon drawing, the discrete scattering peak changes in shape from an arc to more of a horizontal streak. This trend becomes more prominent as HSC increases. This may mean that the crystallites present in the as-spun filaments are broken up into smaller chunks and that their chain axes become preferentially aligned parallel to the fiber axis during drawing. This same phenomenom was observed in the as-spun filament during stretching (discussed in Chapter 8). In hot drawn samples, the SAXS streak is not as broad in the direction perpendicular to the fiber axis as it is in cold drawn filaments. The higher temperature reached during hot drawing allows some crystallite growth and perfection to occur.

Upon annealing, the horizontal streak increases in intensity and becomes sharper, an indication of crystallite growth in the radial direction. The streak is broader in fixed annealed samples than in free annealed samples. This indicates that crystallites in free annealed samples grow much larger in the radial direction than they do in fixed annealed filaments. This is a consequence of

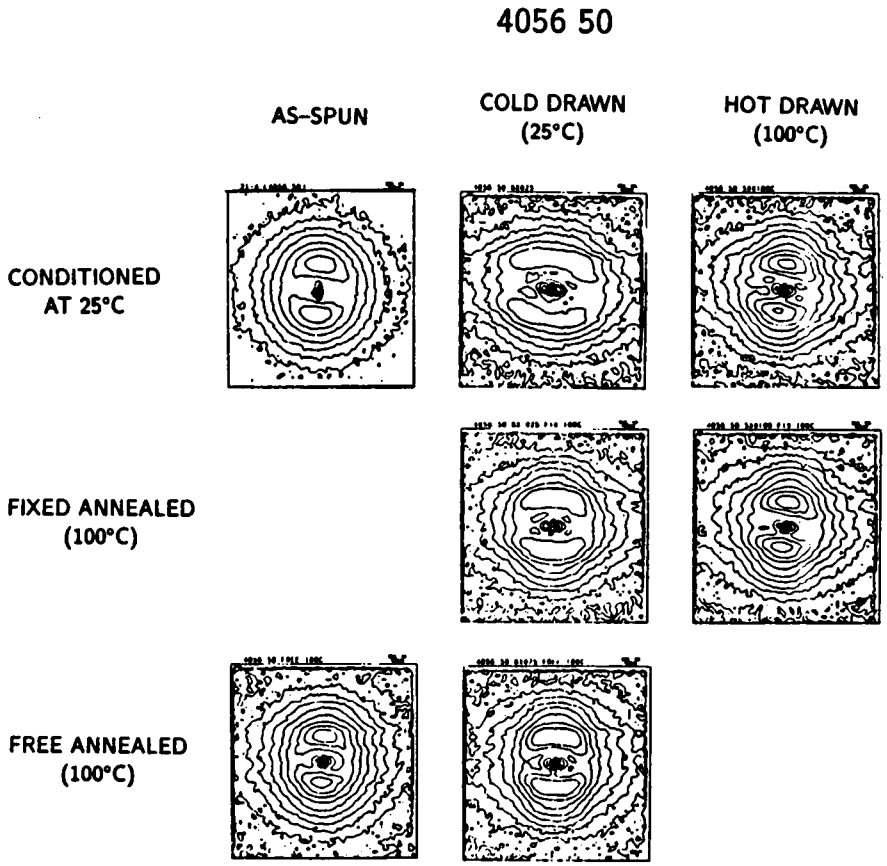


Figure 9.6: SAXS patterns of H4056 processed in different ways.

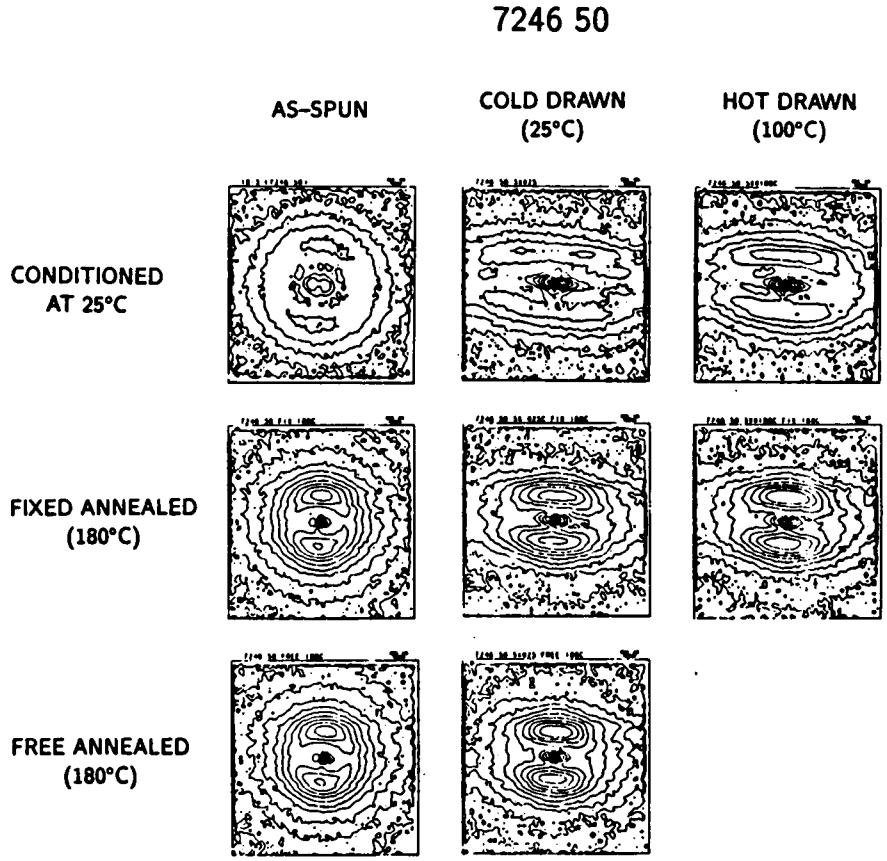


Figure 9.7: SAXS patterns of H7246 processed in different ways.

the greater mobility of the amorphous hard segments in the unrestrained filaments. These results are in agreement with calculations of crystallite size from WAXD data. In filaments spun at 50 m/min, the size of the crystallites after drawing and annealing appear to be smaller and more highly oriented than in filaments annealed without drawing. Similar results are observed in samples spun at 300m/min, except the crystallites are already highly oriented before drawing.

Figure 9.8 shows the crystallite size/perfection index of the filaments as a function of the various processing conditions and composition. The size of the crystallites in drawn "50 m/min" samples are about the same size as those in the unannealed filaments spun at 300 m/min. These crystallites are much smaller than those of as-spun and annealed filaments. Hot drawing produces slightly larger, better developed crystallites than cold drawing, but still smaller than those in as-spun and annealed filaments. Upon annealing, the crystallites in both cold drawn and hot drawn filaments grow much larger, reaching approximately the same size as those in the as-spun and annealed filaments. The crystallites in drawn filaments before and after annealing appear to become smaller as HSC increases (for a given annealing temperature).

There is some change in the crystallite unit cell from an α to a β form during drawing. The relative amount of β form increases as HSC increases as shown in Table 9.5. In the drawn PTMT filament, almost all the crystallites are of the β form. During free annealing, and even fixed annealing, the β form crystallites in the copolymer filaments are able to transform back to the α form.

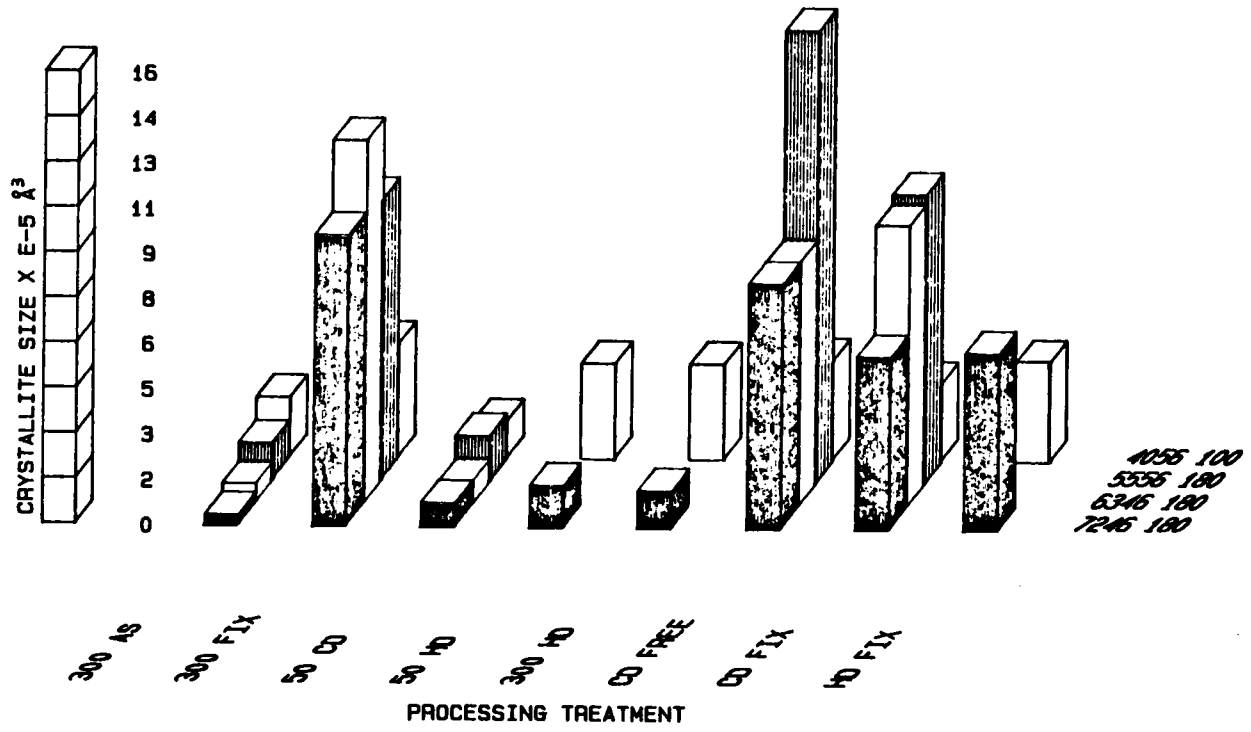


Figure 9.8: Crystallite size index as a function of composition and processing conditions. Filaments were initially spun at 50m/min.

Table 9.5: Type of crystalline phases present in filaments spun at 50 m/min and drawn.

	AS	CD	HD	CD FIX	CD FREE
H4056	α	α, trace β	α, trace β	α	α
H5556	α	α, some β		α	α
H6346	α	α, some β		α	α
H7246	α	α, and β	α, some β	α	α
PTMT	α	β		α, some β	α

Key to headings: AS: as-spun, CD: cold drawn, HD: hot drawn, CD FIX: cold drawn and fixed annealed, CD FREE: cold drawn and free annealed.

In the PTMT filaments, some β form remains after fixed annealing. During free annealing, all the β form crystallites transform back to the α form. In the copolymer filaments, the relaxation of the PTMEG segments after drawing reduces the tension on the crystallites enough to allow the transformation to occur during annealing, even if the filaments are held at fixed length. In the drawn PTMT filaments, a large fraction of the crystallites are under too much tension for the transformation to take place during fixed annealing.

The long period of the drawn filaments are given in Table 9.6. Upon cold drawing, the long period in the H4056 filament spun at 50 m/min decreases, but in H5556, H6346 and H7246 it increases. The change grows larger as HSC increases. Upon hot drawing, the long period increases in all compositions. The long period and crystallite thickness are both about the same after hot drawing whether the filaments were spun at 50 m/min or 300 m/min. The fixed annealing treatment causes an increase in crystallite size and a slight increase in long period similar to that in hot drawn filaments. There do not appear to be any fundamental differences between hot drawing and cold drawing and fixed annealing.

The long period of the drawn filaments increases during both fixed and free annealing. The long periods of the free annealed filaments are slightly higher than they are for the fixed annealed filaments. Also, the long periods of the drawn and annealed filaments are about the same as undrawn and annealed filaments. These results are very interesting considering the large amount of shrinkage that takes place during free annealing.

Table 9.6: Long period (in Å) of filaments spun at 50 m/min and drawn.

	AS	CD	HD	CD FIX	CD FREE
H4056	117	104	131	118	123
H5556	99	108	120	154	153
H6346	77	97	107	142	142
H7246	74	105	110	138	132
PTMT	-	-	-	-	116

Key to headings: AS: as-spun, CD: cold drawn, HD: hot drawn, CD FIX: cold drawn and fixed annealed, CD FREE: cold drawn and free annealed.

The mechanism that determines the long period in these filaments is probably similar to the one reported by Samuels [146, Chap. 4, pg. 224] for drawn PET filaments. In free annealed filaments, the amorphous chains relax first, followed by migration to the growth front and new crystal growth. In PET, the crystallite thickness is determined by the annealing temperature. The long period is in turn determined largely by the crystallite thickness. Thus, the long period is determined by the annealing temperature instead of the amount of shrinkage.

In the drawn copolymer filaments, the DPS is low and the structure is imperfect. During free annealing, the filaments shrink as a result of the contraction of amorphous chains. Shrinkage occurs very quickly (on the order of seconds in boiling water; more slowly in hot air) relative to the time allowed for crystallization (several hours). Much structural reorganization can take place before the hard segments crystallize. As a result, the long period is determined primarily by the annealing temperature rather than by the amount of shrinkage. As discussed in Chapter 6, the long period increases as the amount of undercooling decreases.

9.4 Stress-Strain Behavior and Tensile Properties

Stress-strain curves of H4056 and H7246 filaments are shown in Figures 9.9 and 9.10. The drawn filaments have much steeper stress-strain curves and break at much lower elongations and higher stresses than the as-spun fila-

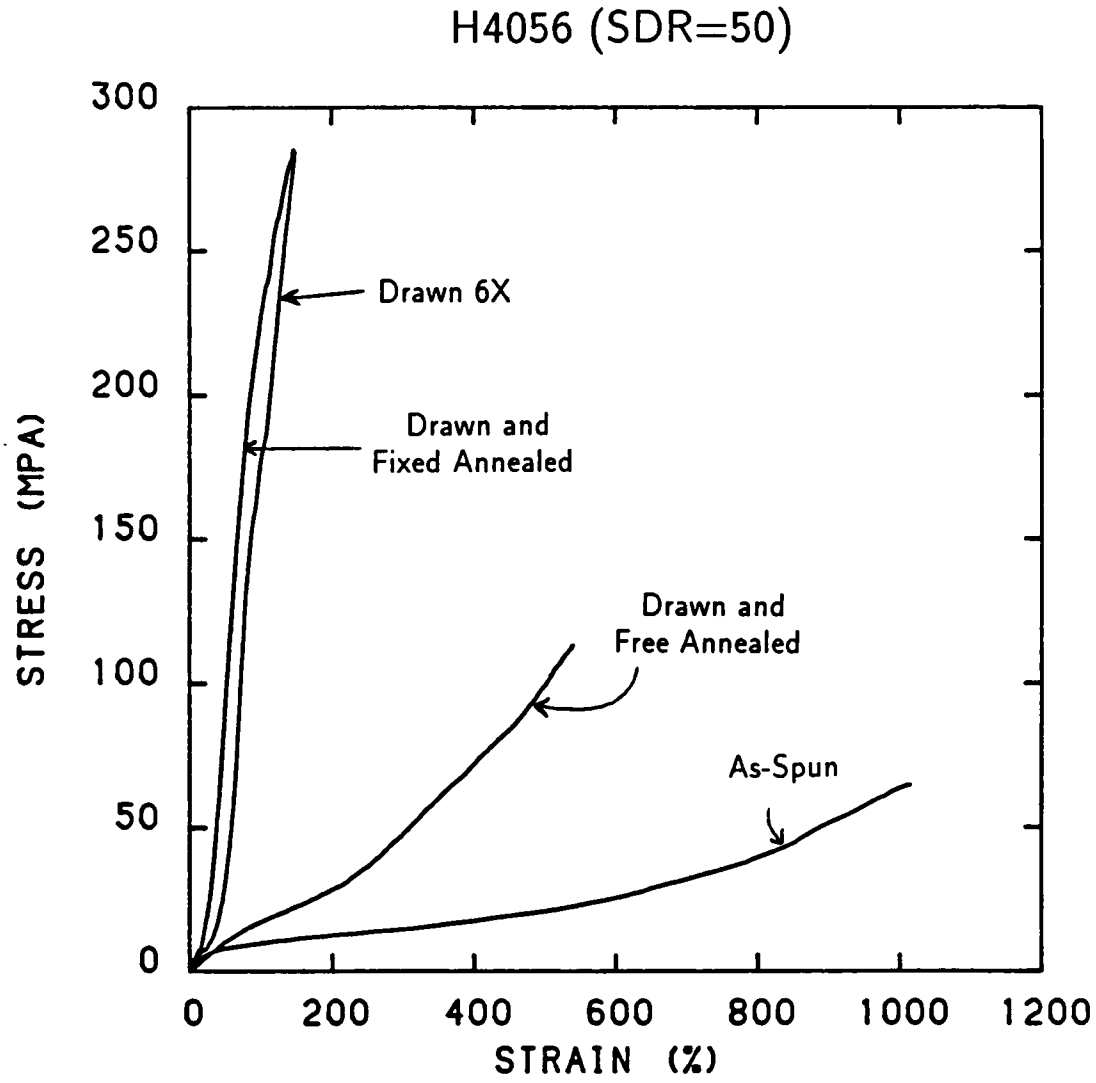


Figure 9.9: Comparison of stress-strain curves of H4056 filaments receiving different drawing and annealing treatments.

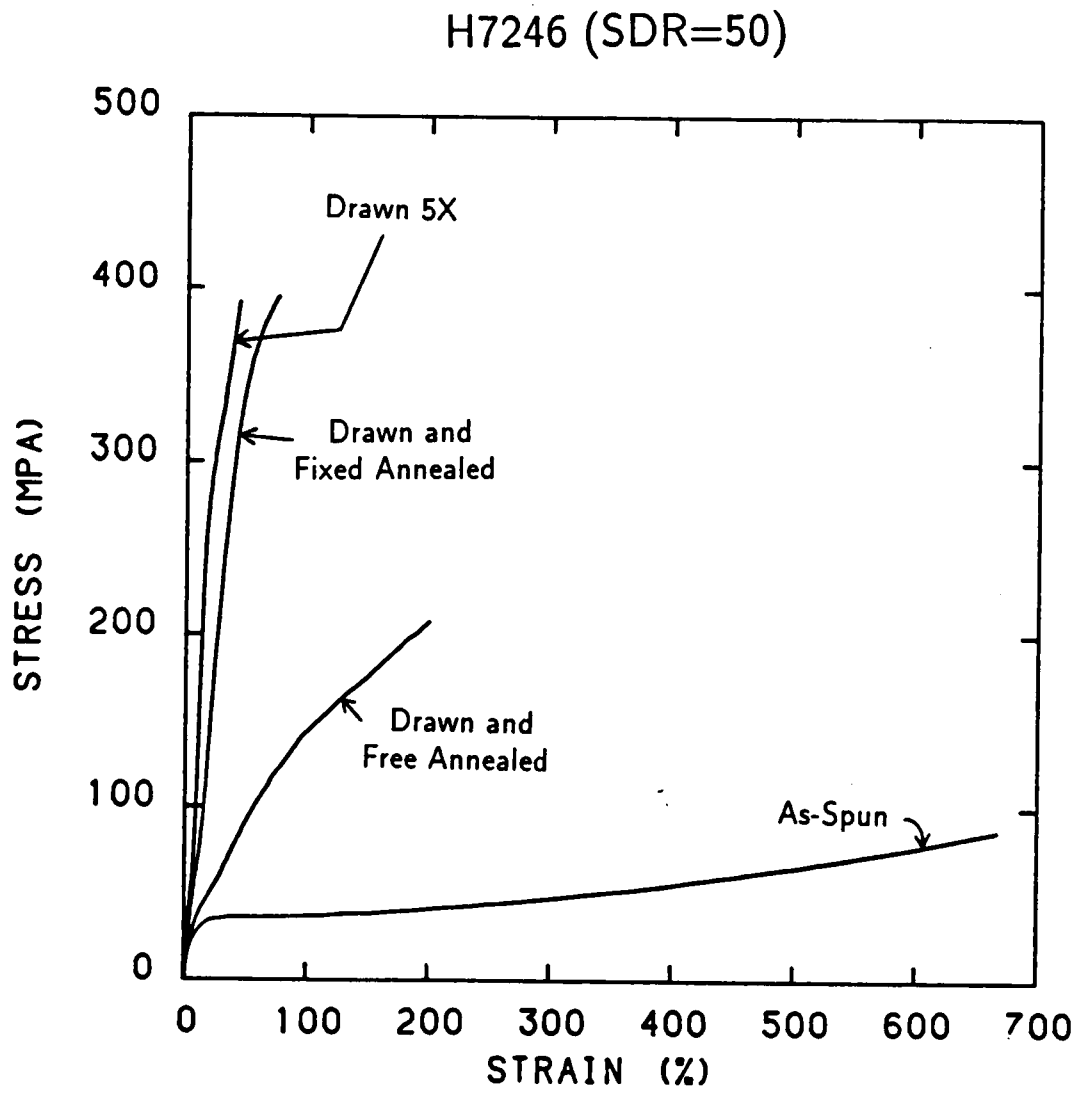


Figure 9.10: Comparison of stress-strain curves of H7246 filaments receiving different drawing and annealing treatments.

ments. The fixed annealed filament shows very similar behavior to the drawn filament. The behavior of the free annealed filament is intermediate to that of the fixed annealed and as-spun filaments.

The elongation to break and tenacity of the various drawn and annealed filaments are shown in Table 9.7 and 9.8. The ultimate strain in the cold drawn filaments range from 136% in H4056 to 17% in PTMT, while tenacities range from 275 MPa to 451 MPa for the same samples. Upon fixed annealing, the elongations to break increase slightly while the tenacities remain about the same. Free annealing produces much higher ultimate elongations than fixed annealing. The tenacities of these filaments are also reduced.

The moduli of the drawn filaments are given in Table 9.9. Except in the case of H4056, both hot and cold drawing increase the moduli of unannealed filaments. Hot drawing produces a lower modulus than cold drawing in the copolymer filaments.

Fixed annealing lowers the modulus of the filaments slightly from that of the drawn but unannealed filament as a result of the higher DPS. As the DPS increases, the modulus of the amorphous phase decreases as discussed in Chapter 7. The modulus of the hot drawn filaments are still lower than those of the cold drawn filaments after fixed annealing. Upon free annealing, the modulus drops to about half that of the unannealed drawn filament.

The modulus is shown as a function of the DPS in Figure 9.11 for filaments processed in many different ways. The overall chain orientation in

Table 9.7: Ultimate elongations ($\frac{L-L_0}{L_0}$) of as-spun and drawn filaments.

SDR = 50 m/min

	H4056	H5556	H6346	H7246	PTMT
As-Spun	9.44	8.53	6.69	7.03	6.68
As & Free	9.94	–	–	6.65	–
As & Fix	–	–	–	7.12	–
Cold Drawn	1.36	0.75	0.91	0.46	0.17
Hot Drawn	1.78	0.89	0.52	0.61	0.21
CD & Fix	1.42	1.25	1.34	0.71	0.30
HD & Fix	1.95	–	–	0.70	–
CD & Free	5.13	4.57	3.44	1.99	0.79

SDR = 300 m/min

As-spun	4.87	4.20	3.72	4.06	5.18
Hot Drawn	1.20	0.73	0.46	0.45	0.48
As & Fix	4.74	4.32	3.68	3.58	3.83

Key to abbreviations: CD: cold drawn, HD: hot drawn, FIX: fixed annealed, FREE: free annealed.

Table 9.8: Tenacities (in MPa) of the drawn filaments.

SDR = 50 m/min

	H4056	H5556	H6346	H7246	PTMT
As-Spun	75	85	107	109	111
As & Free	68	–	–	89	–
As & Fix	–	–	–	95	–
Cold Drawn	275	362	317	413	415
Hot Drawn	227	346	438	402	481
CD & Fix	282	327	267	421	477
CD & Free	114	126	139	211	359
HD & Fix	225	–	–	390	–

SDR = 300 m/min

As-spun	101	127	133	149	120
Hot Drawn	241	281	357	376	345
As & Fix	94	110	132	132	126

Key to abbreviations: CD: cold drawn, HD: hot drawn, FIX: fixed annealed, FREE: free annealed.

Table 9.9: Moduli (in MPa) of the drawn filamants.

SDR = 50 m/min					
	H4056	H5556	H6346	H7246	PTMT
As-Spun	53	173	394	799	1410
As & Free	33	–	–	585	–
As & Fix	–	–	–	596	–
Cold Drawn	50	395	996	1280	3520
Hot Drawn	49	351	712	1170	5260
CD & Fix	46	294	356	914	1330
HD & Fix	40	–	–	878	–
CD & Free	23	152	340	688	–
HD & Free	–	–	–	–	2570
SDR = 300 m/min					
As-spun	70	173	394	799	1410
Hot Drawn	53	214	498	1120	1120
As & Fix	51	172	386	694	2260

Key to abbreviations: CD: cold drawn, HD: hot drawn, FIX: fixed annealed, FREE: free annealed.

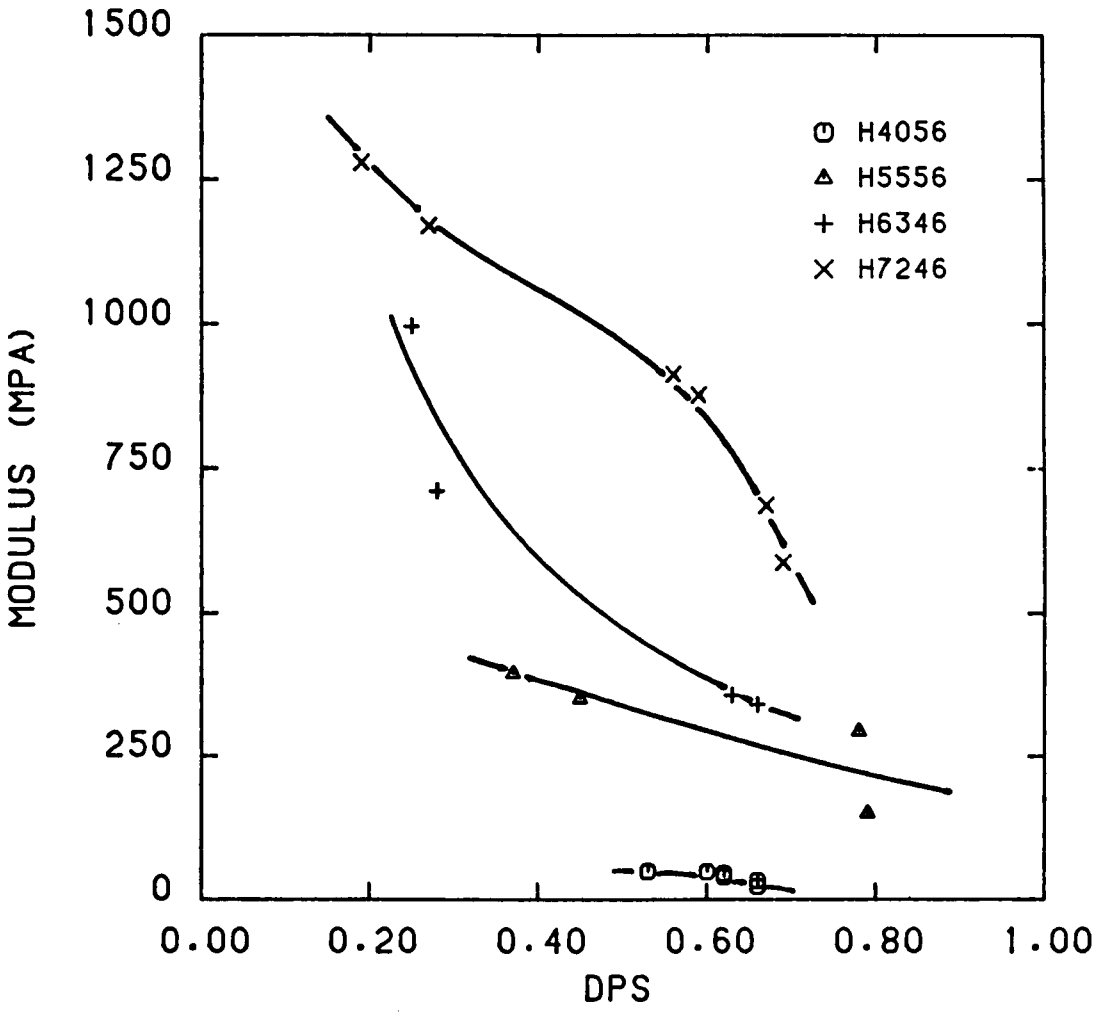


Figure 9.11: Modulus of filaments processed in different ways as a function of their DPS. The elongation to break is generally increasing as the DPS increases in this figure. The increase in DPS and the decrease in chain orientation both act to lower the modulus.

these filaments decreases in the same order as the DPS increases. Both of these effects result in a decrease in modulus.

9.4.1 Discussion of Structure

A hypothesis for the microstructure of these filaments consistent with the above results will now be presented. There can be several types of amorphous chains present in these copolymers as discussed in a paper by Gaylord and Lohse [60] (see Section 2.5.1). There can be cilia, loops, bridges, and floating chains. The bridges are the chain segments that connect one crystalline domain to another. These segments can vary quite widely in their contour length (length when fully extended) and degree of extension. The bridge segments strongly influence mechanical properties such as modulus, ultimate elongation, and elastic recovery. Loops, cilia, and floating chains, on the other hand, contribute much less to the strength and retractive ability of the filaments.

The undrawn filaments spun at 50 m/min are characterized by low orientation in both the amorphous and crystalline phases. There are probably a relatively large portion of loops as compared to bridge segments. The DPS is relatively low in these filaments both before and after drawing.

As the filaments are stretched, the tie molecules and some of the bridge chains become highly extended and exert considerable force on the crystallites. At higher elongations, the crystallites are torn apart and the PTMT segments become highly oriented. There are high enough stresses during drawing to cause some β type crystallites to be formed. Some of the amorphous chains remain partially extended after drawing since they are held in place by the plas-

tically deformed crystalline material. For these reasons, the drawn filaments have a higher modulus and lower ultimate elongation than undrawn samples.

During fixed annealing, the extended amorphous chains may disorient on a localized scale, but are unable to contract much. The crystalline chains retain their high orientation and oriented crystalline growth takes place. Because of the limited mobility of the amorphous PTMT segments, the crystallites are not able to grow freely, and relatively small crystallites are produced. Some stress relaxation takes place as evidenced by the transformation of β form crystallites back to α form. Cross-linking of PTMO segments takes place as the amorphous PTMT segments crystallize. Because of the amorphous chains are unable to recoil, crystallization results in relatively more "bridge" segments. Stress-strain curves quite similar to those of the as-drawn filament are produced (refer to Figures 9.9 and 9.10). The modulus remains relatively high and the elongation to break low. A model of the structure of fixed annealed filaments showing the tie molecules and bridge segments is presented in Figure 9.12.

During free annealing, the amorphous chains are able to relax and assume a more random conformation. This is manifested macroscopically as a shrinkage of the filament in the fiber axis direction. The amount of shrinkage decreases as HSC increases. The lamellar fragments, however, remain highly oriented and oriented crystal growth takes place. Since the PTMT segments are less constrained in free annealed samples than in the fixed annealed filaments, larger crystallites develop. This also results in a slightly higher DPS than in fixed annealed samples. As discussed in Section 9.3.3, the new struc-

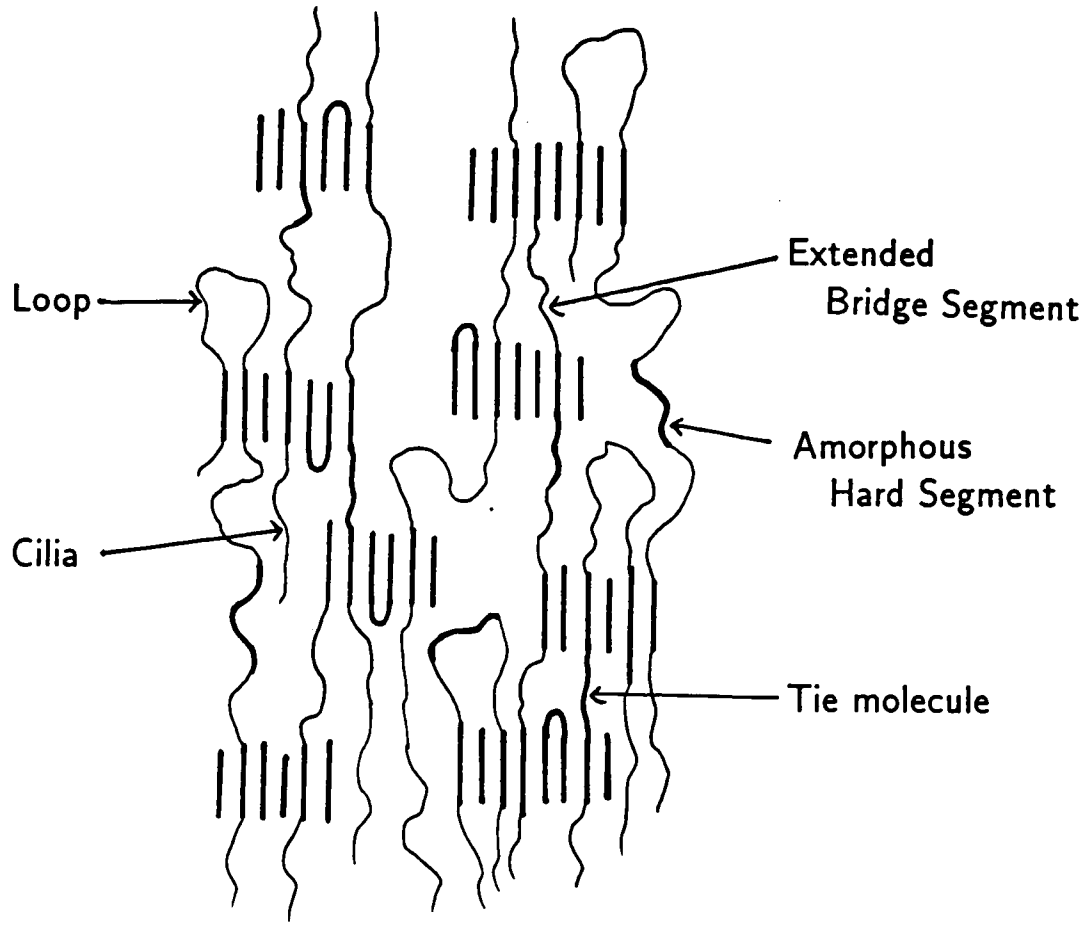


Figure 9.12: Structural model of drawn and fixed annealed filaments.

ture is formed in two steps. First the amorphous chains relax, then migrate to the growth front and crystallize. Since the amorphous chains are more coiled in free annealed filaments than in fixed annealed filaments when crystallization takes place, a larger portion of loops are formed. The more relaxed bridge segments and relatively high number of loops in the free annealed filaments result in lower stresses during stretching and a higher elongation to break than in the fixed annealed filament. The lower modulus is probably due to a higher DPS and fewer, more relaxed tie molecules. A model of the structure of free annealed filaments is shown in Figure 9.13.

After annealing at 180°C, the filaments show very little shrinkage in boiling water. This is the case whether the filaments are annealed with or without constraints. Some of the bridge segments in the fixed annealed filaments remain highly extended and would be expected to contract, but the new crystalline structure apparently prevents this from happening. Since the samples are annealed well above the boiling point of water, the crystalline structure is stable at 100°C. The H4056, however, was annealed at only 100°C, and when placed in boiling water some of the crystalline material may melt, allowing the bridge segments some freedom to relax.

9.4.2 Relationship of Tensile Properties to Structure

Changes in the stress-strain behavior of the filaments upon drawing and annealing are the result of changes in crystalline orientation and to changes in the nature of the interdomain chains. The as-spun samples have low crystalline

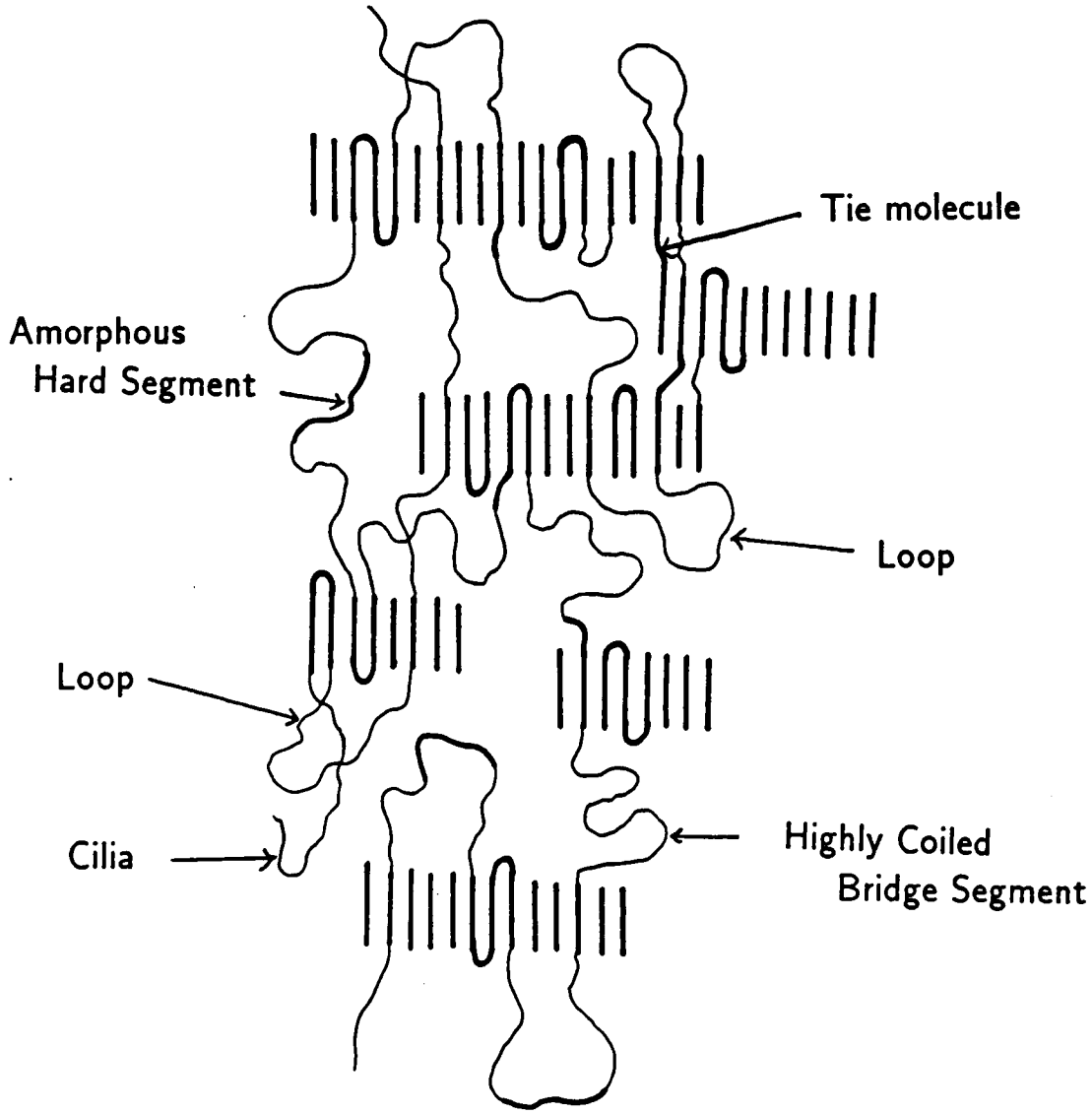


Figure 9.13: Structural model of drawn and free annealed filaments.

orientation and highly coiled amorphous segments which results in large elongations to break and relatively low stresses during stretching. Drawing produces high crystalline orientation, taut tie molecules, and probably some highly extended bridge segments. This causes low elongations to break and much higher stresses during subsequent stretching. During fixed annealing, the orientation of the crystallites and the extension of the bridge chains are largely retained. Crystallization results in more bridge segments. Since the chains are unable to disorient, stress-strain curves very similar to those of the unannealed drawn filaments are produced.

The elongation at break in fixed annealed filaments is only slightly higher than in drawn samples. During free annealing, the orientation of the crystalline chains remain high, but the amorphous segments are able to relax. Crystallization produces a relatively greater number of "loops" than new bridge segments. The resulting stress-strain behavior is intermediate to those of the as-spun filaments and the drawn and fixed annealed filaments. Since the amorphous chains are able to recoil during annealing, the tenacities of these filaments are lower than those of the drawn filaments. These results show that the tenacity and elongation to break depend more on the crystalline orientation and the nature of the amorphous chains than on the DPS. This conclusion is similar to the one reached in Chapter 8 for undrawn filaments.

In Chapter 7, the modulus was shown to depend on the relative number of taut tie molecules and the modulus of the amorphous phase. A large number of taut tie molecules and poor phase separation both act to produce a high

modulus and reduce elastic efficiency. Both hot and cold drawing increase the moduli of unannealed filaments in all compositions except H4056. The higher modulus probably results from a larger number of taut tie molecules and bridge segments. Hot drawing produces a lower modulus than cold drawing in the copolymer filaments. This may be due to the higher DPS produced during hot drawing, although there may be slight differences in chain orientation.

Fixed annealing lowers the modulus of the filaments only slightly from that of the drawn but unannealed filament, even though the DPS is greatly increased. Apparently, the modulus is determined more by the tie molecules and taut bridge segments than by the DPS.

The modulus drops considerably upon free annealing. The DPS is slightly higher than in fixed annealed samples of the same composition, but not enough to explain the large difference. The change in modulus must result from fewer or less taut tie molecules and bridge segments.

9.5 Deformation Behavior

The deformation behavior of drawn samples were studied using SAXS techniques. SAXS patterns were made of the filaments in both the strained and relaxed states just as for the as-spun and annealed filament discussed in Chapter 8. In order to see how the various processing steps affect the deformation behavior of the copolymers, several samples from one composition (H4056) were studied: as-spun and annealed, as-drawn, drawn and fixed annealed, and

drawn and free annealed. A drawn and free annealed filament of H7246 was studied to provide some insight on the effect of composition.

Patterns of the as-drawn filament are shown in Figure 9.14. Small highly oriented crystallites were produced during drawing. As the filaments are stretched to higher elongations, the shape of the scattering peak changes from an arc to more of a streak. This results from the crystallites becoming more preferentially aligned with their chain axes in the stretch direction. WAXD patterns taken of the drawn filament before and after stretching are in agreement with these results. At 65% elongation, the SAXS pattern indicates the crystallites have very small lateral dimensions and are very highly oriented.

The patterns of the filaments after stretching and relaxing are all almost identical to each other and are very similar to that of the original drawn filament before stretching. There is a faint four-point character to the patterns. This is most likely due to a slight tilting of the crystallites away from the fiber axis direction as the filaments relax. The similarity of stretched and relaxed patterns to each other and to the original indicates that no major permanent reorganization of the microstructure has taken place, although the filaments have been stretched to near their ultimate elongation. This observation is in agreement with the cyclic test (discussed in Section 9.1) which shows that most of the plastic deformation takes place on the first stretch and that only small additional amounts occur on subsequent stretches to the same or lower elongations. Stretching the drawn filament 50% brings the total deformation back to 6×, the original extent of deformation during drawing:

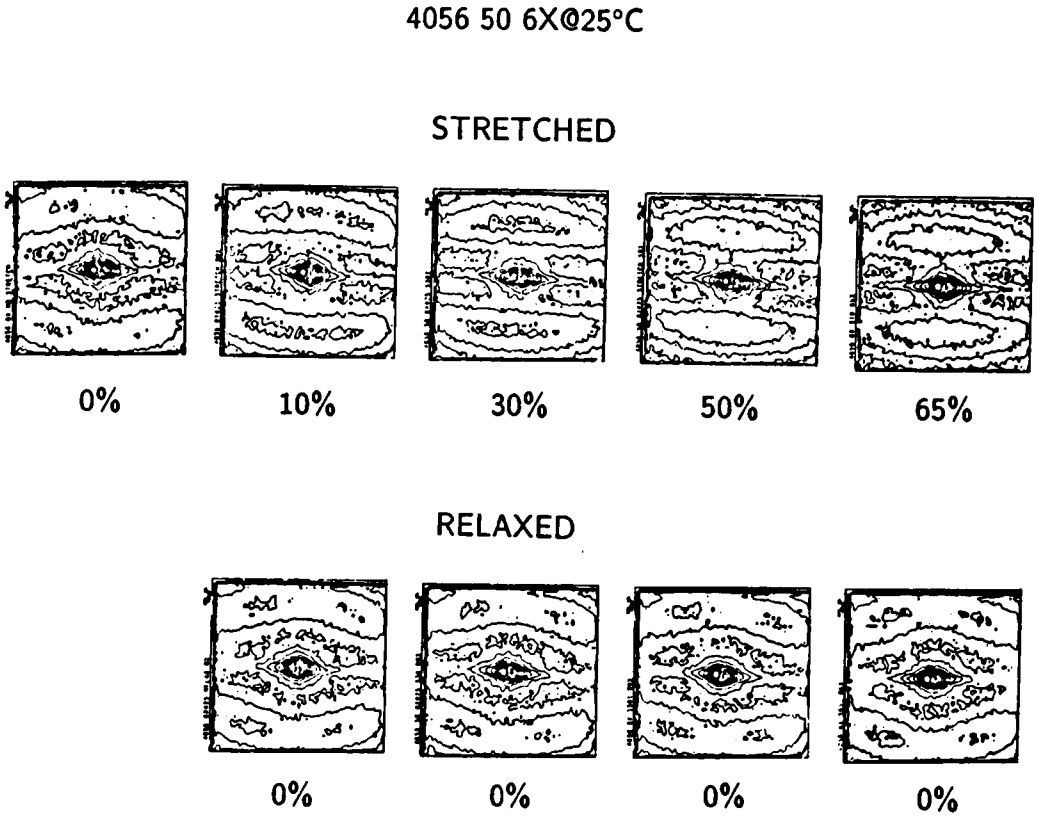


Figure 9.14: SAXS patterns of a drawn H4056 filament. The percent stretch is shown below the patterns in the top row, while the residual elongation is shown below the patterns in the bottom row.

Residual strain: 3.9×

Stretch 50% : $1.5 \times 3.9 = 6\times$

So, little additional plastic deformation would be expected until the filament has been stretched over 50%. The work recovery drops rapidly after 50% elongation, as will be shown in the next section.

One-dimensional scans of the patterns in the meridional direction are shown in Figure 9.15. The scattering vector q is defined as $4\,\pi\,(\sin\theta)/\,\lambda$. The long periods calculated from these data are given in Tables 9.10 and 9.11. The long period increases with stretch ratio in a slightly less than affine manner. At the higher elongations the periodicity starts to break up and the intensity starts to drop off. The SAXS curves of the relaxed samples are superimposable, meaning the crystallites remain largely intact during stretching to these elongations. The tie molecules and taut bridges that have already been pulled loose by the first stretch (drawing) and are not pulled taut again until previous strain levels are exceeded.

The SAXS patterns of the drawn and fixed annealed sample during cyclic deformation are shown in Figure 9.16. The patterns of the stretched filaments are very similar to those of the as-drawn filament. The scattered intensity from the annealed filaments is much higher though, due to their higher DPS. The shape of the peaks begins to change from an arc to a horizontal streak as the filaments are stretched. This indicates the crystalline chains are becoming slightly more preferentially aligned in the direction of the fiber axis as the filaments are stretched. WAXD patterns (not shown) show small changes

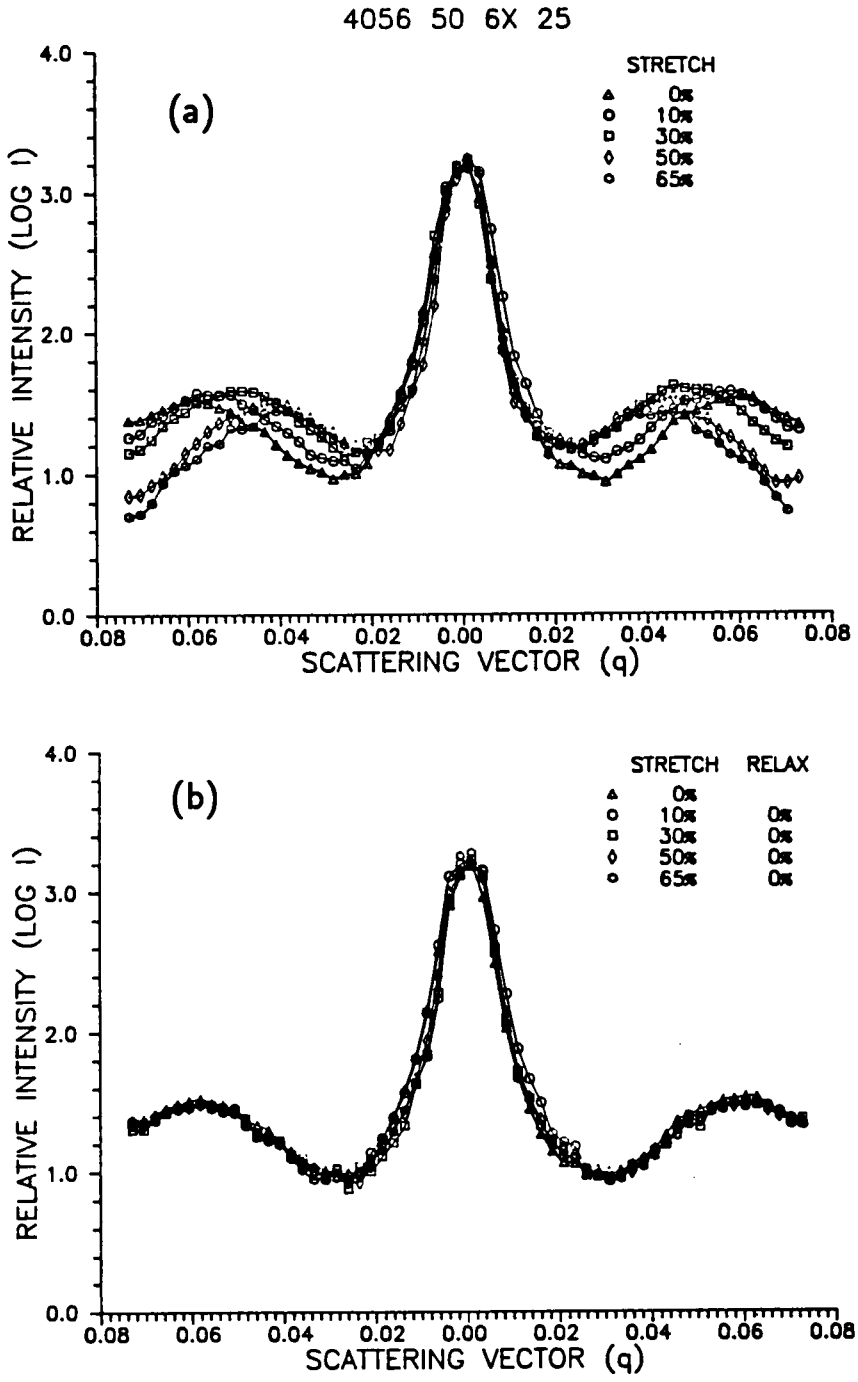


Figure 9.15: One dimensional data slices corresponding to the SAXS patterns shown in Figure 9.14. (a) stretched ; (b) stretched and relaxed. The slices are in the meridional direction.

Table 9.10: Long periods observed for the drawn H4056 filament in the strained state.

STRAIN	OBSERVED L.P. (Å)	EXPECTED L.P. IF AFFINE (Å)
0%	105	105
10%	112	116
30%	129	137
50%	144	158
65%	152	173

Table 9.11: Long periods observed for the drawn H4056 filament after retraction.

INITIAL STRAIN	RESIDUAL STRAIN	OBSERVED L.P. (Å)	EXPECTED L.P. IF AFFINE (Å)
0%	0%	105	105
10%	0%	105	105
30%	0%	105	105
50%	0%	105	105
65%	0%	105	105

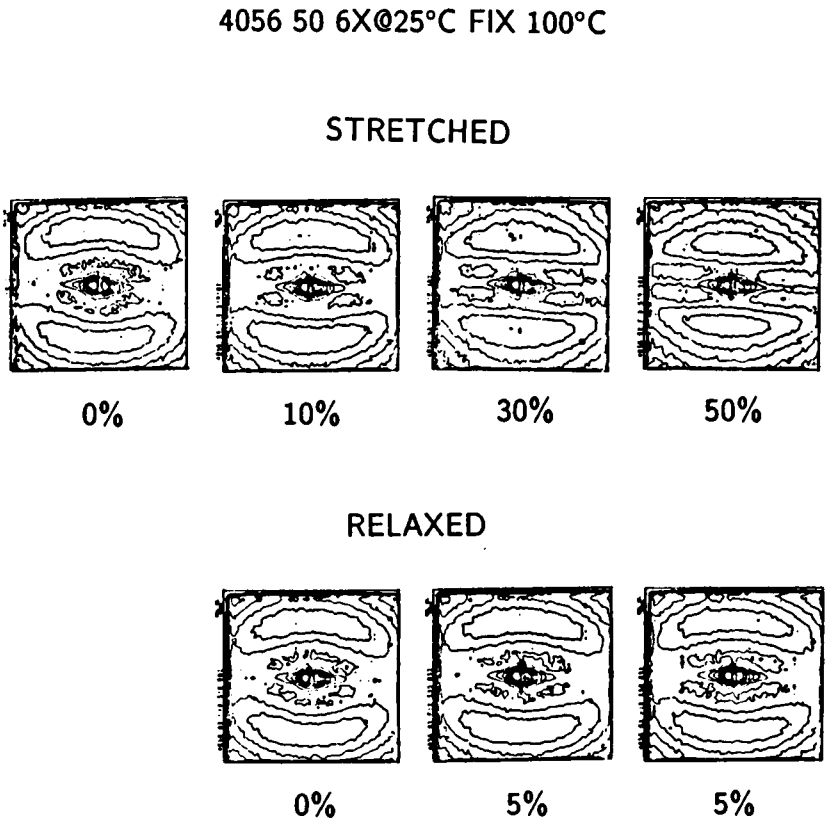


Figure 9.16: SAXS patterns of a drawn and fixed annealed H4056 filament.

in crystallite orientation. After allowing the filaments to relax, the SAXS patterns are almost identical to that of the original unstretched filament. No four-point patterns were observed as they were for the as-spun filament which underwent considerable plastic deformation.

One dimensional scans of the data are shown in Figure 9.17. Long periods calculated from these curves are given in Tables 9.12 and 9.13. The long period increases in a slightly less than affine manner. At 50% elongation, the intensity drops considerably and several "shoulders" appear on the SAXS curve; an indication of several distinct distributions of long spacing. Upon release of the stress the patterns obtained are virtually identical to the pattern of the unstretched filament. The SAXS curves of the relaxed filaments are superimposed, with only a slight intensity loss in the sample stretched 50%. The observed long periods are very near the predicted values. Since the long period and scattering power of the relaxed filaments are almost identical to those of the unstretched filament, the DPS must not change much and the crystalline domains must remain fairly intact during stretching. These data show that most of the deformation takes place in the amorphous phase. Since this phase is highly elastic, the original morphology is largely recovered upon release of the stress. The drawn and fixed annealed filaments show slightly better work recovery than the as-drawn filaments due to their higher DPS.

The free annealed samples behave much differently. They act more like the undrawn and annealed filaments. SAXS patterns of these filaments during cyclic deformation are shown in Figure 9.18. At low elongations, the scattering

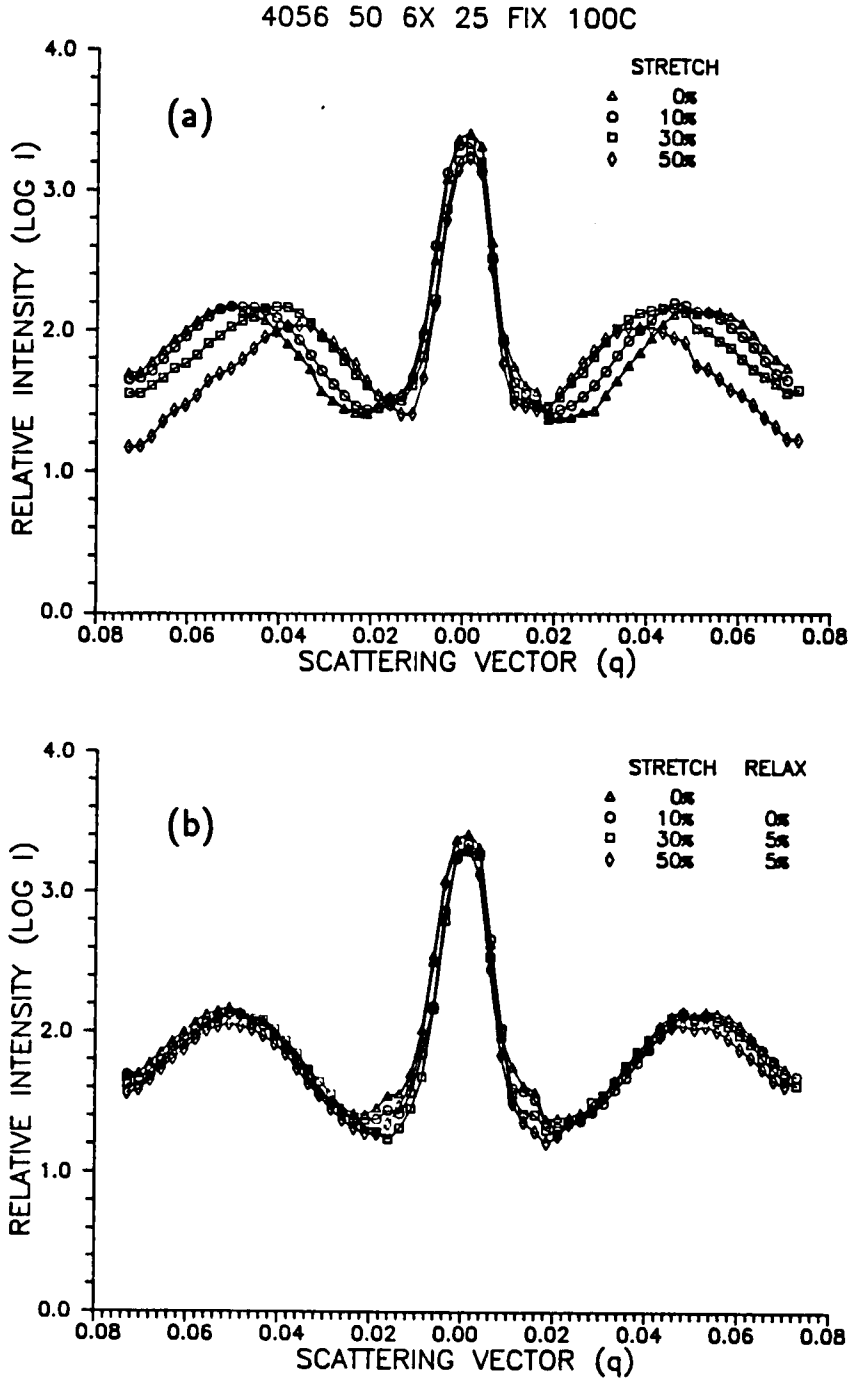


Figure 9.17: One dimensional data slices corresponding to the SAXS patterns shown in Figure 9.16. (a) stretched ; (b) stretched and relaxed. $q = 4\,\pi\,(\sin\theta)/\,\lambda$.

Table 9.12: Long periods observed for the drawn and fixed annealed H4056 filament in the strained state.

STRAIN	OBSERVED L.P. (Å)	EXPECTED L.P. IF AFFINE (Å)
0%	123	123
10%	131	135
30%	148	160
50%	168	184

Table 9.13: Long periods observed for the drawn and fixed annealed H4056 filament after retraction.

INITIAL STRAIN	RESIDUAL STRAIN	OBSERVED L.P. (Å)	EXPECTED L.P. IF AFFINE (Å)
0%	0%	123	123
10%	0%	124	123
30%	5%	125	129
50%	5%	127	129

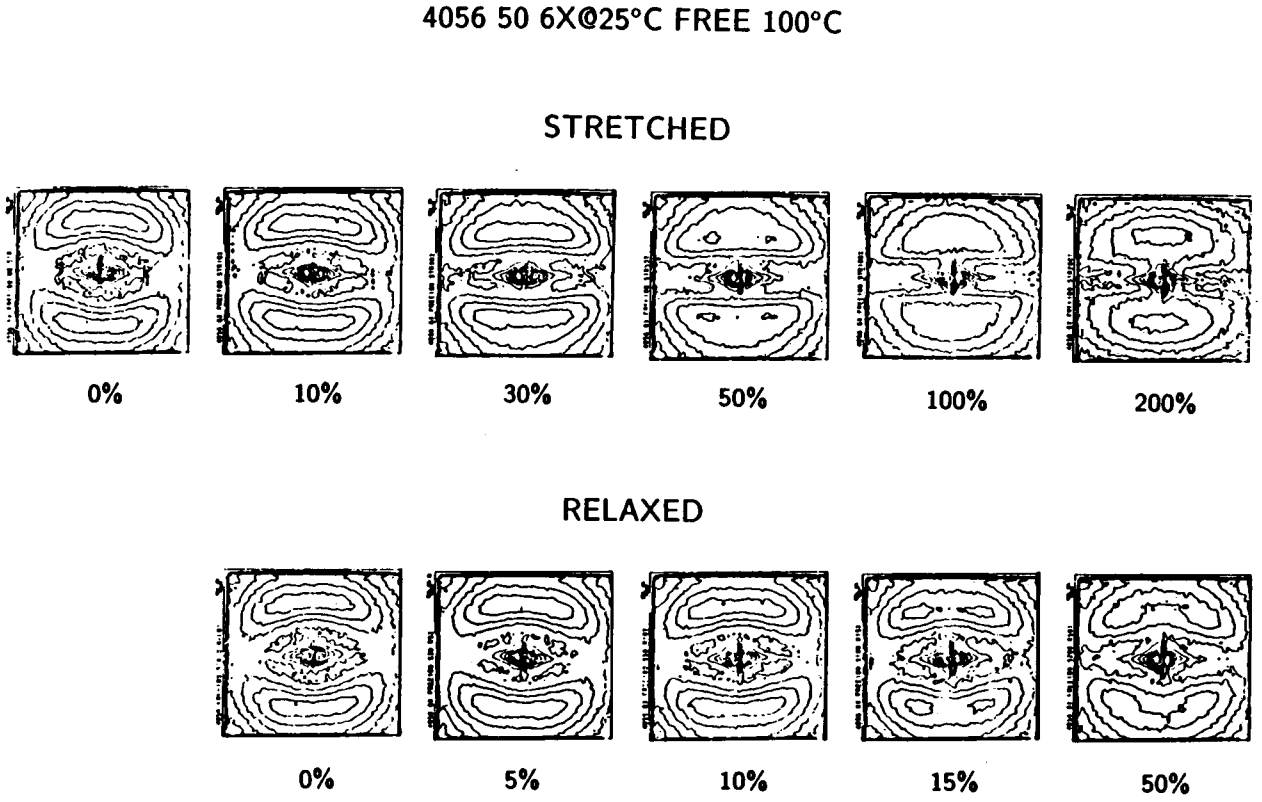


Figure 9.18: SAXS patterns of a drawn and free annealed H4056 filament.

peaks move closer together without much change in shape, but at about 50% elongation a four-point pattern is obtained. By 200% elongation, the discrete scattering has changed in shape from an azimuthal arc to a broad horizontal streak.

Scans of the intensity in the meridional direction are shown for these filaments in Figure 9.19. The long periods are given in Tables 9.14 and 9.15. The long period increases in proportion to the stretch ratio up to about 30% elongation. The relative intensity remains high, up to about 50%, then drops off slowly with increasing elongations. Two distinct populations of long periods are observed at elongations above 50%. As the stretch ratio is increased, the intensity of the peak corresponding to the smaller spacing appears to grow at the expense of the peak associated with the larger spacing.

These results show that the microstructure deforms elastically up to about 30% elongation. At this point, the structure starts to break apart. The filament draws noticeably at elongations greater than about 50%. Apparently, the larger, more widely spaced lamellae are being broken apart into smaller more closely spaced crystalline fragments. The SAXS pattern at 65% elongation indicates that there are small lamellar chunks oriented such that their chain axes very nearly parallel to the fiber axis.

Upon allowing the filaments to relax, the crystallites disorient and patterns almost identical to the original are produced from elongations up to 50%. A four-point pattern is obtained from the filament relaxed from 100%. The pattern of samples relaxed from elongations of 100% and higher no longer closely

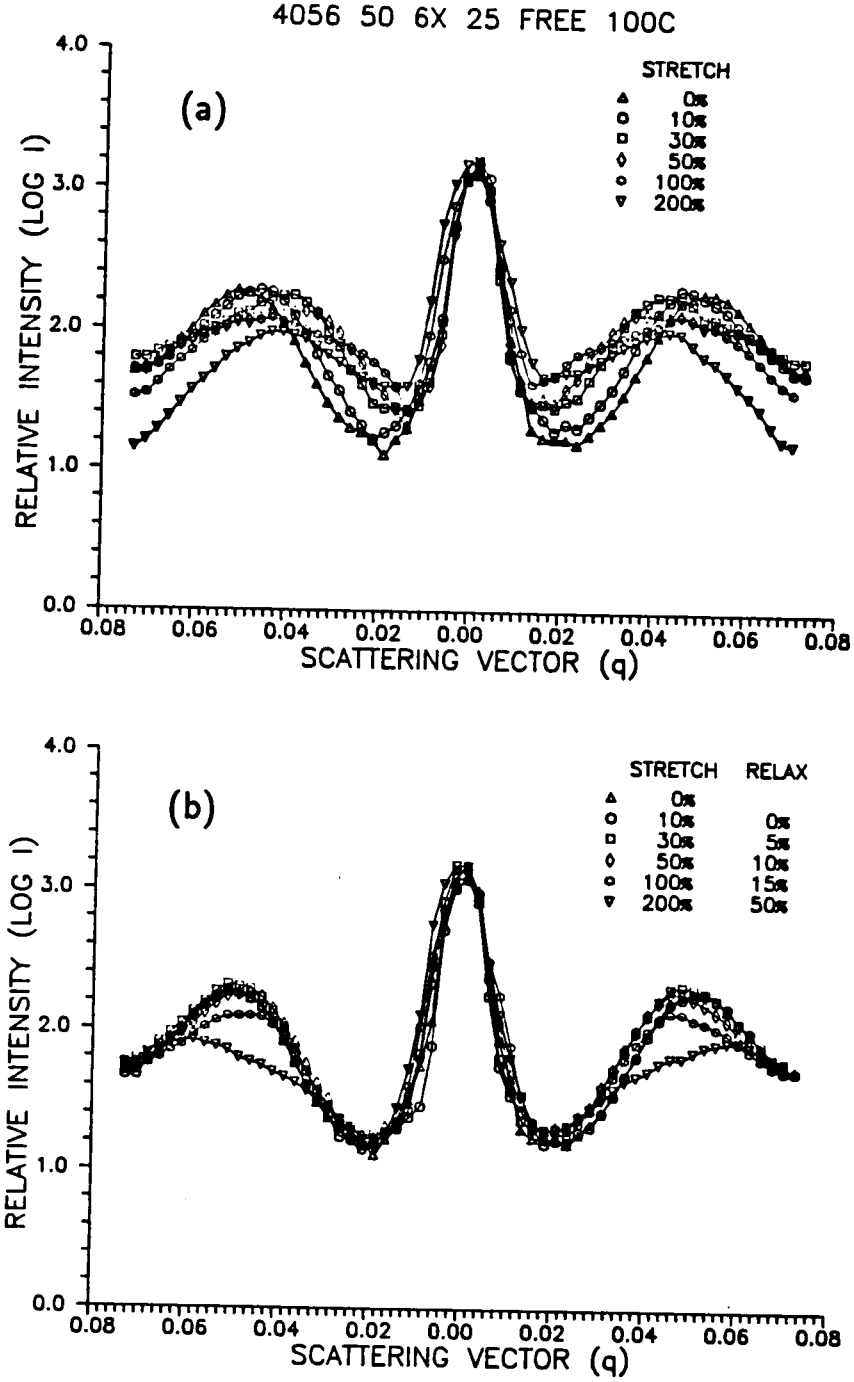


Figure 9.19: One dimensional data slices corresponding to the SAXS patterns shown in Figure 9.18. (a) stretched ; (b) stretched and relaxed. $q = 4\,\pi\,(\sin\theta)/\,\lambda$.

Table 9.14: Long periods observed for the drawn and free annealed H4056 filament in the strained state.

STRAIN	OBSERVED L.P. (Å)	EXPECTED L.P. IF AFFINE (Å)
0%	123	123
10%	136	135
30%	153	160
50%	141–173	186
100%	141	248
200%	148	372

Table 9.15: Long periods observed for the drawn and free annealed H4056 filament after retraction.

INITIAL STRAIN	RESIDUAL STRAIN	OBSERVED L.P. (Å)	EXPECTED L.P. IF AFFINE (Å)
0%	0%	123	123
10%	0%	123	123
30%	5%	128	128
50%	10%	135	135
100%	15%	133	141
200%	30%	106	185

resemble the original. The energy losses incurred in deforming the crystallites results in low work recovery in these filaments as will be shown in the next section. However, this filament has a high elongation to break and there is fairly high strain recovery up to about 200% elongation. This is a direct result of the retraction of the amorphous chains during annealing. The recoiling also results in a greater ratio of loops to bridges in this filament than in the drawn and fixed annealed filament. These loops provide a drawing mechanism in the crystalline domains, which contributes to the higher ultimate elongation.

A drawn and free annealed filament of H7246 was studied in the hopes of gaining some insight into the effect of composition on the deformation behavior. SAXS patterns taken of these filaments during cyclic deformation are shown in Figure 9.20. The scattering peak in these patterns takes the form of a broad horizontal streak. This would be explained by small highly oriented crystallites. The intensity and breadth of the streaks indicate that the crystallites are fairly well developed in the radial direction of the fiber. Upon stretching, the SAXS peaks move closer together and the streak becomes straighter. Thus the crystallites are moving further apart and becomeing more highly oriented. The average long period increases in an almost affine manner up to 50% elongation, but then the distribution of spacings broadens considerably.

The one-dimensional scans in the meridional direction of these patterns are shown in Figure 9.21. The corresponding long periods are given in Tables 9.16 and 9.17. The patterns of filaments stretched up to 30% and allowed to relax are almost identical to the original. The long periods of the relaxed

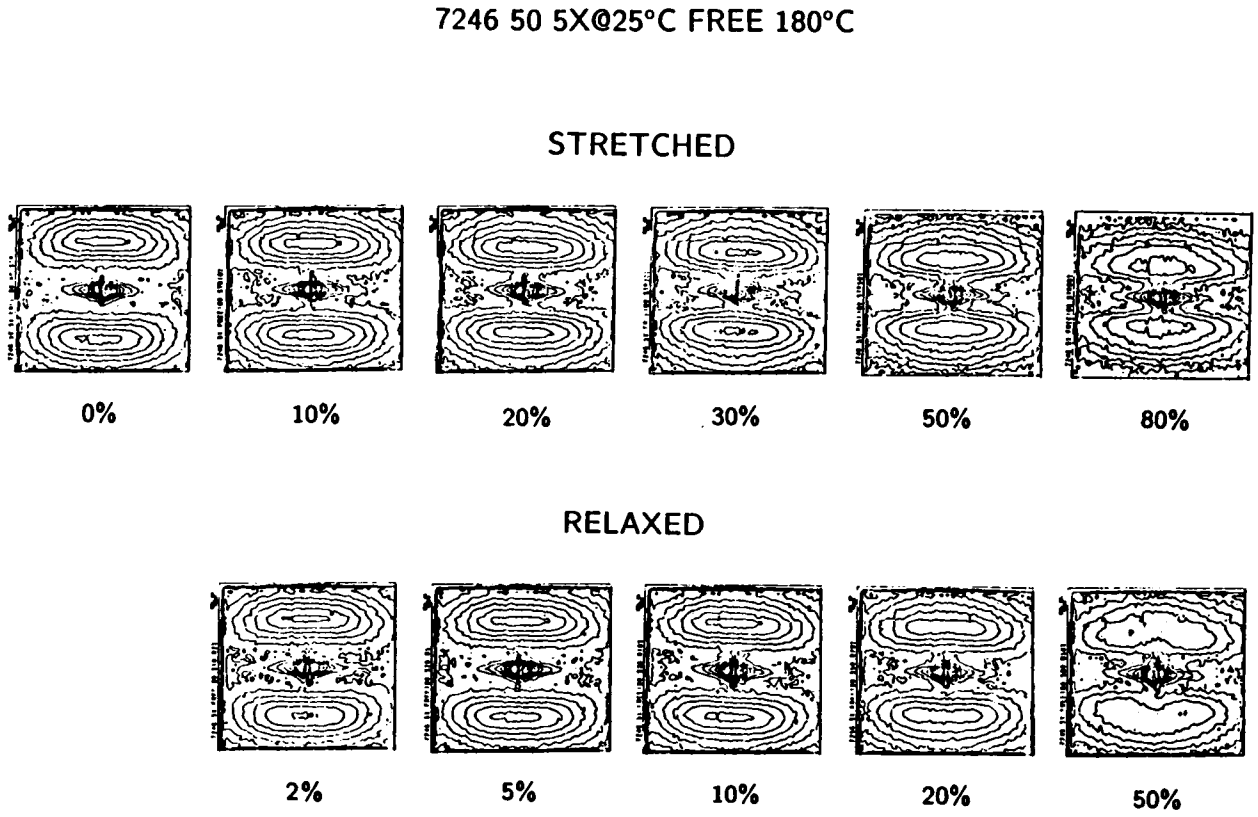


Figure 9.20: SAXS patterns of a drawn and free annealed H7246 filament.

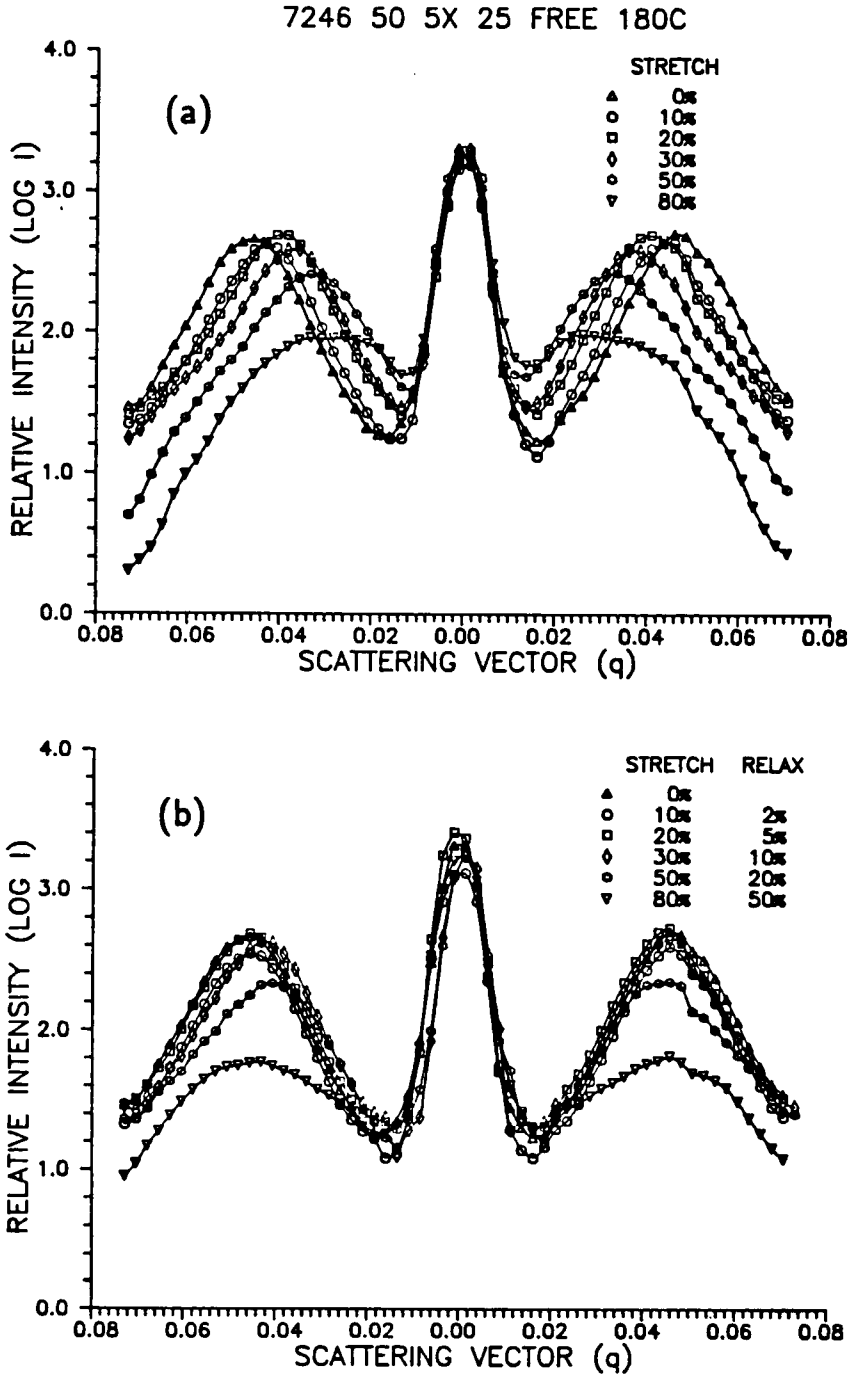


Figure 9.21: One dimensional data slices corresponding to the SAXS patterns shown in Figure 9.20. (a) stretched ; (b) stretched and relaxed. $q = 4\,\pi\,(\sin\theta)/\,\lambda$.

Table 9.16: Long periods observed for the drawn and free annealed H7246 filament in the strained state.

STRAIN	OBSERVED L.P. (Å)	EXPECTED L.P. IF AFFINE (Å)
0%	135	135
10%	144	149
20%	156	162
30%	170	176
50%	192	203
80%	177–266	243

Table 9.17: Long periods observed for the drawn and free annealed H7246 filament after retraction.

INITIAL STRAIN	RESIDUAL STRAIN	OBSERVED L.P. (Å)	EXPECTED L.P. IF AFFINE (Å)
0%	0%	135	135
10%	2%	138	138
20%	5%	139	142
30%	10%	141	149
50%	20%	142–148	162
80%	50%	133–147	203

samples are very close to the predicted values after stretches up to 20%, and there is little loss of scattering intensity. After relaxing from elongations greater than 30%, the long periods are smaller than predicted and there is a considerable loss of scattering power. This means that some plastic deformation starts at relatively low elongations. The tie molecules and taut bridge molecules begin to exert enough force at this point to disrupt the crystalline structure. Above about 50% elongation there is a major change in structure. The peaks broaden in the meridional direction and the intensity drops off sharply. Large scale destruction of the lamellar structure is beginning to take place at this point. Lamellae are being broken up into smaller pieces and the crystallinity is being reduced. Stretching to 80% causes large permanent deformation as shown by the low recovery.

Thus, the crystallites separate in a roughly affine manner up to about 50% elongation, but there is some permanent set as tie molecules and taut bridge molecules start to plastically deform the crystallites. Above 50% elongation, the crystalline domains are being torn apart and the original morphology can not be recovered.

The effect of composition can now be discussed. Since the degree of crystallinity in annealed samples increases in general as HSC increases, the number of tie molecules is also expected to increase. The crystallites also become thicker and more closely spaced as HSC increases. According to Equation 2.1, the extension of the interdomain material relative to the macroscopic extension increases as the ratio of crystallite thickness to the interdomain spacing

increases. Both these factors tend to increase the amount of plastic deformation that occurs at a given elongation. Drawn and free annealed filaments from both compositions can be stretched about 30% with little permanent changes in the morphology. Beyond this point, the structural recovery of H7246 drops off much more rapidly than H4056. Results from the other compositions show that there is a gradual decrease in maximum elongation and elastic recovery as HSC increases.

9.6 Cyclic Testing

Cyclic testing of the drawn filaments was carried out to determine the elastic properties of these filaments. Combined with the structural information now available, it should be possible to develop a better understanding of how the elastic properties are affected by changes in the filament microstructure.

Since H4056 and H7246 represent the two extremes in copolymer composition in this study, most of the work was concentrated on these two compositions.

9.6.1 Elastic Recovery of H7246 Filaments

The effect of SDR, draw temperature, and annealing technique on the elastic properties of the H7246 filaments are presented in this section. (A list of all the strain and work recovery values determined for H7246 filaments can be found in Tables A.2 and A.3 in the Appendix.)

Effect of SDR

The elastic recovery of filaments spun at 50m/min and 300m/min before and after hot drawing are shown in Figures 9.22 and 9.23. The filaments spun at 50m/min were drawn 5×, while the filaments spun at 300m/min were drawn 3×. (Filaments spun at 50m/min and 300m/min and subsequently hot drawn will be denoted as 50HD and 300HD, respectively.) As discussed in Chapter 8, the filaments spun at the higher speed showed an increase in elastic recovery due to the higher crystalline orientation. After hot drawing, both filaments have an f_c of 0.87, but the 50HD filament has a slightly higher elongation to break. The 300HD filament has a slightly higher DPS than the 50HD filament.

The 50HD filament has higher strain recovery than the 300HD filament at all elongations. The 300HD filament has better work recovery below 10% elongation and about the same amount at 20 and 30%.

Although the crystalline orientation produced in these two filaments is about the same, there are apparently some differences in the orientation and nature of the amorphous chains due to the different initial SDR and the different post draw ratio. However, it is difficult to draw any conclusions about the effect of SDR without first studying the effect of post draw ratio on these filaments.

Effect of Draw Temperature

Filaments were drawn at 25°C and 100°C to determine whether there are any major differences in drawing below and above the T_g of PTMT. However, the

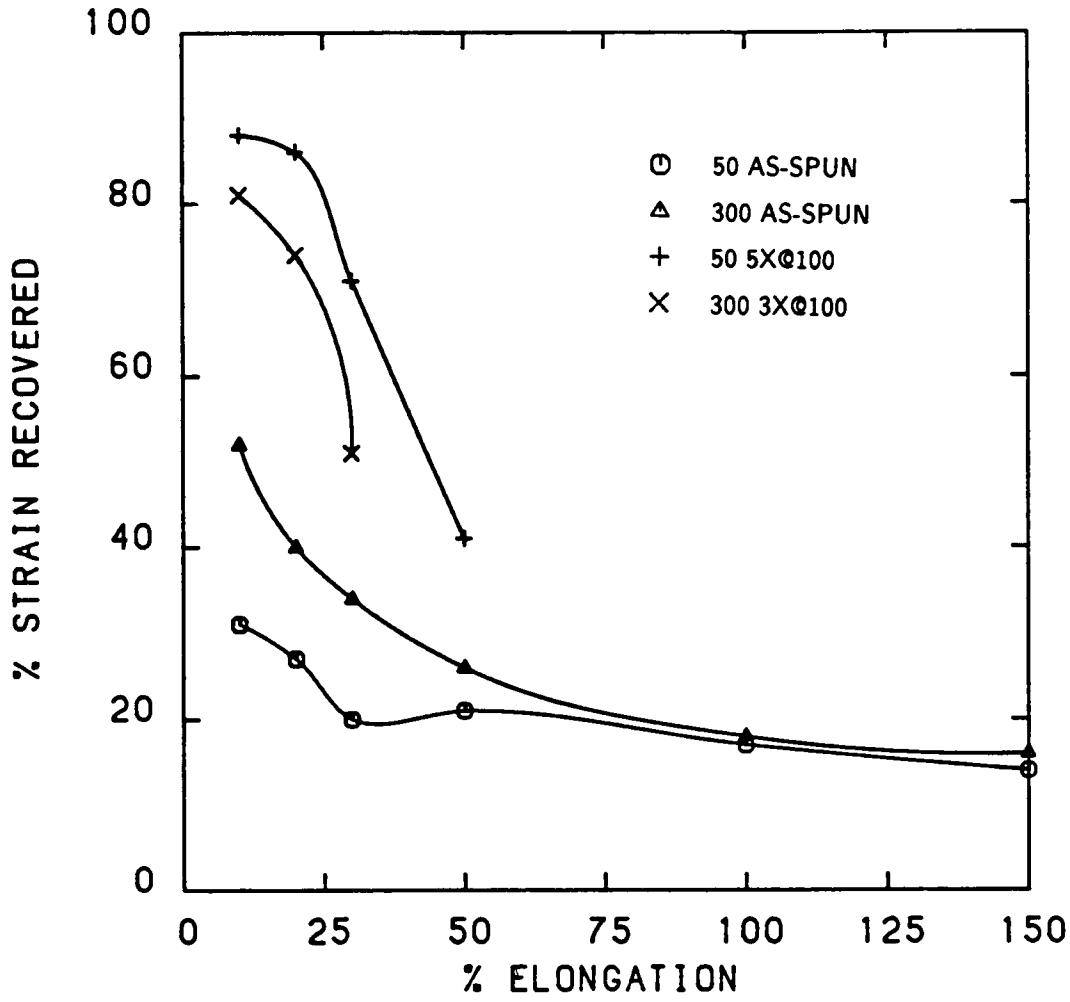


Figure 9.22: Effect of spin draw ratio on the strain recovery of "as-spun" and "hot drawn" filaments of H7246.

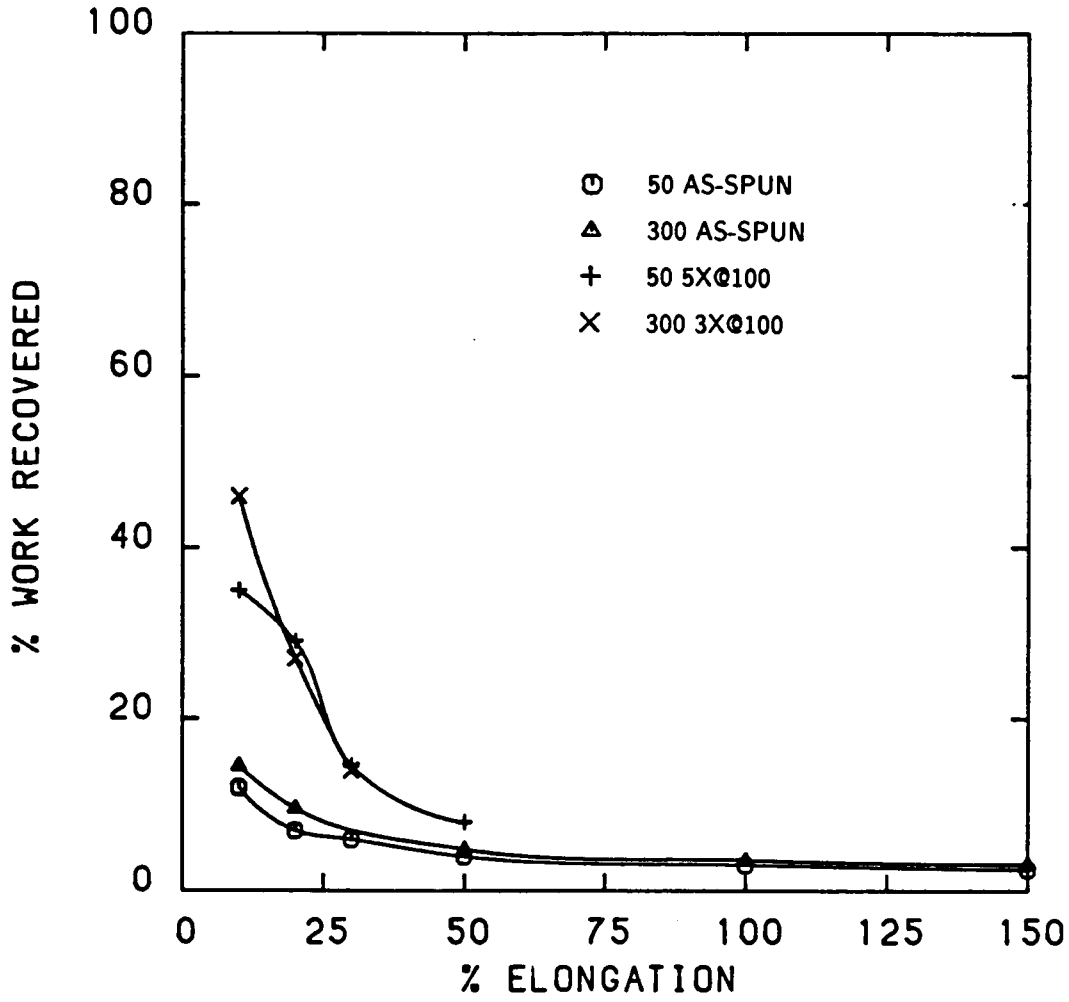


Figure 9.23: Effect of spin draw ratio on the work recovery of "as-spun" and "hot drawn" filaments of H7246.

T_g of the copolymers are determined by the amorphous mixture of PTMT segments and PTMEG segments. The T_g of the copolymers are below that of pure PTMT, and in the compositions low in HSC it is well below the 25°C drawing temperature. As a result, there were no fundamental differences between the morphologies of the copolymer filaments drawn at the two temperatures. The changes produced were more a result of an annealing effect caused by the brief temperature rise in the hot drawn filament. These filaments have a slightly higher DPS. The effect of draw temperature on the H7246 filaments before and after fixed annealing can be seen in Figures 9.24 and 9.25.

A summary of their pertinent structural features and properties are given below:

Sample	f_c	Maximum Strain (%)	DPS
As-spun	0.15	703	0.31
Cold Drawn	0.86	46	0.19
Hot Drawn	0.87	61	0.27
CD & Fix	0.89	71	0.56
HD & Fix	0.89	70	0.59

Some differences which can be attributed to the draw temperature are found in the as-drawn filaments. The hot drawn filament has higher strain recovery than the cold drawn filament at elongations less than 30%. This is attributed to the higher DPS of this sample. There is not much difference in

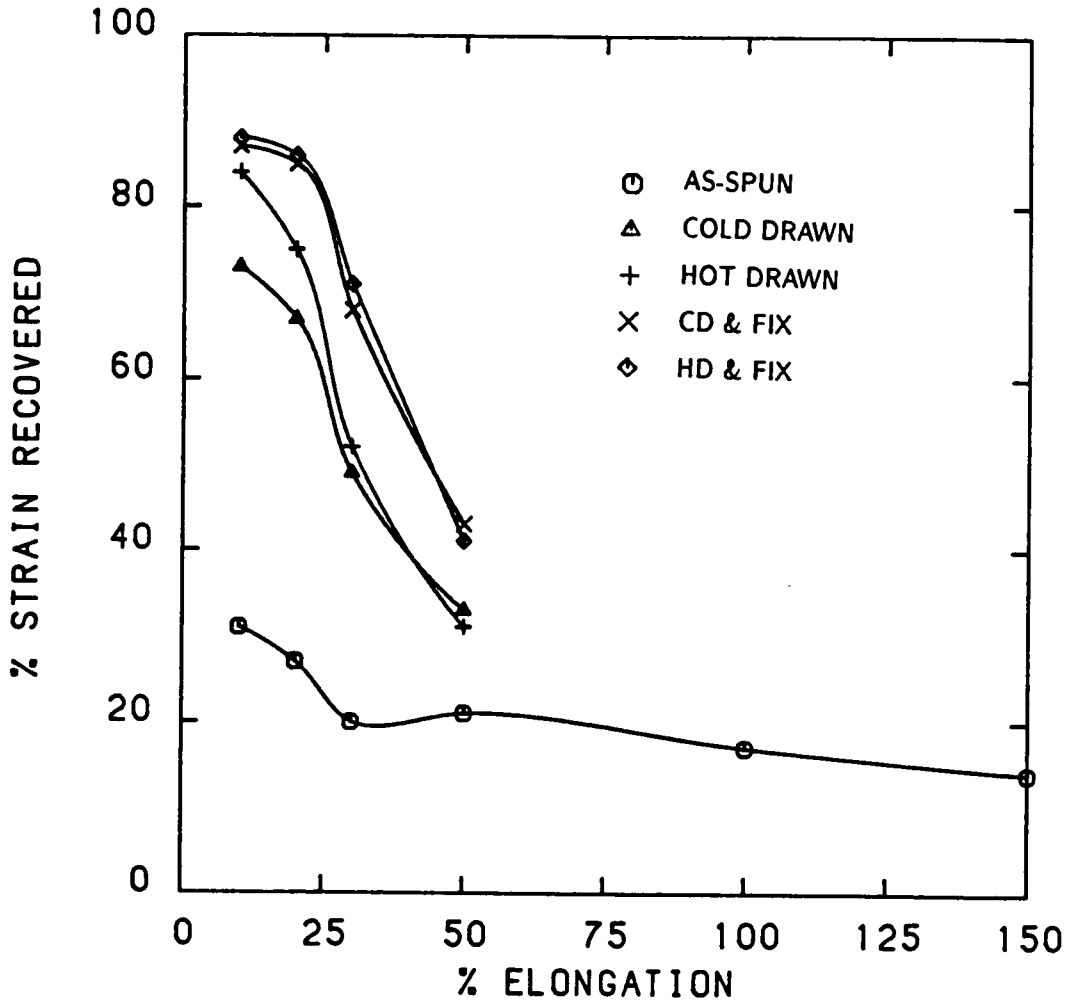


Figure 9.24: Effect of draw temperature on the strain recovery of H7246 filaments before and after annealing.

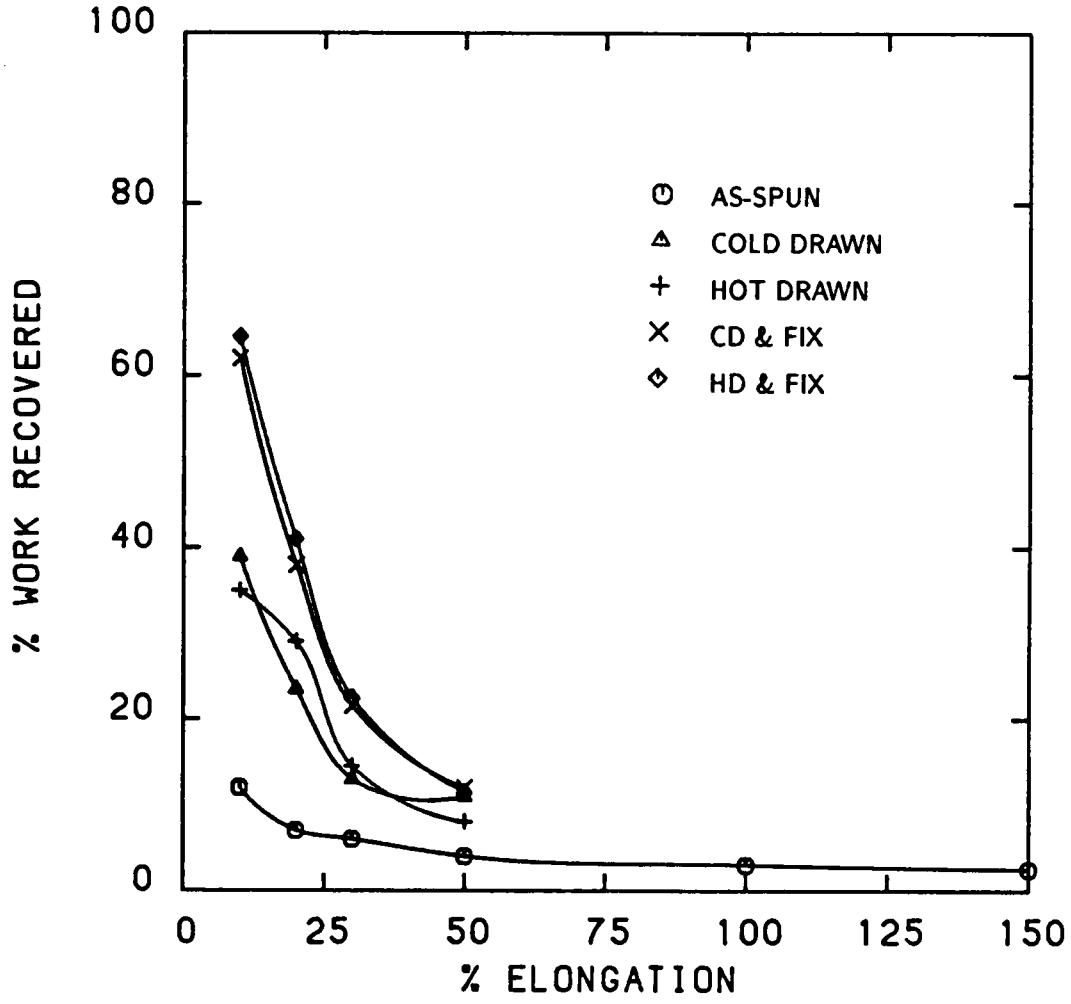


Figure 9.25: Effect of draw temperature on the work recovery of H7246 filaments before and after annealing.

the work recovery of the two drawn filaments.

After fixed annealing, the DPS of the two samples are brought up to the same level. The overall chain orientations of the two are also about the same, judging by the elongation to break, f_c, and shrinkage measurements. For these reasons, there is little dependence of the elastic properties on draw temperature after the annealing step.

Free versus Fixed Annealing

Since the orientation of the amorphous chains in as-spun filaments is low, it makes little difference whether these filaments are fixed or free annealed. The elastic behavior of the samples are virtually the same, either way. Both the fixed and free annealed filaments have greater elastic recovery than the unannealed sample because of their higher DPS.

After drawing, large differences in mechanical behavior are observed between fixed and free annealed filaments. The elastic properties of H7246 filaments annealed each way can be seen in Figures 9.26 and 9.27. Although there are some differences in DPS and crystallite size, most of the property changes can be attributed to differences in the morphology of the amorphous phase. The crystalline orientation is only slightly higher in the fixed annealed filaments, but the chains are more highly extended resulting in more bridge segments and fewer loops than in the free annealed filament. This results in lower elongations to break and higher stress levels. Strain recovery is high in fixed annealed filaments from elongations up to about 20%, but then decreases

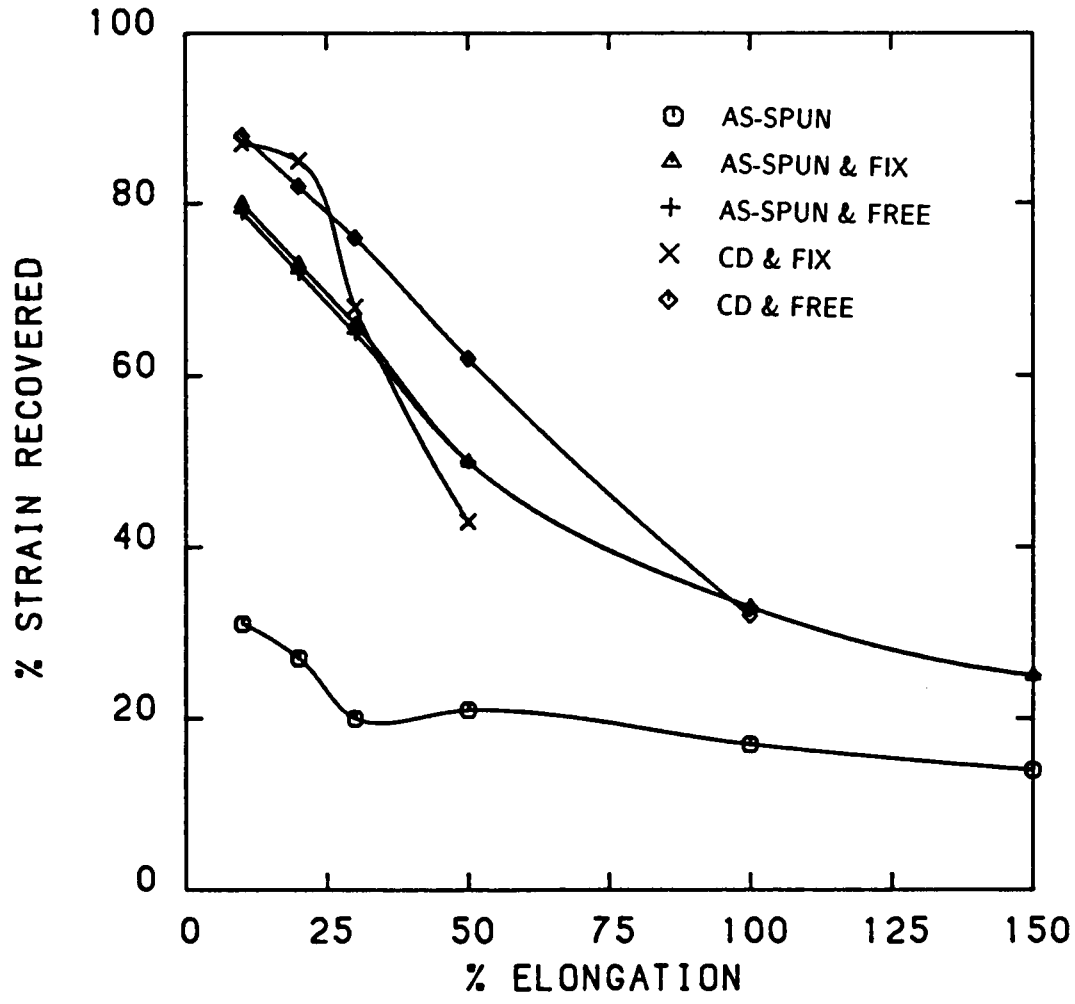


Figure 9.26: A comparison of the strain recovery of fixed and free annealed filaments of H7246 before and after drawing.

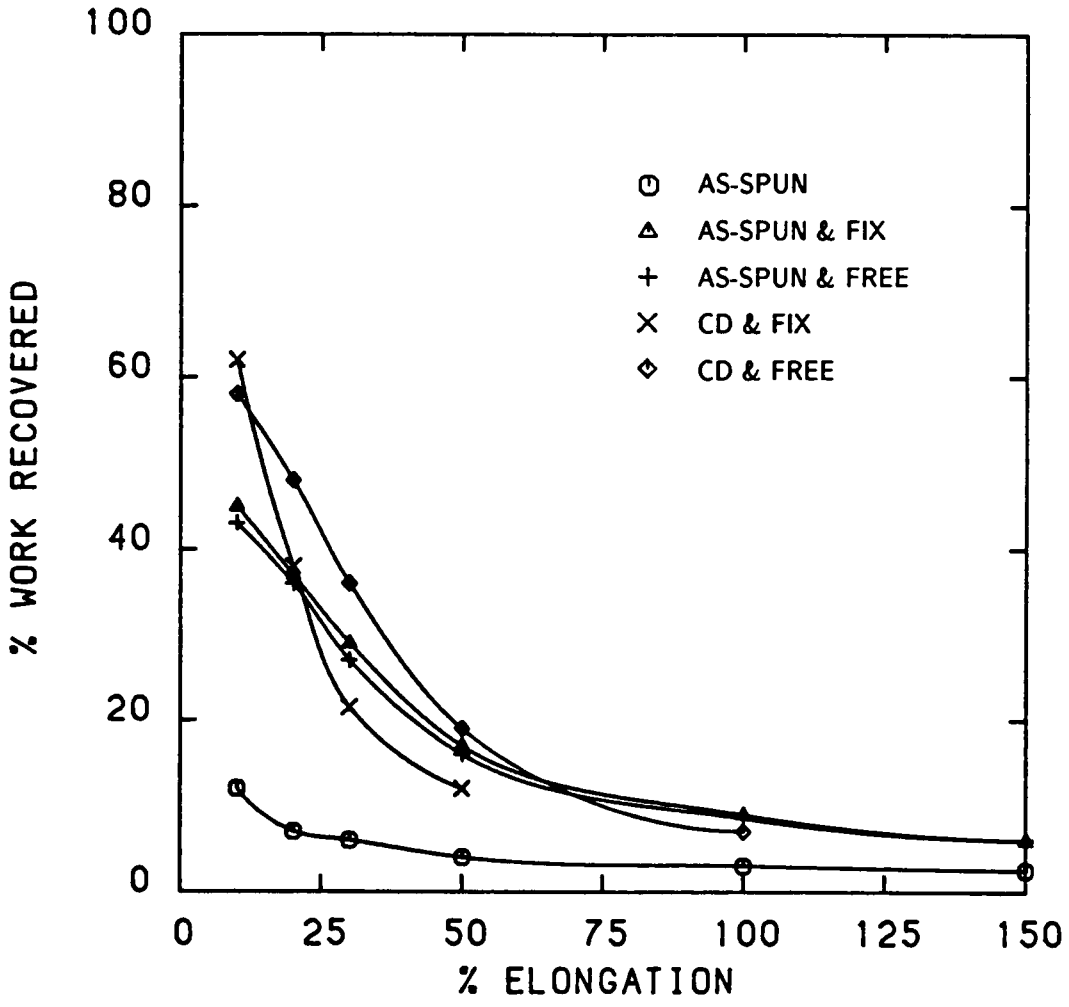


Figure 9.27: A comparison of the work recovery of fixed and free annealed filaments of H7246 before and after drawing.

rapidly as the filament approaches its ultimate elongation. The lower extension of the chains in the free annealed filament result in wider elastic range than in the fixed annealed filament.

Comparison with Undrawn Filaments

The crystalline orientation, elongation to break, and DPS for selected H7246 filaments are shown below:

Sample	f_c	Maximum Strain (%)	DPS
7246 50 Fix 180°C	0.32	712	0.69
7246 300 Fix 180°C	0.85	358	0.70
7246 50 CD	0.86	46	0.19
7246 50 CD Free 180°C	0.88	199	0.67
7246 50 CD Fix 180°C	0.89	71	0.56

The DPS is about the same in all of the annealed filaments except for the cold drawn and fixed annealed sample which has a slightly lower DPS. The crystalline orientation of the filament spun at 300m/min and the three drawn filaments are all about the same, although the elongation to break varies from 46% in the unannealed drawn filament to 358% in the undrawn annealed filament. The filament spun at 50m/min has low crystalline orientation and high elongation to break.

Since the filaments vary widely in their ultimate elongation, they have been compared on a basis of relative or normalized strain (percent elongation

during stretching divided by their ultimate elongation). The effect of the different processing conditions on the elastic behavior of the filaments compared in this way can be seen in Figures 9.28 and 9.29.

The sample spun at 50m/min and annealed shows the lowest elastic recovery. The higher crystalline orientation in the filament spun at 300m/min and annealed produces a substantial increase in elastic recovery at low elongations as discussed in Chapter 8.

During drawing, the crystalline material is deformed and the chains become more highly extended. After removing the drawing stress, the soft segments retract to some extent, but the hard segments remain aligned in the stretch direction. On subsequent stretching, the hard segment domains are more resistent to deformation. As a result, the drawn filament exhibits higher strain and work recovery from moderate to high relative strains than either of the undrawn filaments.

During fixed annealing the highly extended hard segments and taut bridge segments are unable to disorient very much. This results in the formation of an increased number of bridge segments during crystallization. The stress-strain behavior and elongation to break remain about the same as they are in the unannealed drawn filament. However, there is a large improvement in strain recovery and work recovery at low elongations. This can be attributed to the increase in the DPS and crystallite size/perfection. As will be shown in a subsequent section, there is a jump in the elastic recovery as the average crystallite size reaches $1 \times 10^5 \text{Å}^3$ or higher. The properties at the higher

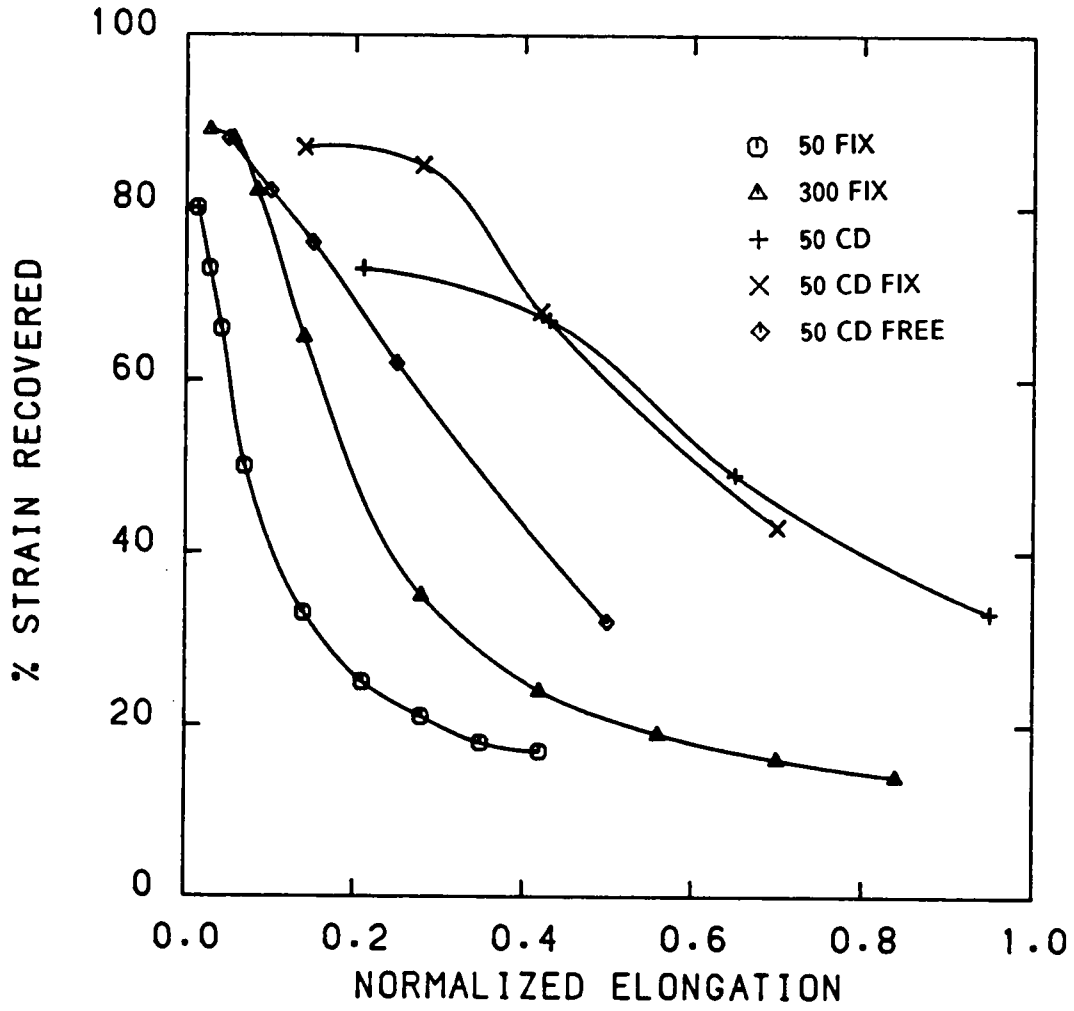


Figure 9.28: Strain recovery of selected H7246 filaments.

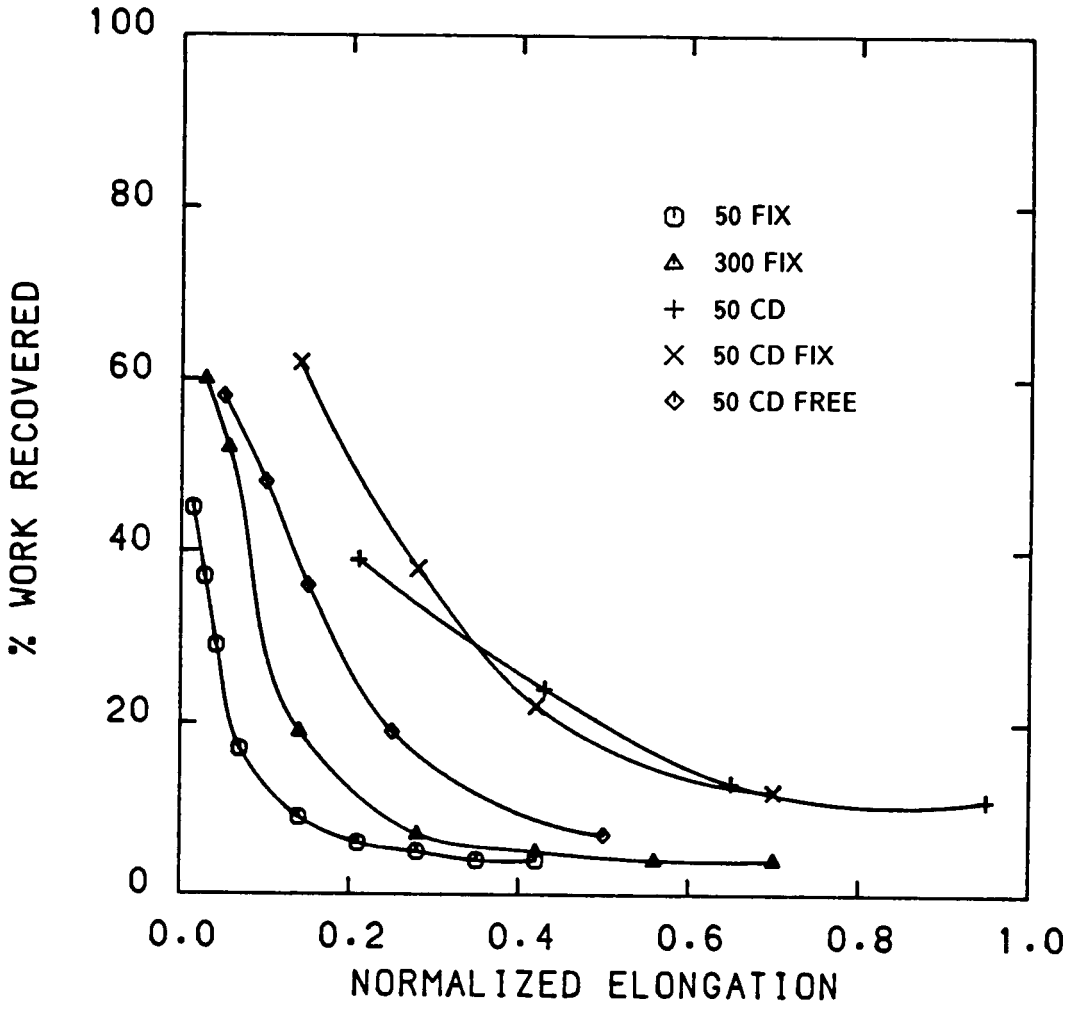


Figure 9.29: Work recovery of selected H7246 filaments.

elongations depend more on the chain orientation than on the initial DPS and crystallite size. Since there is little change in chain orientation during fixed annealing, the drawn and fixed annealed filament has about the same elastic properties as the drawn filament at the higher elongations.

During free annealing, the amorphous chains are able to recoil. The crystalline orientation remains high but some melting and recrystallization takes place. Since the amorphous chains are more highly coiled, a larger number of "loops" are formed than in the fixed annealed filaments. These "loops" provide a drawing mechanism during stretching. As a result, the free annealed filaments have a higher elongation to break than the fixed annealed filaments, but also show more plastic deformation during stretching.

The filament spun at 300m/min and fixed annealed, the drawn and fixed annealed filament, and the drawn and free annealed filament all have about the same crystalline orientation and DPS, but vary widely in their elongation to break and elastic properties. Thus the differences in mechanical properties are mainly the result of differences in the nature of the interdomain chains. The fixed annealed filament has more bridge chains and fewer loops than the free annealed filament which, in turn, has more bridges and fewer loops than the undrawn and annealed filament. As the portion of bridge chains increases, plastic deformation decreases and elastic recovery increases. Unfortunately, the elongation to break also decreases.

Another difference between the drawn and undrawn filaments is in the magnitude of the stresses during stretching and retraction (refer to Figure 9.10

for a comparison of the stresses during extension). Since higher stresses are required to stretch the drawn filaments, the magnitude of the retractive stresses are much greater than those of the undrawn filaments. So, the drawn filaments have greater tenacity, show less plastic deformation during stretching, and have higher retractive stresses than the undrawn filaments. There is however, a trade-off between high elastic recovery and high extensibility.

9.6.2 Elastic Recovery of H4056 Filaments

Pertinent characteristics of selected drawn and undrawn H4056 filaments are given in the table below:

Sample	f_c	Maximum Strain (%)	DPS
4056 50 Free 100°C	0.18	944	0.66
4056 250 Fix 100°C	0.89	474	0.63
4056 50 CD	0.90	136	0.53
4056 50 CD Free 100°C	0.87	513	0.66
4056 50 CD Fix 100°C	0.90	142	0.62

The DPS is about the same in all of the annealed filaments. The crystalline orientation of the filament spun at 250m/min and the three drawn filaments are all about the same, although the elongation to break varies widely. The filament spun at 50m/min and annealed has low crystalline orientation and very high elongation to break.

In Figures 9.30 and 9.31, the effects of drawing and annealing treatment

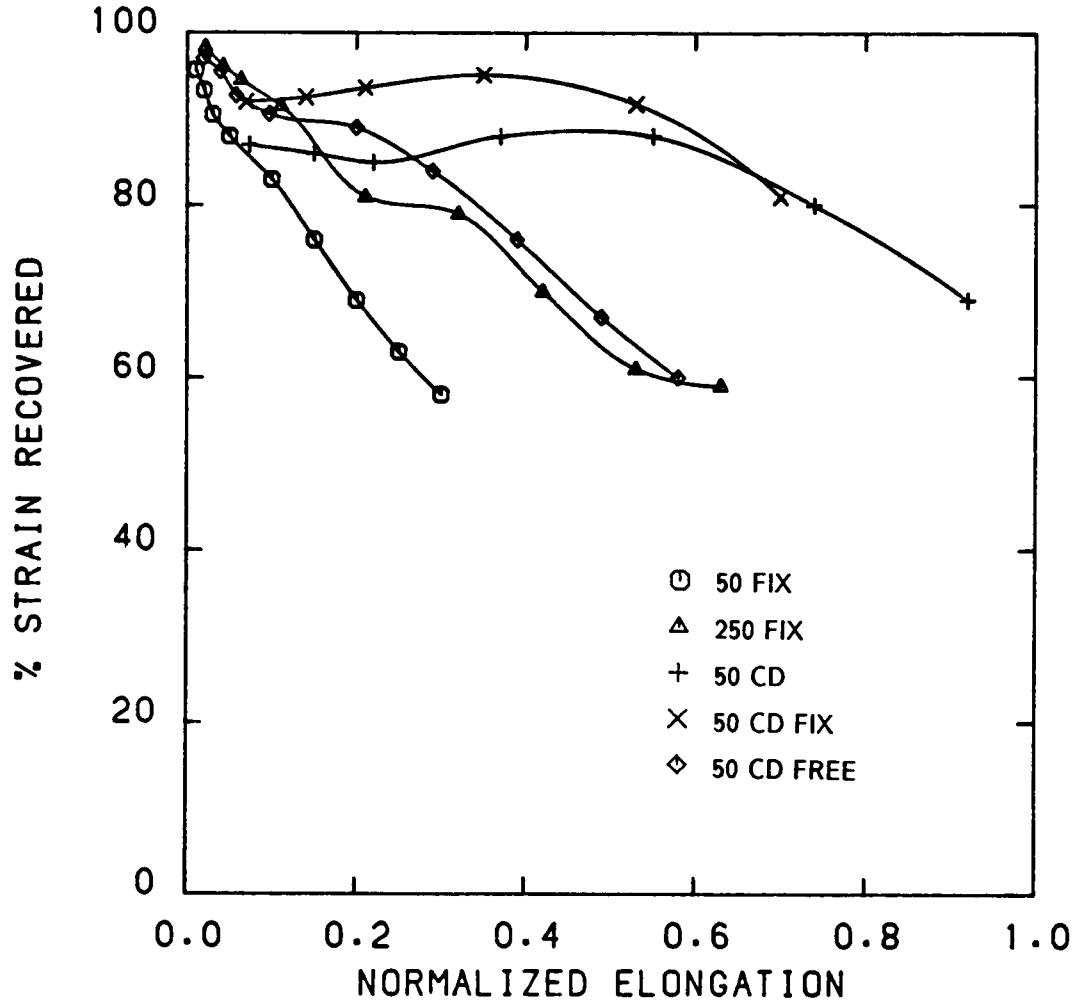


Figure 9.30: Strain recovery of selected H4056 filaments.

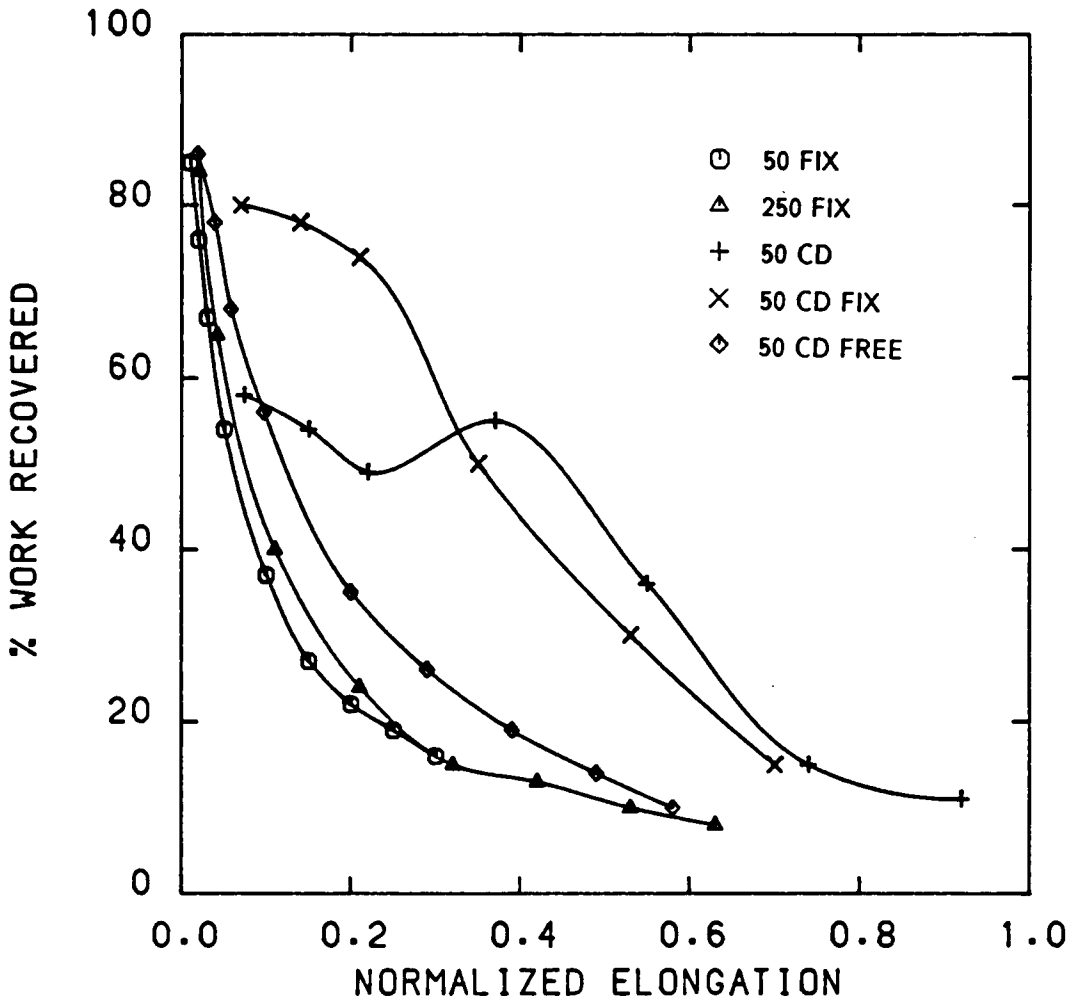


Figure 9.31: Work recovery of selected H4056 filaments.

on the elastic recovery of these filaments can be seen. (A list of all the strain and work recovery values determined for H4056 filaments can be found in Tables A.4 and A.5 in the Appendix.)

During drawing, the tie molecules and shorter bridge chains become taut and deform the crystalline material. When the tension is removed, the amorphous chains relax and the microstructure recovers to some extent. Upon subsequent stretching, little additional plastic deformation of the crystallites occurs until the amount of strain exceeds levels previously reached. In the drawn H4056 filament, this occurs at about 50% elongation. The peak in the strain and work recovery curves of this filament correspond to this point. As a result of the reduction in plastic deformation, the drawn filament has much higher strain and work recovery at moderate to high relative elongations than either of the undrawn filaments.

During fixed annealing, the chains are unable to recoil so the stress–strain behavior of the drawn and fixed annealed filament is almost identical to that of the unannealed drawn filament. The elongation to break and tenacity of the two filaments are about the same. However, there is a some improvement in strain recovery and work recovery at low elongations as a result of the increase in the DPS. The peak in the work recovery curve is no longer observed after annealing because of the increase in recovery at low elongations.

As discussed in the previous section, free annealing produces more "loops" and fewer "bridges" than fixed annealing. This results in more plastic deformation and relatively lower elastic recovery than in a structure having

more bridges between the crystalline domains. The elastic recovery of the free annealed filament is only slightly higher than that of the undrawn filament spun at 300m/min when compared on a normalized basis. However, the free annealed filament has a higher load bearing capacity during extension and greater retractive stresses from a given elongation than the undrawn filament. (The higher stress during extension combined with the greater percent work recovery mean higher retractive stresses.)

9.6.3 Effect of Crystallite Size

The crystallite size appears to be an important factor in determining the amount of strain recovery after stretching the filaments. The strain recovery of H7246 filaments subjected to various processing conditions, is shown as a function of crystallite size in Figure 9.32. Small crystallites result in low strain recovery. As crystallite size increases up to 10^5 Å^3, the amount of recovery rapidly increases. Above this size, there is only a gradual increase in elastic recovery with crystallite size. In H4056, all the filaments studied had an average crystallite size index of over 10^5 Å^3. As shown in Figure 9.33, all of these filaments exhibited high strain recovery.

These results suggest that there is a minimum crystallite size/perfection below which poor elastic properties will be observed. Apparently, crystallites below a critical size tear apart much more easily than do larger crystallites. The physical cross-link density in these samples may also be lower, leaving fewer junction points to hold the network together.

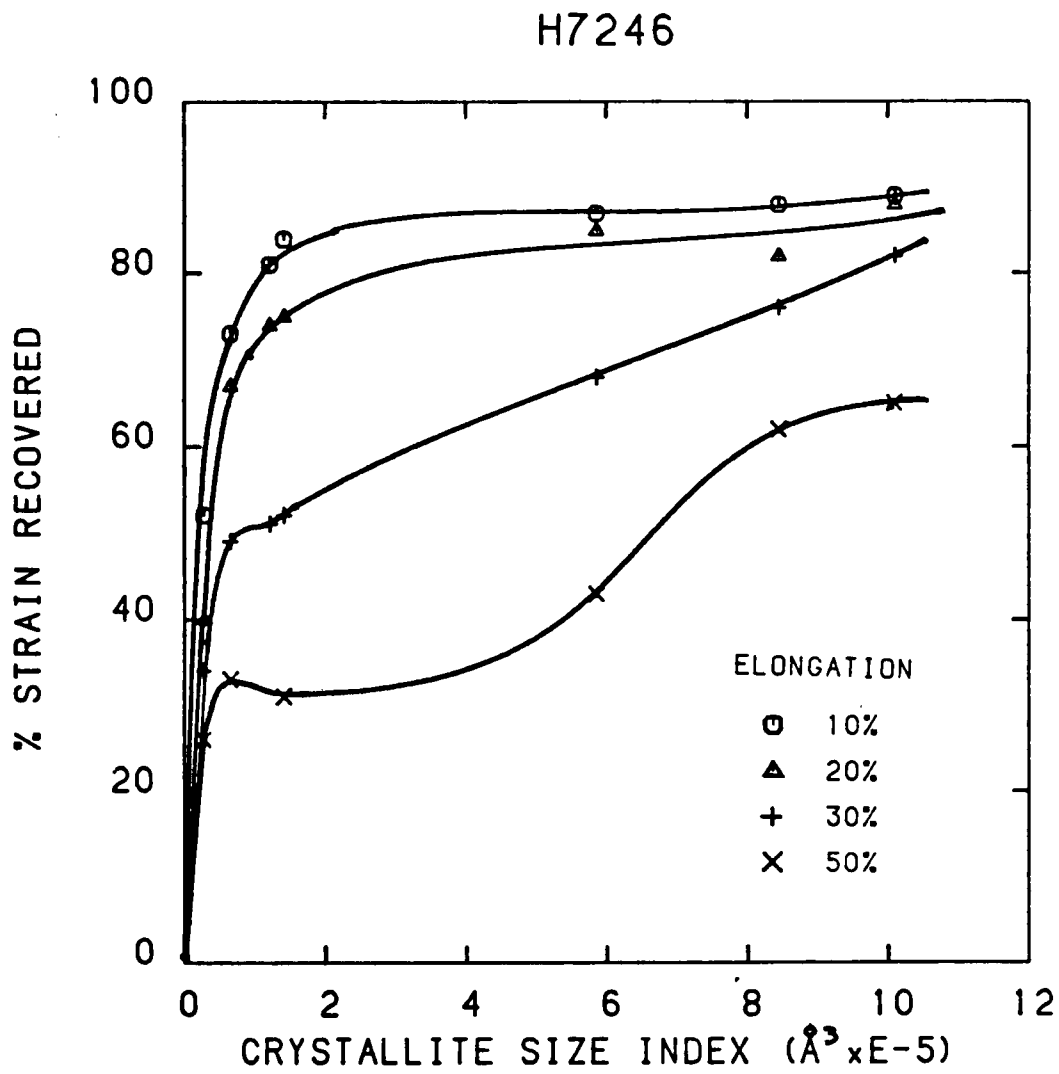


Figure 9.32: Effect of crystallite size on the strain recovery of H7246 filaments stretched to different levels of extension.

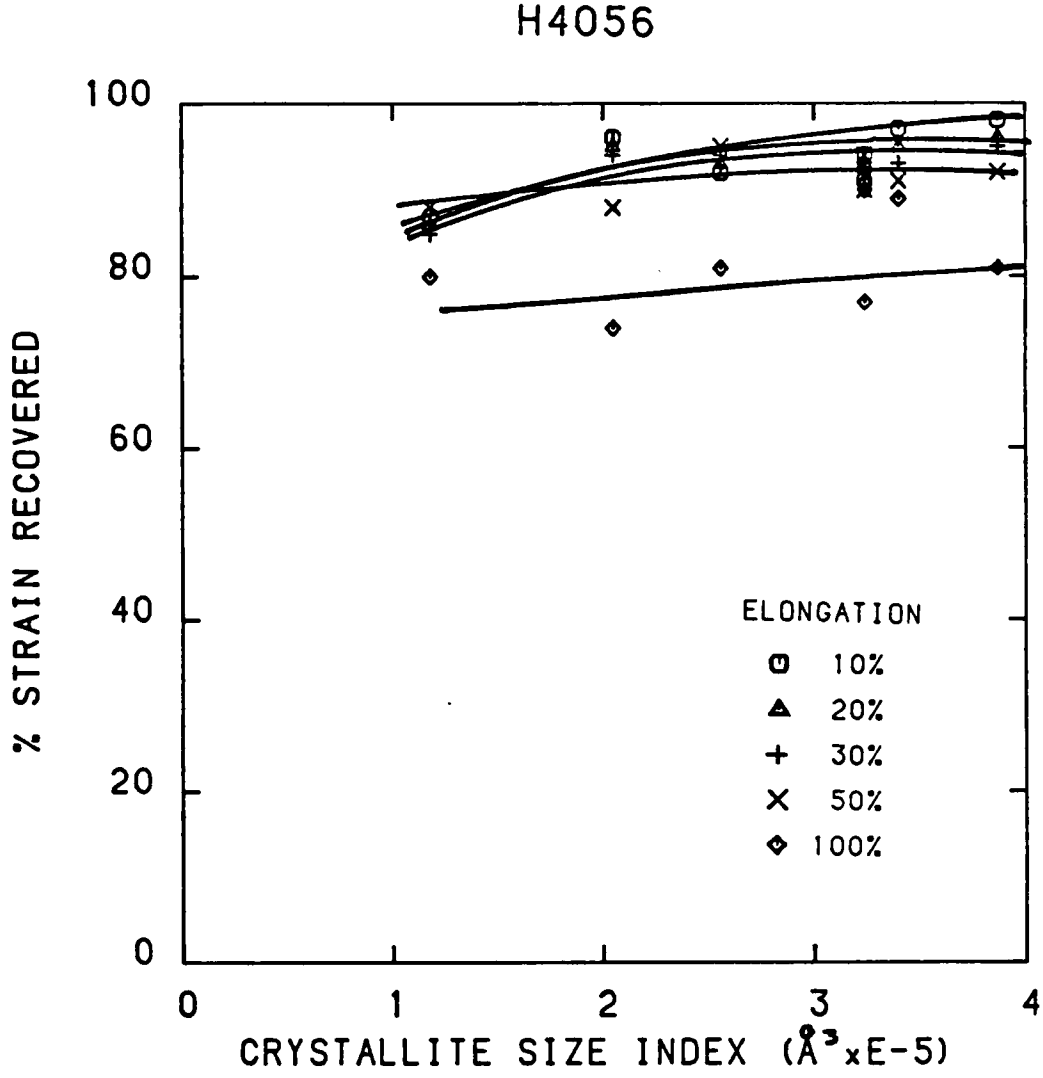


Figure 9.33: Effect of crystallite size on the strain recovery of H4056 filaments stretched to different levels of extension.

9.6.4 Effect of Composition

The effect of composition on the elastic behavior of drawn and annealed filaments can be seen in Figures 9.34, 9.35, 9.36, and 9.37. The differences between free and fixed annealing on the elastic properties are quite apparent in these figures. As HSC decreases, the strain recovery, work recovery and elongation to break generally increase, whether free or fixed annealed. Some values for these properties are presented in Table 9.18. A more complete list of the strain recovery and work recovery values for these filaments can be found in Tables A.6 and A.7 in the Appendix.

As HSC decreases, there are fewer hard segments in the elastomeric phase, T_g drops, and the amorphous phase becomes more fluid like. The crystallites are also spaced further apart. For these reasons, the relative number of tie molecules and taut bridges decrease as HSC decreases, and there is less destruction of crystallites at higher elongations. Thus, the elongation to break and elastic recovery both increase as HSC decreases.

9.7 Discussion and Conclusions

During cyclic loading of the H4056 filament to 250% elongation, the force required to stretch the filament decreased enormously between the first and second cycles, yet the retactive force remained the same. Thus, drawing appears to provide a viable route for reducing the plastic deformation of the copolymer filaments during subsequent stretching. The effects of drawing and

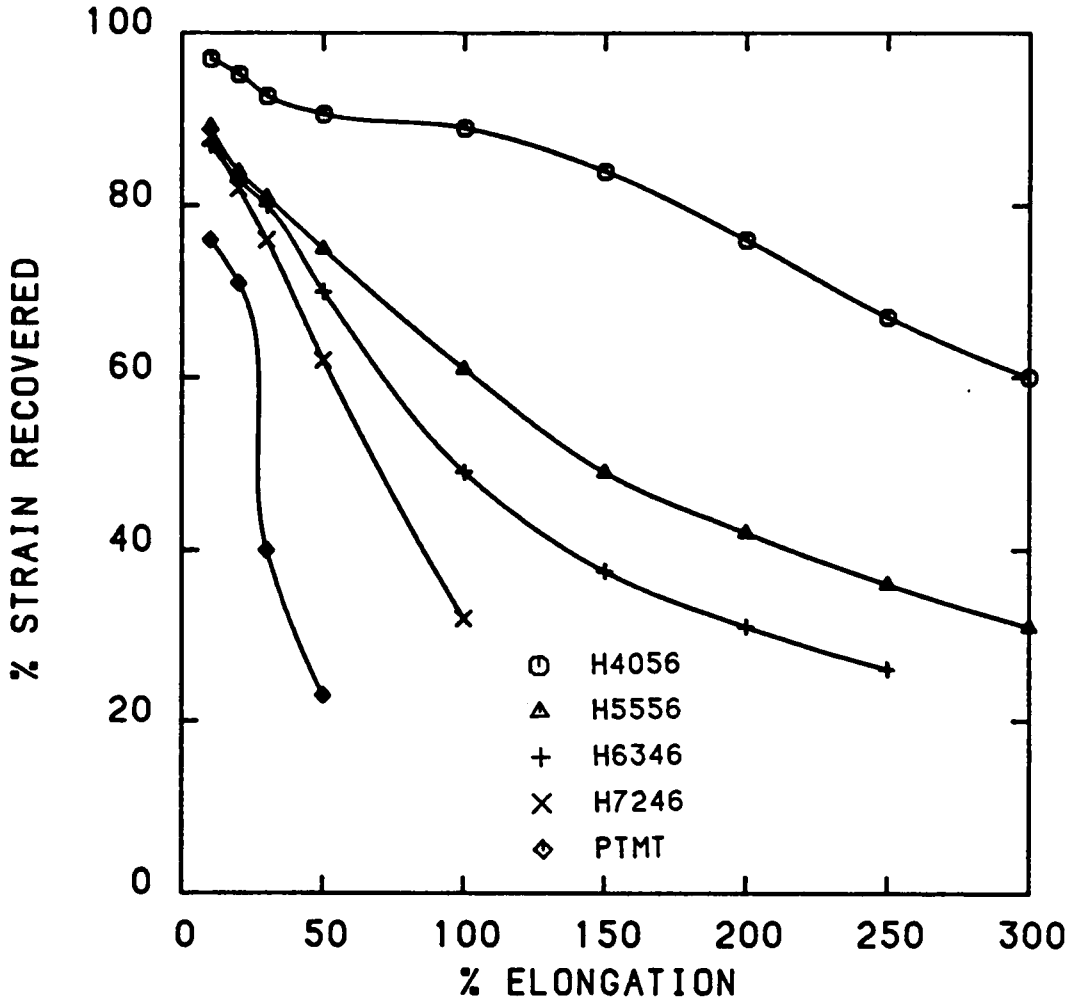


Figure 9.34: Effect of composition on the strain recovery of drawn and free annealed filaments.

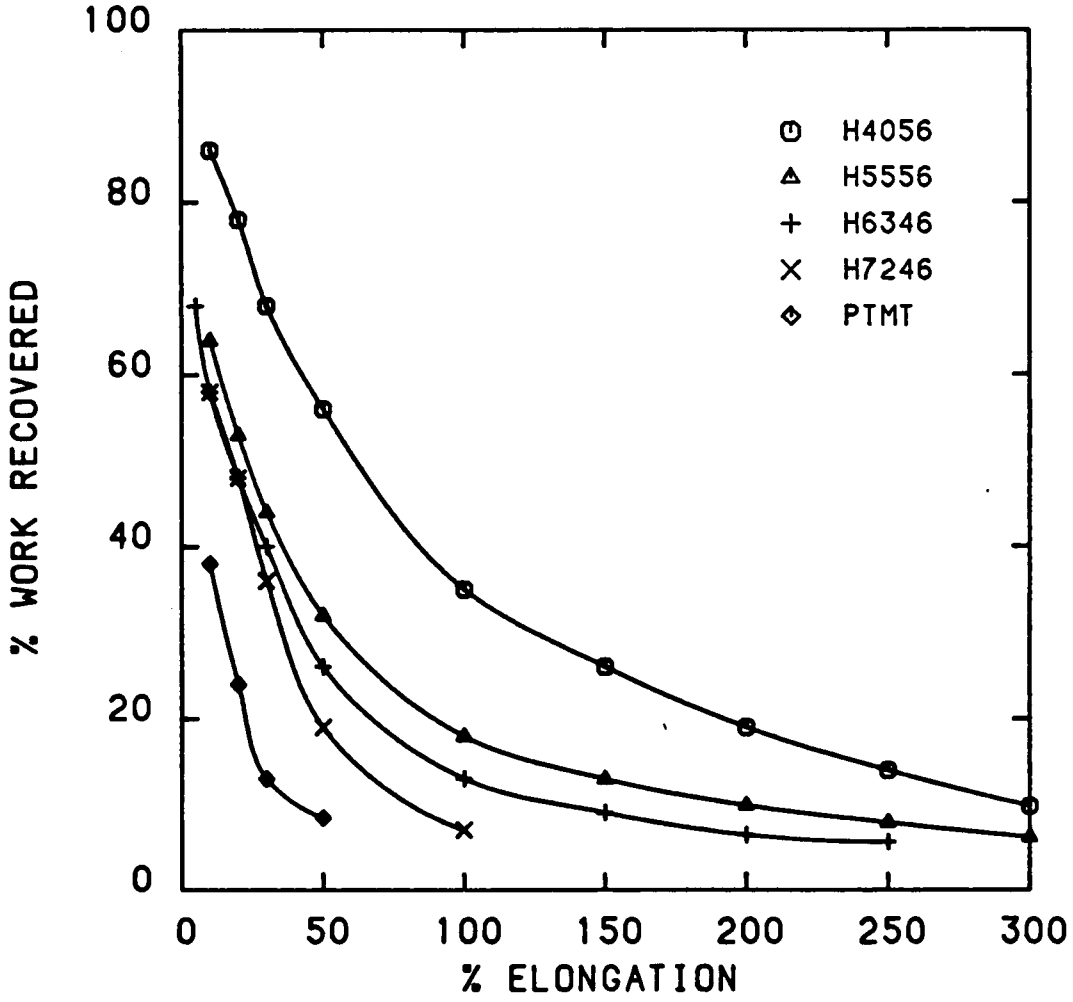


Figure 9.35: Effect of composition on the work recovery of drawn and free annealed filaments.

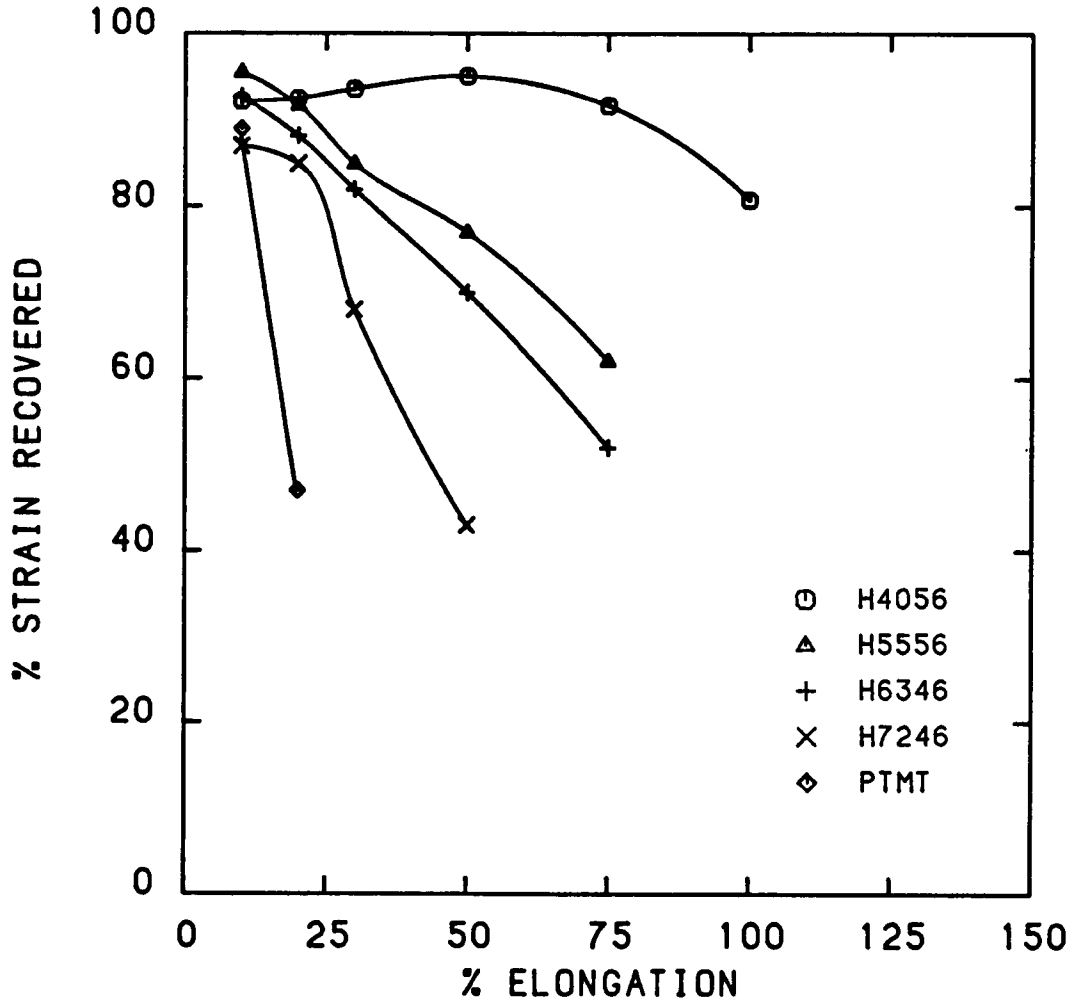


Figure 9.36: Effect of composition on the strain recovery of drawn and fixed annealed filaments.

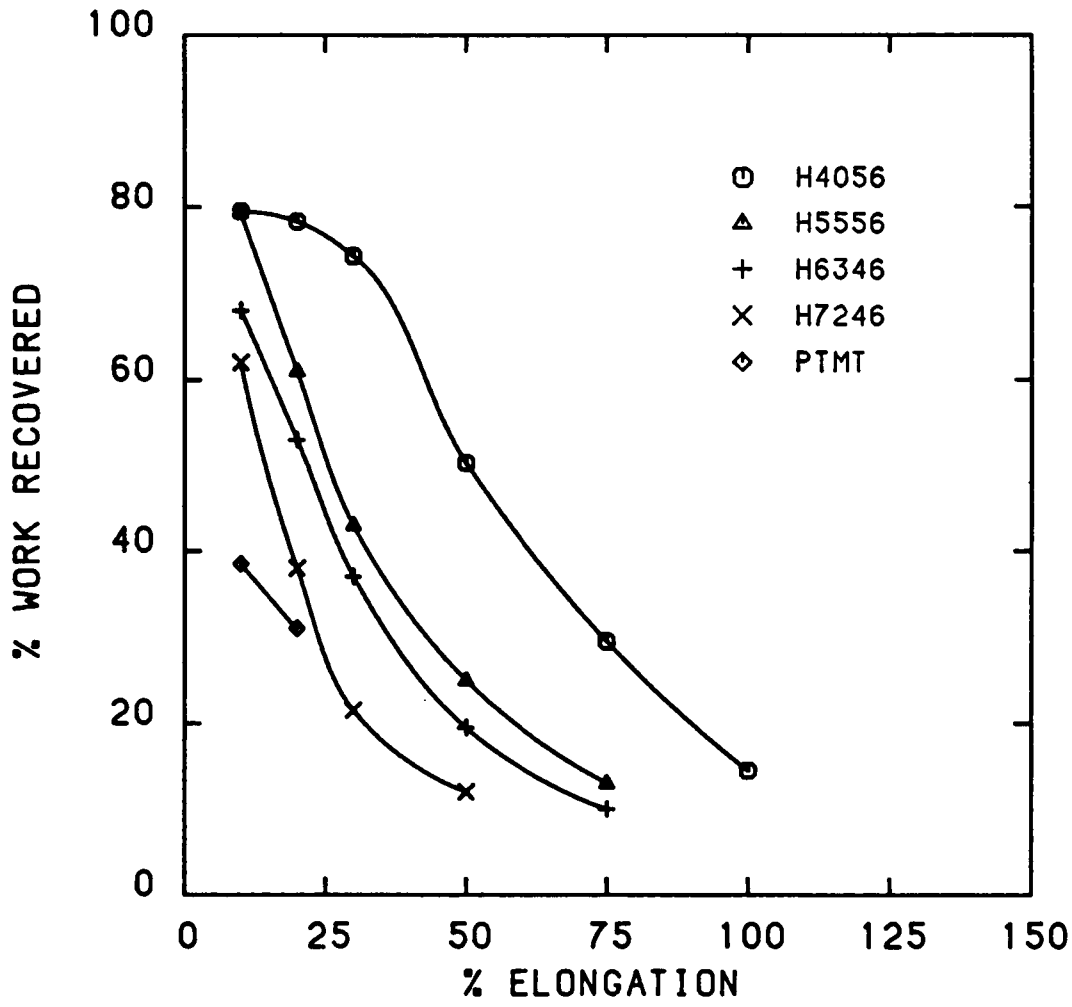


Figure 9.37: Effect of composition on the work recovery of drawn and fixed annealed filaments.

Table 9.18: Effect of composition on maximum elongation and elastic properties.

	Ultimate Elongation (%)		% Strain Recovery From 50% Elongation		% Work Recovery From 50% Elongation	
	Fix	Free	Fix	Free	Fix	Free
H4056	142	513	92	97	95	91
H5556	125	457	96	89	77	75
H6346	134	344	93	87	70	70
H7246	71	199	87	88	43	62
PTMT	30	79	89	76	–	23

Note: These filaments were spun at 50m/min and cold drawn before annealing. The H4056 filaments were annealed at 100°C, while the others were annealed at 180°C.

annealing treatments on the structure and elastic properties of these filaments are discussed below.

The filaments draw more smoothly and evenly at 100°C than at 25°C, especially at high HSCs. No fundamental changes in the microstructure of the copolymer filaments result from increasing the draw temperature from 25°to 100°C. The changes that do result are just a matter of degree. The original reason for using these two draw temperatures was to investigate the difference in drawing above and below the glass transition temperature of the PTMT segments. However, the critical factor was found to be the T_g of the amorphous mixture of PTMT and PTMO segments in the copolymers, instead. In H4056, H5556, and H6346 most of the glass transition region is below 25°C. With these compositions, both draw temperatures are above the T_g of the filament, so no fundamental differences in drawing behavior result. Drawing at the higher temperature reduces the tension in the filaments and less β-form crystallites are produced. There is also a small annealing effect on the filaments resulting from the higher temperature. In H7246, a major portion of the glass transition region is above 25°C. Raising the temperature to 100°C makes these filaments draw much more smoothly and easily. The neck in the draw region is much less pronounced.

The T_g of pure PTMT is between the two draw temperatures and there is a major difference between the drawing behaviors at these two temperatures. During cold drawing there is a very pronounced neck region and numerous voids are created in the filament. The filaments draw very unevenly and often

break before fully drawing. The large stresses produce predominantly β-form crystallites. At 100°C, the filaments draw much more smoothly and few voids are created. The tension is much lower and α as well as β-form crystallites are produced. The effect of drawing temperature and tension on PTMT filaments have been investigated in more detail by Lu and Spruiell [115].

During drawing, the tie molecules and taut bridge segments disrupt the crystalline domains and cause the hard segments to become highly oriented. The amorphous chains are unable to completely disorient after removal of the drawing stress due to the deformed crystalline superstructure. There are apparently some differences in the conformations of the interdomain chains in fully drawn filaments that result from differences in initial SDR, but it is difficult to separate these effects from those of post drawing.

During fixed annealing, much of the orientation produced by drawing is retained. Crystallization of the hard segments in the more extended amorphous chains results in the formation of additional "bridge" segments. Relatively small crystallites are produced because of the limited mobility of the amorphous PTMT segments. The stress–strain curves of the fixed annealed filaments are very similar to those of the drawn filament.

During free annealing, the amorphous chains are able to recoil to a large extent and the crystallites disorient slightly. Because the amorphous chains are more highly coiled, crystallization results in the formation of more "loops" in these filaments than in the fixed annealed filaments. Free annealing produces larger crystallites and a higher DPS than in fixed annealing because of the

greater mobility of the amorphous PTMT segments.

The stress–strain behavior and elastic recovery of these filaments are determined by the composition, crystalline orientation, DPS, and by the nature of the interdomain chains. Elastic recovery increases, in general, as HSC decreases within the range of compositions studied. High f_c and high DPS have been shown to increase elastic recovery. Drawing greatly reduces the plastic deformation that occurs in these filaments during subsequent stretching. The drawn filaments build up stress much more quickly, are stronger, and have higher retractive stresses than the undrawn filaments. The type and relative proportion of interdomain chains play an important role in determining the stress–strain behavior and elastic properties of these filaments. Taut bridge molecules lead to high stresses during extension and reduced plastic deformation, but result in lower elongations to break. The "loops" provide a drawing mechanism which results in more plastic deformation, higher elongations to break, and lower elastic recovery.

Two types of mechanical behavior are observed depending on whether the drawn filaments are fixed annealed or free annealed. Because of the greater portion of bridge type segments in the fixed annealed filaments, they can be stretched to substantially greater portions of their ultimate elongation than free annealed filaments without major reorganization of the crystalline domains. As a result, they exhibit less plastic deformation than the free annealed filaments. The fixed annealed filaments have much steeper stress–strain curves than free annealed filaments. This means they build up stress more rapidly

during stretching and have higher retractive stresses than the free annealed filaments, but have only limited extensibility. These filaments would be good for applications demanding high strength and good retractive ability but requiring only low fiber extensions. Some copolyester filaments made in this way are being used as sutures.

Free annealed filaments have a lower modulus, a much higher elongation to break and a wider elastic range than fixed annealed filaments, but exhibit more plastic deformation during stretching and have a lower tensile strength. Thus, there is a trade-off between high elastic recovery and high extensibiblity.

CHAPTER 10

CONCLUSIONS

10.1 Structure Development in As-spun Filaments

Studies of the crystallization kinetics show that the crystallization rate and optimum crystallization temperature both decrease as hard segment content decreases. The sluggish crystallization kinetics of the copolyester-ethers low in HSC do not allow them to crystallize on-line when spinning into air. The filaments produced in this manner are very tacky and stick together during take-up. By spinning through a water quench bath, the filaments are cooled much more quickly and solidify enough to prevent a sticking problem. Thus, elastic filaments can be produced from all compositions by this route.

The filaments are rapidly quenched to the bath temperature during spinning and most of the crystallization is believed to take place after quenching. The crystallization rate and DPS are controlled by the composition and the difference between the bath temperature and the optimum crystallization temperature for that composition. The H5556 filaments crystallize most rapidly, followed by H6346 and H7246. The sluggish crystallization kinetics of the H4056 composition cause it to crystallize very slowly on the spinline although it reaches a high degree of phase separation after aging at room temperature for some time.

The filament microstructure consists of small lamellar-like crystallites dispersed in an amorphous matrix. The crystallites become more closely spaced as HSC increases, and more highly oriented as SDR increases. No appreciable orientation of the amorphous phase could be detected in the as-spun filaments.

The degree of phase separation in the quenched filaments decreases as HSC increases. Only the shorter sequences are believed to crystallize at the bath temperature (~26.5°) because of the high degree of undercooling. Annealing produces large increases in the DPS and the size of the crystallites in all compositions except H4056, which reaches a relatively high level of phase separation and has fairly well developed crystallites after aging at room temperature. During annealing at small ΔT_u, the longer sequences are able to diffuse to the growth front and crystallize.

In compositions high in HSC, the crystallites are able to thicken upon annealing just as in the homopolymer. The thickness depends primarily on the degree of undercooling and is not too sensitive to composition except when the sequence length is shorter than the optimum needed by the growing crystal. The crystallites grow primarily by the addition of chain stems to their equatorial surfaces.

The large increase in the long period of some of the copolymers upon annealing can not be explained by an increase in the thickness of the crystallites alone. The thickness of the amorphous layer in the copolymers must also increase as the degree of undercooling is reduced. There is evidence that the smaller crystallites, which probably form from shorter sequences, melt during

annealing. The net effect is that only larger more widely spaced crystallites are left after annealing.

Thus, fractionation according to sequence length may occur during crystallization and annealing. Only a portion of the sequences are able to crystallize at any given degree of undercooling. Long hard segments diffuse very slowly at high undercooling, while crystallites composed of short sequences are thermodynamically unstable at low undercoolings. The highest DPS may be achieved by crystallizing or annealing at low ΔT_u, and then cooling the sample slowly to the end use temperature. Both long and short segments would be crystallized in this manner.

10.2 Modulus–Structure Relationships

Models of the mechanical response of various types of microstructures show that the crystalline and amorphous phases in the copolyester filaments should be considered to be co-continuous. The crystallites are dispersed in a amorphous matrix, but are connected by tie molecules in the axial direction. Calculations of γ_c based on β_c and the estimated degree of crystallinity in these samples suggests that the crystallites do not impinge upon one another in the radial direction.

The model suggests that the number of tie molecules increases, in general, as the HSC increases; probably as a result of the longer hard segments and the shorter distance between crystallites. The number of tie molecules

also increases as the degree of crystallinity increases. The number of taut tie molecules may increase during annealing as a result of crystallite growth or as a result of a tightening of loose tie molecules as the crystallites thicken.

The modulus of the amorphous phase is raised by the presence of dissolved hard segments. The increase in the macroscopic modulus observed as HSC increases is probably the result of both an increase in the number of taut tie molecules and an increase in E_a as the fraction of hard segments dissolved in the amorphous phase increases. The amorphous modulus decreases in any given composition as the DPS increases. This results from the increase in the proportion of PTMO segments in the amorphous phase as the dissolved hard segments crystallize.

Thus, the relationship between modulus and annealing temperature can be understood. The as-spun filaments have a relatively low DPS and only a few tie molecules. Upon annealing, the DPS and number of tie molecules both increase. At large ΔT_u, the crystallinity is low and there are too few taut tie molecules to have much effect on the modulus. The increase in DPS, however, causes the modulus of the amorphous phase to drop significantly resulting in a reduction of the macroscopic modulus. At small ΔT_u, the number of tie molecules has grown large enough to have a considerable influence on the macroscopic modulus. At some point, the increase in modulus caused by the tie molecules begins to outweigh the decrease caused by the drop in E_a. An increase in the macroscopic modulus is then observed.

10.3 Deformation Behavior and Mechanical Properties of As-Spun Filaments

SAXS experiments show that the microstructure deforms in a nearly affine manner at low elongations and that the original microstructure is recovered upon release of the stress. At these elongations, nearly all of the strain takes place in the amorphous phase and there is little plastic deformation of the crystalline phase. At higher elongations, the stresses exerted by the tie molecules and taut bridge segments become large enough to pull apart the crystallites. Plastic deformation of the crystalline phase reduces the elastic performance of the filaments.

The stress at elongations above the yield point increases as HSC increases because of more dissolved hard segments in the amorphous phase and an increase in the number of tie molecules between crystallites. The stress also increases upon annealing. This is believed to result from an increase in the number of tie molecules and physically cross-linked elastomeric chains as the crystallites grow larger. The bridge molecules play a more important role in determining the stress at these elongations than they do in determining the modulus.

The elastic properties are influenced greatly by the microstructure of the filaments. The relative amounts of each phase, the size, spacing and orientation of the crystallites, the number of the tie molecules, and the degree of phase separation all influence the elastic behavior. The composition deter-

mines the relative amounts of each phase and to some extent the number of tie molecules. As HSC decreases, the crystallites are spaced further apart and the hard segments become shorter. Both effects make it more difficult for a PTMT segment to bridge the amorphous region between crystallites. Fewer hard segment tie molecules mean less plastic deformation. This is one reason much better elastic properties are observed in H4056 than H7246. Annealing promotes phase separation and reduces the amorphous orientation. A greater DPS results in higher elastic recovery by increasing the number of amorphous chains that are cross-linked and by driving dissolved hard segments out of the elastomeric phase. Increasing the SDR increases the orientation of the crystalline chains and produces lamellae that are preferentially aligned with their long axis perpendicular to the fiber axis. This reduces rotation and shearing of the lamellae during stretching since the chains are aligned in the direction of the applied force.

In the copolyester filaments, tenacity increases as HSC and crystalline chain orientation increase. Filaments high in HSC may, in some cases, exhibit higher breaking stresses than pure PTMT filaments as a result of the energy dissipation mechanism provided by the domain structure. The elongation to break is reduced as HSC and orientation increase. Much of the domain structure is destroyed during very large deformations, and as a result, the initial DPS has only a secondary effect on these properties. Thus, the HSC and orientation of the hard segments play a significant role in determining the fracture behavior, while the DPS has only a minor effect.

10.4 Structure and Properties of Drawn Filaments

During cyclic loading of the H4056 filament to 250% elongation, the force required to stretch the filament decreased enormously between the first and second cycles, yet the retactive force remained the same. Thus, it seemed that drawing might provide a viable route for reducing the plastic deformation of the copolymer filaments during subsequent stretching. In this spirit, the effects of drawing and annealing treatments on the structure and elastic properties of these filaments were then studied. The results are discussed below.

The filaments draw more smoothly and evenly at 100°C than at 25°C, especially at high HSCs. No fundamental changes in the microstructure of the copolymer filaments result from increasing the draw temperature from 25°to 100°C. The changes that do result are just a matter of degree.

During drawing, the tie molecules and taut bridge segments disrupt the crystalline domains and cause the hard segments to become highly oriented. The amorphous chains are unable to completely disorient after removal of the drawing stress due to the crystalline superstructure. There are apparently some differences in the conformations of the interdomain chains in fully drawn filaments that result from differences in initial SDR, but it is difficult to separate these effects from those of post drawing.

During fixed annealing, much of the orientation produced by drawing is retained. Crystallization of the hard segments in the more extended amorphous chains results in the formation of additional "bridge" segments. Relatively

small crystallites are produced because of the limited mobility of the amorphous PTMT segments. The stress–strain curves of the fixed annealed filaments are very similar to those of the drawn filament.

During free annealing, the amorphous chains are able to recoil to a large extent and the crystallites disorient slightly. Because the amorphous chains are more highly coiled, crystallization results in the formation of more "loops" in these filaments than in the fixed annealed filaments. Free annealing produces larger crystallites and a higher DPS than in fixed annealing because of the greater mobility of the amorphous PTMT segments.

The stress–strain behavior and elastic recovery of these filaments are determined by the composition, crystalline orientation, DPS, and by the nature of the interdomain chains. Elastic recovery increases, in general, as HSC decreases within the range of compositions studied. High f_c and high DPS have been shown to increase elastic recovery. Drawing greatly reduces the plastic deformation that occurs in these filaments during subsequent stretching. The drawn filaments build up stress much more quickly, are stronger, and have higher retractive stresses than the undrawn filaments. The type and relative proportion of interdomain chains play an important role in determining the stress–strain behavior and elastic properties of these filaments. Taut bridge molecules lead to high stresses during extension and reduced plastic deformation, but result in lower elongations to break. The "loops" provide a drawing mechanism which results in more plastic deformation, higher elongations to break, and lower elastic recovery.

Two types of mechanical behavior are observed depending on whether the drawn filaments are fixed annealed or free annealed. Because of the greater portion of bridge type segments in the fixed annealed filaments, they can be stretched to substantially greater portions of their ultimate elongation than free annealed filaments without major reorganization of the crystalline domains. As a result, they exhibit less plastic deformation than the free annealed filaments. The fixed annealed filaments have much steeper stress–strain curves than free annealed filaments. This means they build up stress more rapidly during stretching and have higher retractive stresses than the free annealed filaments, but have only limited extensibility. These filaments would be good for applications demanding high strength and good retractive ability but requiring only low fiber extensions. Some copolyester filaments made in this way are being used as sutures.

Free annealed filaments have a lower modulus, a much higher elongation to break and a wider elastic range than fixed annealed filaments, but exhibit more plastic deformation during stretching and have a lower tensile strength. Thus, there is a trade-off between high elastic recovery and high extensibiblity.

LIST OF REFERENCES

LIST OF REFERENCES

[1] A.S. Abhiraman, Y.M. Kim, and K.P. Wagener, *J. Polym. Sci.: Polym. Phys.*, **25**, 205-228 (1987).

[2] D. Acierno, J. Dalton, J. Rodriquez, and J.L. White, *J. Appl. Polym. Sci.*, **15**, 2395 (1971).

[3] S.L. Aggarwal, *Block Copolymers,* (New York: Plenum Press, 1970) pg. 102.

[4] L.E. Alexander, *X-Ray Diffraction Methods in Polymer Science,* (Huntington, New York: Krieger Publishing Company, 1979) pg. 342-343.

[5] S.S. Alexandriĭskiĭ, B.V. Petukhov, V.I. Briantsev, and Z.P. Vysotskaya, *Khimicheskiye Volokna,* (3) 22, (1971).

[6] D.C. Allport and A.A. Mohajer in *Block Copolymers,* D.C. Allport and W.H. Janes, Eds. (New York: Halstead Press, 1973) Chap. 8C.

[7] E. Andrews, *Brit. J. Appl. Phys.*, **10**, 39 (1959).

[8] S. Arakawa, in *Fiber Formation and Development of its Fine Structure,* edited by the Society of Fiber Science and Technology Japan, Kaguka Dojin, Kyoto, 1969.

[9] J.E. Ashton, J.C. Halpin and P.H. Petit, *Primer on Composite Composite Materials: Analysis,* (Stamford, Connecticut: Technomic Publishing Co., 1969) Chapter 5.

[10] M. Avrami, *J. Chem. Phys.*, **7**, 1103 (1939).

[11] M. Avrami, *J. Chem. Phys.*, **8**, 212 (1940).

[12] M. Avrami, *J. Chem. Phys.*, **9**, 177 (1941).

[13] D.V. Badami, F.P. Chappel, M.F. Culpin,D.M. Jones, and T.C. Tranter, *Rheol. Acta,* **1**, 639 (1961).

[14] F.J. Balta-Calleja and A. Peterlin, *J. Macromol. Sci., Phys.*, **B4**, 519 (1970).

[15] F.J. Balta-Calleja and A. Peterlin, *Makromol. Chemie*, **141**, 91 (1971).

[16] U. Bandara and M. Droscher, *Colloid & Polymer Sci.*, **261**, 26-39 (1983).

[17] D.C. Basset, *Principles of Polymer Morphology,* (New York: Cambridge University Press, 1981) pg. 124-143.

[18] J.F. Beecher L. Marker, R.D. Bradford, and S.L. Aggarwal, *J. Polym. Sci., Part C,* **26**, 117-134 (1969).

[19] Jayendra Bheda, Ph.D. Dissertation, The University of Tennessee, Knoxville (1987).

[20] J.W. Van Bogart, P.E. Gibson, and S.L. Cooper, *Rubb. Chem. Tech.,* **54**, 963-975 (1981).

[21] J.W. Van Bogart, A. Lilaonitkul, and S.L. Cooper, *Adv. in Chem. Series,* **176**, 4-29 (1979).

[22] H. Böhringer, *Faserforschung u. Textiltech.,* **3**, 381 (1952); *Textilfasern* **8**, 745 (1953).

[23] R. Bonart, *J. Macromol. Sci., Phys.,* **B2(1)**, 115-138 (1968).

[24] R. Bonart, L. Morbitzer, and G. Hentz, *J. Macromol. Sci., Phys.,* **9**, 447 (1974).

[25] R. Bonart and E.H. Müller, *J. Macromol. Sci., Phys. Ed.,* **10**, 177 (1974).

[26] C.M. Boussias, R.H. Peters, and R.H. Still, *J. Appl. Polym. Sci.,* **25**, 855-867 (1980).

[27] C.M. Boussias, R.H. Peters, and R.H. Still, *J. Appl. Polym. Sci.,* **25**, 869-878 (1980).

[28] F.A. Bovey, *Pure Appl. Chem.,* **54(3)**, 559-568 (1982).

[29] G. Bragato and G. Gianotti, *Eur. Polym. J.,* **19(9)**, 795 (1983).

[30] G. Bragato and G. Gianotti, *Eur. Polym. J.,* **19(9)**, 803 (1983).

[31] M.G. Brereton, G.R. Davies, R. Jakeways, T. Smith, and I.M. Ward, *Polymer,* **19**, 17-26 (1978).

[32] R.M. Briber and E.L. Thomas, *Polymer,* **26**, 8-16 (1985).

[33] W.H. Buck *Rubb. Chem. Technol.,* **50**, 109-126 (1977).

[34] W.H. Buck, R.J. Cella,Jr., E.K. Gladding and J.R. Wolfe,Jr., *J. Polym. Sci.: Symp.No.48,* 47-60 (1974).

[35] J.E. Callear and J.B. Shortall, *J. Mater. Sci.,* **12**, 141-152 (1977).

[36] W.H. Carothers and J.W. Hill, *J. Amer. Chem. Soc.,* **54**, 1579 (1932).

[37] R.J. Cella, *J. Polym. Sci.,* **42**, 727-740 (1973) and *Encycl. Polym. Sci. Technol., Suppl.Vol.2,* 485-510 (1977).

[38] M. Cesari, G. Perego, and A. Mazzei, *Makromol. Chemie,* **83**, 196-206 (1965).

[39] Eng-Pi Chang and E.L. Slagowski, *J. Appl. Polym. Sci.,* **22**, 769-779 (1978).

[40] E.S. Clark in *Structure and Properties of Polymer Films,* R.W. Lenz and R.S. Stein, Eds. (New York: Plenum Press, 1972).

[41] E.S. Clark in *Encyclopedia of Polymer Science and Technology,* Vol. 5, (New York: John Wiley & Sons, 1986) pgs. 408-415.

[42] S.B. Clough and N.S. Scneider, *J. Macromol. Sci.: Phys.,* **B2(4)**, 553-566 (1968).

[43] M. Compostella, A. Coen and F. Bertinotti, *Angew. Chemie.,* **74**, 618 (1962).

[44] Monroe Cooper in *High Technology Fibers,* **Part A**, Chapter 2. Edited by M. Lewin and J. Preston, (Marcel Dekkar, Inc.: New York, 1985).

[45] A.Y. Coran and R. Patel, *Rubb. Chem. Technol.,* **53(3)**, 781-794 (1980).

[46] John R. Dees, Ph.D. Dissertation, The University of Tennessee (1974).

[47] J.R. Dees and J.E. Spruiell, *J. Appl. Polym. Sci.,* **18**, 1053 (1974).

[48] C.R. Desper, N.S. Schneider, J.P. Jasinski, and J.S. Lin, *Macromolecules,* **18**, 2755-2761 (1985).

[49] J.V. Dawkins in *Block Copolymers,* D.C. Allport and W.H. Janes, Eds. (New York: Halstead Press, 1973) Chap. 8A.

[50] P. Dreyfuss, L.J. Fitters, and D.R. Hansen, *Rubb. Chem. Technol.,* **53(3)**, 728-771 (1980).

[51] Hans-Georg Elias, *Macromolecules,* Vol. 1 (New York: Plenum Press, 1977), pp. 386-405.

[52] G. Farrow and J. Bagley, *Textile Research Journal,* , 587-598 (1962).

[53] J.A. Faucher, *J. Polym. Sci.: Polym. Phys.,* **12**, 2153-2155 (1974).

[54] E. Fischer and J.F. Henderson, *J. Polym. Sci., Part C,* **26**, 149-160 (1969).

[55] M.J. Folkes and A. Keller, *Polymer,* **12**, 222 (1971).

[56] M. Fujimura, T. Hashimoto, and H. Kawai, *Rubb. Chem. Tech.,* **51**, 215-224 (1978).

[57] P.Y.-F. Fung and S.H. Carr, *J. Macromol. Sci., Phys.*, **B6(4)**, 621 (1972).

[58] P.Y.-F. Fung, E. Orlanda, and S.H. Carr, *Polym. Eng. Sci.*, **13**, 295 (1973).

[59] Abdul Ghaffar, Isaac Goodman, and Ivan Hall, *Br. Polym. J.*, **5**, 315-325 (1973).

[60] R.J. Gaylord and D.J. Lohse, *Polym. Eng. Sci.*, **18(5)**, 359-365 (1978).

[61] R.J. Gaylord, *Polym. Eng. Sci.*, **19(14)**, 955-965 (1979).

[62] V.E. Geller, B.V. Petukhov and Z.P. Vysotskaya, *Khimicheskiye Volokna,* (1), 47, (1968).

[63] V.E. Geller, Z.P. Vysotskaya and E.M. Eisenstein, *Khimicheskiye Volokna,* (2), 14, (1971).

[64] H.H. George, A. Holt, A. Buckley, *Polym. Eng. Sci.*, **23(2)**, 95 (1983).

[65] J. Gianchandani, J.E. Spruiell, and E.S. Clark, *J. Appl. Polym. Sci.*, **27**, 3527 (1982).

[66] M. Gilbert and F.J. Hybart, *Polymer,* **15**, 408 (1974).

[67] O. Glatter and O. Kratky, *Small Angle X-ray Scattering,* (New York: Academic Press, 1982).

[68] W. Glenz and A. Peterlin, *J. Macromol. Sci., Phys.*, **B4**, 473 (1970).

[69] W. Glenz, A. Peterlin, and W. Wilke, *J. Polym. Sci., A-2,* **9**, 1243 (1971).

[70] F. Gornick, and L. Mandelkern, *J. Appl. Phys.*, **33**, 907 (1962).

[71] A. Sh. Goykhman, *et al., Khimicheskiye Volokna,* (4), 69 (1968).

[72] A.S. Goykhman, M.P. Nosov and Y.P. Tretiakov, *Khimicheskiye Volokna,* (6), 54 (1965).

[73] I.H. Hall and M.G. Pass, *Polymer*, **17**, 807-816 (1976).

[74] A. Hamidi, A.S. Abhiraman, and P. Asher, *J. Appl. Polym. Sci.*, **28**, 567 (1983).

[75] C.D. Han and D.A. Rao, *J. Appl. Polym. Sci.*, **24**, 225-234 (1979).

[76] Z. Hashin and S. Shtrikman, *J. Mech. Phys. Solids,* **11**, 127, (1963).

[77] J.W.S. Hearle, *Polymers and their Properties, Vol. 1: Fundamentals of Structure and Mechanics*, (New York: Holstead Press, 1982) pgs. 418–420.

[78] K. Hess and H. Kiesseg, *Z. Physik. Chem.*, **A193**, 196 (1944).

[79] H.M. Heuval and R. Huisman, *J. Appl. Polym. Sci.*, **22**, 2229 (1978).

[80] H.M. Heuval and R. Huisman, *J. Appl. Polym. Sci.*, **26**, 713 (1981).

[81] S.Y. Hobbs and R.C. Bopp, *Polymer*, **21**, 559-563 (1980).

[82] S.Y. Hobbs and C.F. Pratt, *J. Appl. Polym. Sci.*, **19**, 1701-1722 (1975).

[83] S.Y. Hobbs and C.F. Pratt, *Polymer*, **16**, 462-464 (1975).

[84] M. Hoffman, G. Kampf, H. Kromer, and G. Pampus, *Adv. Chem. Ser.*, **99**, 351 (1971).

[85] V. Hurt, M. Jambrich and M. Javorek, *Chemickè Zvesti*, **12**, 401 (1958); **14**, 137 (1960).

[86] K. Imada, T. Miyakawa, Y. Chatani, H. Tadokoro, and S. Murahashi, *Makromol. Chemie*, **83**, 113-128 (1965).

[87] T. Ishibashi, K. Aoki, and T. Ishii, *J. Appl. Polym. Sci.*, **14**, 1597 (1970).

[88] O. Ishizuka, *Sen-I Gakkaishi*, **18**, 198 (1962).

[89] K. Jäckel, *Kolloid Z.*, **115**, 130 (1954).

[90] R. Jakeways, I.M. Ward, and M.A. Wildings, *J. Polym. Sci., Polym. Phys.*, **13**, 799-813 (1975).

[91] M. Jambrich and I. Diačik, *Faserforschung u. Textiltech.*, **12**, 522 (1961).

[92] L.W. Jelinski, F.C. Schilling, and F.A. Bovey, *Macromolecules*, **14**, 581-586 (1981).

[93] R. Kaiser, *Kolloid Z.*, **152**, 8 (1957); **157**, 27 (1958).

[94] R.P. Kane, *J. Elast. Plast.*, **9**, 416-438 (1977).

[95] S. Kase and T. Matsuo, *J. Polym. Sci., Part A*, **3**, 2541 (1965).

[96] S. Kase and T. Matsuo, *J. Appl. Polym. Sci.*, **11**, 251 (1967).

[97] K. Katayama, T. Amano, K. Nakamura, *Kolloid Z. Z. Polym.*, **226**, 125 (1968).

[98] S. Kavesh and J. Schultz, *J. Polym. Sci.*, **9A-2**, 85 (1971).

[99] H. Kawakami, N. Mari, H. Sato, and A. Miyoshi, *Sen-I Gakkaishi,* **16**, 155 (1960).

[100] E.H. Kerner, *Proc. Phys. Soc. London,* **69B**, 802 and 809, 1956.

[101] J.B. Knox, *Polym. Age,* **4**, 357-359 (1973).

[102] Y. Kobayashi, S. Okajima, and H. Kosuda, *J. Appl. Polym. Sci.,* **11**, 2525 (1967).

[103] J.T. Koberstein and R.S. Stein, *J. Polym. Sci.: Polym. Phys. Ed.,* **21**, 1439-1472 (1983).

[104] K. Koyama and J.E. Spruiell, Univ. of Tennessee, unpublished manuscript (1987).

[105] O. Kratky and A. Sekora, *Kolloid Z.,* **108**, 169 (1955).

[106] M. Kretz, B. Meurer, P. Spegt, and G. Weill, *J. Polym. Sci., Polym. Phys.,* **26**, 1553-1568 (1988).

[107] D.W. Van Krevelen, *Properties of Polymers,* (Amsterdam: Elsevier Publishing Co., 1972) pg. 388.

[108] S. Krimm, *J. Appl. Phys.,* **23**, 287 (1952).

[109] S. Krimm and A.V. Tobolsky, *J. Polym. Sci.,* **6**, 57 (1951).

[110] P.R. Lewis and C. Price, *Polymer,* **13**, 20 (1972).

[111] A. Lilaonitkul and S.L. Cooper, *Macromolecules,* **12(8)**, 1146-1156 (1979).

[112] A. Lilaonitkul and S.L. Cooper, *Rubb. Chem. Technol.,* **50(1)**, 1-23 (1977).

[113] A. Lilaonitkul, G. Estes, and S.L. Cooper, *ACS Polym. Preprints,* **18(2)**, 500-505 (1977).

[114] A. Lilaonitkul, J. West, and S.L. Cooper, *J. Macromol. Sci.-Phys.*, **B12(4)**, 563–597 (1976).

[115] F. Lu and J.E. Spruiell, *J. Appl. Polym. Sci.,* **31**, 1595-1607 (1986).

[116] H. Ludewig, *Polyesterfasern,* (New York: Interscience, 1971).

[117] J.A. Manson and L. Sperling, *Polymer Blends and Composites,* (New York: Plenum Press, 1976) pgs. 67–72.

[118] I. Marshall and J.R. Whinfield, in *Fibres From Synthetic Polymers,* Ed. by R. Hill, (New York: Elsevier, 1953).

[119] E. Mastowski, L. Fiszer, and J. Cypryk, *Polimery,* **12**, 566 (1967).

[120] M. Matsuo, *Encycl. Polym. Sci. Technol.,* Suppl. Vol. 2, 404-422 (1977).

[121] M. Matsuo, *Jpn. Plast.,* **2**, 6 (1968).

[122] T. Matsuo, *Sen-I Gakkaishi* (Japan), **24**, 366 (1968).

[123] R.J. Matyi and B. Crist, Jr., *J. Polym. Sci.: Polym. Phys. Ed.,* **16**, 1329-1354 (1978).

[124] Z. Mencik, *J. Polym. Sci., Polym. Phys.,* **13**, 2173-2181 (1975).

[125] T. Mochizuki, *Nippon Kagaku Zasshi,* **81**, 15 (1960).

[126] R.C. Mody and G.L. Wilkes, *ACS Polym. Preprints,* **20(2)**, 539-542 (1979).

[127] F.H. Müller, in *Strukture und Physikalische Verhalten der Kunstoffe,* K.A. Wolf, Ed., (Berlin: Springer-Verlag, 1962).

[128] H.P. Nadella, H.M. Henson, J.E. Spruiell, and J.L. White, *J. Appl. Polym. Sci.,* **21**, 3003 (1977).

[129] A. Nakai, S. Yoshikawa, and S. Oya *Sen-I Gakkaishi,* **17**, 997 (1961).

[130] K. Nakamura, T. Watanabe, K. Katayama, T. Amano, *J. Appl. Polym. Sci.,* **16**, 1077 (1972).

[131] L.E. Nielson, *ACS Polym. Preprints,* **15(1)**, 190-194 (1974).

[132] H.D. Noether and W. Whitney, *Kolloid Z. Z. Polym.,* **251**, 991 (1973).

[133] G. Perez and C. LeCluse, *High Speed Spinning of Polyethylene Terephthalate by Pneumatic Take-Up,* Text presented at the 18th *International Man-Made Conference* in Dornbirn, Austria (June 20-22, 1979).

[134] G. Perez, *Some Effects of the Rheological Properties of Polyethylene Terephthalate on Spinning Line Profile and Structure Developed in High Speed Spinning,* Rhone-Poulenc Fibres, France, July 30, 1982.

[135] R. Perret and A. Skoulious, *Macromol. Chem.,* **162**, 147-163 (1972).

[136] A. Peterlin and G. Meinel, *Makromol. Chemie,* **142**, 227 (1971).

[137] H. Petzold, *Thesis,* Dresden, 1959.

[138] A. Prietzschk, unpublished work, cited in *Physik der Hochpolymeren,* Vol. 3, Ed. by H.A. Stuart, (Berlin: Springer-Verlag 1955), p. 366.

[139] A. Reichle and A. Prietzchk, *Angew. Chemie.,* **74**, 562 (1962).

[140] M.B. Rhodes and R.S. Stein, *J. Appl. Phys.*, **32**, 2344 (1961).

[141] G.C. Richeson, M.S. Thesis, The University of Tennessee, Knoxville (1982) pg. 94.

[142] E.J. Roche, R.S. Stein, and E.L. Thomas, *J. Polym. Sci.; Polym. Phys.*, **18**, 1145-1158 (1980).

[143] S.S. Rosenhaus, L.P. Repina, and E.M. Eisenstein, *Khimicheskiye Volokna*, (2), 11 (1971).

[144] W. Roth and R. Schroth, *Faserforschung u. Textiltech.*, **11**, 365 (1960).

[145] R.J. Samuels, *J. Polym. Sci.; Polym. Phys. Ed.*, **17**, 535–568 (1979).

[146] R.J. Samuels, *Structured Polymer Properties*, (New York: John Wiley & Sons, 1974), Chap. 4.

[147] S.L. Samuels and G.L. Wilkes, *J. Polym. Sci.; Polym. Symp.*, **43**, 149-178 (1973).

[148] P. Scherrer, *Götinger Nachrichten*, **2**, 98 (1918).

[149] C.S. Schollenberger and Hewitt, *SPE Annual Tech. Conf.*, **36th**, April, 1977, p. 48-50, published by SPE: Greenwich, CT.

[150] R. Schroth, *Faserforschung u. Textiltech.*, **20**, 561 (1969).

[151] R. Schroth and E. Klein, *Sen-I Gakkaishi*, **17**, 466 (1966).

[152] G. Schubert, *Situation Report on High-Speed Spinning at the Start of the Eighties*,.

[153] J. Schultz, *Polymer Materials Science*, (Englewood Cliffs, New Jersey: Prentice-Hall, Inc.) pg. 193.

[154] R.W. Seymour, G.M. Estes, and S.L. Cooper, *Macromolecules*, **3**, 579 (1970).

[155] R.W. Seymour, G.M. Estes, and S.L. Cooper in *Recent Advances in Polymer Blends, Grafts, and Blocks*, L.H. Sperling, Ed. (New York: Plenum Press, 1974) pgs. 225-242.

[156] R.W. Seymour, J.R. Overton, and L.S. Corley, *Macromolecules*, **8(3)**, 331-335 (1975).

[157] W.C. Sheehan and T.B. Cole, *J. Appl. Polym. Sci.*, **8**, 2359 (1964).

[158] M. Shen, *Adv. Chem. Ser.*, **176**, 181-204 (1979).

[159] M. Shen, U. Mehra, and M. Nunomi, *J. Appl. Phys.,* **45(10)**, 4182-4189 (1974).

[160] J. Shimizu, *Sen-i Gakkaishi,* **33(5)**, 1977.

[161] Jiro Shimizu, *Sen-I Gakkaishi,* **38(11)**, P-499 (1982).

[162] Jiro Shimizu, N. Okui, Y. Imai, *Sen-I Gakkaishi,* **35(10)**, T-405 (1979).

[163] Jiro Shimizu, N. Okui, Y. Imai, *Sen-I Gakkaishi,* **36(4)**, T-166 (1980).

[164] Jiro Shimizu, N. Okui, A. Kanelo, and K. Toriumi, *Sen-I Gakkaishi,* **34(2)**, T-64 (1978).

[165] Jiro Shimizu, N. Okui, and T. Kikutani, *Sen-I Gakkaishi,* **37(4)**, T-135 (1981).

[166] Jiro Shimizu, N. Okui, T. Kikutani, A. Ono, and A. Takaku, *Sen-I Gakkaishi,* **37(4)**, T-143 (1981).

[167] Jiro Shimizu, N. Okui, T. Kikutani, and K. Toriumi, *Sen-I Gakkaishi,* **34(3)**, T-93 (1978).

[168] Jiro Shimizu, O. Norimasa, I. Yoshitaka, S. Nishide, and A. Takaku, *J. Appl. Sci., Polym. Phys. Ed.,* **21**, 275 (1983).

[169] Jiro Shimizu, K. Toriumi, K. Tamai, *Sen-I Gakkaishi,* **33(5)**, (1977).

[170] H.W. Siesler, *J. Poly. Sci., Polym. Lett.,* **17**, 453-458 (1979).

[171] H.W. Siesler, *Makromol. Chem.,* **180**, 2261-2263 (1979).

[172] A. Sippel, *Z. Elektrochem.,* **50**, 256 (1944).

[173] A. Skoulios, *J. Polym. Sci., Polym. Symp.,* **58**, 369-380 (1977).

[174] T.L. Smith and R.A. Dickie, *J. Polym. Sci., Part C,* **26**, 163-187 (1969).

[175] E. Sorta and G. Fortuna, *Polymer,* **21**, 728-732 (1980).

[176] B.S. Sprague, *J. Macromol. Sci.,Phys.,* **8**, 157 (1973).

[177] J.E. Spruiell, D.E. McCord, and R.A. Beuerlein, *Trans. Soc. Rheol.,* **16(3)**, 535 (1972).

[178] J.E. Spruiell and J.L. White, *Polym. Eng. Sci.,* **15**, 660 (1975).

[179] B. Stambaugh, J.L. Koenig, and J.B. Lando, *J. Poly. Sci., Polym. Phys.,* **17**, 1053-1062 (1979).

[180] B. Stambaugh, J.L. Koenig, and J.B. Lando, *J. Poly. Sci., Polym. Phys.*, **17**, 1063-1071 (1979).

[181] W.O. Statton in *Newer Methods of Polymer Characterization,* B. Ke (editor), (New York: Interscience, 1964) Chap. 6.

[182] R.S. Stein and A. Misra, *J. Poly. Sci., Polym. Phys.*, **18**, 327-342 (1980).

[183] J.C. Stevenson and S.L. Cooper, *J. Poly. Sci., Polym. Phys.*, **26** 953-966, (1988).

[184] M. Takahashi, *Sen-I Gakkaishi*, **17**, 1100 (1961).

[185] M. Takahashi, *Sen-I Gakkaishi*, **17**, 1024 (1961).

[186] M. Takayanagi, H. Harima, and Y. Iwata, *Mem. Fac. Eng., Kyushu Univ.*, **23**, 1 (1963).

[187] M. Takayanagi, K. Imada, and T. Kajiyama, *J. Polym. Sci.; Part C*, **15**, 263–281 (1966).

[188] T. Takigami, K. Yamaura, S. Matsuzawa, M. Ishikawa, and K. Miyasaka, *Polym. Eng. Sci.*, **26**, 1323-1331 (1986).

[189] K. Tashiro, Y. Nakai, M. Kobayashi, and H. Tadokoro, *Macromolecules*, **13**, 137-145 (1980).

[190] A.B. Thomson, *Fiber Structure*, ed. J.W.S. Hearle and R.H. Peters (London: Butterworth, 1963).

[191] L.R.G. Treloar, *Trans. Faraday Soc.*, **37**, 84 (1941).

[192] L.R.G. Treloar, *Trans. Faraday Soc.*, **43**, 284 (1947).

[193] S. Oya, A. Yasuda, and A. Nakai, *Sen-I Gakkaishi*, **17**, 1088 (1961).

[194] I.M. Ward and M.A. Wilding, *J. Polym. Sci., Polym. Phys.*, **14**, 263-274 (1976).

[195] G. Wegner, T. Fujii, W. Meyer, and G. Lieser, *Die Angewandte Makromol. Chemie*, **74**, 295-316 (1978).

[196] S.C. Wells, *J. Elastoplastics*, **5**, 102-121 (1973).

[197] S.C. Wells, *Handbook of Thermoplastic Elastomers*, (Atlanta: Van Nostrand Reinhold Co., 1979), Chapter 4.

[198] J.C. West and S.L. Cooper, *Science and Technology of Rubber*, (New York: Academic Press, 1978), Chapter 13.

[199] R.E. Wetton and G. Allen, *Polymer,* **7**, 331-365 (1966).

[200] J.L. White, *J. Appl. Polym. Sci.,* **8**, (1964).

[201] J.L. White, K.C. Dharod and E.S. Clark, *J. Appl. Polym. Sci.,* **18**, 2359 (1974).

[202] J.L. White and J.E. Spruiell, *J. Appl. Polym. Sci.: Appl. Polym. Symp.,* **33**, 91 (1978).

[203] K.H. Whittock, *Plastica,* **26(10)**, 438-448 (1973).

[204] G.L. Wilkes and J.A. Emerson, *J. Appl. Phys.,* **47(10)**, 4261-4264 (1976).

[205] W.K. Witsiepe, *Adv. Chem. Ser.,* **129**, 39–60 (1973).

[206] J.R. Wolfe, Jr., *Rubb. Chem. Technol.,* **50**, 688-703 (1977).

[207] Bernard Wunderlich, *Macromolecular Physics,* Vol. 2 (New York: Academic Press, 1976).

[208] H. Yasuda, H. Sugiyami, and H. Yanagawa, *Sen-I Gakkaishi,* **35(9)**, T-370 (1979).

[209] M. Yokouchi, Y. Sakakibaru, Y. Chatani, and H. Tadokaro, *Macromolecules,* **9(2)**, 266-273 (1976).

[210] N. Yoshihara, A. Fukushima, Y. Watanabe, A. Nakai, S. Nomura, and H. Kawai, *Sen-I Gakkaishi,* **37(10)**, T-387–T413 (1981).

[211] G. Zaiser, *Plastics Engineering,* **34(5)**, 61–64 (1978).

[212] Andrzej Ziabicki, *Fundamentals of Fiber Formation,* (New York: John Wiley & Sons, 1976) Chapters 6-7.

[213] A. Ziabicki, *J. Appl. Polym. Sci.,* **2**, 24 (1959).

[214] A. Ziabicki, *Kolloid Z.,* **167**, 132 (1959).

[215] A. Ziabicki, *Kolloid Z.,* **175**, 14 (1961).

[216] A. Ziabicki and K. Kedzierska, *J. Appl. Polym. Sci.,* **2**, 14 (1959).

[217] A. Ziabicki and K. Kedzierska, *J. Appl. Polym. Sci.,* **6**, 111 (1962).

[218] A. Ziabicki and K. Kedzierska, *J. Appl. Polym. Sci.,* **6**, 361 (1962).

[219] A. Ziabicki and K. Kedzierska, *Kolloid Z.,* **171**, 51 (1960).

[220] A. Ziabicki and K. Kedzierska, *Kolloid Z.,* **171**, 111 (1960).

[221] A. Ziabicki and K. Kedzierska, unpublished report, Gorzów, 1958.

[222] L. Zhu and G. Wegner, *Macromol.Chem.,* **182**, 3625-3638 (1981).

[223] L. Zhu, G. Wegner, and U. Bandara, *Macromol.Chem.,* **182**, 3639-3651 (1981).

[224] Y.A. Zubov, V.I. Selikhova, and V.A. Kargin, *Vysokomol. Soedinenya,* **9A**, 353 (1967).

[225] M.P. Zverev and L.A. Polovikhina, *Khimicheskiye,* **3**, 43 (1969).

APPENDIX

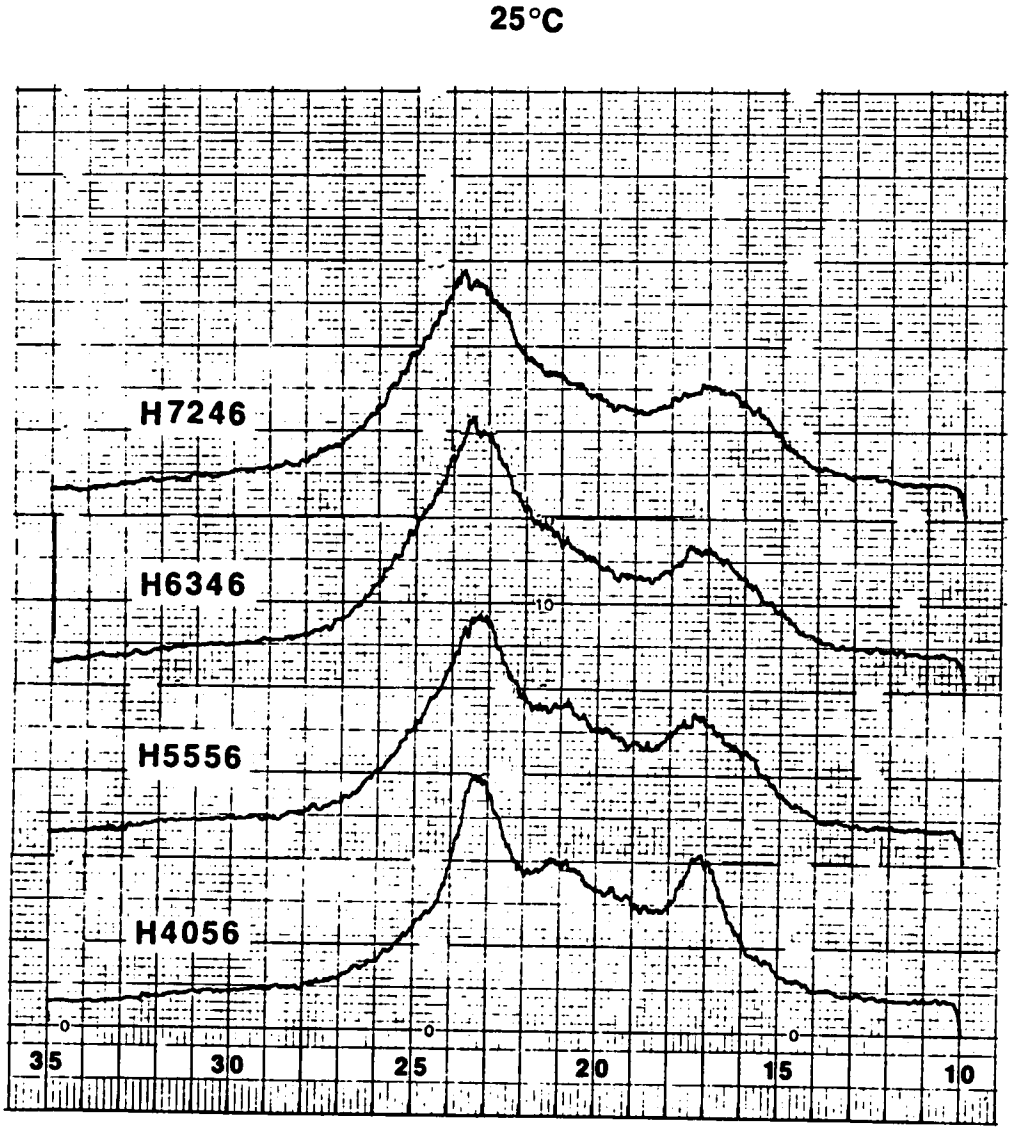


Figure A.1: Equatorial WAXD scans of filaments spun at 300m/min and aged at room temperature.

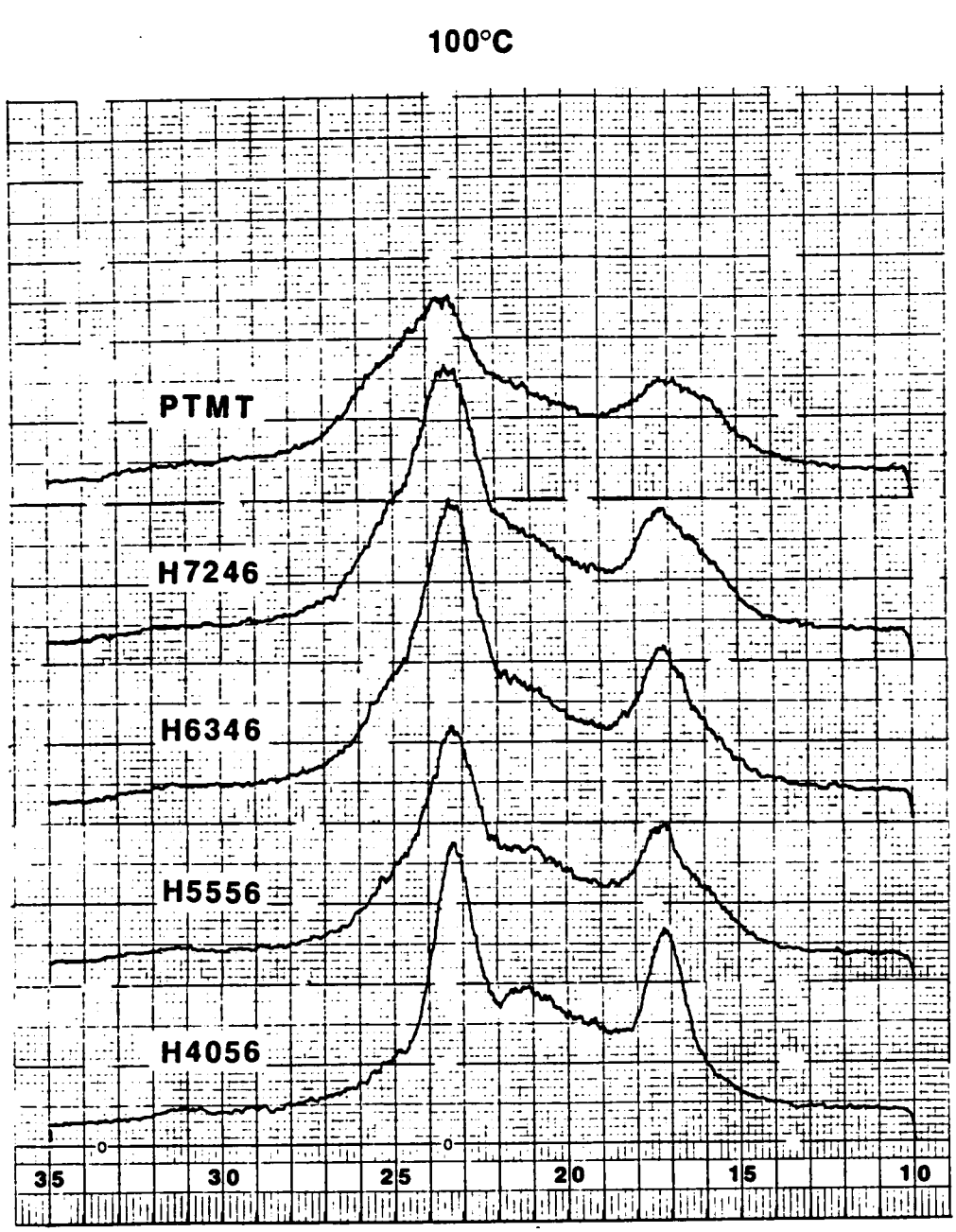


Figure A.2: Equatorial WAXD scans of filaments spun at 300m/min and annealed at 100°C.

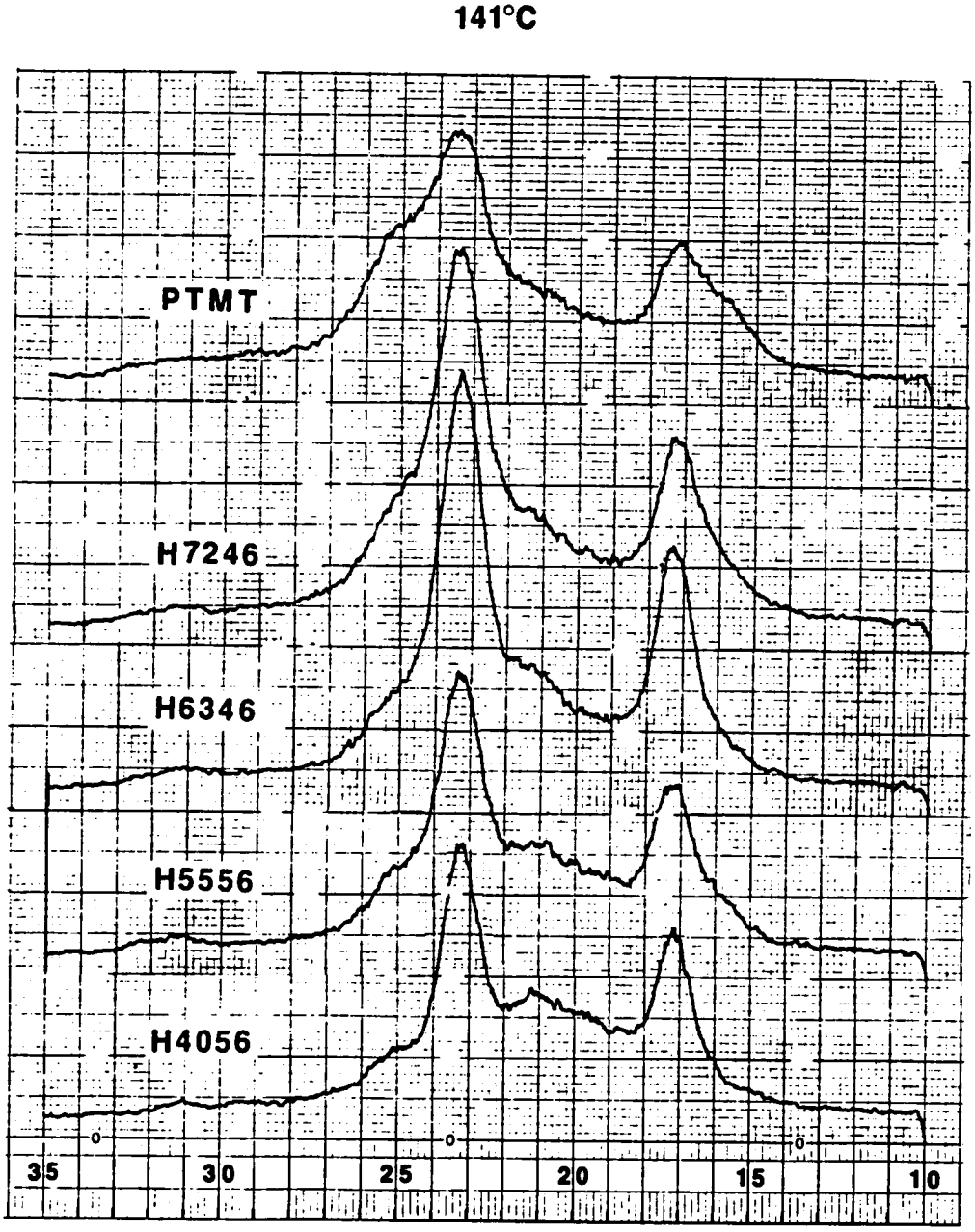


Figure A.3: Equatorial WAXD scans of filaments spun at 300m/min and annealed at 141°C.

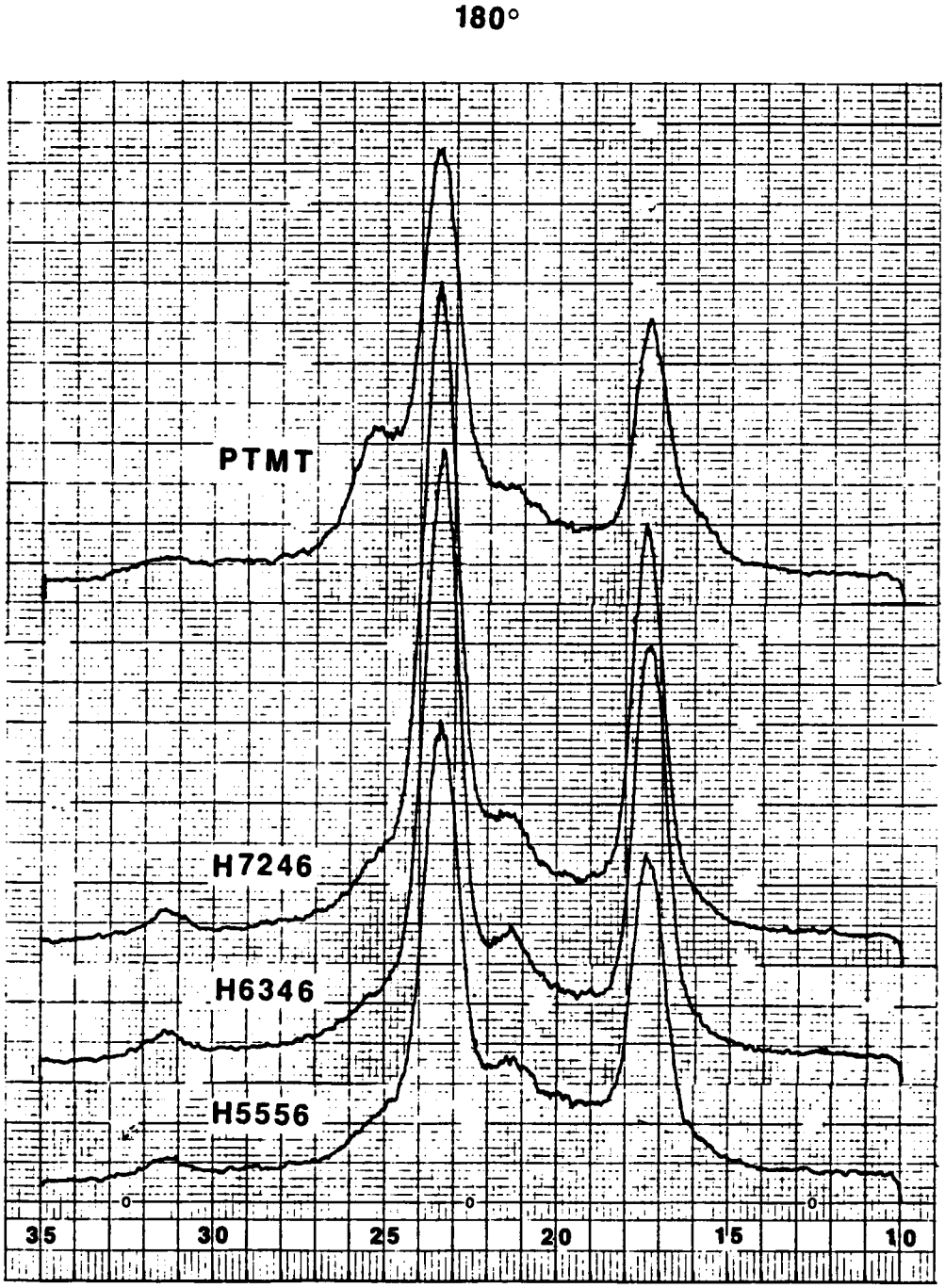


Figure A.4: Equatorial WAXD scans of filaments spun at 300m/min and annealed at 180°C.

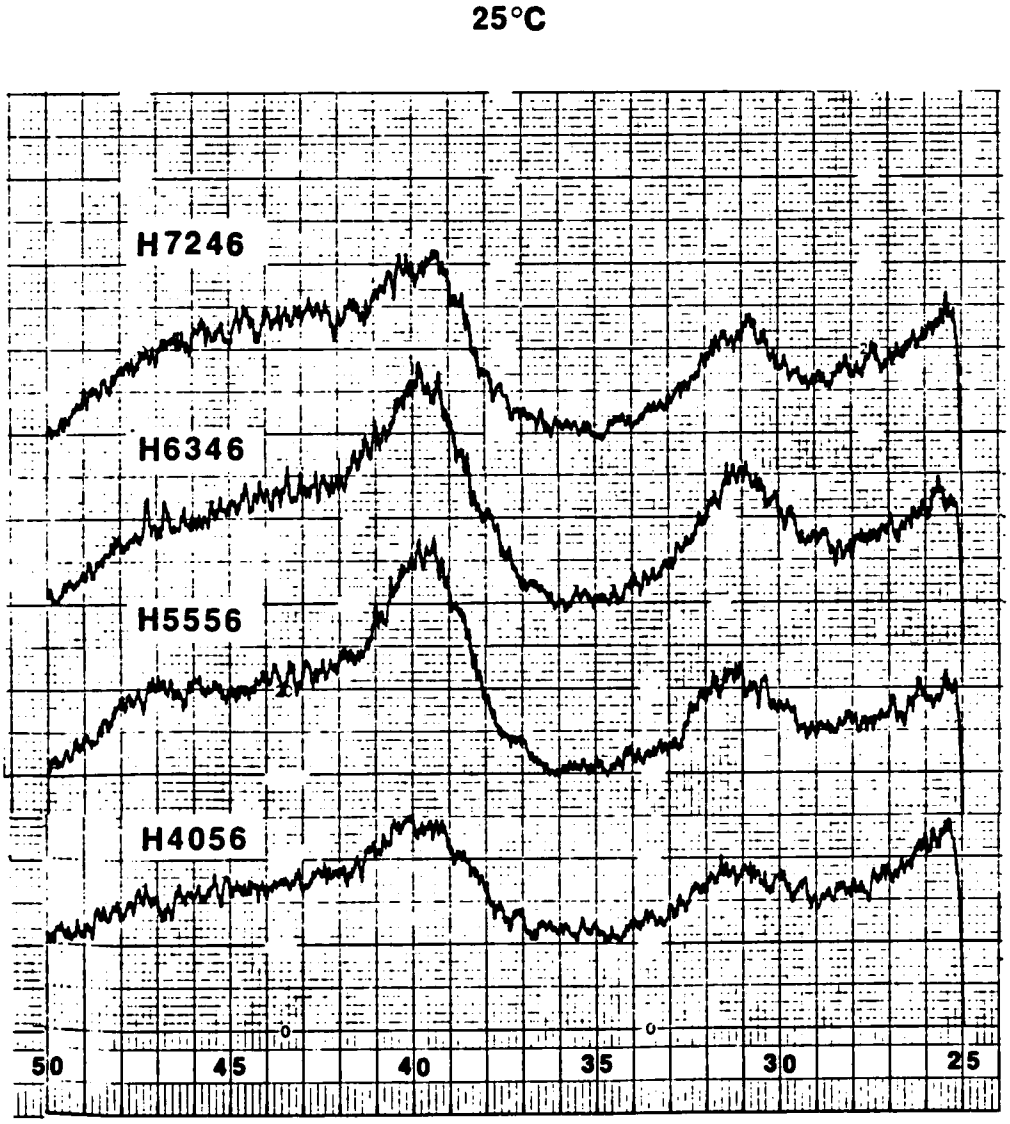


Figure A.5: Meridional WAXD scans of filaments spun at 300m/min and aged at room temperature (25°C).

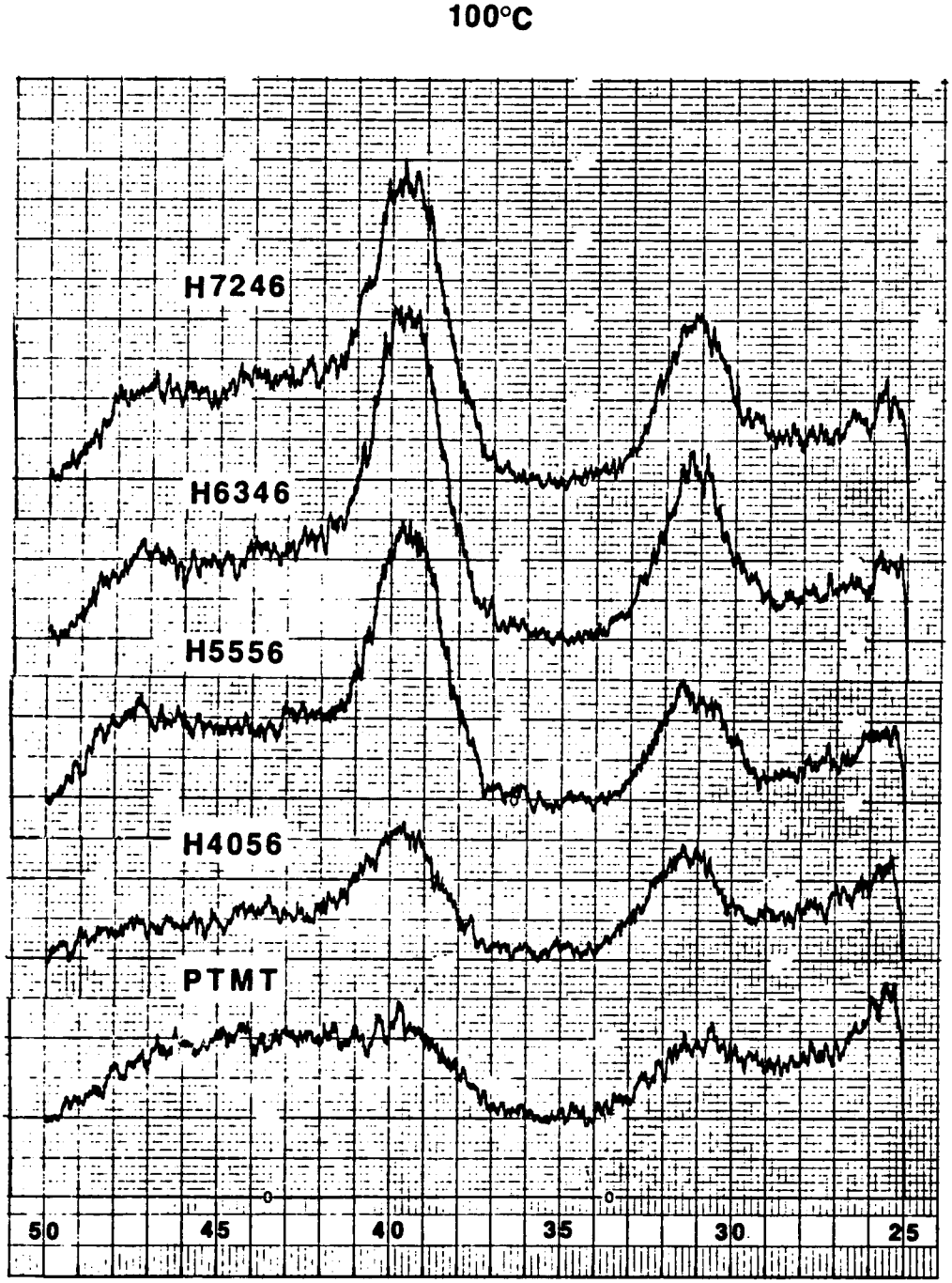


Figure A.6: Meridional WAXD scans of filaments spun at 300m/min and annealed at 100°C.

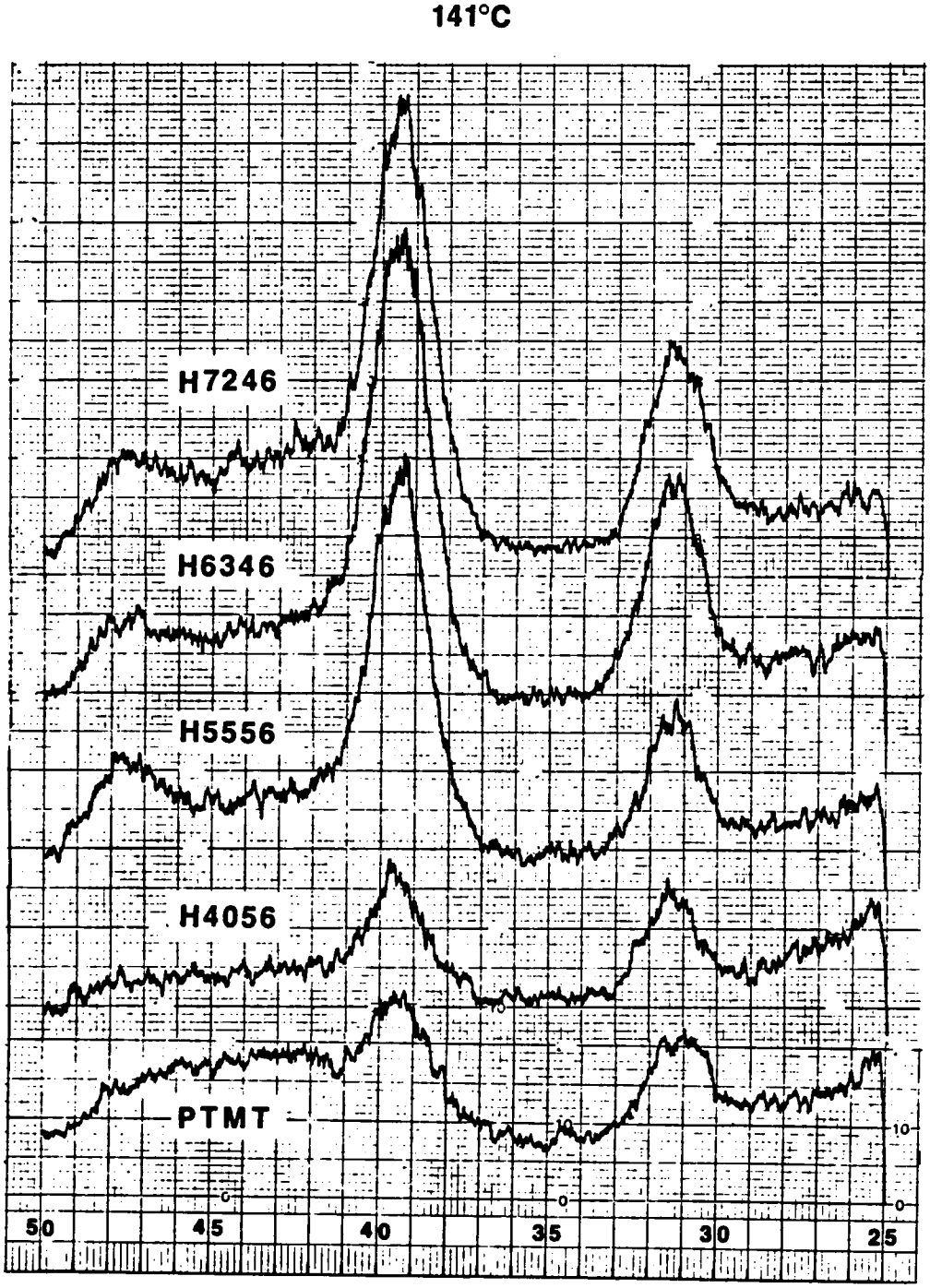


Figure A.7: Meridional WAXD scans of filaments spun at 300m/min and annealed at 141°C.

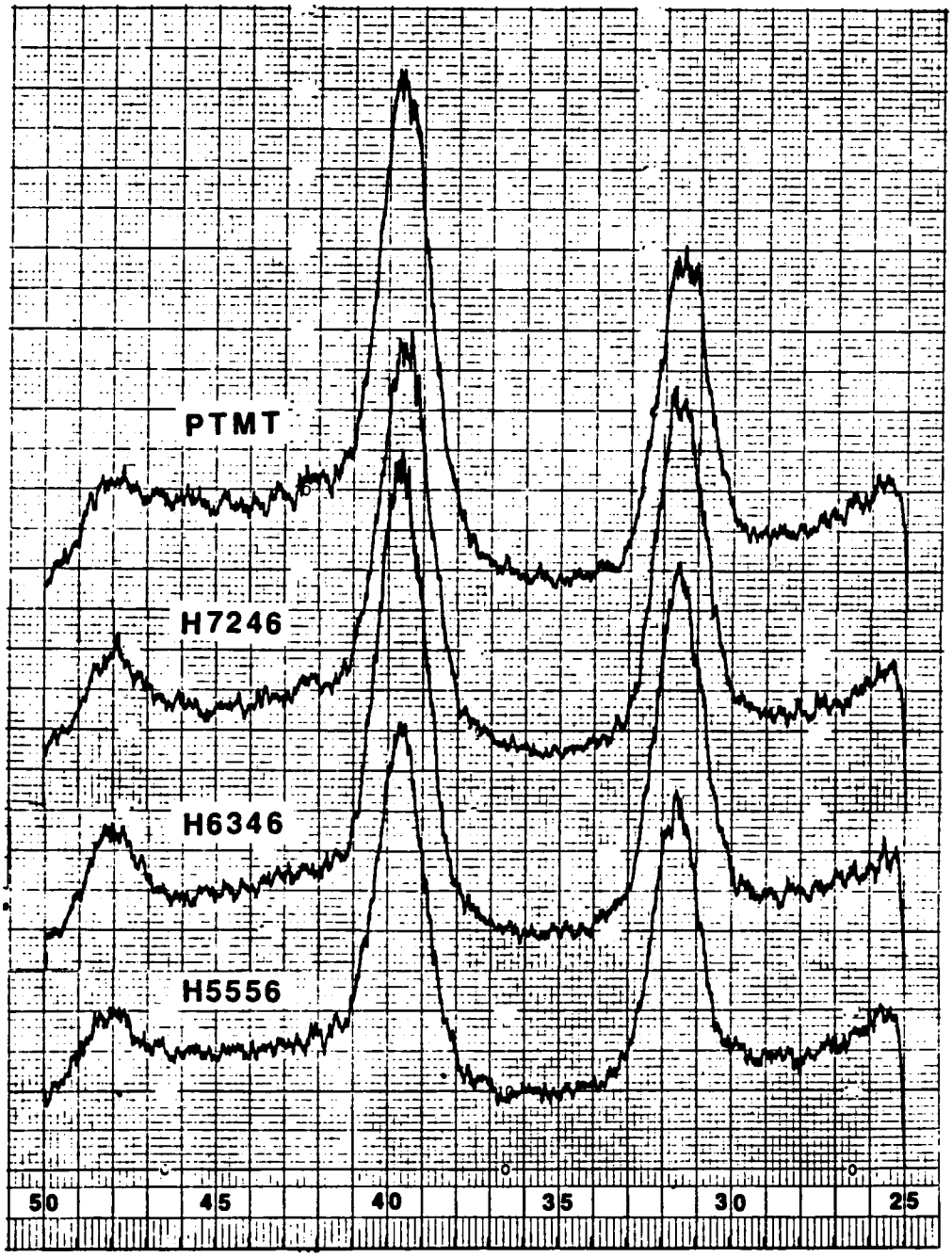


Figure A.8: Meridional WAXD scans of filaments spun at 300m/min and annealed at 180°C.

Table A.1: Degree of phase separation of drawn filaments.

50m/min				
Sample	H4056	H5556	H6346	H7246
AS	0.57	0.52	0.36	0.31
As FREE	0.66	–	–	0.70
CD	0.53	0.37	0.25	0.19
HD	0.60	0.45	0.28	0.27
CD FIX	0.62	0.78	0.63	0.56
HD FIX	0.62	–	–	0.59
CD FREE	0.66	0.79	0.66	0.67
250–300m/min				
AS	0.56	–	–	0.29
FIX	0.67	–	–	0.59
HD	0.60	0.46	0.33	0.30

Key to headings: AS: as-spun, AS FREE: as-spun and free annealed, CD: cold drawn, HD: hot drawn, CD FIX: cold drawn and fix annealed, HD FIX: hot drawn and fix annealed, CD FREE: cold drawn and free annealed. H4056 annealed at 100°C; other compositions annealed at 180°C.

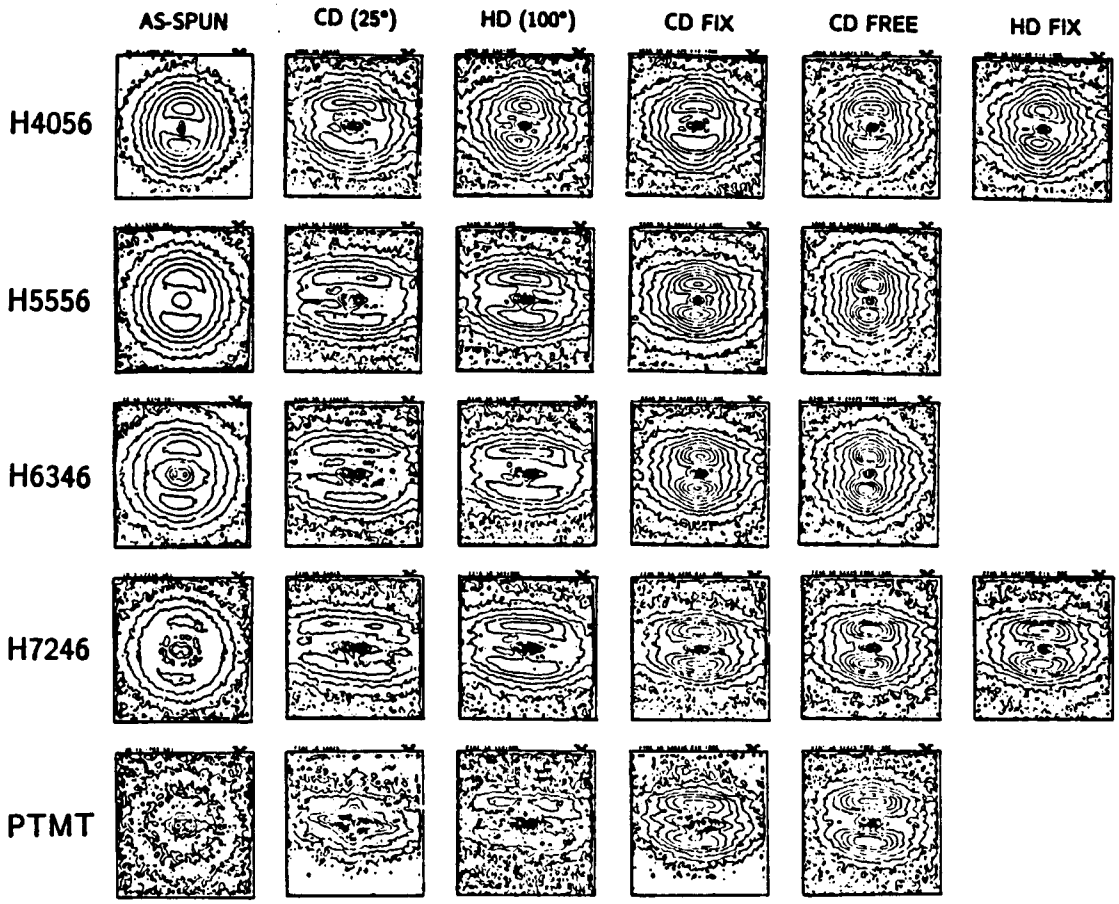


Figure A.9: SAXS patterns of drawn and annealed filaments. The as-spun filaments are shown for comparison.

Table A.2: Strain recovery of H4056 filaments.

50m/min

% Strain →	10	20	30	50	75	100	125	150	200	250	300
Sample	% Recovery										
AS	94	87	84	80	–	68	–	60	56	–	50
FREE	96	93	91	88	–	83	–	76	69	63	58
CD	87	86	85	88	88	80	69				
HD	94	93	93	94	94	90	81				
CD FREE	97	95	93	91	–	89	–	84	76	67	60
CD FIX	92	93	94	95	92	81					

250–300m/min

AS	96	95	94	88	–	74	–	65	61	56	52
FIX	98	96	95	92	–	81	–	79	70	61	59
HD	91	91	92	90	83	77					

Key to headings: AS: as-spun, FREE: free annealed, CD: cold drawn, HD: hot drawn, CD FIX: cold drawn and fixed annealed, CD FREE: cold drawn and free annealed. The annealing temperature is 100°C.

Table A.3: Work recovery of H4056 filaments.

50m/min

% Strain →	10	20	30	50	75	100	125	150	200	250	300
Sample	% Recovery										
AS	78	61	55	39	–	25	–	20	18	–	14
FREE	85	76	67	54	–	37	–	27	22	19	16
CD	58	54	49	55	36	15	11				
HD	72	63	63	46	23	13	9	7			
CD FREE	86	78	68	56	–	35	–	26	19	14	10
CD FIX	80	78	74	50	30	15					

250–300m/min

AS	69	54	–	31	–	19	–	13	11	–	7
FIX	84	65	–	40	–	24	–	15	13	10	8
HD	73	64	71	27	15	10					

Key to headings: AS: as-spun, FREE: free annealed, CD: cold drawn, HD: hot drawn, CD FIX: cold drawn and fixed annealed, CD FREE: cold drawn and free annealed. The annealing temperature is 100 °C.

Table A.4: Strain recovery of H7246 filaments.

50m/min

% Strain →	10	20	30	50	100	150	200	250	300
Sample	% Recovery								
AS	31	27	20	21	17	14	13		
FREE	79	72	65	50	33	25	21	18	16
FIX	80	73	66	50	33	25	21	18	17
CD	73	67	49	33					
HD	84	75	52	31					
CD FREE	88	82	76	62	32				
CD FIX	87	85	68	43					
HD FIX	88	86	71	41					

250–300m/min

AS	52	40	34	26	18	16	15	14	–
FIX	89	88	82	65	35	24	19	16	14
HD	81	74	51						

Key to headings: AS: as-spun, FREE: free annealed, FIX: fixed annealed, CD: cold drawn, HD: hot drawn, CD FREE: cold drawn and free annealed, CD FIX: cold drawn and fixed annealed, HD FIX: hot drawn and fixed annealed. The annealing temperature is 180°C.

Table A.5: Work recovery of H7246 filaments.

50m/min

% Strain →	10	20	30	50	100	150	200	250	300
Sample	% Recovery								
AS	12	7	6	4	3	3	4	–	3
FREE	43	36	27	16	9	6	5	4	3
FIX	45	37	29	17	9	6	5	4	4
CD	39	24	13	11					
HD	35	29	15	8					
CD FREE	58	48	36	19	7				
CD FIX	62	38	22	12					
HD FIX	65	41	23	12					

250–300m/min

AS	15	10	–	5	4	3	4	4	
FIX	60	52	–	19	7	5	4	4	
HD	46	27	14						

Key to headings: AS: as-spun, FREE: free annealed, FIX: fixed annealed, CD: cold drawn, HD: hot drawn, CD FREE: cold drawn and free annealed, CD FIX: cold drawn and fixed annealed, HD FIX: hot drawn and fixed annealed. The annealing temperature is 180°C.

Table A.6: Strain recovery of cold drawn and annealed filaments.

% Strain →	10	20	30	50	75	100	150	200	250	300
Sample	% Recovery									
H4056 CD FREE	97	95	93	91	–	89	84	76	67	60
H4056 CD FIX	92	93	94	95	92	81				
H5556 CD FREE	89	84	81	75	–	61				
H5556 CD FIX	96	92	85	77	62					
H6346 CD FREE	87	83	80	70	–	49	38	31	26	
H6346 CD FIX	93	88	82	70	52					
H7246 CD FREE	88	82	76	62	–	32				
H7246 CD FIX	87	85	68	43						
PTMT CD FREE	76	71	40	23						
PTMT CD FIX	89	47								

Key to headings: CD FREE: cold drawn and free annealed, CD FIX: cold drawn and fixed annealed. The annealing temperature is 100 °C for H4056 and 180°for the other compositions.

Table A.7: Work recovery of cold drawn and annealed filaments.

% Strain →	10	20	30	50	75	100	150	200	250	300
Sample	% Recovery									
H4056 CD FREE	86	78	68	56	–	35	26	19	14	10
H4056 CD FIX	80	78	74	50	30	15				
H5556 CD FREE	64	53	44	32	–	18				
H5556 CD FIX	79	61	43	24	13					
H6346 CD FREE	58	48	40	26	–	13	9	6		
H6346 CD FIX	68	53	37	20	10					
H7246 CD FREE	58	48	36	19	–	7				
H7246 CD FIX	62	38	22	12						
PTMT CD FREE	38	24	13	8						
PTMT CD FIX	39	31								

Key to headings: CD FREE: cold drawn and free annealed, CD FIX: cold drawn and fixed annealed. The annealing temperature is 100 °C for H4056 and 180°for the other compositions.

VITA

The author, Galen C. Richeson, graduated from Bradshaw High School in Florence, Alabama in 1974. He received his B.S. degree in Industrial Chemistry from the University of North Alabama in 1977. He then worked for the Reynold's Metals Company in Muscle Shoals, Alabama until he entered the Polymer Engineering Program at The University of Tennessee in Knoxville. The author received his M.S. degree in Polymer Engineering in August, 1982 and his Ph.D in the same program in December, 1988. He then began work for the Exxon Chemical Company at the Baytown Polymers Center in Baytown, Texas.